

THERMODYNAMIC SIMULATION OF SOLAR THERMAL POWER PLANTS

von
Ernst SATTLER, BSc

als Masterarbeit der Kommission zur Abhaltung der Masterprüfung der
Studienrichtung Wirtschaftsingenieurwesen-Maschinenbau an der
Technischen Universität Graz über das Institut für Wärmetechnik vorgelegt.

Betreuer

Dipl.-Ing. Dr. techn. Peter PECHTL
(VTU Energy GmbH)

Beurteiler

Univ.-Prof. Dipl.-Ing. Dr. techn. Christoph HOCHENAUER

Graz, im März 2013

STATUTORY DECLARATION

I declare that I have authored this thesis independently, that I have not used other than the declared sources / resources, and that I have explicitly marked all material which has been quoted either literally or by content from the used sources.

Graz,

.....

(Signature)

KURZFASSUNG

Titel: Thermodynamische Simulation von Solarthermischen Kraftwerken

Autor: Ernst Sattler

1. Stichwort: CSP
2. Stichwort: Solarturmkraftwerk
3. Stichwort: Simulation

Das Hauptziel der vorliegenden Masterarbeit ist die Erstellung eines möglichst realistischen Modells eines Solarturmkraftwerkes. Nach einer eingehenden Literaturrecherche wurde der Stand der Technik abgebildet und Schritt für Schritt ein EBSILON Professional Modell aufgebaut.

Um den Receiver und den Speicher akkurat simulieren zu können, wurde ein Microsoft Excel Programm erstellt. Dieses Berechnungsprogramm ermittelt analytisch Inputdaten für den Receiver und den Speicher. Eine möglichst optimale Größe des Speichers und der Turbine konnte ermittelt werden, indem auf Basis echter Wetterdaten eines Standortes in den Vereinigten Arabischen Emiraten Jahreszyklen durchgerechnet wurden.

Die Betriebsgrundlagen eines Solarturmkraftwerkes wurden genauso detailliert beschrieben, wie die Funktionen und Eigenschaften der einzelnen Kraftwerkskomponenten. Die gewählte Kraftwerkskonfiguration beinhaltet zwei Speichertanks, die Salzschnmelze beinhalten, welche auch als Wärmeträgermedium dient und eine 38 MW Dampfturbine, die bei geeigneten Wetterbedingungen ganztägig Strom erzeugen kann. In das Modell wurden auch verschiedene Betriebsmodi sowie Hoch- und Niederfahrvorgänge eingebaut.

Durch zahlreiche Sensibilitätsanalysen wurden die Einflüsse verschiedener Parameter auf die Jahrestromeinspeisung untersucht. Weiters wurden Tagesanalysen durchgeführt, die das Verhalten des Modells bei unterschiedlichen Wetterbedingungen abbilden. Abschließend wurde ermittelt mit welcher Kraftwerkskonfiguration ein Ganzjahresbetrieb unter Turbinenvollast möglich wäre.

ABSTRACT

Title: Thermodynamic Simulation of Solar Thermal Power Plants

Author: Ernst Sattler

1st keyword: CSP

2nd keyword: solar-tower

3rd keyword: simulation

The aim of this master thesis is the preparation of a realistic model of a solar tower power plant. After a literature research the state of the art was documented and an EBSILON Professional model was built up step by step.

For an accurate simulation of the receiver and the storage, a Microsoft Excel program was created. It calculates input data for the receiver and the storage analytically. To design the power plant with an optimum turbine and storage size, several time series simulations were run by using weather data for a place in the United Arab Emirates.

The basics of the operation of a solar tower power plant were documented, as well as a detailed functional description of the modeled power plant. The chosen plant configuration includes twin tank storage for molten salt (which is also used as a heat transfer fluid) and a 38 MW turbine that is capable of running the whole day in appropriate weather conditions. Different operating modes including startup and shutdown transitions were also modeled.

Several conditions were varied in sensitivity analysis in order to investigate the impact on the annual power plant output. Furthermore, day analysis provided an overview of the models behavior during different weather conditions. Finally an attempt was made, which plant configuration would be necessary to realize a full year and full load operation of the turbine for the chosen heliostat field.

VORWORT

Zuerst möchte ich mich besonders bei Dr. Peter Pechtl von VTU Energy GmbH aus Grambach dafür bedanken, dass er mir die Anfertigung dieser für mich überaus interessanten Masterarbeit ermöglicht hat. Im Zuge dieser Arbeit durfte ich im Rahmen meiner Literaturrecherche auch bei der Konferenz „SolarPACES 2012“ in Marrakesch, Marokko teilnehmen, wobei die Kosten dafür übernommen wurden. Diese hilfreiche Reise stellte einen unvergesslichen Höhepunkt meiner Tätigkeit dar und ich bin sehr dankbar für diese nette Geste und den damit verbundenen Vertrauensvorschuss.

Weiters waren auch die vielen Betreuungsstunden durch Dr. Pechtl sehr lehrreich und hilfreich bei meiner Arbeit, wobei mir auch immer Freiraum gegeben wurde um eigene Vorschläge einzubringen und Lösungswege zu entwickeln. Dabei möchte ich auch das angenehme und humorvolle Gesprächsklima nicht unerwähnt lassen, welches unsere Meetings stets begleitete.

Ich möchte mich auch bei allen anderen Mitarbeitern von VTU Energy recht herzlich bedanken, die mir immer freundlich zur Hilfe kamen, wenn ich Fragen hatte und oftmals sehr zuvorkommend waren.

Sehr hilfreich waren auch die Informationen von Dr. Tobias Hirsch und Dr. Stefano Giuliani vom Deutschen Zentrum für Luft- und Raumfahrt, Institut für Solarforschung, die zahlreiche Fragen freundlich und sehr umfassend beantworten konnten.

Mein Dank gilt auch Univ.-Prof. Christoph Hochenauer vom Institut für Wärmetechnik an der TU Graz, der diese Masterarbeit unterstützt und mitbetreut hat. In den gemeinsamen, sehr motivierenden Meetings, gab er mir zahlreiche hilfreiche Antworten und Gedankenanstöße, die in diese Arbeit miteingeflossen sind.

Abschließend möchte ich mich noch bei meiner Familie, meinen Freunden und meiner Freundin dafür bedanken, dass sie Geduld hatten, wenn ich während meiner Masterarbeit als auch während meines Studiums manchmal nicht soviel Zeit für sie aufbringen konnte. Herzlichen Dank auch an meinen Bruder für den Druck dieses Werkes. Besonders möchte ich mich auch bei meinen Eltern bedanken, dass sie während meines Studiums immer hinter mir gestanden sind.

Graz, 01.03.2013

Ernst Sattler

CONTENTS

NOMENCLATURE

<u>1</u>	<u>INTRODUCTION AND TASKS</u>	<u>1</u>
<u>2</u>	<u>STATE OF THE ART</u>	<u>3</u>
2.1	Collector Technologies	3
2.1.1	Parabolic Trough	4
2.1.2	Linear Fresnel Reflector	6
2.1.3	Dish Stirling System	8
2.1.4	Solar Power Tower	9
2.2	Heat Transfer Fluids	10
2.3	Heat Storage	11
2.4	Hybridization with Conventional Power Plants	12
<u>3</u>	<u>SOLAR POWER TOWER</u>	<u>14</u>
3.1	Heliostat Field	14
3.1.1	Heliostat Design	14
3.1.2	Arrangement	16
3.2	Receiver	18
3.2.1	Tube Receiver	18
a)	External Receiver	18
b)	Cavity Receiver	19
3.2.2	Volumetric Receiver	19
a)	Open or Atmospheric Receiver	20
b)	Pressurized Receiver	20
3.2.3	Fluid/Particle Receiver	20
<u>4</u>	<u>HEAT STORAGE OPTIONS</u>	<u>21</u>
4.1	Heat stored in Liquids	21
4.1.1	Twin Tank Liquid Storage	21
4.1.2	Thermocline Single Tank Storage	22
4.2	Heat stored in Liquids and Solids (Thermocline)	23
4.3	Heat stored in Solids	23
4.3.1	Packed Bed Storage (Gas operated)	23
4.3.2	Concrete Storage	24
4.3.3	Sand-based Heat Storage	24
4.4	Latent Heat Storage	25

4.4.1	Phase Change Media	26
4.4.2	Steam Accumulators	26

5 PLANT DESCRIPTION 27

5.1	Site Criteria	27
5.2	Functional Description	31
5.2.1	Main Systems	32
a)	Energy Collection System	32
b)	Thermal Storage System	32
c)	Energy Conversion System	32
5.2.2	Other systems	33
a)	Master Control System	33
b)	Electric Heat Tracing System	34
c)	Balance of Plant	34
5.3	Process Flow Diagrams	35
5.4	Operating States and Transitions	38
5.4.1	Energy Collection System	38
a)	States	38
b)	Transitions between the States	39
5.4.2	Energy Conversion System	40
a)	States	40
b)	Transitions between the states	41
5.5	Realized Plant Structure in EBSILON Professional	42
5.6	Energy Collection System	46
5.6.1	Predefined Heliostat Field and Receiver Properties	46
5.6.2	Non-Predefined Heliostat Field Properties	49
a)	Specific Tracking Consumption	49
b)	Minimum DNI for Tracking Activation	50
c)	Maximum tolerated Wind Speed	50
d)	Correction Factor for Atmospheric Attenuation	51
5.6.3	Heliostat Field Equations	51
5.6.4	Heliostat costs	52
5.6.5	Non-Predefined Receiver Properties	53
a)	Optical Efficiency (Absorptivity)	54
b)	Emissivity	54
5.6.6	Receiver Equations	54
5.6.7	Receiver Additional Information	56
5.6.8	States and Transitions	59
5.7	Heat Storage and Tank Heaters	62
5.7.1	Heat Storage Properties	62
5.7.2	Heat Storage Additional Information	62
5.7.3	Heat Storage Cost Estimation	63
5.7.4	Tank Heaters Properties	66

5.7.5	Tank Heaters Additional Information	66
5.7.6	Tank Heater States	67
5.8	Energy Conversion System	69
5.8.1	Heat Recovery Steam Generator	71
5.8.2	Steam Turbine and Generator	72
5.8.3	Condenser	75
5.8.4	Regenerative Feedwater Preheating	75
5.8.5	States and Transitions	77

6 THERMODYNAMIC SIMULATION **83**

6.1	EBSILON Professional	83
6.2	Plant Analysis	84
6.2.1	Receiver Design	84
a)	Determination of Pressure Loss	85
b)	Determination of Design Wall Temperature Difference	87
c)	Determination of the Combined Convection Coefficient (Outside)	89
d)	Part Load Investigation	91
6.2.2	Storage Design	94
6.3	Time Series Analysis	97
6.3.1	Theoretic Considerations for Storage and Turbine Size Optimization	99
6.3.2	Storage and Turbine Size Optimization	103
6.3.3	Annual Output Sensitivity Analysis	107
a)	Daily varying Ambient Conditions	108
b)	Atmospheric Attenuation	109
c)	Heliostat Reflectivity	110
d)	Absorptivity and Emissivity	111
e)	Heliostat Field Tracking Consumption	112
f)	Heliostat Field maximum tolerated Wind Speed	112
g)	Heliostat Field minimum DNI for tracking activation	113
6.3.4	Day Analysis	114
6.3.5	Theoretic Attempt for an Integration of a Longtime Storage	122

7 SIMULATION RESULTS **126**

8 CONCLUSIONS **129**

LITERATURE **131**

APPENDIX **139**

NOMENCLATURE

Abbreviations:

ADAS	Administrative and Data Analysis System
ASM	Advanced Stretched Membrane
ATS	Advanced Thermal Systems
BCS	Beam Characterization System
BOP	Balance Of Plant
CFD	Computational Fluid Dynamics
CLFR	Compact Linear Fresnel Reflector
CS	Collector System
CSP	Concentrated Solar Power
DAPS	Dynamic Aim Processing System
DCS	Distributed Control System
DISS	Direct Solar Steam
DLR	Deutsches Zentrum für Luft- und Raumfahrt
DNI	Direct Normal Irradiation
DSG	Direct Steam Generation
EHT	Electric Heat Tracing
EHTS	Electric Heat Tracing System
EPGS	Electric Power Generation System
HAC	Heliostat Array Controller
HC	Heliostat Controller
HMI	Human Machine Interface
HRSG	Heat Recovery Steam Generator
HTF	Heat Transfer Fluid
IEA	International Energy Agency
ISCC	Integrated Solar Combined Cycle
I/O	Input/Output
LFR	Linear Fresnel Reflector
MCC	Motor Control Center
MCMS	Material Control and Maintenance System
MCS	Master Control System
MIS	Management Information System
NC	Normally Closed
NO	Normally Open
ORC	Organic Rankine Cycle
PCM	Phase Change Media
PCN	Personal Computer Network
PFD	Process Flow Diagram
PLC	Programmable Logic Controllers
RS	Receiver System
SAPS	Static Aim Processing System

SGS	Steam Generation System
STP	Solar Tower Power plant
SEGS	Solar Energy Generating Systems
SR::EPOS	Save Resources :: EBSILON Performance and Optimization System
SSPS	Small Solar Power Systems
SST	Siemens Steam Turbine
TS	Time series calculation
TSS	Thermal Storage System
UAE	United Arab Emirates
UPS	Uninterruptable Power Supply

General variables:

Latin characters:

A	-	Washing cost fit parameter
C	kWh _{th}	Thermal tank capacity
CF	-	Capacity Factor
K	\$	Total specific storage cost
P _{Cy}	MW	Nominal thermal input power of the steam cycle
P _{out}	MW	Nominal output
P _{Re}	MW	Thermal output power of the receiver
Q	kJ	Heat
s	kJ/kgK	Specific entropy
SM	-	Solar Multiple
T	°C	Temperature
U*	m/s	Shear velocity
v _r	m/s	Known wind speed at a certain height
v(z)	m/s	Wind speed at a desired height
W _a	MWh	Nominal yearly output
z	m	Height above the ground
z _r	m	Height above the ground for known wind speed
z ₀	m	Surface roughness

Greek characters:

α	-	Absorptivity factor
γ_c	-	Charging utilization factor
γ_d	-	Discharge utilization factor
γ_{St}	-	Annual storage loss factor
δ_{St}	-	Fraction of annual absorbed receiver energy to storage
ε	-	Emissivity factor
$\eta_{\text{Energy Conversion}}$	-	Energy conversion system efficiency
κ	-	Von-Kármán constant

Variables used in Microsoft Excel:

Latin characters:

A	m ²	Storage surface on the inside
A	m ²	Receiver area
A _i	m ²	Pipe inside cross section area
cp	J/kgK	Specific heat capacity of the heat transfer fluid
cp,m	J/kgK	Average specific heat capacity of the storage medium
cp,w	J/kgK	Specific heat capacity of the heat transfer fluid, wall
d	m	Pipe wall thickness
D	m	Storage diameter on the inside
D _a	m	Outer pipe diameter
D _i	m	Inner pipe diameter
D _{rec}	m	Receiver diameter
Gr	-	Grashof number
H	m	Receiver height
H	m	Height of the storage inside volume
H _f	m	Free board height
H _{min}	m	Height of tank heel level
H _p	m	Pump barrel length
H _u	m	Usable storage height
k	W/m ² K	Heat transfer coefficient
k _{ΔT,cold}	W/m ²	Area specific heat loss, cold tank
k _{ΔT,hot}	W/m ²	Area specific heat loss, hot tank
k _{req,c}	W/m ² K	Required k-value of the cold tank insulation
k _{req,h}	W/m ² K	Required k-value of the hot tank insulation
m.	kg/s	Mass flow of the heat transfer fluid in the receiver
m _{min}	t	Minimum storage level
m _{max}	t	Maximum storage level
m _u	t	Usable storage capacity
n	-	number of pipes for the complete receiver
n _{pa}	-	Number of serial panels
n _{ppp}	-	Number of pipes per serial panel
Nu	-	Nusselt number
Nu _{f,o}	-	Nusselt number of the forced convection outside
Nu _{n,o}	-	Nusselt number of the natural convection outside
Nu _{l,i}	-	Nusselt number for laminar flow inside the pipe
Nu _{2300,i}	-	Nusselt number for Re=2300 inside the pipe
Nu _{10⁴,i}	-	Nusselt number for Re=10 ⁴ inside the pipe
Nu _{t,i}	-	Nusselt number for turbulent flow inside the pipe
Nu _i	-	Nusselt number inside the pipe
Pr	-	Prandtl number
Pr _w	-	Prandtl number at the inside wall of the pipe
Q _{loss,c}	kW	Heat loss of the cold tank

$Q_{\text{loss,h}}$	kW	Heat loss of the hot tank
$Q_{\text{loss,ts,c}}$	kW/K	Temperature specific heat loss of the cold tank
$Q_{\text{loss,ts,h}}$	kW/K	Temperature specific heat loss of the hot tank
Q_{tot}	MWh _{th}	Total heat capacity of the storage
Re	-	Reynolds number (inside the pipe)
Re_o	-	Reynolds number of the whole receiver in the airflow
Q_{eff}	kW	Heat absorbed in the receiver by the heat transfer fluid
r_f	-	Wall roughness factor
T_1	°C	Temperature of the heat transfer fluid at receiver inlet
T_2	°C	Temperature of the heat transfer fluid at receiver outlet
T_{amb}	°C	Ambient temperature
T_{cold}	°C	Cold storage tank nominal temperature
T_{hot}	°C	Hot storage tank nominal temperature
T_m	°C	Average temperature of the heat transfer fluid in storage
$T_{a,a}$	°C	Average air temperature
$T_{a,f}$	°C	Average temperature of the heat transfer fluid
$T_{a,m}$	°C	Mean ambient temperature
$T_{w,a,m}$	°C	Mean wall temperature at the receiver outside surface
$T_{w,i,m}$	°C	Mean inside wall temperature
v_a	m/s	Average flow velocity of the heat transfer fluid
V_a	m ³ /s	Average volumetric flow of the heat transfer fluid
$V_{a,p}$	m ³ /s	Average volumetric flow per pipe
V_{max}	m ³	Maximum needed volume for a storage tank
v_w	m/s	Wind speed at receive height

Greek characters:

$\alpha_{f,o}$	W/m ² K	Forced convection coefficient outside the receiver
α_i	W/m ² K	Convection coefficient inside the pipe
$\alpha_{n,o}$	W/m ² K	Natural convection coefficient outside the receiver
α_o	W/m ² K	Combined convection coefficient outside the receiver
α_o'	W/m ² K	Corrected combined convection coefficient outside
β	1/K	Volumetric thermal expansion coefficient
Δp	bar	Pressure loss in the receiver
ΔT	K	Design wall temperature difference
ξ	-	Pipe friction number
$\eta_{a,a}$	mPas	Average dynamic viscosity of the air
$\eta_{a,f}$	mPas	Average dynamic viscosity of the heat transfer fluid
$\eta_{a,f,w}$	mPas	Average dynamic viscosity of the heat transfer fluid, wall
$\lambda_{a,a}$	W/mK	Average thermal conductivity of the air
$\lambda_{a,w}$	W/mK	Average thermal conductivity of the pipe wall
λ_t	W/mK	Thermal conductivity of the heat transfer fluid
$\lambda_{t,w}$	W/mK	Thermal conductivity of the heat transfer fluid at the wall
$\nu_{a,a}$	m ² /s	Average kinematic viscosity of the air
$\nu_{a,f}$	m ² /s	Average kinematic viscosity of the heat transfer fluid

$\rho_{a,a}$	kg/m ³	Average air density
$\rho_{a,f}$	kg/m ³	Average density of the heat transfer fluid
$\rho_{h,f}$	kg/m ³	Density of the heat transfer fluid in the hot tank

Variables used in EBSILON Professional:

ALPHA	W/m ² K	Heat transfer coefficient of the receiver surface
AREC	m ²	Receiver surface area
AREFL	m ²	Total reflectivity area of all heliostats
CORATM	-	Correction Factor for atmospheric attenuation
DATETIMEDES	-	Date and time, for which the heliostat was designed
DNIDES	W/m ²	Design direct normal irradiation
DP12N	bar	Nominal receiver pressure drop
DTWDES	K	Design wall temperature difference
EMIS	-	Emissivity factor of the receiver surface
ETAFIELD	-	Total efficiency of the heliostat field
ETAMAT	-	Heliostat field efficiency (fully tracked and reflecting)
ETAOPT	-	Optical efficiency of the receiver
ETAWIND	-	Losses due to spillage at higher wind loads
FRECFORM	-	Code of the receiver form
H1	kJ/kg	Enthalpy of the heat transfer fluid at the receiver inlet
H2	kJ/kg	Enthalpy of the heat transfer fluid at the receiver outlet
HEIGDES	m	Design height above sealevel
HELDENS	m ² /m ²	Ratio between reflective area and used land area
K	-	Weighting factor
LATIDES	°	Design latitude
LEVACT	t	Actual heat transfer fluid content of a tank
LEVMAX	t	Maximum heat transfer fluid content of a tank
LEVMIN	t	Minimum heat transfer fluid content of a tank
M1	kg/s	Heat transfer fluid mass flow in the receiver
MAXFLOWPUMP	kg/s	Maximum allowed receiver pump flow rate
MINTRACK	W/m ²	Minimum direct normal irradiation for tracking activation
NHEL	-	Number of heliostats
PATRACK	W/m ²	Heliostat tracking consumption per reflective area
QINC	kW	Incident power on receiver aperture
QINCDES	kW	Design intercept power at the receiver aperture
QLOSSR	kW/K	Specific tank heat loss
QSOLAR	kW	Useable solar power
RECDIAM	m	Receiver diameter
RECELEV	m	Receiver elevation above the ground
RECHEI	m	Receiver height
RECTILT	°	Receiver tilt angle
RECVIEW	°	Receiver view angle
REFL	-	Reflectivity of the heliostats

REFLDES	-	Design reflectivity of the heliostats
RFOCUS	-	Ratio of focused heliostats
RSAZIM	-	Sun azimuth
RSHEIGHT	°	Sun elevation
RTAMB	°C	Ambient temperature
RTREC	°C	Receiver surface temperature
RQEFF	kW	Heat absorbed by the heat transfer fluid in the receiver
RQINC	kW	Incident power on receiver aperture (=QINC)
RQLOSS	kW	Total losses of the receiver
RQLOSSOP	kW	Optical receiver losses
RQLOSSCO	kW	Convective receiver losses
RQLOSSRA	kW	Radiation losses of the receiver
SCONV	-	Factor of wind influence on receiver convection losses
SIGMA	kW/m ² K ⁴	Stefan-Boltzmann constant
T1	°C	Heat transfer fluid temperature on the receiver inlet
T2	°C	Heat transfer fluid temperature on the receiver outlet
TSTO	°C	Temperature of a storage tank

1 INTRODUCTION AND TASKS

Preamble

The economic affluence that we know in the economically developed countries is highly based on energy intensive services, products and processes. The relatively cheap and easy utilization of fossil fuels (coal, mineral oil, and natural gas) enabled the step from a labor intensive, agriculture- and craft-oriented society towards an industrialized affluent society possible.

The larger part of the world's population lives in less developed countries which try to reach a similar affluence as the industrialized countries. So, today's enormous world energy demand will rise in the future even more. In this case, rationalization efforts may only attenuate this trend. Yet, it is the shortage of low cost fossil fuels which in combination will lead to rising prices. Furthermore, the emission of carbon dioxide, which is a product of burning fossil fuels, must be minimized to a large extent in order to at least retard the global warming.

These named factors lead to a higher demand on other sources of primary energy, particularly on regenerative forms of energy. Many of them are subject to temporal variability, such as sun power, wind power and hydropower. In order to adapt this variable offer to the differing energy demand, there is the possibility to use reserve power stations or to use energy storage. If low-cost energy storage is available, this variant is to favor.

Solar thermal power plants are well suitable to generate high amounts of electricity on demand in the sunny regions of the world due to the high global potential of solar power and the possibility to buffer thermal energy at comparatively low cost. Currently, the most research activities focus on the solar tower power plant technology. Amongst other benefits, it has higher efficiencies than other technologies.

Aim of the master thesis

The aim of this thesis is a preferably realistic model of a solar tower power plant using the EBSILON Professional® [16] software (Sometimes simply named "EBSILON" in the following). Also, all modeled and non-modeled details will be documented for a comprehensive overview. The power station should contain thermal energy storage as well as a steam turbine. Further constraints are the consideration of practical aspects in the operation of the power plant and the detection of relevant losses.

Procedure

First of all, literature research was done to collect as much practical information about the operation of solar thermal power plants as possible. The main focus was on solar tower

technology, thermal storage technology and plant operation. To gain information about the state of the art in research, it was possible to attend the SolarPACES 2012 conference in Marrakech, Morocco.

After the conference, an EBSILON model was built up based on information from literature. An Excel calculation program was established in order to analytically calculate input values for the solar tower and the storage. To gain these values, the EBSILON-Excel interface was used partly in combination with an iterative calculation.

In the progress of the project, the EBSILON model was more and more improved by integrating new information and functions. To see a realistic behavior of the power plant in time-series simulation, macros were established to structure the power plant and to simulate different operation modes and transients between these modes. After completing the model, a number of time series investigations were done, including storage and turbine sizing optimization, sensitivity analysis, and day analysis.

All collected information and data in this thesis should provide an overview of the function and the challenges of solar tower power plants with included storage.

Overview of this thesis

In **chapter 2**, “State of the Art”, a summary of the concentrating technologies used in solar thermal power plants is presented. After that, an overview of different heat transfer fluids and heat storage options is provided and an introduction to the topics of hybridization with conventional power plants is given.

In **chapter 3**, “Solar Power Tower”, more detailed information about the selected technology is provided. At the beginning, the particulars of the heliostat field will be analyzed and the different receiver technologies will be explained and compared.

In **chapter 4**, “Heat Storage Options”, the various kinds of storage will be explained in more detail considering their development status.

Chapter 5, “Plant Description”, describes the details of the modeled power plant. Aspects of the different components like function, control, loss assumptions and modeling assumptions will be discussed in detail.

The **chapter 6**, “Thermodynamic Simulation”, introduces the software EBSILON Professional® and describes the various thermodynamic simulation scenarios.

Chapter 7, “Simulation Results”, provides a summary of the simulations and analyzes the results.

An overall summary and some words about the result of the work as well as an outlook in **chapter 8** conclude this thesis.

2 STATE OF THE ART

In contrast to photovoltaic systems, solar thermal power plants work by converting solar irradiation to heat. There are many technologies available for this purpose. Also, there are many different solutions how to transport the heat, how to store it and how to convert it into another useful form of energy.

This chapter shows an overview of solar thermal power plant collector technologies, heat transfer fluids and storage options. After that, the hybridization with conventional power plants will be discussed briefly.

2.1 Collector Technologies

There are numerous methods for the collection of solar radiation and the conversion into heat. Generally, these systems can be divided into non-concentrating and concentrating systems, as shown in Figure 2-1. Also, a very rough overview of the possible concentration ratio, the approximate temperature level and power level per unit is provided.

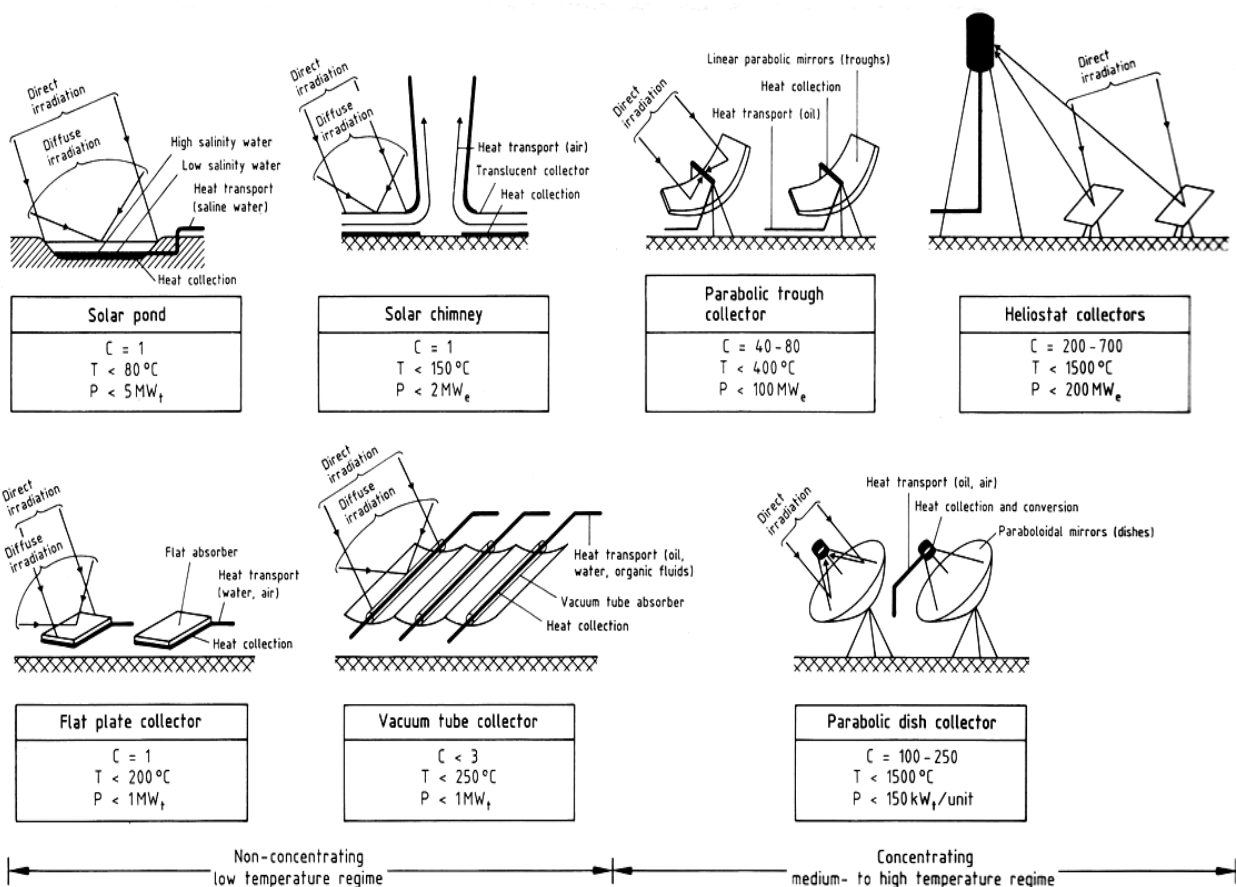


Figure 2-1: Principle methods of solar radiation collection, absorption and conversion (Linear Fresnel collectors are not shown) [72]

Non-concentrating technologies work at lower temperatures. Today flat plate and vacuum tube collectors are mainly used for heating purposes and process heat but they would also be suitable to generate electricity by an organic Rankine cycle (ORC) or a Stirling cycle. Because of their simplicity, solar ponds are still in use to generate electricity by driving an organic Rankine cycle. The pond captures the heat at the bottom of it assisted by a vertical salinity gradient which acts as an insulation [65]. Another quite different way to generate electricity is the solar chimney. Air is heated up under a large area of glass. The heated air is lighter than the air outside and flows into a chimney in the middle of the glass roof where a wind turbine is located [55].

The concentrating technologies can be divided into line-focusing systems (parabolic trough reflectors and concentrated linear Fresnel reflectors) and point-focusing systems (solar power tower and dish Stirling systems). These technologies (also called CSP - concentrated solar power) are discussed in more detail in the following.

2.1.1 Parabolic Trough

Most of all solar thermal power plants in operation are based on the parabolic trough reflector technology, which is comparatively the oldest and most proven technology. The first demonstration plant was built in Egypt in 1913, and in the late 1970s and 1980s, the technology was developed further in response to the sudden oil price increase. The idea is to heat a fluid in a long horizontal receiver by a trough-shaped mirror which focuses the radiation of the sun directly on a receiver. This is realized by a parabolic geometry of the mirror cross section, shown in Figure 2-2. [72]



Figure 2-2: Parabolic trough receiver unit at Andasol-1, Spain [77]

The receiver contains a dark absorber tube (see Figure 2-3) which is coated by a selective coating to maximize the absorption of solar radiation (at short wavelengths) and to minimize radiation losses (at longer wavelengths). To avoid high convective losses, the absorber tube is surrounded by an evacuated glass sleeve. Metal bellows are attached on both ends of the receiver to compensate heat expansions between the elements.



Figure 2-3: Parabolic trough receiver [59]

The energy absorbed in the tube is transferred to a HTF (heat transfer fluid) that is pumped through the tube. The hot fluid from many parabolic troughs is then transported to heat exchangers by a collection piping in order to produce steam and/or to heat up storage media. Each trough consists of a ca. 150-meter-long metal support structure with mirror segments mounted on it. This division can be seen in Figure 2-4.



Figure 2-4: Andasol-1, Spain [58]

The aperture of the troughs, which means the breadth of them, is typically about 6 meters. The torques required to hold and rotate the mirrors are transferred to the trough from the drive unit via a very stiff metal construction of about 150 meters that is connected to the mirror support structure over its entire length. Due to stability reasons, the rotation axis of the trough normally does not lie in the absorber tube axis but behind the mirrors. Therefore, it is necessary to link

the receiver with the collection piping by a flexible connection (see Figure 2-2) that often uses complex sealing. [70]

A benefit of this technology is that the sun-tracking only needs a single axis, which is aligned in north-south direction. Also, as mentioned before, the technology is comparatively proven. One of the disadvantages is that a lot of piping for the whole plant is necessary, including the mentioned complex sealing between the receiver and the collection piping. Most of the parabolic trough power plants use thermal oil as HTF. This HTF remains in the pipes during the night and has to be heated to avoid freezing, which causes parasitic losses. Also, common thermal oils are just stable up to about 400°C [21], which leads to a lower Carnot efficiency in the end.

Great expectations have been cherished concerning the principle of direct steam generation (DSG), which promises considerable cost savings compared to heat transfer by a HTF. The high temperatures in comparison to oil-cooling and the elimination of a separate steam generator are advantages of this system. Yet, new problems arise, like high pressures and two phases (vapor/liquid) in the absorber tubes leading to complex flow and heat-transfer properties. The technology was tested in Almería/Spain at the DISS test facility [85] and for the first time is currently built commercially with parabolic troughs at TSE 1 in Kanchanaburi, Thailand [30]. Moreover, heat storage integration for DSG is more complicated. A comparison with HTF-based parabolic trough power plants was made by Feldhoff et al. [18] in order to find out advantages and disadvantages. In current research activities, the use of molten salt as an HTF in combination with higher concentration ratios is also investigated ([31], [50], [7]) in order to gain higher efficiencies. The use of molten salt in parabolic trough power plants is a challenge due to the high risk of salt solidification in the large piping systems [70].

2.1.2 Linear Fresnel Reflector

A technology related to the parabolic trough technology is the linear Fresnel reflector (LFR). The tracking of the sun is also provided by a single axis rotation, but in this case, there are many flat (or nearly flat) mirror stripes instead of large bended mirrors in order to focus the solar irradiation (see Figure 2-5). The mirror stripes are all at the same height above the ground and rotated around their long axes to reflect the sunlight to a focus line at a height of 10 to 15 meters, which remains fixed over time. Along this line, a receiver up to 1000 meters is mounted and in it, water is directly vaporized. The steam from many parallel absorber tubes then operates a turbine. [70]

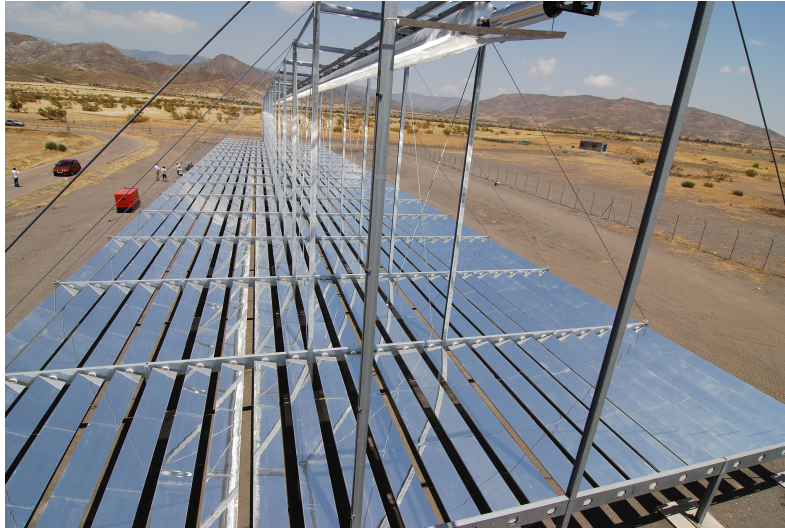


Figure 2-5: Fresnel collector prototype at Plataforma Solar de Almería, Spain [15]

In the common Solarmundo design [25], the receiver (see Figure 2-6) has a different configuration compared to the parabolic trough absorber pipes. The absorber tube is similar, and the surrounding room is filled with air or another gas. At the front side of the receiver, a glass window is installed, and on the backside, a double parabolic mirror reflects the larger part of the incoming radiation towards the absorber pipe. The smaller part of the radiation reaches the pipe directly. The secondary mirror allows a high concentration ratio in spite of the large mirrors. At the back of the mirror, insulation is attached to reduce heat losses. Each absorber tube is served by a mirror field located about 30 meter wide directly below it containing many strip mirrors, each around 1 meter wide, mounted closely together. [70]

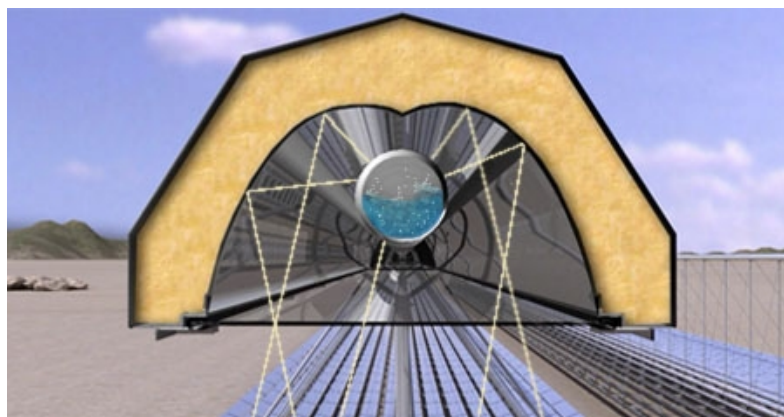


Figure 2-6: Scheme of a receiver for a linear Fresnel collector [40]

In Australia, another variant is in favor, which is known as compact linear Fresnel reflector (CLFR). In this concept, the individual mirrors are not associated with a particular absorber tube but instead channel the radiation, depending on the position of the sun, to different parallel absorber tubes in a cost-optimized way. Respectively, they alternate between one particular absorber tube and its neighbor. This strategy is used to make optimal use of the given land area. There is no secondary mirror used, but the mirrors are slightly curved by elastic deformation so that the focus lines of the mirror field are sufficiently sharp. [70]

In comparison to the one-axis tracking parabolic trough reflector, one advantage is that the mirrors are relatively inexpensive and flat. They may be mounted with slight curvature produced by elastic deformation. Also, the receiver does not need to be moved, which allows simpler machinery and offers the advantage that the absorber tubes can be attached via fixed connections to the steam collection pipes. These connections still represent one of the major development problems for the parabolic trough technology. A disadvantage compared to the parabolic trough receivers is that the concentration ratio is lower, which leads to lower reachable temperatures and efficiencies. In addition, owing to its flat construction, the system misses about 30% of the incident solar radiation for a given reflector area as compared to parabolic troughs. Furthermore, shadowing can be an issue which, however, can be minimized by optimization [35]. The integration of thermal energy storage is, as mentioned before in the parabolic trough chapter, more difficult for DSG. [70]

The largest plant, Puerto Errado 2 (Spain), uses direct steam generation [34] which produces saturated steam to produce power. On Puerto Errado 1 (Spain), tests considering the generation of superheated steam were also successful, which opens the way to higher efficiencies [36]. Also, thermal oil as well as molten salt [37] could be feasible as HTF.

2.1.3 Dish Stirling System

These systems also use a parabolic geometry to concentrate solar radiation; in contrast to parabolic trough collectors, the geometry is a paraboloid in this case. Using a paraboloid-shaped mirror (reflector), solar radiation can be highly concentrated. Due to precise manufacturing, nowadays concentration ratios up to 1000-3000 are feasible. The system tracks the sun so that the incoming radiation is always parallel to the mirror symmetry axis. For the dish concentrator, there are three types of construction: It can be made with a continuous mirror surface (Figure 2-7, left) or composed of many closely spaced, slightly curved individual mirrors (Figure 2-7, middle) or composed by separate concentrators having a common focal point (Figure 2-7, right). [70]



Figure 2-7: Dish Stirling construction types ([74], [76], [53])

The surface of the mirror is typically in the range of 50-100 m². The receiver is attached rigidly to the concentrator and reaches temperatures of about 800°C on its absorption area. Electrical energy is produced by a thermal engine which is coupled with an electric generator. The first choice for this purpose is a Stirling motor, which in principle is predestined to use an external heat source. Together with the receiver and an electric generator, it forms a unit to generate

about 10-50 kW in recent applications. Also, micro-turbines are discussed to convert the thermal energy in combination with DSG ([66], [10]) as well as the use of molten salt as HTF for very large dishes [13]. Molten salt can then be stored as well, which introduces an integration of energy storage into dish systems for the first time. [70]

The advantages of this technology is its high efficiency and compact design, which makes the technology usable for power plant up to a certain size or to provide local energy supplies in sunny regions. But the current technology does not seem to be competitive compared to other CSP technologies for larger plant sizes. For larger plants, hundreds or thousands of Stirling motors or micro-turbines are necessary, which leads to higher costs compared to single high output steam turbines of other CSP technologies.

2.1.4 Solar Power Tower

The solar power tower also uses a Fresnel principle by using a large-area field of moveable, nearly planar mirrors (heliostats) which focus the solar radiation at a single-fixed “point.” At this central point, a central receiver is mounted on a high tower. High temperatures are obtained on this tower (up to 600-1200°C [70]), depending on the cooling medium and the receiver type.

In Figure 2-8 the Gemasolar power plant is shown, which is capable of producing electricity during the whole day. The Ivanpah power plant illustrated in Figure 2-9 will be the largest solar tower power plant complex in the world after being commissioned.



Figure 2-8: Gemasolar solar tower power plant near Sevilla, Spain (20 MW) [81]



Figure 2-9: Ivanpah solar tower power plant complex, California, USA (392 MW) [73]

More of this technology will be discussed in chapter 3.

2.2 Heat Transfer Fluids

If no direct steam generation is realized, for example because of the need of an energy storage concept or technical issues related to DSG, heat transfer fluids are necessary to cool the receiver, to store the heat and to release it at a heat exchanger. In Table 2-1, the properties of the most common HTF are listed, whereas grey shaded HTF were primarily used in the past. Where available, the varying property numbers are related to their minimum and maximum temperature of the operating range.

Thermal oil is mostly a mixture of oils with high temperature stability. Therminol VP-1 (trademark of SOLUTIA Inc., USA) is one of the most used thermal oils considering solar thermal power plants; therefore, the properties are taken from it representatively. It is a eutectic mixture of diphenyl and diphenyl oxide [21] and costs about 3-4 \$/kg [87] or 57.5 \$/kWh [41].

Also, Solar Salt is widely used as an HTF, which is a eutectic mixture of sodium nitrate and potassium nitrate. The operating range of Solar Salt is higher than thermal oil, which leads to higher efficiencies, but a higher crystallization temperature has to be accepted as well. Possible suppliers are SQM S. A., Chile and Coastal Chemical LLC, USA. The price for solar salt is about 0.5 \$/kg [87] or 5.8 \$/kWh [41].

Table 2-1: Summary of the most common HTF

Name	Operating range [°C]	Solidification point [°C]	Density [kg/m ³]	Dynamic viscosity [mPas]	Specific heat [kJ/kgK]	Thermal conductivity [W/mK]
Thermal oil [21] (Therminol VP-1)	20-400	12	1064-694	4.29-0.15	1.546 - 2.628	0,136 - 0,076
Solar Salt [63] (60% NaNO ₃ + 40% KNO ₃)	260-593	238	1925-1713	4.34-1.03	1.488 - 1.545	0.492 - 0.556
HiTec [11] (53% KNO ₃ + 40% NaNO ₂ + 7% NaNO ₃)	150-538	142	1975-1690	16-1	0.461 - 1.549	0.441 - 0.163
Liquid sodium [72]	270-530	98	Ø 850	Ø 3.4	Ø 1.3	Ø 76

HiTec (Trademark of Coastal Chemical LLC, USA) heat transfer salt is a eutectic mixture of sodium nitrite, sodium nitrate and potassium nitrate. Its operating range is between Solar Salt and thermal oil. Due to its lower freezing point, it is easier to handle than Solar Salt. Despite this fact, the usage of HiTec is regressing, partly due to the toxicity of sodium nitrite and the higher price of about 0.93 \$/kg or 10.7 \$/kWh [41]. The production of a variant called HiTecXL with an even lower melting point was discontinued [12]. In the recent development, salt mixtures with more than three components and relatively low melting point (53-110°C) were found [3] and could be used as HTF.

Despite the nominal operating range [72], sodium can be used up to temperatures of about 873°C (boiling point), which would lead to a large operating range combined with high-cycle efficiencies. The disadvantage of sodium is its high combustibility when in contact with water (a particular problem is a sodium/water heat exchanger). If air is also present, there is a high risk of explosion due to the production of hydrogen. However, this risk can be controlled. In the nuclear industry sodium is in use for cooling purposes since the 1950s. Sodium was used in the IEA-SSPS project in a solar tower receiver in the 1980s (including a sodium-fire event), but today, the focus is more on a few research activities because the added fire risks must be justified. The costs for sodium are/amount to about 2 \$/kg [6].

2.3 Heat Storage

Solar thermal power plant output must satisfy the demands of the utility market. During peak demand periods, kilowatt-hour prices are high and so are financial incentives for guaranteed supply. Solar thermal power plant input is limited by daily, seasonal and weather-related

insolation changes. In order to cope with these changes, the solar input may be backed up by fossil fuels, or the solar changes may be mitigated by a buffering heat storage system. [72]

In general, heat storage can be divided into two relevant possibilities, thermal and chemical heat storage (Figure 2-10). Chemical heat storage can be realized either by the principle of sorption or endo- and exothermic chemical reactions. The principle of sorption is mainly used in absorption heat pumps, where a continuous process of absorption and desorption is used for “pumping” the heat. For CSP-related high temperature heat storage, no relevant applications are known yet. A more researched principle in this relation is the use of endo- and exothermic reactions. Especially the production of solar fuels, mainly hydrogen, by an endothermic process cycle using metal oxides and water as reactants is a wide research field ([54], [14], [43]). Also, the endothermic splitting of ammonia into nitrogen and hydrogen and – after storage – the exothermic catalytic recombination are under investigation [32].

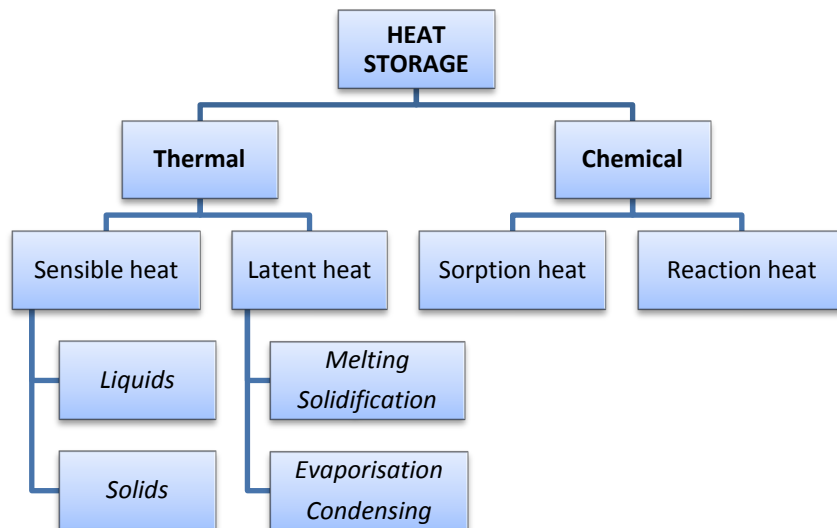


Figure 2-10: Systematic of storage possibilities

Today, the most used storage principle is the thermal heat storage, which is divided into sensible and latent heat storage. For the sensible heat storage, only the solid and liquid phase is truly relevant because of the low specific heat capacity of gases. The latent heat storage contains melting/solidification and evaporation/condensing. In **Chapter 4**, various heat storage options only based on the thermal heat storage principle will be considered because of their higher relevance for this work.

2.4 Hybridization with Conventional Power Plants

The hybridization with conventional power plants, often called ISCC (Integrated solar combined cycle), means the integration of heat produced by solar thermal collectors into a conventional power plant steam cycle. The advantage of this combination for the solar part is that an existing big turbine is used to convert the heat into energy efficiently, and the fossil fired part profits of a

fewer fuel consumption when sun energy is available. Several ISCC power plants have been realized by now. The Martin Next Generation Solar Energy Center (Figure 2-11) in Indianatown in Florida has the highest peak solar power output with 75MW. The parabolic trough farm is integrated into the natural gas-powered combined cycle Martin County Power Plant with a nominal output of 3705 MW [19].

In addition to this thesis, the research of Spelling et. al. [62] might be interesting because of its combination of an open volumetric receiver solar tower, packed bed storage and a combined cycle power plant.



Figure 2-11: Martin County Power Plant (foreground) with the integrated Martin Next Generation Solar Energy Center [19]

3 SOLAR POWER TOWER

In chapter 2.1.4, the solar power tower was already introduced briefly. The following chapter provides an overview of some details about the heliostat field (heliostat design and field arrangement) and the different receiver technologies. At this point, it should be mentioned that the heliostat field and the receiver are an integral system. The matching of both components is very important and requires an integrated design in the development stage. The solar power tower is the chosen technology for the solar thermal power plant in this thesis; therefore, it is discussed in more detail.

3.1 Heliostat Field

The heliostat field provides concentrated solar irradiation for the receiver of the solar tower. There are more or less different concepts for the design of the heliostats including different sizes as well as different arrangement philosophies. It has not really been clarified yet which constellation is the most economic one. The different systems will be shown below.

3.1.1 Heliostat Design

According to [70], for a solar tower power plant of the 100-MW-class the economic optimum for the reflective area of a single heliostat could be in the range of 100-200m², or possibly still larger. The currently built 392 MW Ivanpah solar tower power plant uses heliostats with a reflective area of each 14m² [42]. The actually used heliostats contain models with a continuous reflecting surface as well as models that consist of several (e.g. 10 or even only 2) individual mirrors. The support structure for the mirror is nearly always held in the middle by a post and can be turned around two axes through this support point. In order to track the position of the sun accurately, the use of two rotation axes is required [70].

In Figure 3-1 to Figure 3-3, some large-scale (around 150 m²) heliostat prototypes are shown. The ATS H150 was developed in 1984 and consists of 100 mirrors. The ASM 150 is a stretched metal membrane heliostat and was developed in 1995. The membrane design makes the heliostat more lightweight and cheaper but is also very sensitive at high wind loads. It uses special mechanics in order to track the sun's position. A collection of numerous smaller membranes is the heliostat developed and manufactured by SAIC Energy Products Division in 1998. It has a big reflective area but also reflection losses due to the gaps in between its membrane facets. [33]

Some heliostat examples currently in use in solar tower power plants are shown in Figure 3-4 to Figure 3-8. The heliostats at the solar test field in Jülich, Germany, rank among the smallest in operation (8 m²). The heliostats of a concept promoted by eSolar are even smaller (1.136 m²) and operated at the Sierra Sun Tower power plant in Lancaster, California. The stability of the heliostat mounting point is provided by a field-integrated scaffold. Advantages of smaller heliostats could be an easier mass production and installation. Nevertheless, a higher amount of heliostats has to be coordinated and calibrated [52]. For example, the established solar tower

3 Solar power tower

power plants PS10/PS20 and Gemasolar (both in Andalucía/Spain) use heliostats of around 120 m² each. As mentioned before, the large Ivanpah power plant uses, opposing the trend, comparatively small 14-m²-heliostats. Time will tell which system(s) will have a breakthrough.



Figure 3-1: ATS H150, 148m² [33]



Figure 3-2: ASM 150, 150m² [33]

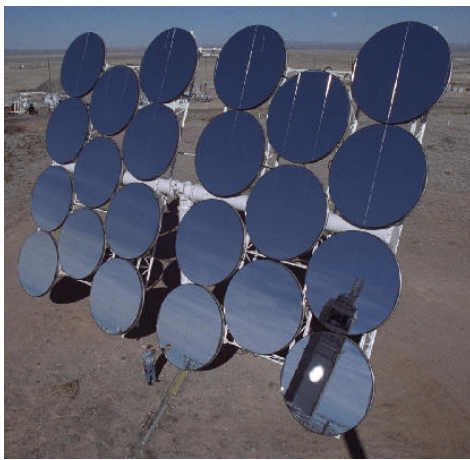


Figure 3-3: SAIC, 171m² [33]



Figure 3-4: Jülich, 8m² [70]



Figure 3-5: PS10/PS20, 121m² [70]



Figure 3-6: Gemasolar, 120m² [75]



Figure 3-7: eSolar, 1.136m² [52]



Figure 3-8: Ivanpah, 14m² [82]

3.1.2 Arrangement

The arrangement of the heliostats in the heliostat field is a quite complex topic. There are three kinds of losses which should be minimized as far as possible during the optimization process: shadowing, blocking and cosine losses. As schematically shown in Figure 3-9, internal shadowing losses occur if one heliostat shadows another one in the course of a day. Reflected solar radiation, which hits another heliostat instead of the solar tower receiver, causes blocking losses. Blocking and shading are likely to occur at low sun angles. Finally, cosine losses are losses of solar irradiation if the reflecting surface of the heliostat is not aligned perpendicularly to the rays of the solar irradiation. These losses usually have the highest magnitude and are even more relevant for the south field than for the north field (see Figure 3-10). This is the reason why the emphasis of the heliostat placement always is more or less on the north side of the heliostat field (on the northern hemisphere). Comparatively small solar tower power plants mostly only have a north field. There are several computer programs for the optimization of the heliostat field as well as different new algorithms, like using biometric layouts [39], constraining the heliostat boundary by the receiver geometry [71] or using non-restricted optimization combined with the Monte Carlo method [8].

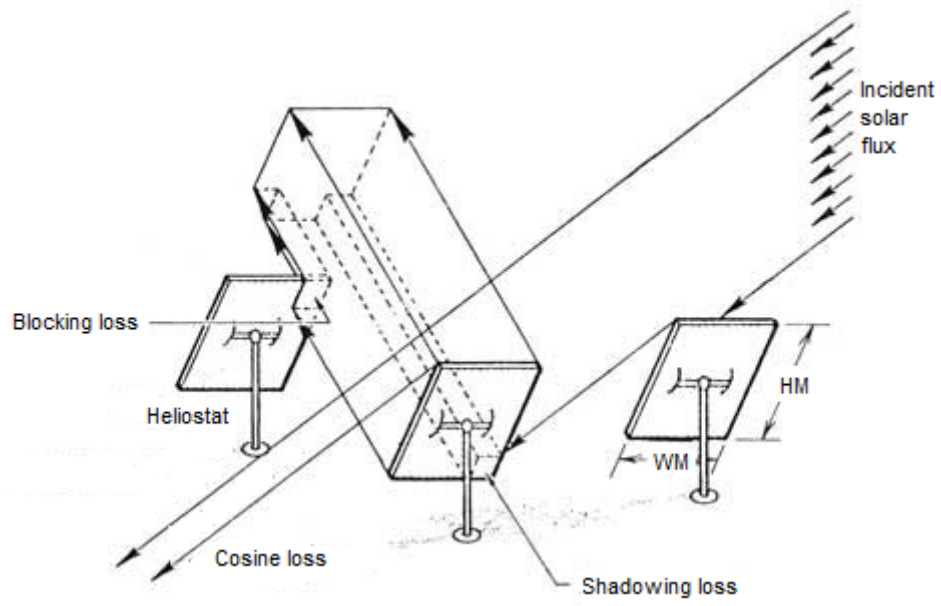


Figure 3-9: Loss mechanisms in a heliostat field [64]

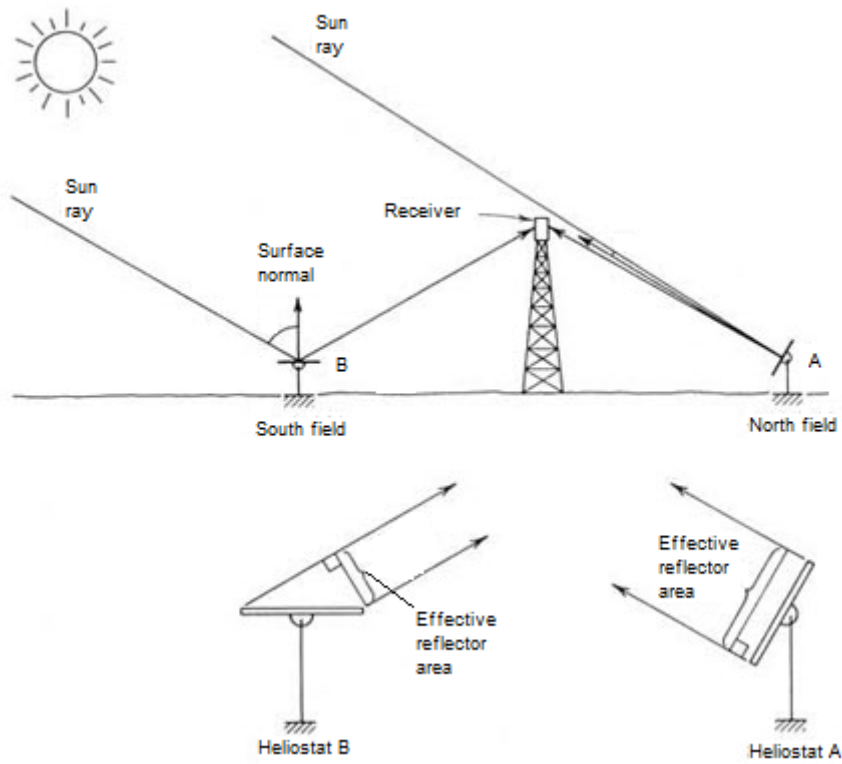


Figure 3-10: Visualization of the cosine loss in south field and north field [64]

3.2 Receiver

The receiver has to convert the incoming radiation into heat which is used in a subsequent process. There are three technologies how to realize this conversion: tube receivers, volumetric receivers and particle receivers. For all receiver technologies, it can be said that smaller receivers generate fewer losses due to convection and radiation but the maximum heat flux density restricts the minimum receiver size. Reflective and atmospheric attenuation losses are independent of the receiver size, because they reduce the incoming radiation by a fixed factor. Other loss factors like radiation spillage, internal heat conduction and piping losses are very individual for each receiver construction, also in different situations. The named loss mechanisms are summarized and presented in Figure 3-11.

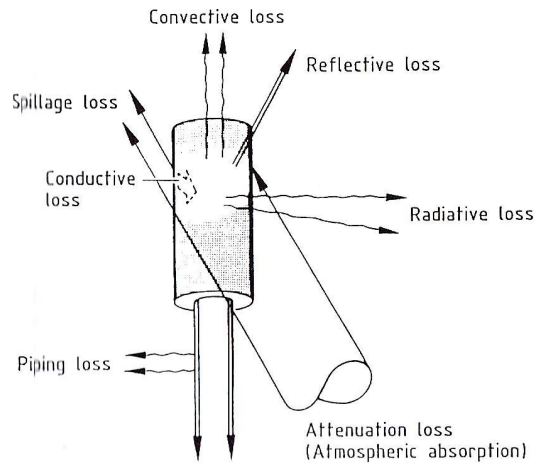


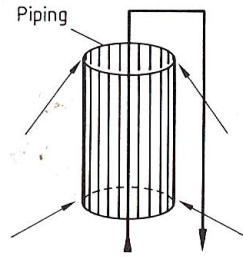
Figure 3-11: Optical and thermal losses [72]

3.2.1 Tube Receiver

The radiation is received at the outside of the tubes. The heat is then conducted through the wall and exchanged to the HTF carried on the inside. In high-temperature applications, the tubes may be protected from thermal losses by placing them in a cavity; in medium-temperature applications, equivalent loss protection is achieved by placing the tubes inside of infrared reflecting glass envelopes. *Tube receivers act as recuperative heat exchangers.* [72]

a) External Receiver

An external receiver needs to be as small as possible to keep its losses low. The thermal radiation from the receiver area is emitted directly into the environment and the vertical hot surface is cooled by the resulting high natural convection. Also high forced convection is given by constant blowing winds at receiver height. External receivers are comparatively technically mature today. In Figure 3-12, a schematic layout of an external receiver is shown as well as average and maximal allowed heat flux densities, which represent values for orientation.



External

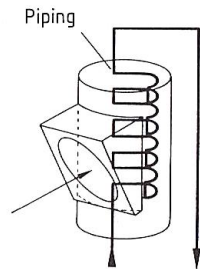
Conduction through tube wall

HTF	$\left(\frac{\dot{Q}}{A}\right)_{\text{avg}} \left[\frac{\text{kW}}{\text{m}^2}\right]$	$\dot{q}_{\text{max}} \left[\frac{\text{kW}}{\text{m}^2}\right]$
Liquid	800	2500

Figure 3-12: External receiver [72]

b) Cavity Receiver

The cavity receiver (Figure 3-13) can have a larger, low-flux density absorptive surface, irradiated and protected only by a small aperture (orifice). In the enclosed region behind the orifice, a diffuse ray portion and a larger absorptive area can be tolerated. In this case, the average heat flux density at the absorber may range as low as 100 kW/m². Also, cavity receivers are comparatively technically mature today. [72]



Cavity

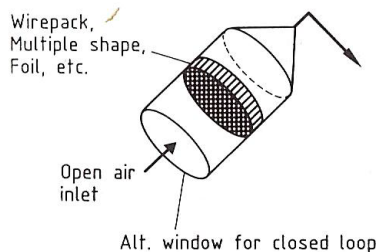
Conduction through tube wall

HTF	$\left(\frac{\dot{Q}}{A}\right)_{\text{avg}} \left[\frac{\text{kW}}{\text{m}^2}\right]$	$\dot{q}_{\text{max}} \left[\frac{\text{kW}}{\text{m}^2}\right]$
Gas	50 to 100	200
Liquid	300	900

Figure 3-13: Cavity receiver [72]

3.2.2 Volumetric Receiver

Wires, foam or appropriately shaped walls within a volume are used to enhance the absorptive surface area which receives the radiation, converts it into heat and transfers thermal energy by convection to air passing by. *Volumetric receivers operate as convective heat exchangers.* [72]



Volumetric

Convection back from wall

HTF	$\left(\frac{\dot{Q}}{V}\right)_{\text{avg}} \left[\frac{\text{kW}}{\text{m}^3}\right]$	$\dot{q}_{\text{max}} \left[\frac{\text{kW}}{\text{m}^2}\right]$
Gas	unknown	1000
Open air	unknown	(2500)

Figure 3-14: Volumetric receiver [72]

a) Open or Atmospheric Receiver

This receiver consists of a volume, filled, as mentioned before, with wires, foam, porous materials or foils, built from metallic, ceramic or other suitable materials (depending on the operating temperature level). An advantage of this concept is the absence of bending stress limitations which determine low cycle fatigue and lifetime for tubes. In volumetric receivers, the concentrated irradiation heats the material of the volume, which then heats up the passing air convectively. Air is a relatively trouble-free material for heat transfer. Open volumetric receivers are on the way to commercialization. [72]

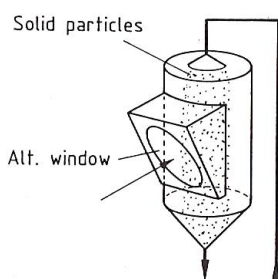
A solar tower power plant with open volumetric receiver comparable to the one in Jülich, Germany (also shown in Figure 3-4) is currently planned to be integrated in an ISCC power plant in Algeria [49].

b) Pressurized Receiver

In a pressurized receiver, higher pressure than atmospheric one can be used in a closed loop if the receiver is protected by a window. Transparency, stability and durability are still problems to be solved concerning the windows as well as other components since these kinds of receivers usually operate at very high temperatures. Pressurized receivers with windows are still under research. Current projects with pressurized receivers like PEGASE tend to variants without windows [5].

3.2.3 Fluid/Particle Receiver

Fluids or particle streams receive the incoming radiation directly and immediately absorb it in their volume or on their surfaces. The heat exchange process can be realized with or without chemical reactions taking place within the fluid or the particles. If a chemical process is incorporated, the receiver has to be equipped with windows. Currently, a lot of research is done related to this kind of receivers including numerical simulations [23], testing prototypes [28] and investigation of scattering in particle mists [44]. *Fluid/Particle receivers operate as a direct heat exchanger* [72].



Particles and Liquids

Direct absorption - Heat transport without reaction
 - Heat transport with reaction

HTF	$\left(\frac{\dot{Q}}{V}\right)_{\text{avg}} \left[\frac{\text{kW}}{\text{m}^3}\right]$	$\dot{q}_{\text{max}} \left[\frac{\text{kW}}{\text{m}^2}\right]$
Solid particles	unknown	(2500)
Liquids	unknown	(2500)
Reacting mixture	unknown	(2500)

Figure 3-15: Fluid/Particle receiver [72]

4 HEAT STORAGE OPTIONS

The systematic of heat storage was already discussed in Chapter 2.3. In this chapter, this systematic is continued and all heat storage options currently in use or being developed are organized in liquid, combined liquid and solid, solid and latent heat storage.

4.1 Heat stored in Liquids

An easy way to store heat is using the HTF as the fluid for a storage tank. In this case, there is no need for a heat exchanger between HTF and storage fluid. But this is not always a good option, as for instance thermal oil is comparatively expensive (see Table 2-1) and the storage needs a high amount of fluid (although thermal oil was used as a storage fluid in SEGS I, Daggett, California according to [72]). The mostly used storage fluid today is Solar Salt. It is relatively cheap, has a fairly low viscosity and is stable up to high temperatures. It also has a good heat conductivity and specific heat capacity. The disadvantage of currently used molten salt mixtures is that they have still relatively high melting temperatures. This can cause a freezing of the salt when the fluid temperature drops too far. For the operation, it is crucial to keep the molten salt always well above the freezing point. This is provided for the tanks by tank heaters. [63]

At this point, it should be mentioned that a molten salt storage for an oil-cooled parabolic trough power plant is larger (and therefore more expensive) than for a solar tower power plant with molten salt receiver by a factor of about 2.75. This is because the maximum temperature of the molten salt in the hot storage tank is limited by the maximum temperature of the thermal oil minus a few degrees for the heat exchange. So, the molten salt is just used in a temperature range between 290°C and 390°C. As a comparison, the Gemasolar solar tower power plant near Sevilla, Spain, uses the molten salt in a range of 290°C up to 565°C [70].

4.1.1 Twin Tank Liquid Storage

Today, almost only twin tank storages are used, one tank for the fluid at the lower temperature level (“cold tank”), and one tank for the fluid at the higher temperature level (“hot tank”). A system built in this way is shown in Figure 4-1. An advantage of this separation is that the hot and the cold fluid are not in contact with each other, which avoids internal tank losses. One of the disadvantages is the need of two tanks (higher investment costs) and a higher total surface due to the use of two separate tanks. The empty space in both tanks is filled with ullage gas which can be also air [86].



Figure 4-1: Andasol twin (cold and hot) molten solar salt storage tanks [78]

4.1.2 Thermocline Single Tank Storage

It is also possible to use a single tank for the whole heat storage by using the principle of thermal stratification. In this case, there is roughly just the volume of one tank necessary compared to the twin-tank principle. In this compact design, some of the heat from the hot fluid is transferred to the cold fluid via a narrow transition zone [70].

Figure 4-2 schematically illustrates the principle of thermocline storage. To charge the storage volume (a – d), hot fluid is pumped into the tank from above. The transition zone moves downwards, and cold fluid is pumped out from below. The discharge procedure is vice versa (d – a).

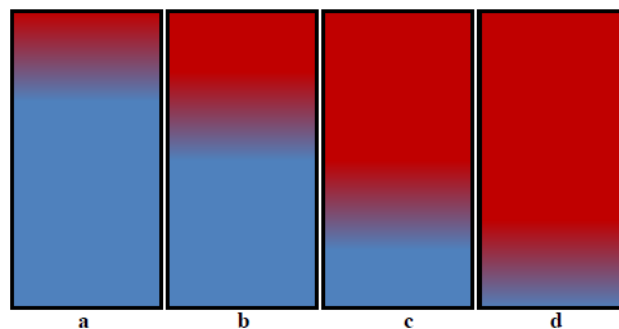


Figure 4-2: Schematic principle of a thermocline single tank storage [47]

The required amount of fluid can be reduced by adding low-cost solid material which stores a major portion of the heat energy. This is discussed in the next chapter.

4.2 Heat stored in Liquids and Solids (Thermocline)

A packed bed of low-cost material (e.g. a mixture of silica sand and quartzite, a mineral derived from sandstone) is used to fill thermocline storage in order to replace the bigger part of the liquid. In this case, the named transition zone moves upwards or downwards through the packed bed. Thereby, the heat is transferred into or out of the packed bed in this transition zone. This principle was used for example in the solar tower power plant Solar One in Barstow, California (rock/mineral oil). Thermocline storage systems using molten salt have been investigated in recent years especially in the USA. The reader should refer to a very good description of the principle and of recent research work by Pacheco et al. (2001) [46] and Flueckinger et al. (2011) [20]. By the replacement of a large amount of molten salt in the storage by packed bed, the price of the molten salt becomes less important. Therefore, more expensive salt mixtures (or even other HTF) with lower melting points could be used because of their lower risk of solidification. Currently, thermocline storages are not in use in commercial solar thermal power plants. [70]

4.3 Heat stored in Solids

Solids like filling material for heat storage are attractive due to the comparatively low price for solid material (especially sand, stone and concrete) and their high thermal stability. Currently, a lot of research is done in this section, investigating different concepts. The most important of these are described in the following.

4.3.1 Packed Bed Storage (Gas operated)

The difference of this packed bed storage in comparison to the one in chapter 4.2 is the use of a gas in order to load and unload the storage. This kind of storage is linked with the technology of volumetric receivers (Chapter 3.2.2). The used gas can therefore also be air.

The experimental solar tower power plant in Jülich, Germany, uses storage of 1.5 hours with a packed bed of small ceramics combined with an open volumetric receiver. The packed bed could also consist of concrete balls or especially shaped so-called saddles (of ca. 2 cm in size). The size of the pieces is a matter of optimization. Smaller pieces lead to higher pressure drops, for larger pieces, the total surface of the storage material is smaller, therefore, the heat exchange happens slower. The storage material is relatively cheap, but the need of air blowers lead to higher auxiliary electricity consumption compared to the use of pumps where a fluid is used. [70]

Currently, the production of an industrial-scale design is investigated which could provide a 24-hour-operation for a 26MW_{el} solar thermal power plant with a storage outflow of minimum 590°C hot air during discharge [84].

4.3.2 Concrete Storage

Concrete thermal storages were conceived for oil-cooled parabolic-trough systems. The construction of this kind of storage is in principle quite simple. Pipes filled with thermal oil are laid into a latticework of steel matting, so that their spacing is fixed. This structure is then filled with concrete in order to produce units of blocks. A schematic principle of the pipe arrangement in a concrete storage is illustrated in Figure 4-3. The number of pipes (with the same size) per square meter determines the heat transfer properties. For a 24-hour-operation, the storage is charged and discharged slowly during the day. For short-time storage of 1 hour, the concrete storage must be capable of being charged and discharged even faster. The faster charging/discharging, the more piping per square meter is necessary. At the moment, only two storage-test installations exist that are larger than a laboratory model. The first one is located in Almería, Spain, which was tested between 2003 and 2005 with a capacity of 320 kWh_{th}. The second one is located near Stuttgart, Germany, and is tested by the DLR. It consists of two modules each with 400 MWh_{th} of thermal capacity. Although the construction industry has already become involved, this research area seems to be underfinanced. [70]

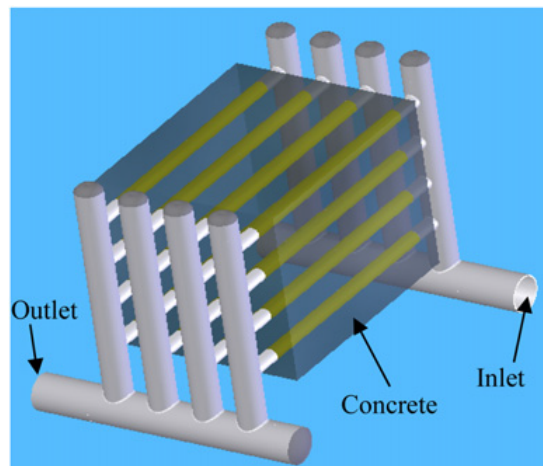


Figure 4-3: Schematic principle of a concrete thermal storage [2]

Concrete thermal storages are suitable for any kind of HTF, including also air and direct steam generation. Especially the combination of a concrete thermal storage with a steam accumulator is interesting. The concrete storage could be used in this case to superheat the saturated steam from the steam accumulator [2]. This technology is also still under research.

4.3.3 Sand-based Heat Storage

This storage concept is relatively new. In most of the investigated concepts, the hot air from the receiver is passed through quartz sand which is heated and then transported to a storage tank. This tank can be discharged by the use of a fluidized-bed heat exchanger for steam generation. The cooled sand can then be stored in a second tank. The sand-based heat storage has two advantages compared to the packed bed storage in chapter 4.3.1: First, the material costs are

extremely low, and second, the pressure gradient within the air circuit is smaller and does not depend on the size of the storage. [70]

An extreme abrasion resistance of the components in contact with the hard quartz sand is necessary for a long-time operation. As for the packed bed storage, a certain amount of auxiliary energy is needed to power the air blowers to transport the sand, and a temperature gradient between charging and discharging is given. The latter can partly be compensated by a higher input temperature which is connected with a higher receiver temperature. [70]

An example concept called “sandTES” is investigated by Vienna University of Technology. This sand-based heat storage variant is suitable for different applications (see Figure 4-4) like direct steam generation and volumetric receiver solar tower power plants. Also, the use for Adiabatic Compressed Air Energy Storage (ACAES) plants should be possible. [56]

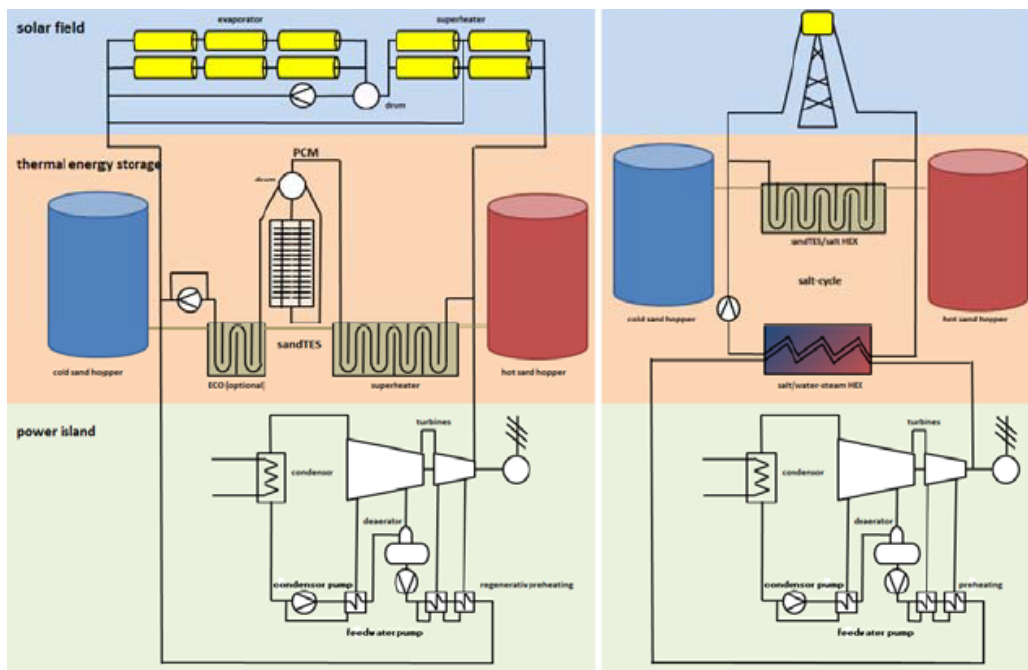


Figure 4-4: Applications of the sand-based heat storage “sandTES” (left: direct steam generation, right: volumetric receiver solar tower power plants) [56]

If a particle receiver is used (see chapter 3.2.3), the sand can be stored directly without using complex heat exchangers between the HTF (including air) and the sand. Yet, one heat exchanger is always necessary to power the steam cycle.

4.4 Latent Heat Storage

Latent heat storage media store heat at a constant temperature by changing their phase. When speaking of Phase change media (PCM) in the context of heat storage, usually material with phase transition between solid and liquid is meant. But one important phase transition between

liquid and gaseous is also used, namely in steam accumulators. Both will be discussed in the following.

4.4.1 Phase Change Media

Phase change media (PCM) provide high volumetric storage capacities and heat availabilities at almost constant temperatures. Energy storage systems using the latent heat released on melting eutectic salts and metals have to cope with difficulties at the heat exchange between HTF and storage medium when the storage medium solidifies. This is the main reason why PCM are still primarily a research focus [72].

Currently, the integration of heat pipes into the heat exchangers is investigated in order to improve the heat transfer process. First achievements have been documented [38] [51].

PCM heat storages can be combined with sensitive media heat storages in a storage concept where sensitive media are used to preheat the feedwater and to superheat the steam, and the PCM is used to evaporate the feedwater.

4.4.2 Steam Accumulators

At least in theory, a good option for energy storage, for direct steam generation, are steam accumulators. The steam accumulator is initially partly filled with cold water. Steam from the receiver enters the accumulator at the bottom and partly condenses when getting in contact with the cold water and thereby heats it up. The rest of the steam fills the space above the water. At the end of the charging phase, the pressure and temperature of the steam accumulator will have risen and the water level will be higher. When discharging the accumulator, the pressure drops and the water begins to boil and sets the accumulated steam free again.

The main advantage of this system is that the storage fluid is water, which is cheap and eliminates negative environmental impacts. Also, no heat exchangers are necessary. The disadvantages of the accumulator design include the cost and complexity of manufacturing the tanks and the unfavorable relationship between the volume and the energy stored. Also scaling up is quite difficult because the high pressure in the accumulator leads to thick walls of steel. [48]

As a conclusion, it can be said that steam accumulators are feasible for heat buffering for a comparatively short time but not for long-time operations.

5 PLANT DESCRIPTION

This chapter will provide an overview of the details of the chosen plant configuration. At first, an interesting site with available weather data was selected. After that, it was tried to find an appropriate plant configuration that fits the existing boundary conditions. It was decided to design a solar thermal power plant based on the solar power tower technology using a molten salt receiver and molten salt twin tank storage because of the apparently high potential of this technology. An EBSILON Professional model was created and more and more improved based on information from literature.

At the same time, an Excel calculation program was established in order to calculate input values for the solar tower and the storage analytically. To gain these values, the EBSILON-Excel interface was used partly in combination with an iterative calculation.

To get a realistic behavior of the power plant in time series simulation, macros were established to structure the power plant and to simulate different operation modes and transients between these modes.

5.1 Site Criteria

Figure 5-1 shows a global map of the annual sum of DNI for potential sites that are a suitable location for solar thermal power plants [68]. The focus for this thesis was on the Arab peninsula, which offers a high solar potential.

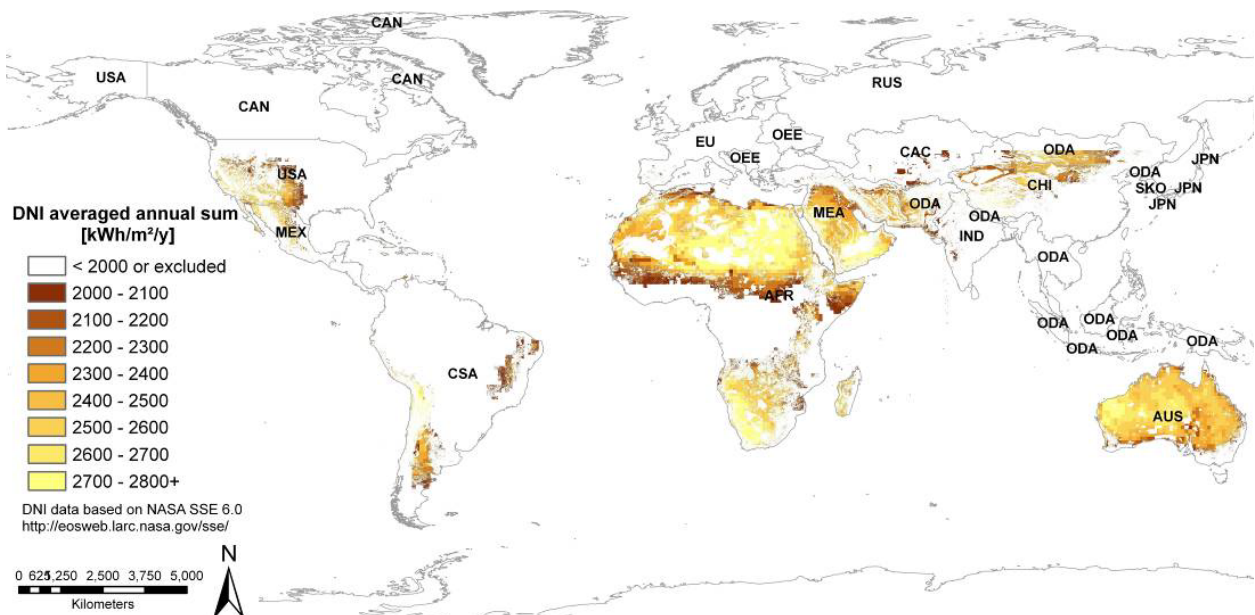


Figure 5-1: Map of the annual sum of DNI for potential global CSP sites [68]

5 Plant description

Weather data for Al Mirfa, United Arab Emirates, was already available [88]; therefore, the theoretic location of the power plant was set to 24.090° northern latitude and 53.489° eastern longitude. A specific challenge for solar thermal power plants in arid areas like UAE is the dust content in the atmosphere, which leads to significant atmospheric attenuation of solar radiation. Especially sand storms transport high amounts of dust that blocks the sunlight and is responsible for soiling and abrasion of the heliostat mirrors. Figure 5-2 shows a satellite picture and a DNI map of the UAE on a clear day, and Figure 5-3 shows the same for a day with sand storm.

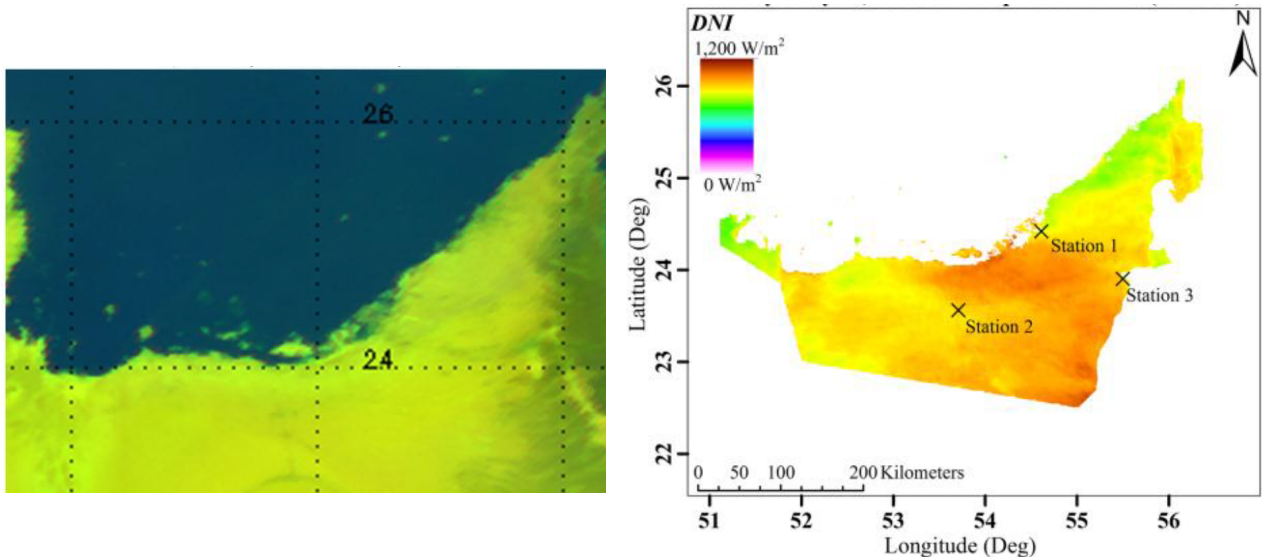


Figure 5-2: Satellite picture and DNI map of the UAE on a clear day (May. 28, 2009, at 12:15pm) [17]

The sandstorm highly reduces the DNI reaching the surface. The impressive visual barrier can be seen from space as a large dust cloud that also covers large areas above the sea.

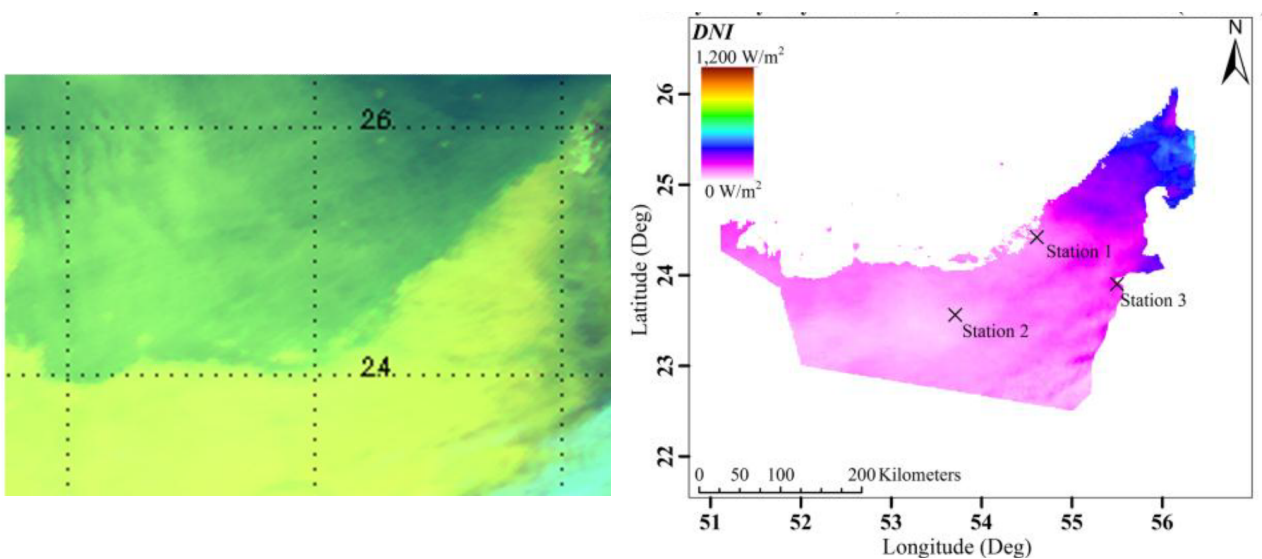


Figure 5-3: Satellite picture and DNI map of the UAE on a day with sand storm (Feb. 12, 2009, at 12:15pm) [17]

The weather data was taken from the database METEONORM 6.1.0.20, kindly provided by Zuniga F. [88]. According to him, the uncertainty for this data is about $\pm 15\%$. The data provides average values of DNI, ambient temperature and wind speed in height of 10 meters for each of the 8760 hours in the year 2005. For the later described solar tower, the wind speed in a height of 190 meters above the ground was also needed. Therefore, the data of the 10 meter wind speed had to be extrapolated to a height of 190 meters.

The lower atmosphere is divided into Prandtl-layer (up to 60-100 meters above the ground) and into Ekman-layer (60-100 meters up to 1000 meter above the ground). The distribution of the wind speed in the Prandtl-layer can be approximated by the log wind profile with a constant wind direction, for the Ekman-layer, more complex relationships apply. If the wind direction is not that important, the log wind profile for a height of 190 meters can be applied with comparatively small errors. [83]

The wind speed at a certain height $v(z)$ is defined by Eq. 5-1, where U^* is shear velocity, κ is the von-Kármán constant, z the desired height and z_0 the surface roughness [29].

$$v(z) = \frac{U^*}{\kappa} \ln \left(\frac{z}{z_0} \right) \quad \text{Eq. 5-1}$$

If instead of U^* and κ a wind speed at a certain height is already known, the formula above can be converted into Eq. 5-2.

$$\frac{v(z)}{v_r} = \frac{\ln \left(\frac{z}{z_0} \right)}{\ln \left(\frac{z_r}{z_0} \right)} \quad \text{Eq. 5-2}$$

Now the wind speed v_r at a certain height z_r can be used as input variable. The surface roughness factor z_0 can be taken from literature. For a sand desert, this factor is 0.001m [29]. The resulting factor for calculating the 10-meter-wind speed into a 190-meter-wind speed is 1.32. This correction factor is shown in Figure 5-4 for a height up to 200 meters above the ground. One can see that wind speed does not change very much anymore at high altitudes, whereas the speed gradient at lower altitudes is very high.

5 Plant description

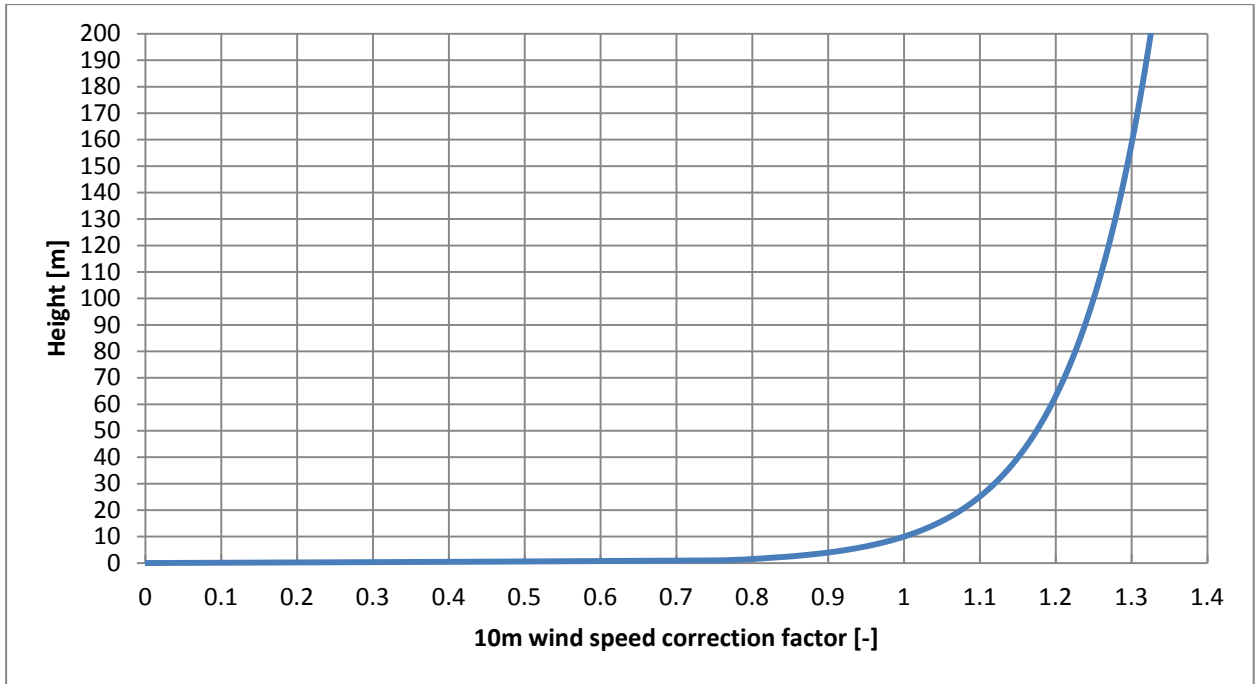


Figure 5-4: 10m wind speed correction factor for a height between 0 and 200 meter

After gaining the correction factor for the wind speed at 190 meters, all necessary weather data for a simulation of the power plant was analyzed via duration lines for the whole year in Figure 5-5.

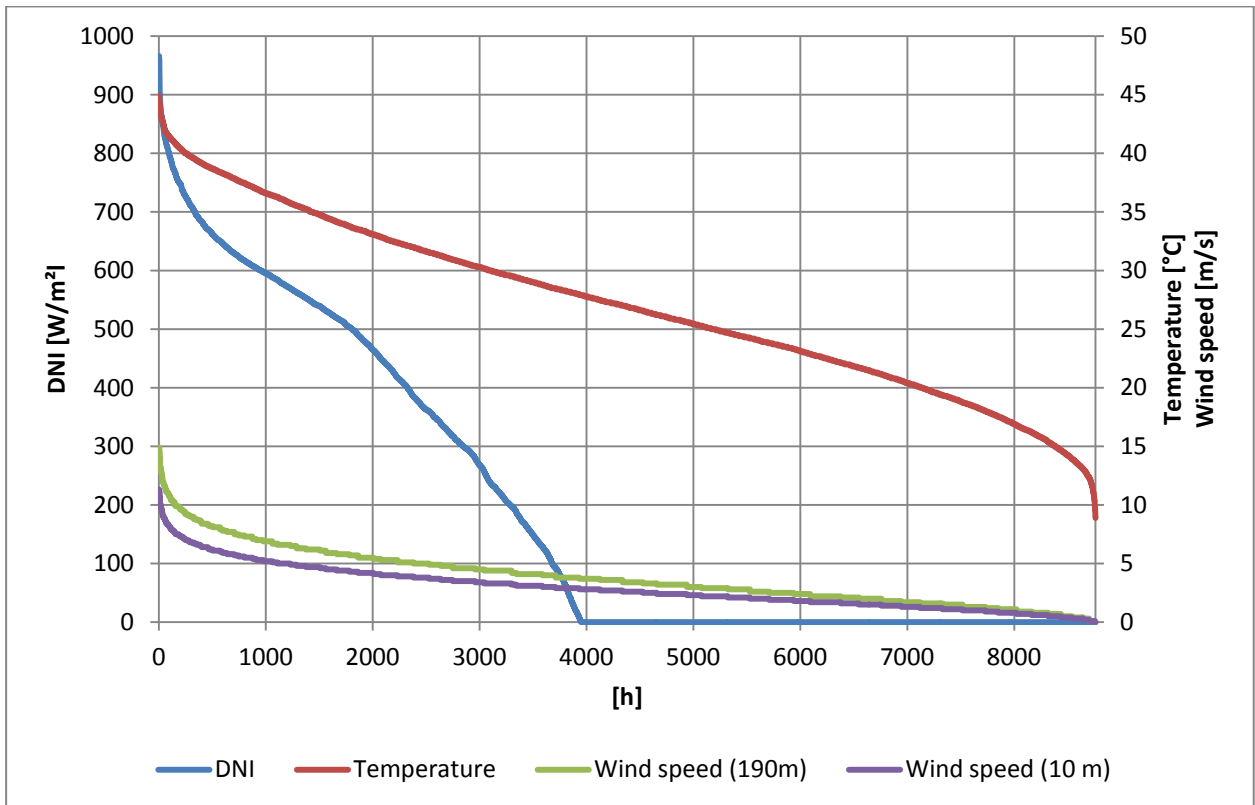


Figure 5-5: Duration lines for DNI, temperature and wind speed over the period of one year for Al Mirfa / UAE

The 10m wind speed was still necessary at all, because it is the relevant value for the heliostat maximum allowed wind speed. All ambient conditions show sharp tips around their maximum values, which means that these values occur quite seldom. The ambient temperature also has a tip at its minimum values.

5.2 Functional Description

The major Solar Tower Power Plant (STP) system elements are described in the following. Depending on the literature, sometimes also the term Solar Power Tower Plant (SPT) is used, but for the sake of a continuous nomenclature, the term STP will be used. The systematic of the systems is referred to [86] (see Figure 5-6). For a better overview, the systems were split in Main Systems and Other Systems. Furthermore, the Collector System (CS) and the Receiver System (RS) are a part of the Energy Collection System as well as the Steam Generation System (SGS), and the Electric Power Generation System (EPGS) are a part of the Energy Conversion System.

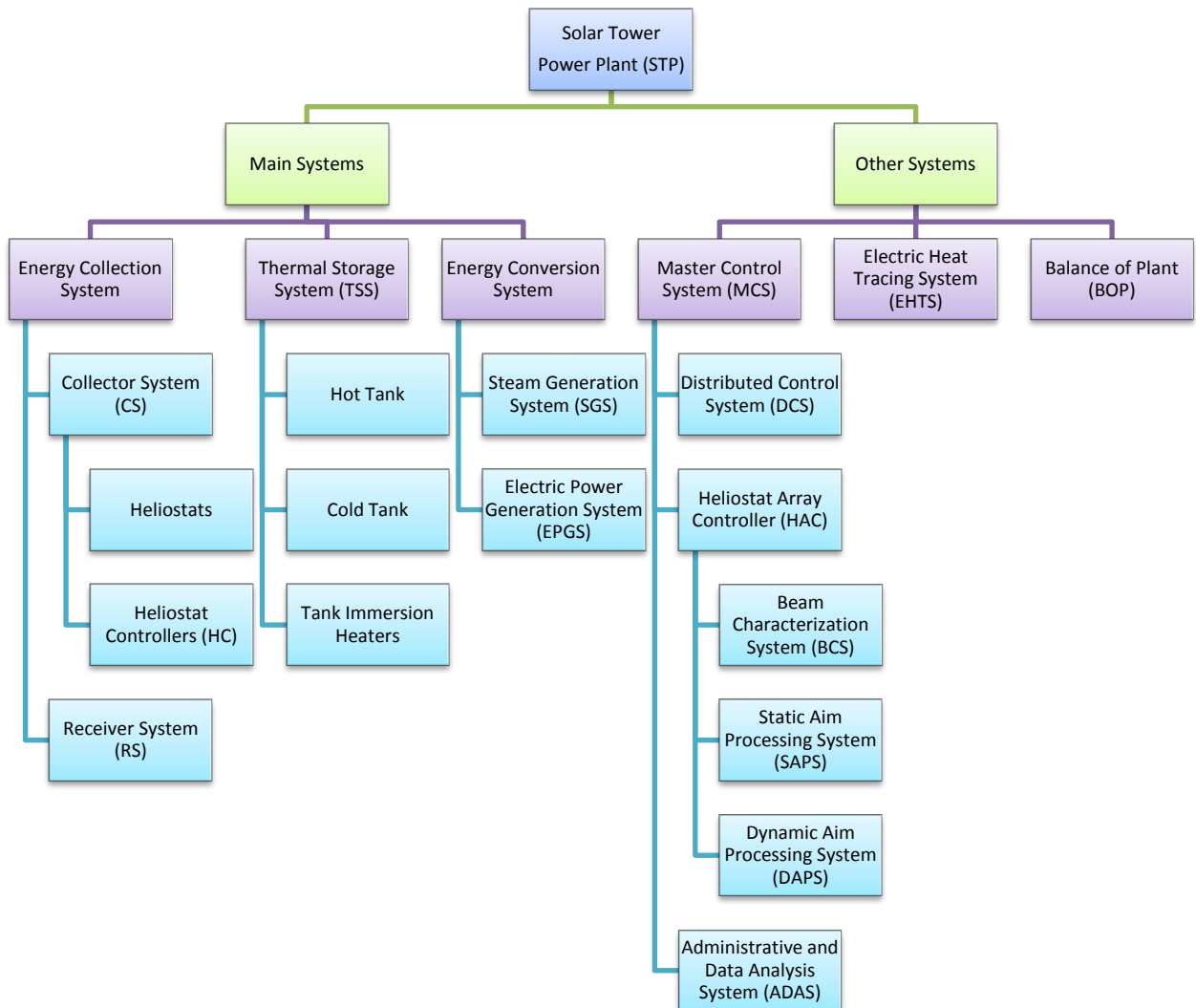


Figure 5-6: Systematic of Solar Tower Power Plant Systems referring to [86]

5.2.1 Main Systems

STP with integrated heat storage can be divided into three main systems (see Figure 5-7) based on the energy flow from DNI to grid.

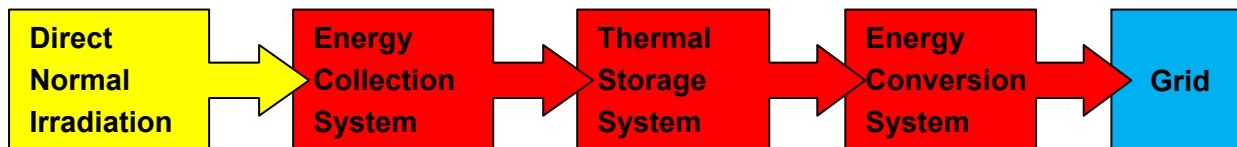


Figure 5-7: The three main systems of a solar thermal power plant with included heat storage

a) Energy Collection System

The Energy Collection System collects DNI and heats up HTF with this energy. It can be further divided into Collector System (CS) and Receiver System (RS).

The Collector System (CS) contains the heliostat field. The major system elements are the two-axis tracking heliostats and the heliostat controllers (HCs), which are connected via a communications link to the Heliostat Array Controller, which is described in chapter 5.2.2. [86].

The Receiver System (RS) consists of a cylindrical tube wall receiver that heats Solar Salt from 290°C to 565°C. The other system components of the RS are receiver pumps, receiver inlet and outlet vessel. A cold salt pump is installed on a structure on top of the cold tank. [86]

b) Thermal Storage System

The Thermal Storage System (TSS) stores high temperature Solar Salt with 565°C from the receiver for use by the steam generator in a hot tank. It also stores low temperature nitrate salt of 290°C from the steam generator for use by the receiver in a cold tank. A minimum temperature for both tanks is guaranteed by Immersion heaters for each tank. [86]

c) Energy Conversion System

The Energy Conversion System consists of the Steam Generator System (SGS) and the Electric Power Generation System (EPGS).

The SGS uses thermal energy from the hot Solar Salt to produce superheated steam at the conditions required by the turbine-generator and auxiliary steam systems. The SGS System components are: shell and tube exchangers including superheater, reheater, evaporator, preheater, a startup feedwater heater, a steam drum, steam drum mixer, steam generator evaporator feedwater pump and steam generator preheater feedwater circulation pump. The SGS circulation pump is installed on a structure on top of the hot tank and the SGS attemperation pump is installed on a structure on top of the cold salt tank. [86]

The EPGS converts the energy in the main steam into electric power for delivery to the electric grid. It consists of the turbine-generator, deaerator, condenser, condensate system, feedwater system, circulating water system including the cooling tower, water sampling system, turbine lubrication oil system and associated pumps and rotating equipment. [86]

5.2.2 Other systems

The Master Control System (MCS), the Electric Heat Tracing System (EHTS) and the Balance of Plant (BOP) are described in the following and are also very important systems for the operation of the plant.

a) Master Control System

The MCS controls and monitors all STP process functions for all system equipment through all states and transitions in response to operator commands. The MCS is comprised of the following major subsystems: the Distributed Control System (DCS), the Heliostat Array Controller (HAC) and the Administrative and Data Analysis Systems (ADAS). MCS functions tie all plant systems together in a common database encompassing the CS, RS, TSS, SGS, EPGS, EHTS and BOP. [86]

The DCS provides operator interface and interaction. It consists of the Human Machine Interface (HMI) – operator consoles, redundant Personal Computer Network (PCN) servers, network server, redundant Programmable Logic Controllers (PLCs), PLC remote input/output (I/O) devices and cabinets, data historian and network communications, peripherals and software. [86]

The HAC resides in the control center and maintains master control of the entire CS and includes the Beam Characterization System (BCS), the Static Aim Processing System (SAPS) and the Dynamic Aim Processing System (DAPS) software. [86]

The BCS provides correction offsets to the HAC to compensate errors. Each heliostat accumulates errors in pointing over time due to electromechanical system wear, pedestal movements, errors in drive motor revolution counts, canting alignment errors etc. The BCS consists of the BCS target (a projection surface on the tower), cameras and automatic software on the HAC [86].

The SAPS shifts the heliostat image up or down from the receiver equator to establish a uniform flux on the receiver. This aim point varies by time of year, time of day and ambient temperature and is used for an active control of the CS. [86]

The DAPS is used to automatically preheat and postheat the receiver on a daily basis [86].

Finally, the ADAS is linked to the DCS and HAC with read-only access and consist of the Management Information System (MIS), Material Control and Maintenance System (MCMS) and STP administrative systems, peripherals and software. [86]

b) Electric Heat Tracing System

The EHTS provides molten salt freeze protection to all the process equipment and components, thermal conditioning of all process equipment and components for plant startup and protects equipment from extreme thermal gradients and excessive thermal stresses. The EHTS encompasses all STP equipment, component thermal conditioning and molten salt freeze protection systems. [86]

The following components belong to the EHTS [86]:

- All electric heat tracing (EHT) circuits and zones
- Installation hardware (cold leads, termination kits)
- Temperature elements (either thermocouples or resistant temperature detectors)
- Temperature signal conditioning instrumentation and transmitters
- Power conditioning equipment solid state contactors

The control of the EHTS is provided by the PLCs and the DCS. The EHTS is a process critical system, and its control is an integral part of the MCS. The installation of EHT is required on equipment, piping, instruments, valves, vents, drains, pressure relief valves, tank immersion heaters and RS ovens. Thermal insulation is also part of the system on which it is installed. The insulation design and installation details are an integral part of the EHTS. [86]

c) Balance of Plant

The BOP supports all other plant systems.

It includes [86]:

- Switch yard/main power distribution system including main power transformers and secondary transformers
- Emergency and uninterruptible power supply (UPS) system
- RS tower cranes providing RS receiver panel access, RS and SGS pump access, SGS exchanger tube bundle access
- Fire protection and detection systems
- Plant security system
- Compressed air system
- Potable water system
- Cooling water system
- Service water system
- Nitrogen supply system
- Water treatment system
- Deionized water system
- Sanitary waste and industrial waste systems
- Oil/water separator

The BOP also includes the power distribution system feeding the individual process system Motor Control Centers (MCCs), grounding, lightning protection, lighting with associated raceway conduit and wire. It also includes all site civil (grading, drainage, fencing), buildings, receiver

tower structure and bridging structures over the TSS. The BCS target is included in the BOP. [86]

5.3 Process Flow Diagrams

In this chapter, two STP Process Flow Diagrams (PFDs) are illustrated and described which show a baseline STP configuration. Some of the components will be mentioned later in chapter 5.4. On the diagrams, valves and instruments for the primary process control function are also displayed.

The molten salt systems PFD in Figure 5-8 shows the molten salt flow paths for the RS, TSS and SGS. Both storage tanks use a sparger to dispense the incoming molten salt in the tank and an overpressure protection for the case of a tube rupture that releases steam or feedwater into the molten salt system. Additionally, the hot tank uses an agitator to prevent thermal gradients in the tank. The hot tank also contains the SGS circulation pump, which provides molten salt for steam generation. The cold tank contains the receiver circulation pump that supplies the receiver with cold molten salt and the SGS attemperation pump that supplies the steam generator with cold molten salt to keep temperature when switched off or to mix it with the hot molten salt in the cold salt mixer during transitions. All named pumps are vertical turbine pumps with variable speed drives and all molten salt piping is insulated and electrically heat-traced. The receiver panel is split in two panel sets (A and B) connected by a receiver crossover. Both panel sets are also integrated into a connection in parallel which connects the receiver inlet vessel and the receiver outlet vessel. A receiver by-pass line can alternatively be used for this connection. The inlet vessel is initially controlled by level; after establishing receiver flow and vessel ullage pressure, it is switched to pressure control. In the case of a pump defect, the pressurized inlet vessel is able to supply the receiver with cold molten salt until the heliostats are defocused. The inlet vessel is located 2 m below the bottom of the receiver panels, the outlet vessel is located 2 m above the top of the receiver panels. [86]

In Figure 5-9, the SGS feedwater and steam generation side of the process are covered. First, the feedwater from the regenerative feedwater preheaters passes a startup feedwater heater that is only used at startup. After that, it is mixed with feedwater coming from the steam drum in order to maintain a minimum feedwater temperature of 260°C in the preheater for security reasons. Finally, it enters the steam drum in a steam drum feedwater mixer where it becomes evaporated in a forced circulation evaporator. The larger part of the saturated steam proceeds to the superheater and after that to the turbine; the smaller part is used as auxiliary steam. After the high-pressure section of the turbine, the steam flows back to a reheater and then enters the low pressure section. All heat exchangers and the steam drum are electrically heat-traced and insulated in order to support startup thermal conditioning. The steam drum also includes immersion heaters. [86]

5.4 Operating States and Transitions

The introduced division of the power plant main systems into Energy Collection System, TSS and Energy Conversion System is reasonable especially when considering different states and transients. The Energy Collection System is usually active when sufficient solar irradiation is available and the Energy Conversion System is active when the TSS is loaded and operation is desired. Therefore, both systems work almost independently and their states and transitions must be analyzed separately.

5.4.1 Energy Collection System

The Energy Collections system operates in five states and nine transitions according to [86]. These states and transitions are also illustrated in Figure 5-10.

a) States

- **Long-Term Hold / Overnight Hold:** The heliostats are in stow position, the receiver is drained and electric heat trace circuits are inactive.
- **Standby:** The heliostats are focused on the standby aim points and the receiver pump is in operation. Molten salt is flowing in the riser, the receiver bypass line and the downcomer.
- **Preheat:** The receiver electric heat trace circuits are active, the preheat heliostats are focused on the receiver and the receiver pump is in operation. Molten Salt is flowing in the riser, the receiver bypass line and the downcomer.
- **Normal Operation:** All available heliostats are focused on the receiver and the receiver pump is in operation. Molten salt is flowing in the riser, the receiver bypass line and the downcomer.
- **Cloud standby:** All available heliostats are focused on the receiver; the receiver flow rate is controlled to achieve an outlet temperature of 510°C under theoretical clear sky conditions and the electric heat trace circuits are de-energized at the normal operation temperature set points.

- **Preheat to Normal Operation:** First, the receiver is filled by flooding, then serpentine flow is established with a flow rate corresponding to clear sky conditions. After that, the heliostats are moved from the standby (or preheat) aim points to the normal aim points and the flow rate is controlled to achieve a nominal outlet temperature of 565°C
- **Normal Operation to Cloud Standby:** Automatic temperature control is suspended and the flow rate is controlled to achieve an outlet temperature of 510°C under theoretical clear sky conditions.
- **Cloud Standby to Normal Operation:** Automatic temperature control is resumed and the flow rate is controlled to achieve a nominal outlet temperature of 565°C.
- **Normal Operation to Standby:** The heliostats are moved from the normal aim points to the standby aim points, the inlet vessel is vented to the atmosphere and the receiver is drained.
- **Cloud Standby to Standby:** The heliostats are moved from the normal aim points to the standby aim points, the inlet vessel is vented to the atmosphere and the receiver is drained.
- **Standby to Long Term Hold:** The heliostats are moved from tracking the standby aim points to the stow position, the receiver pump is stopped and the electric heat trace circuits are inactive.

5.4.2 Energy Conversion System

The Energy Conversion System operates in five states and seven transitions according to [86]. These states and transitions are also illustrated in Figure 5-11.

a) States

- **Long-Term Hold:** The steam generator is drained and the electric heat trace circuits and steam drum immersion heaters are inactive.
- **Overnight Hold:** The attemperation pump supplies the steam generator with cold molten salt to keep the steam drum hot but with no steam production. The steam turbine is rotated by the turning gear. Steam drum immersion heaters are de-energized at overnight hold temperature set points.
- **Auxiliary Steam:** A low saturated steam flow rate is established by the auxiliary (electric) steam generator. Sealing steam is delivered to the turbine shaft seals and a vacuum is established in the condenser using the auxiliary steam generator temperature set points. Auxiliary steam demand to preheat piping systems and other equipment will be supplied by the SGS.
- **Turbine Synchronization:** A certain steam flow rate with a temperature of 400°C and a pressure of 80 bars is established. The turbine-generator is synchronized with the grid and a minimum turbine output is established. The steam drum immersion heaters are de-energized at normal operation set points.
- **Normal Operation:** The extraction feedwater heaters are placed in service. A live steam flow with operational steam parameters is established and the nominal turbine generator output is provided. The steam drum immersion heaters are de-energized at normal operation temperature set points.

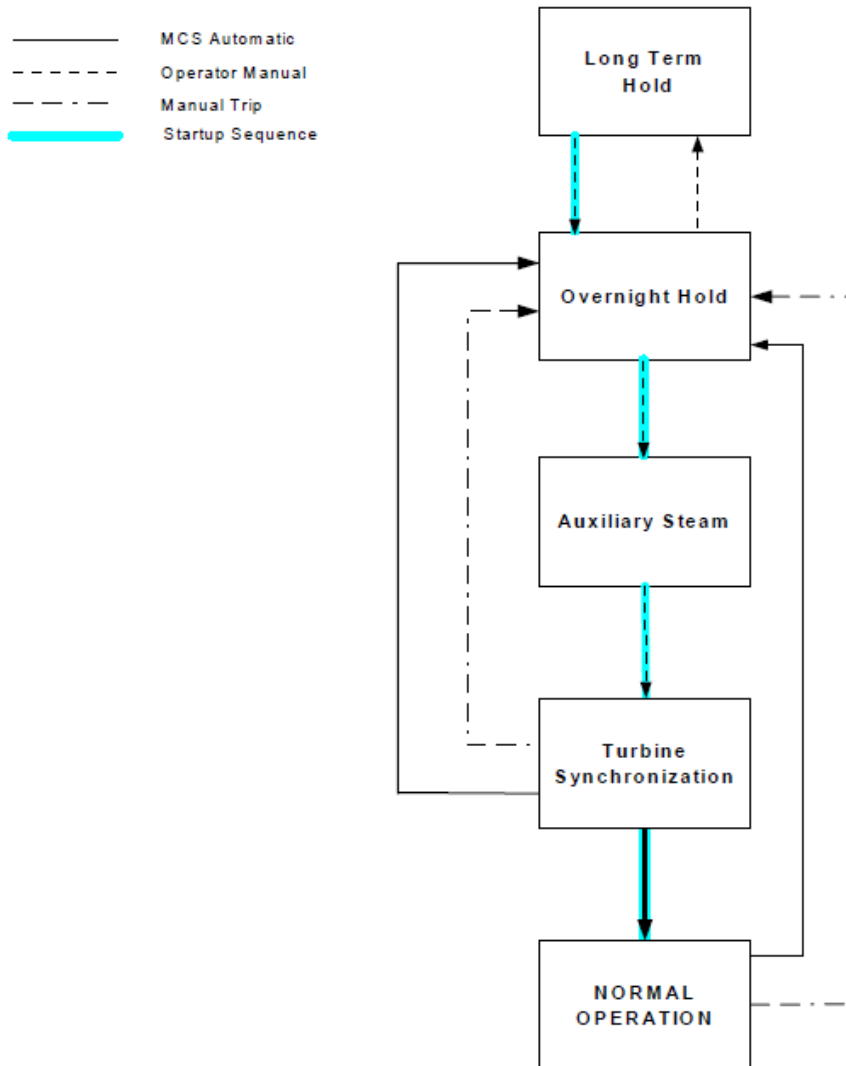


Figure 5-11: Operating states and transitions of the Energy Collection System [86]

b) Transitions between the states

- **Long-Term Hold to Overnight Hold:** The temperatures of the steam generator heat exchanger and intervessel piping are raised to 260°C by the EHTS. The SGS attemperation pump is started, and a flow of cold salt is established through the heat exchangers.
- **Overnight Hold to Auxiliary Steam:** The auxiliary (electric) steam generator is started, a flow of saturated steam is established to the turbine shaft seals and a vacuum is drawn in the condenser. Makeup water for the auxiliary steam generator is provided by a variable speed, positive displacement auxiliary feedwater pump.
- **Auxiliary Steam to Turbine Synchronization:** The SGS circulation pump is started and the speed of the pump is increased so that the temperature of the mixed molten salt at the inlet of the superheater increases at a rate of 500°C per hour. The live steam is throttled and sent to the condenser. As soon as the live steam achieves a superheat of 60°C, the turbine is accelerated to its nominal number of revolutions per minute and is

synchronized with the grid. The live steam throttle valve to the condenser is closed and a minimum turbine output is established.

- **Turbine Synchronization to Normal Operation:** The turbine is transferred from evaporator pressure control to speed control, the extraction feedwater heaters are placed in service and the reheater is placed in service. The attemperation flow of cold salt is reduced consistent with an allowable rate of temperature change in the heat exchangers of 500°C per hour and the flow rate of hot salt is increased to the design value.
- **Normal Operation to Overnight Hold:** The attemperation cold molten salt flow is started and temperature of the mixed molten salt at the inlet of the superheater is reduced consistent with an allowable rate of 500°C per hour. The output of the turbine is reduced, the live steam throttle valve to the condenser is placed in operation, the turbine is tripped and live steam is throttled to the condenser and the temperature of the heat exchangers is reduced to 285°C. Steam for the shaft seals is provided by the auxiliary (electric) boiler.
- **Turbine Synchronization to Overnight Hold:** The output of the turbine is reduced, the live steam throttle valve to the condenser is placed in operation, the turbine is tripped, live steam is throttled to the condenser and the temperature of the heat exchangers is reduced to 285°C. Steam from the turbine shaft seals is provided by the auxiliary (electric) boiler.
- **Overnight Hold to Long Term Hold:** The attemperation pump is stopped and the electric heat trace system is turned off.

5.5 Realized Plant Structure in EBSILON Professional

Before the creation of the final EBSILON Professional model, it was tried to find a preferably realistic model that is based on the plant structure described before, also including operating states and transitions between these states. Figure 5-12 shows a preview of the realized plant structure in Ebsilon Professional.

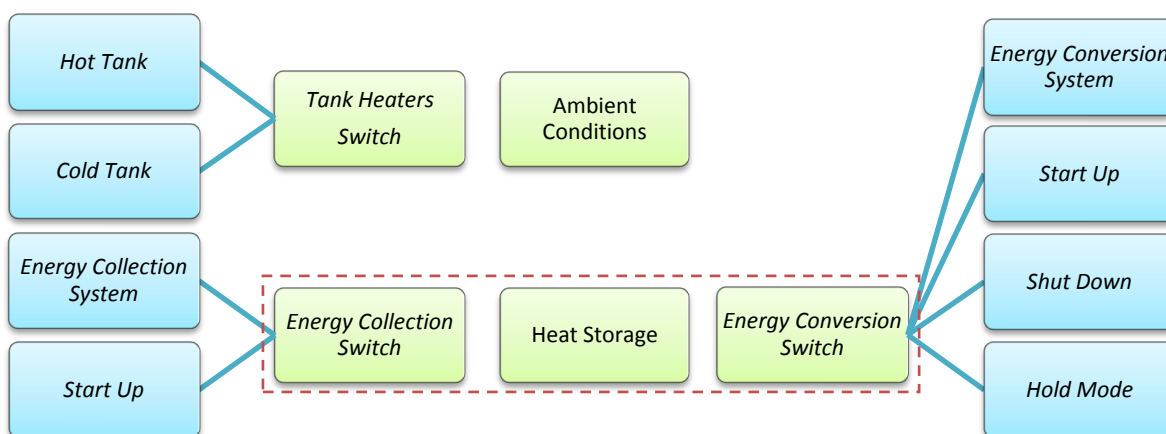


Figure 5-12: Schematic Solar Tower Power Plant structure in EBSILON Professional

The three main systems are marked with a red dashed frame. As mentioned in 5.2.1, these are the Energy Collection, the Heat Storage and the Energy Conversion. Together with the Tank Heaters and the Ambient Conditions, these elements are the core group that is visible when opening the model (visualized with green color). All elements written in italics are organized in macros within EBSILON Professional, the macros with “Switch” at the end are able to switch on/off the blue colored sub-macros that are integrated into them. The **Heat Storage** consists of the two storage tanks, and the **Ambient Conditions** only consist of the “Sun” component.

The **Energy Collection Switch** macro consists of the two sub-macros Energy Collection System and Start Up. A *Hold Mode* is provided by switching off the Energy Conversion System. The Standby and Preheat states are united in a *Start Up* macro, which is always initiated when the Energy Conversion System is switched on. *Normal Operation* is provided by switching on the Energy Conversion System. Cloud Standby is not implemented because cloud passing cannot be simulated, instead of that, Hold Mode is entered when DNI is falling below its bottom limit during daytime.

The **Energy Conversion Switch** consists of the four sub-macros Energy Conversion System, Start Up, Shut Down and Hold Mode. Long Term Hold is not implemented because this mode is often manually initiated by power plant operator decisions based on long-time bad weather forecast or maintenance. The *Hold Mode* implements the features of the Overnight Hold. Auxiliary Steam and Turbine Synchronization are combined in the *Start Up* Macro, which is always initiated when the Energy Conversion System is switched on. If the latter is switched on, the *Normal Operation* is established. To model the transition when the Energy Conversion System is switched off, the *Shut Down* macro was created.

The **Tank Heaters Switch** monitors the molten salt temperatures in both tanks and initiates the gas-powered immersion heaters for the appropriate tank in order to maintain a temperature of 260°C (this value can be adjusted for each of the tanks).

In Figure 5-13, the Solar Tower Power Plant structure in EBSILON Professional is shown for the design case (see text field of the “Sun” component) with full hot storage tank. A picture of the heliostat field is also shown with its standard design values. Each of the macros has piping interfaces where the grey ones indicate the HTF, the pink ones the electric lines and the violet ones the natural gas. The grey-green dashed line indicates the attemperation HTF and the black logic lines used for the calculation of efficiencies and power ratings. In Eq. 5-3 up to Eq. 5-6 the composition of these efficiencies and power ratings (also shown in Figure 5-13) is explained.

$$\text{Gross Efficiency Conversion System} = \frac{\text{Generator Power}}{\text{HTF Heat Usage}} \quad \text{Eq. 5-3}$$

$$\text{Net Efficiency Conversion System} = \frac{\text{Generator Power} - \text{Auxilliary Conversion Equipment}}{\text{HTF Heat Usage}} \quad \text{Eq. 5-4}$$

5 Plant description

$$\text{Gross Efficiency Conversion System} = \frac{\text{Generator Power} - \text{Total Auxiliary Equipment}}{\text{HTF Heat Usage}} \quad \text{Eq. 5-5}$$

$$\text{Net Power} = \text{Generator Power} - \text{Auxilliary Conversion Equipment} \quad \text{Eq. 5-6}$$

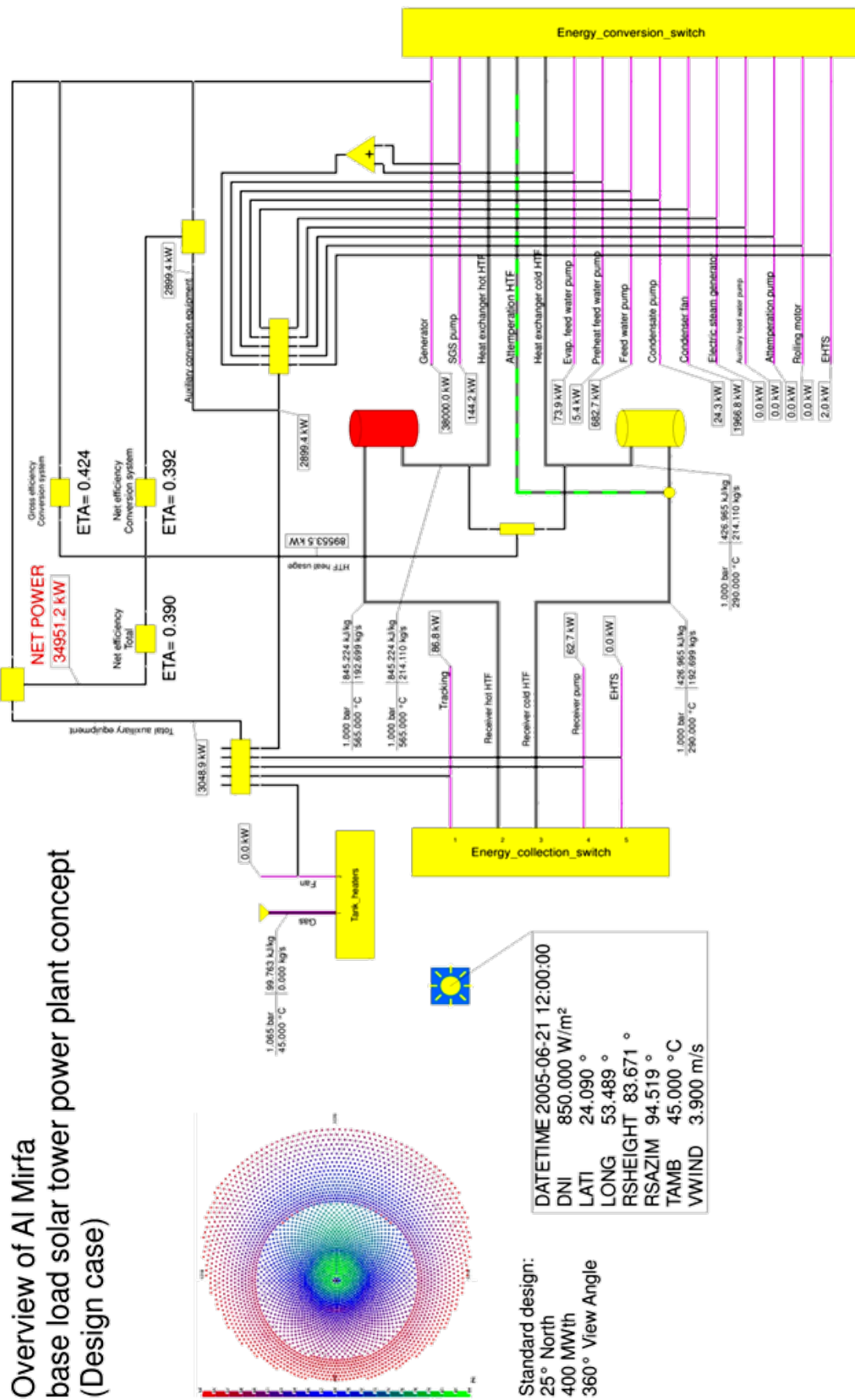


Figure 5-13: Solar Tower Power Plant structure in EBSILON Professional

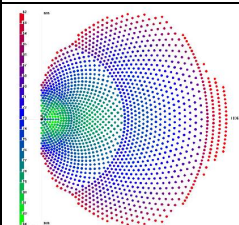
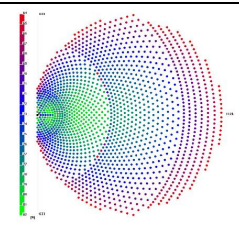
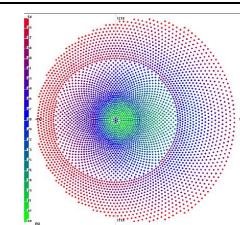
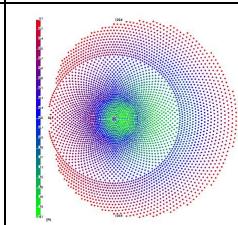
5.6 Energy Collection System

In this chapter the Energy Collection System will be discussed in detail. It consists of the heliostat field and the receiver. The simulation of different operation states and the transitions will be also explained.

5.6.1 Predefined Heliostat Field and Receiver Properties

Some characteristics of the heliostat field were already discussed in chapter 3.1. In EBSILON Professional, four heliostat fields were already predesigned; the most important properties are shown in Table 5-1. In the left column, the EBSILON variables are named, which are described below. It is important to know that the heliostat field and the receiver are designed simultaneously and represent a single system. Therefore, a part of the receiver properties is also stored in the heliostat field.

Table 5-1: Overview of the predesigned Heliostat fields available in EBSILON Professional [16]

	180° / 25°N / 100MWth	180° / 35°N / 100MWth	360° / 25°N / 400MWth	360° / 35°N / 400MWth
				
AREFL [m ²]	173800	170500	868000	876200
NHEL [-]	1738	1705	4340	4381
AREC [m ²]	223.56	246.77	1200	1109.68
QINCDES [kW]	106400	107000	471100	470010
RECELEV [m]	126.9	126.9	190	190
FRECFORM [-]	3	3	3	3
RECDIAM [m]	16.87	17.73	14.57	14.01
RECHEI [m]	16.87	17.73	26.22	25.22
RECTILT [°]	24.52	20.65	0	0
RECVIEW [°]	180	180	360	360
HELDENS [-]	0.1771	0.1543	0.1973	0.1863
LATIDES [°]	25	35	25	35
HEIGDES [m]	0	0	0	0
DATETIMEDES	21.03.2011 12:00	21.03.2011 12:00	21.03.2011 12:00	21.03.2011 12:00
DNIDES [W/m ²]	850	850	850	850
REFLDES [-]	0.8841	0.8841	0.8841	0.8841

The chosen heliostat field is the **360° / 25°N / 400 MWth** field. Al Mirfa is located at 24.09°N, which is acceptable [26], and the 400 MWth field was preferred to the 100 MWth field. AREFL quantifies the total reflectivity area of the mirrors and NHEL the number of heliostats. This leads to a reflective area of one heliostat of 200 m². AREC is the receiver surface, and QINCDES represents the design intercept power at the receiver aperture. The division of QINCDES/AREC leads to the specific flux density of the receiver, which is lies at 393 kW/m². RECELEV is the

receiver elevation above the ground, and FRECFORM is the receiver form; the value 3 represents a cylindrical receiver (corrected according to [26]). RECDIAM and RECHEI respectively denote the receiver diameter and its height. RECTILT is the receiver tilt angle, and RECVIEW represents the receiver view angle. In the case of a cylindrical receiver, its shape is a full cylinder at 360° or a half cylinder at 180° view angle [26]. The value of HELDENS shows the ratio between the total reflectivity area of the mirrors to the used land area. LATIDES and HEIGDES respectively represent the design latitude and the height above sea level [16].

DATETIMEDES is the date and time for which the heliostat field is designed [16]; this data results in a specific sun position. Although the heliostat field is designed for noon at vernal equinox (which is the best compromise seen over the full year), the chosen design case in EBSILON was noon at summer solstice. This is because the components of the solar tower including the receiver pump should be capable to run at the highest sun position over the year as well. The value DNIDES represents the design direct normal irradiation [16], and the value of 850 W/m² was also used for the EBSILON model. In a few hours of the year, the average hourly DNI reaches values up to 966 W/m² in the weather data. The receiver pump is able to run up to 110% of its nominal load [86], while the receiver could accept around 110-115% of its nominal load [26]. Therefore, a part of the heliostats must be defocused in order to not exceed 110% of the nominal load to avoid damage on the receiver.

The last value REFLDES is the design reflectivity of the heliostats. It is composed of three factors [26] as shown in Eq. 5-7.

$$REFLDES = \text{Clean Mirror Reflectivity} \cdot \text{Cleanliness} \cdot \text{Availability} \quad \text{Eq. 5-7}$$

Because REFLDES had been predefined, a realistic combination of these three factors was found in literature. The clean mirror reflectivity initially depends on the manufacturer and then decreases at a certain degradation rate, which can be very individual for each manufacturer and the existing ambient conditions. For parabolic trough mirrors, this was tested in Abu Dhabi, UAE [67]; the results can be seen in Figure 5-14.

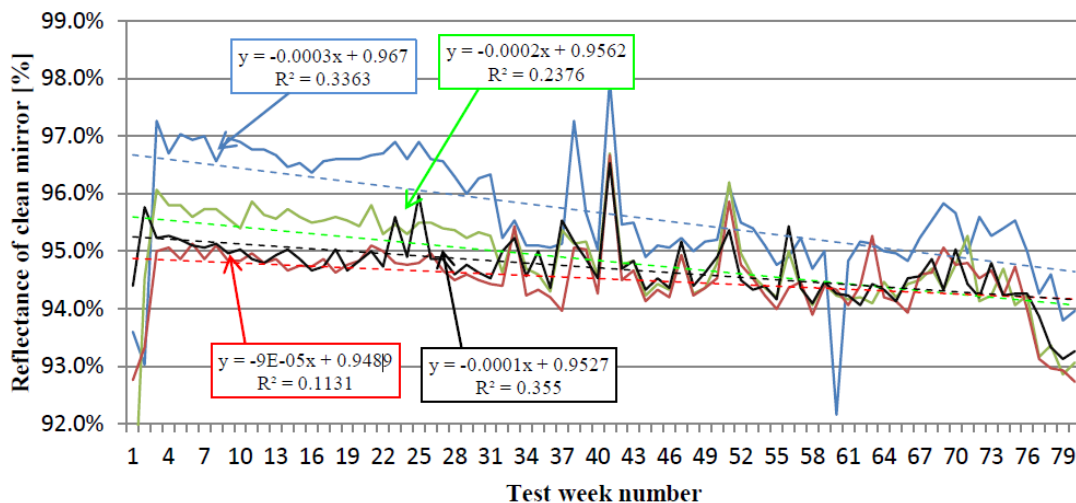


Figure 5-14: Degradation of clear reflectance, Test site Al Wagan, UAE [67]

The slope of the linear fit represents the degradation rate of the clean mirror plotted against time. Figure 5-14 shows the reflectance of the clean mirrors of the manufacturers 1, 2, 3 and 4 in black, blue, red and green respectively as a function of the test week number. In Table 5-2, the summarization of the collected data is shown [67].

Table 5-2: Initial reflectivity values for four manufacturers and reflectance degradation rates [67]

Manufacturer	Initial reflectance - Manufacturer's value [%]	Reflectance degradation rate [% per year]
1	95.0	0.52
2	96.7	1.56
3	94.95	0.52
4	95.6	1.04

For the EBSILON simulation, an average clean mirror reflectivity for the first year is calculated. Therefore, the later calculated annual plant output is just valid for the first year of operation. The data of manufacturer 4 was chosen because of its values ranging in the middle of the field. The **average clean mirror reflectivity** for the first year is therefore $95.6 - 1.04 \cdot 0.5 = 95.08 \%$.

The average cleanliness factor is mainly an economic question. Each cleaning procedure is connected with costs that over-proportionally grow with higher average reflectivity (see Figure 5-15). High average reflectivity, however, provides higher plant productivity and therefore more income.

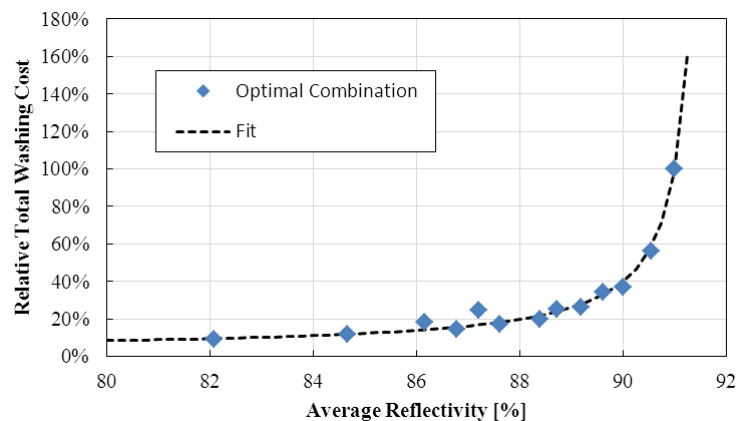


Figure 5-15: Exemplary relation between relative total washing cost and average reflectivity achieved [27]

The determination of the exact average cleanliness factor needs a detailed knowledge of economic numbers. In Figure 5-16, the optimum average reflectivity versus the proportion of heliostat washing to solar field cost is shown. The parameter A is the washing cost fit parameter. One can see that for rising heliostat washing cost, the optimum average reflectivity decreases. A detailed explanation and determination of all factors influencing this diagram would go beyond the scope of this thesis. The interested reader may refer to the work of Kattke et al. (2012) [27].

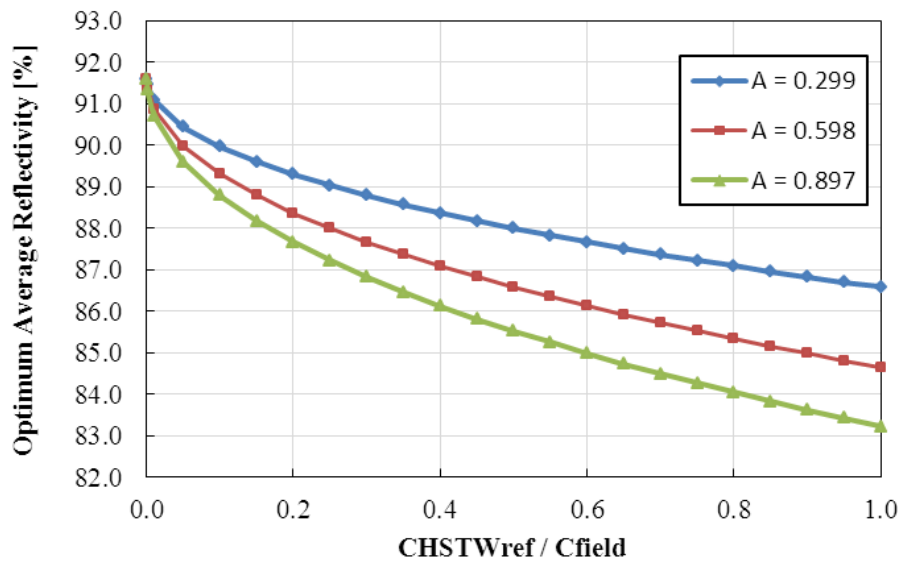


Figure 5-16: Optimum average reflectivity vs. proportion of heliostat washing to solar field cost [27]

In order to determine a suitable value for an optimum **cleanliness factor**, an estimation of **96%** according to [26] is used.

With the determination of the cleanliness factor, all factors of Eq. 5-7 are given but the availability factor. The latter was not clearly determined in literature anyway. The necessary **availability factor** derived from Eq. 5-7 is now given with **96.86%**. This means that over a total year, in average this percentage of heliostats must be in operation. During the year, a certain amount of heliostats will be out of operation due to cleaning, high wind loads, maintenance, defocusing to avoid receiver overload, calibration by DCS and malfunctions. Also mirror breaking can be an issue.

5.6.2 Non-Predefined Heliostat Field Properties

These values should be defined by the user. They were found in literature and/or self defined by logic considerations.

a) Specific Tracking Consumption

The specific tracking consumption (PATRACK) in Watts per square meter mirror area is consumed by the heliostats in order to track the sun. This factor could also be neglected and set to zero [26], but for the sake of a preferably accurate modeling, this value was estimated with the help of literature.

As an example, the GM100 Heliostat has two asynchronous electric motors installed which have a power of 370W each, and the mirror surface is 105 m² [45]. It is assumed that the total power of 740W is needed all 15 s for exactly 0.25 s (stepwise operation as indicated by [26]). This leads to an average power consumption of the mirror of 12.1W. This value is divided by the mirror surface, which leads to a consumption of roughly **0.1 W/m²**.

b) Minimum DNI for Tracking Activation

The absolute minimum DNI for receiver operation is at about 55 W/m². At this value, all incoming radiation is converted into losses, and the cooling mass-flow of molten salt for the receiver is 0 kg/s. This value was found by an iterative setting of DNI and observing the resulting cooling mass-flow.

To find the minimum DNI for tracking activation (MINTRACK), the heat absorbed by fluid (RQEFF) must be sufficient to compensate the electrical consumption of the heliostat field. Therefore, the energy conversion system efficiency $\eta_{\text{Energy Conversion}}$ was assumed with 0.42 (see Eq. 5-8)

$$RQEFF_{min} = \frac{PATRACK \cdot AREFL}{\eta_{\text{Energy Conversion}}} = \frac{0.1 \frac{W}{m^2} \cdot 868000 m^2}{0.42} \approx 207 kW \quad \text{Eq. 5-8}$$

At a DNI of 56.5 W/m², RQEFF is slightly higher than 207 kW (a small change in DNI has a high impact on the heat absorbed by fluid). The minimum DNI for tracking activation is therefore set to **56.5 W/m²**.

c) Maximum tolerated Wind Speed

In Table 5-3, wind definitions for heliostat structural design are shown. The heliostat must be designed for wind level W3 in the worst case operational orientation and for W4 in the high wind stow orientation. Nevertheless, W2 represents the stowage limit due to security reasons and the high impact of the wind on heliostat tracking and beam quality [86].

In the weather data, an hourly averaged value of the 10 m wind speed is given. Therefore, the mean wind speed at wind level W2 of **10 m/s** is taken as maximum wind speed tolerated by the heliostat. The data for Table 5-3 is from 1992 [86], but recent heliostats also have a maximum tolerated wind speed of 10-12 m/s (mean) [26].

Table 5-3: Wind Definitions for Heliostat Structural Design [86]

Wind Level	Condition	Wind Speed m/s (mph) @10m
W1	Operational performance requirements.	12 m/s (27 mph) Gust 8 m/s (18 mph) Mean
W2	Stowage limit (Heliostat moving from an operating mode to either normal stow or high wind stow position. Refer to Section 3.2.2.3).	16 m/s (35 mph) Gust 10 m/s (22 mph) Mean
W3	Survival in any orientation. Survival wind speed in any orientation may be adjusted to reflect site specific requirements.	22 m/s (50 mph) Gust 14 m/s (31 mph) Mean
W4	Survival in high-wind stow orientation (Based upon ASCE 7 -98 - Western United States). Survival wind speed may be adjusted to reflect site specific requirements.	40 m/s (90 mph) Gust 25 m/s (56 mph) Mean

d) Correction Factor for Atmospheric Attenuation

This factor (CORATM) takes into account the attenuation of the radiation between heliostat and receiver. There is currently a lot of research in this area, as a rough approximation **0.8** could be used for the region of the UAE [26].

5.6.3 Heliostat Field Equations

The usable solar power (QSOLAR) can be determined like shown in Eq. 5-9 [16]:

$$QSOLAR = AREFL \cdot DNI \quad \text{Eq. 5-9}$$

Due to optical losses only a fraction of this power is usable in the receiver; QINC is the incident power in receiver aperture (Eq. 5-10). RFOCUS is a factor, which considers the defocusing of a certain percentage of heliostats in order to not overload the receiver. REFL is the heliostat reflectivity; in the calculations of this thesis this value is equal to REFLDES. The factor ETAWIND considers losses due to spillage at higher wind loads. This factor was not used in this thesis because it is based in relation to the wind speed, which relies on research experience which was not found in the literature. [16]

$$\begin{aligned} QINC &= QSOLAR \cdot RFOCUS \cdot REFL \cdot ETAMAT \cdot ETAWIND \cdot CORATM \\ &= QSOLAR \cdot ETAFIELD \end{aligned} \quad \text{Eq. 5-10}$$

The last factor, heliostat field efficiency ETAMAT of the fully tracked (RFOCUS=1) and fully reflecting (REFL=1) field, is determined from the two-dimensional field efficiency matrix MXFIELDEFF. ETAMAT depends on the sun elevation RSHEIGHT (NY-axis) and the sun azimuth RSAZIM (NX-axis), which can be seen in Figure 5-17. [16]

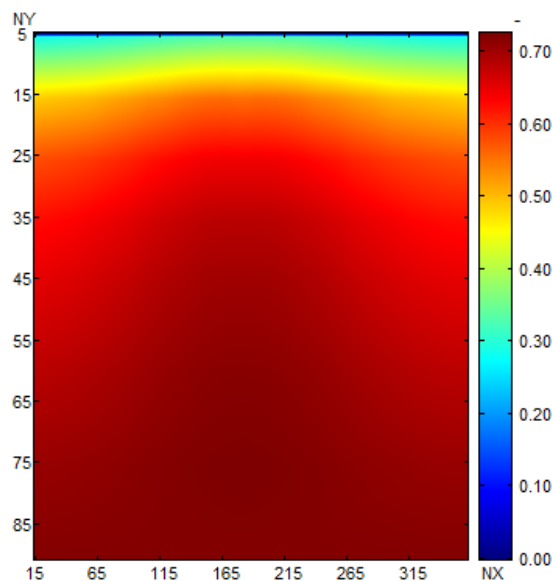


Figure 5-17: The two-dimensional field efficiency matrix MXFIELDEFF for the chosen field

The field efficiency is the result of multiplying four different efficiency matrices together. In addition to chapter 3.1 already mentioned cosine, blocking and shading efficiencies the atmospheric and intercept efficiencies were added. Atmospheric efficiency considers the attenuation of the radiation coming from the heliostats for Spanish atmosphere conditions [26], therefore other locations have to be taken into account with CORATM. The intercept efficiency represents losses due to spillage as mentioned in chapter 3.2. [16]

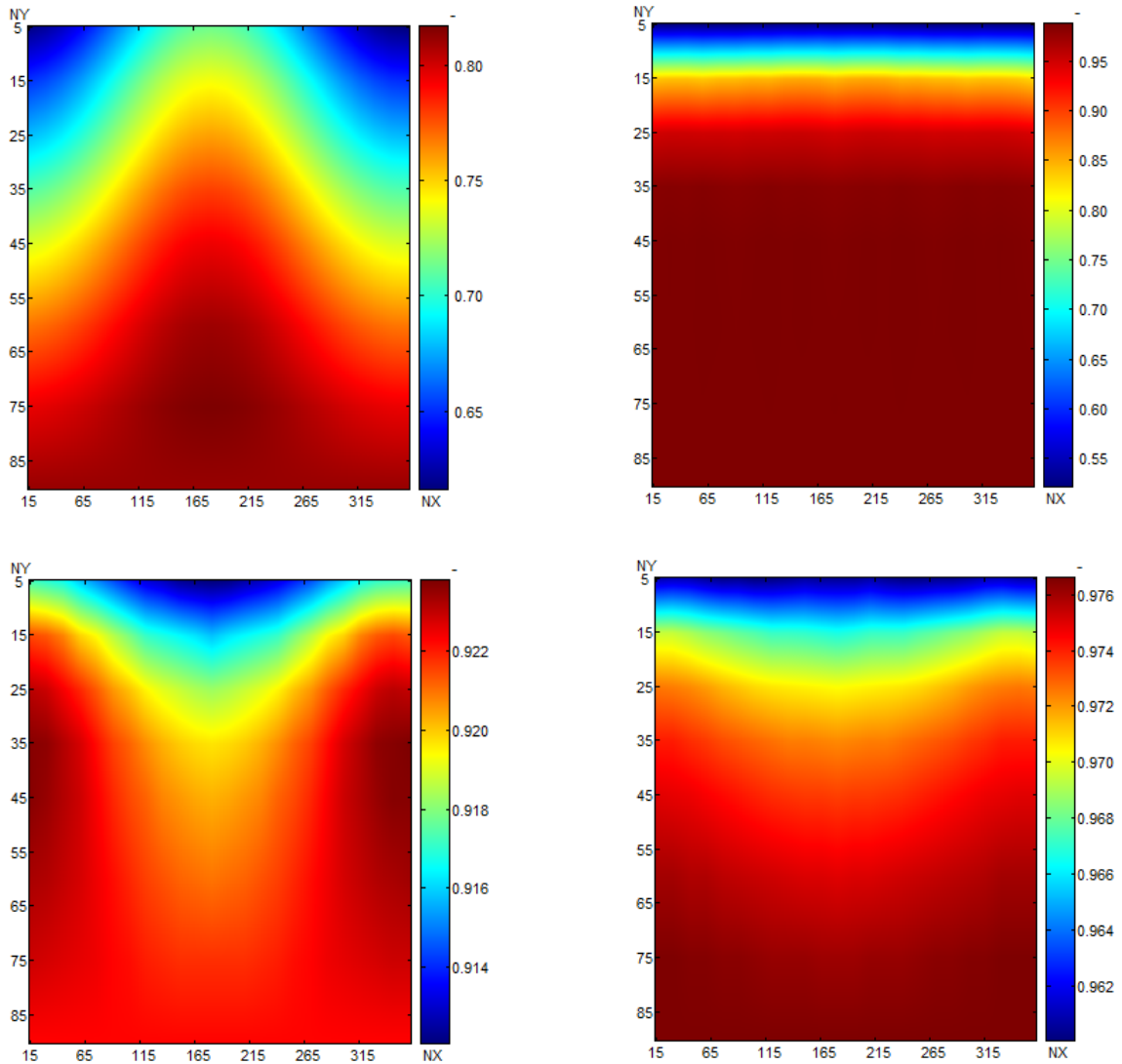


Figure 5-18: Cosine- (top left), blocking- and shading- (top right), atmospheric- (bottom left) and intercept-efficiencies (bottom right) for the chosen heliostat field

5.6.4 Heliostat costs

The cost buildup of a heliostat from past experiences in % of the overall heliostat system cost is as follows (according to [86]):

- Drive 40-50%
- Structure 15-20%
- Facets 15-25%
- Foundation 2%

- Field wiring 6%
- HC and controls 7%

5.6.5 Non-Predefined Receiver Properties

In this chapter, values are defined, which do not need a detailed calculation of the heat transfer. The calculation of the heat transfer coefficient of the receiver outside surface (ALPHA), the design wall temperature difference (DTWDES), and the nominal receiver pressure drop (DP12N) will be explained in chapter 6.2.1. The here explained receiver properties are optical ones.

Primarily the receiver coating determines the optical properties of the receiver surface. The absorptivity factor α describes the ratio of the incoming radiation that is absorbed by the receiver surface. The incoming solar radiation mainly consists of shorter wavelengths, therefore α is the ratio of these wavelengths absorbed by the receiver coating.

In Figure 5-20 the energy distribution for the related wavelengths of the electromagnetic spectrum of solar radiation is schematically illustrated. The incoming radiation from the sun on the earth's surface consists of ultraviolet, visible and infrared components. The highest amount of energy is transferred by visible radiation and the emphasis of the energy lies at shorter wavelengths. For information purposes, the ratio of the radiation that can be theoretically converted by photovoltaic cells is also shown.

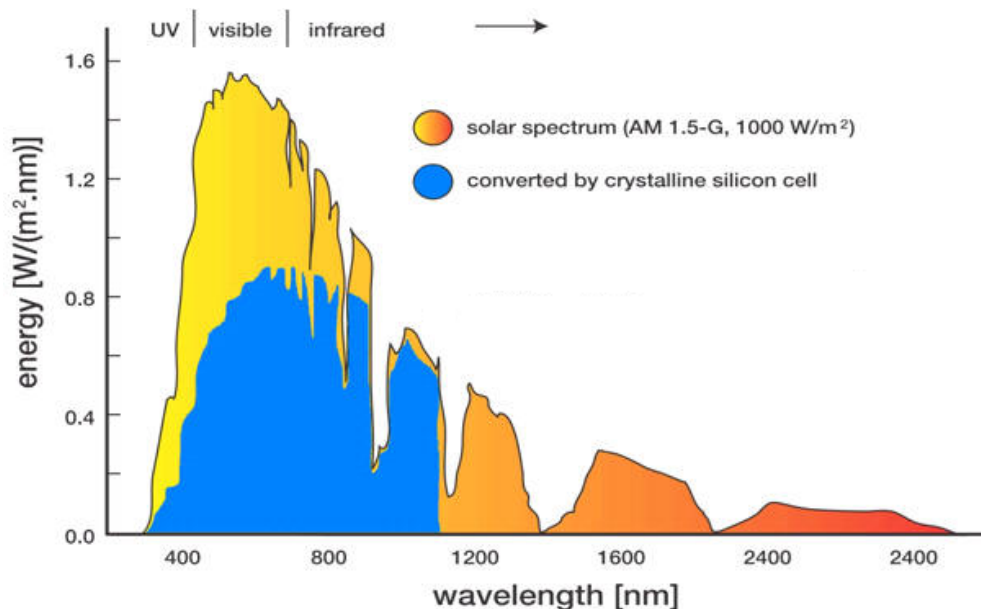


Figure 5-19: Schematic energy distribution for each wavelength of solar radiation on earth's surface [79]

The receiver is hot during operation and emits thermal radiation in the infrared band (longer wavelengths) of the electromagnetic spectrum. The ratio of the emitted thermal radiation to the theoretical maximum is expressed by the emissivity factor ε .

a) Optical Efficiency (Absorptivity)

The variable η_{OPT} is mainly determined by the absorptivity factor α of the receiver coating. However, other optical loss effects could be taken into account with this variable [26].

Pyromark Series 2500 high-temperature paint is currently the standard for CSP central receivers. It is low cost and easy to apply, but degrades over time when operating in air causing a decline in performance and added operating costs for CSP facilities. [24]

Selective coatings are currently under development for this high temperature application but they are not competitive yet [26].

The absorptivity of Pyromark is measured with 0.96 [24] when new and **0.93** [26] represents an average value over lifetime (The absorptivity is getting lower when the coating is getting older).

b) Emissivity

The emissivity (EMIS) ε of Pyromark lies at **0.83**, which leads to large thermal losses during high temperature operation. This value could be reduced down to around 0.2 by the use of selective coatings. [24]

5.6.6 Receiver Equations

As mentioned before, the calculation of ALPHA, DTWDES and DP12N will be explained in chapter 6.2.1.

The heat input into the HTF is given by Eq. 5-11. M_1 is the HTF mass-flow, H_2 the enthalpy of the HTF at the outlet and H_1 at the inlet port of the receiver. [16]

$$M_1 \cdot (H_2 - H_1) = R_{QEFF} \quad \text{Eq. 5-11}$$

The effective heat input R_{QEFF} is the result of the incident power R_{QINC} minus the losses of the receiver R_{QLOSS} (Eq. 5-12). [16]

$$R_{QEFF} = R_{QINC} - R_{QLOSS} \quad \text{Eq. 5-12}$$

The total heat loss R_{QLOSS} is composed of three terms: the optical losses $R_{QLOSSOP}$, the convective heat losses $R_{QLOSSCO}$, and the radiation heat losses $R_{QLOSSRA}$ (Eq. 5-13). [16]

$$R_{QLOSS} = R_{QLOSSOP} + R_{QLOSSCO} + R_{QLOSSRA} \quad \text{Eq. 5-13}$$

These losses were calculated by a model considering a variable receiver temperature. For higher receiver loads, the surface of the receiver has a higher temperature. This is a more advanced calculation model compared to the assumption of a constant receiver temperature, but it is still a rough approximation since the heliostats provide a non-uniform heat flux

distribution on the receiver. Figure 5-20 shows thermography pictures of the Gemasolar receiver from four directions that show different surface temperatures. Unfortunately no caption for the different colors was available.

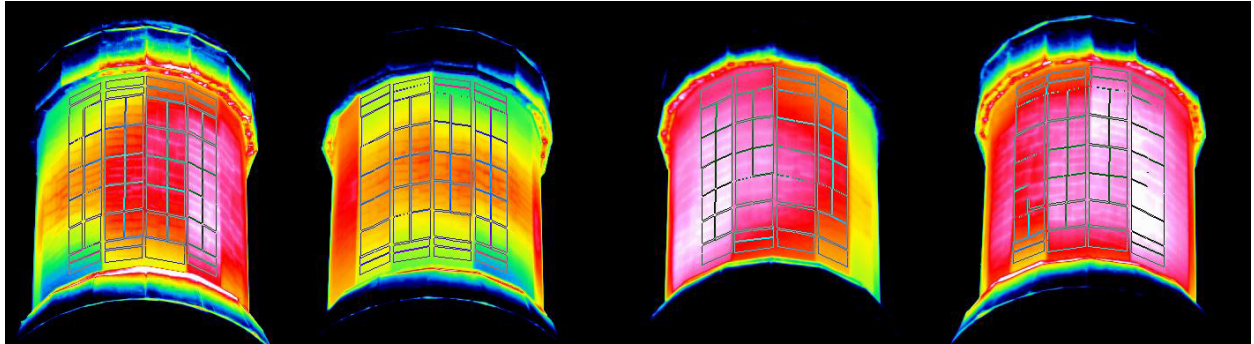


Figure 5-20: Thermography pictures of the Gemasolar receiver in operation from four directions [9]

The optical losses (Eq. 5-14 [16]) do not depend on the receiver temperature, only on the factor $ETAOPT$, which basically represents the receiver absorptivity α .

$$RQLOSSOP = (1 - ETAOPT) \cdot RQINC \quad \text{Eq. 5-14}$$

The calculation of the convective losses (Eq. 5-15 [16]) consists of the heat transfer coefficient $ALPHA$, the receiver surface temperature $RTREC$, the ambient temperature $RTAMB$ and the receiver area $AREC$. With the term $SCONV$, the influence of the wind could be integrated as a factor depending on the wind speed. However, a different calculation method based on Nusselt numbers was used in chapter 6.2.1.

$$RQLOSSCO = SCONV \cdot ALPHA \cdot (RTREC - RTAMB) \cdot AREC \quad \text{Eq. 5-15}$$

$RTREC$ is calculated as shown in Eq. 5-16 [16]. $T1$ is the HTF temperature at the inlet port of the receiver and $T2$ at its outlet port. Factor K is a weighting factor, which is set to 0.5. $DTWDES$, is the already mentioned design wall temperature difference.

$$RTREC = T1 + K \cdot (T2 - T1) + DTWDES \quad \text{Eq. 5-16}$$

The calculation of the radiation losses is shown in Eq. 5-17 [16]. All factors in this equation but $SIGMA$ were already explained. $SIGMA$ is the Stefan-Boltzmann constant with a value of $5.6705 \cdot 10^{-11} \text{ kW}/(\text{m}^2\text{K}^4)$.

$$RQLOSSRA = EMIS \cdot SIGMA \cdot [(RTREC + 273.15)^4 - (RTAMB + 273.15)^4] \cdot AREC \quad \text{Eq. 5-17}$$

The use of the ambient temperature $RTAMB$ for the re-radiating environment in this equation is an approximation. For average receiver temperatures in the magnitude of 400-500°C this leads only to very small errors because the term including $RTREC$ is some orders of magnitude higher than the term including $RTAMB$ because both are to the power of 4.

5.6.7 Receiver Additional Information

In this section, selected additional information about the receiver is provided to give an overview of its design properties.

The RS baseline system elements are (in accordance to [86]) comprised of:

- The variable-speed receiver circulation pump, which is a vertical turbine pump mounted on top of the cold storage tank supplying cold molten salt to the receiver inlet vessel
- Receiver inlet vessel, which is a pressure vessel with an air pressure blanket and a capacity to provide 60 seconds of uninterrupted flow to the receiver in the case of pump or power loss.
- Two receiver flow loops, which start at the north side of the receiver inlet vessel, flow through the receiver in serpentine flow and exit from the receiver at the south side into the outlet vessel. The piping includes interconnecting receiver piping to the receiver panel headers, crossovers, fill and drain lines.
- Receiver absorber panels made of high nickel alloy including tubes, tube clips and headers.
- Structural elements of the receiver interfacing with the receiver panel support frame, receiver oven boxes and proving support.
- A receiver tower crane that provides access to the receiver panels for installation and replacement.

The receiver panels are supported at the top and are allowed to grow freely in a downward direction. The panel design allows the receiver panels to be filled uniformly using either a serpentine or flood flow (all panels are filled bottom-up) technique. The receiver tubes included in the panels are thin walled (e.g. 1.25mm) and welded to the thick walled inlet and outlet header/nozzles. The interface nozzle-to-header is the location of highest thermal stresses which are induced by rapid temperature changes due to cloud transients and the difference in wall thickness. The design flux on the nickel alloy receiver tubes is nominally 1 MW/m². [86]

A receiver vent and drain system is responsible to fill the receiver during daily startup and drain the receiver during shutdown. The functions of vent and drain system are [86]:

- Uniform filling of the receiver and assuring that no air is trapped in the receiver panels, which would result in receiver damage.
- Allowing a rapid shut down and draining of the receiver in less than one minute to preclude freezing salt in the panels

Panel headers, inlets and outlets, are protected by removable insulated and thermally conditioned (electrical heated) oven boxes. The oven box radiant heaters are required to preheat the header assemblies to 315°C within 30 minutes during the transition from preheat to normal operation. In Figure 5-21 a conceptual sectional view of the oven box assembly is illustrated. [86]

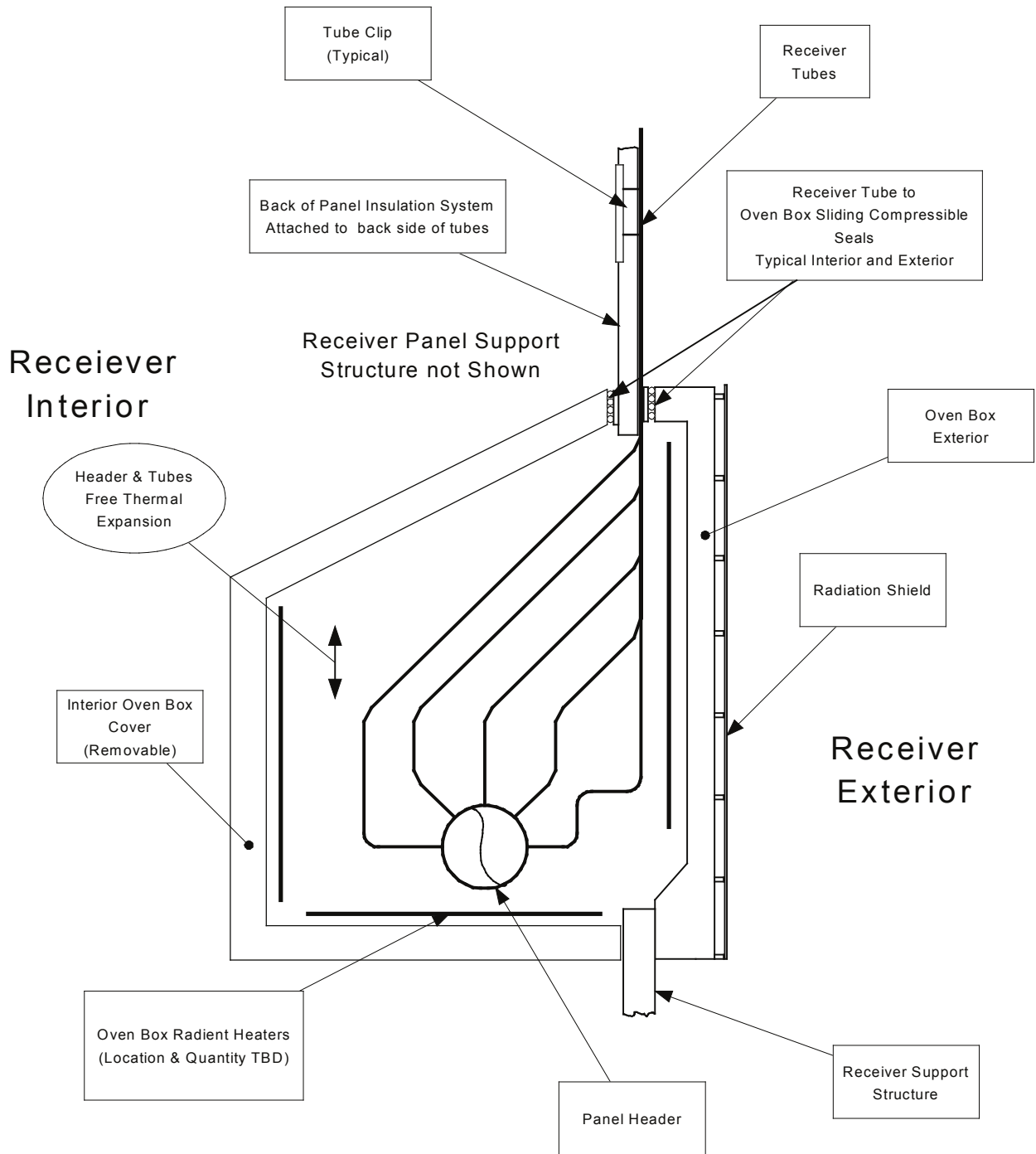


Figure 5-21: Conceptual sectional view of the oven box assembly [86]

In Figure 5-22 a possible piping scheme for a receiver is also illustrated as described before.

5 Plant description

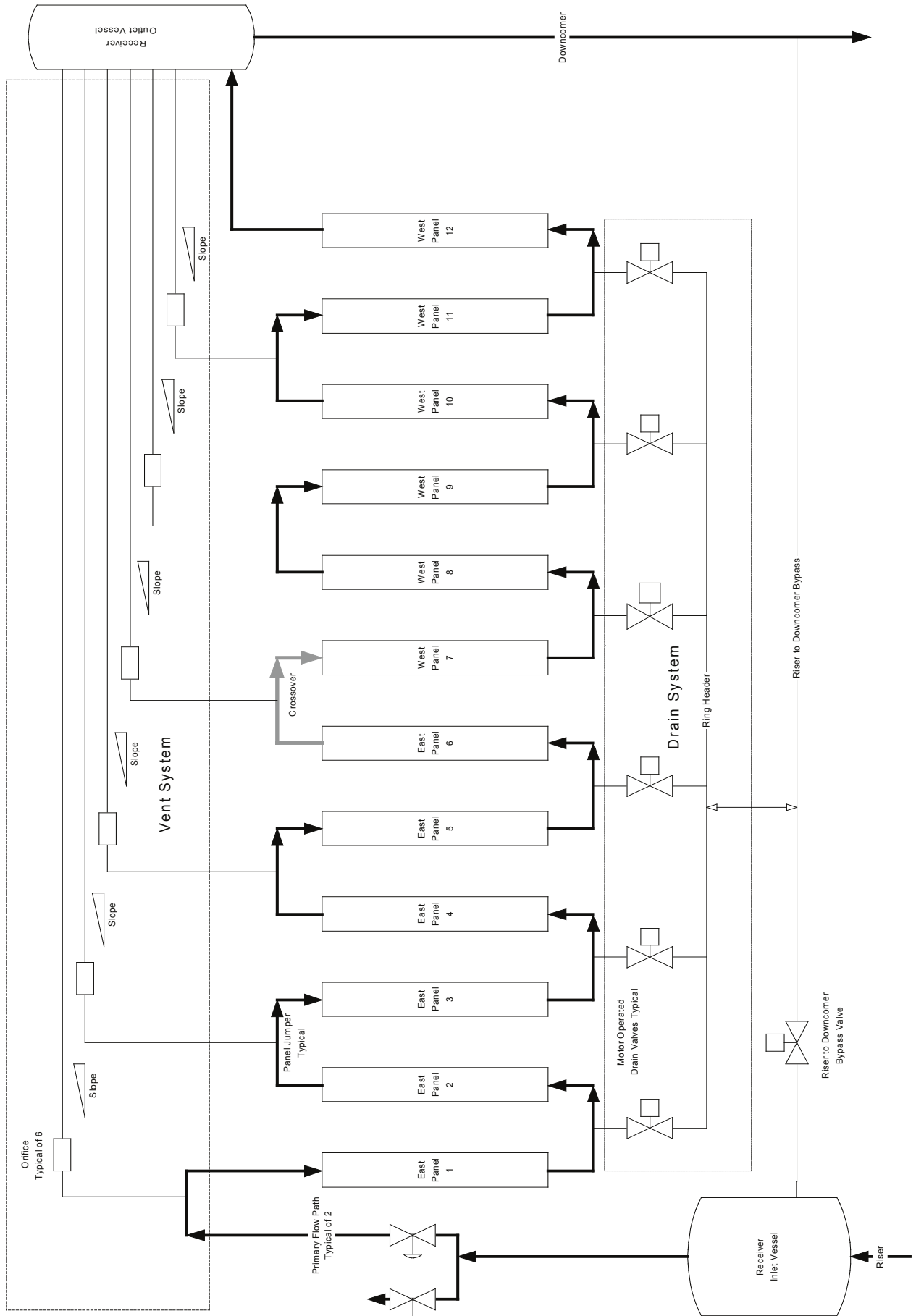


Figure 5-22: A possible receiver piping scheme [86]

5.6.8 States and Transitions

As discussed in chapter 5.5, the Energy Collection Switch macro consists of the two sub-macros Energy Collection System and Start Up. A *Hold Mode* is provided by switching off the Energy Conversion System. The Standby and Preheat states are united in a *Start Up* macro, which is always initiated when the Energy Conversion System is switched on. *Normal Operation* is provided by switching on the Energy Conversion System. Cloud Standby is not implemented because cloud passing cannot be simulated, instead of that Hold Mode is entered when DNI is falling below its bottom limit during daytime.

As mentioned before, the Start Up macro is just initiated when the receiver is started for the first time. This initialization lasts for one time step, in this case for one hour. Even though the additional electric consumption of tracking, receiver pump and EHTS need different time spans each, the determined power of them must be recalculated for the time span of one hour. These determined power values must be derived from detailed analysis of the Start-Up phase which needs a lot of experience. They also could not be found in literature. Therefore it was tried to find reasonable values by estimations:

- Additional tracking consumption of 10kW in order to align the heliostats
- Additional receiver pump consumption of 20kW to fill and startup the receiver
- EHTS consumption of 200kW in order to preheat piping and oven box

In the Energy Collection Switch macro (Figure 5-23), pink colored lines indicate electric lines for tracking, receiver pump and EHTS. The grey lines indicate pipes containing cold HTF flowing to the receiver and hot HTF coming back from the receiver. The figure illustrates a situation, where the receiver is already started with no additional consumptions for tracking, receiver pump and EHTS. As the name implies, the interface connects the content of the Energy Collection Switch with the higher-ranking element, in this case the content of Figure 5-13.

In the Start Up macro (Figure 5-24) the mentioned additional electric consumptions are defined.

The Energy Collection System macro (Figure 5-25) four main components can be seen: a heliostat field, a solar tower, a receiver pump and its motor. For the heliostat field and the solar tower component the most important properties are listed in order to provide an overview. The receiver pump generates the required flow for the receiver. The pressure drop in the pipes is implemented by piping components.

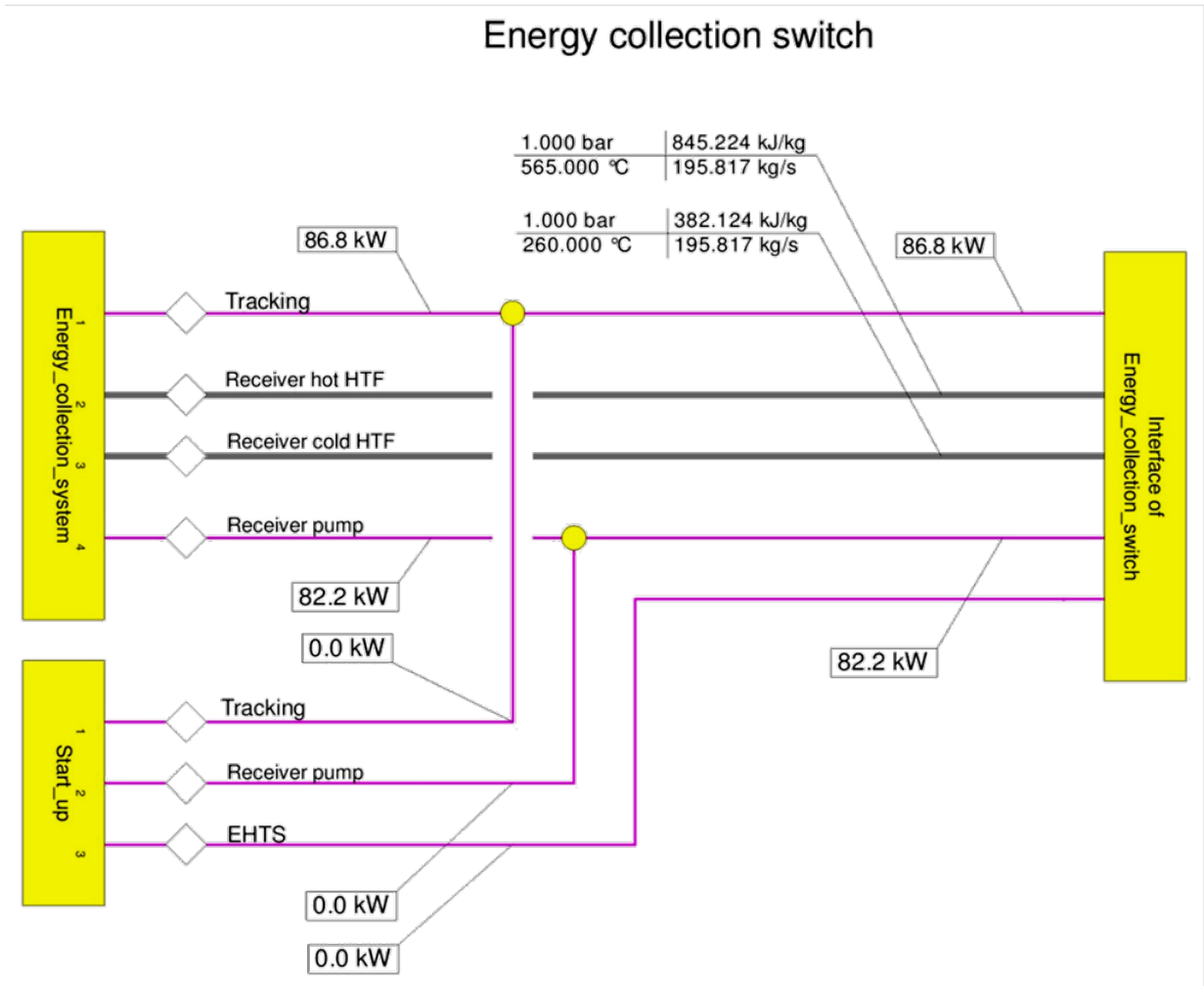


Figure 5-23: Content of the Energy Collection Switch macro

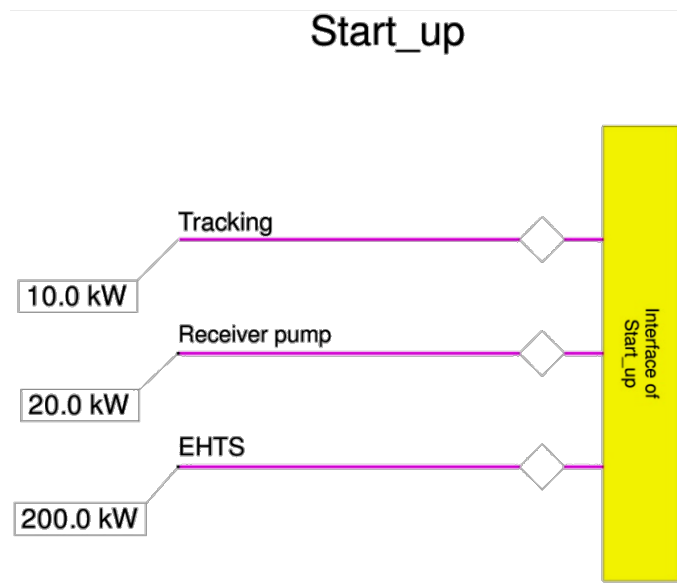


Figure 5-24: Content of the Start Up macro

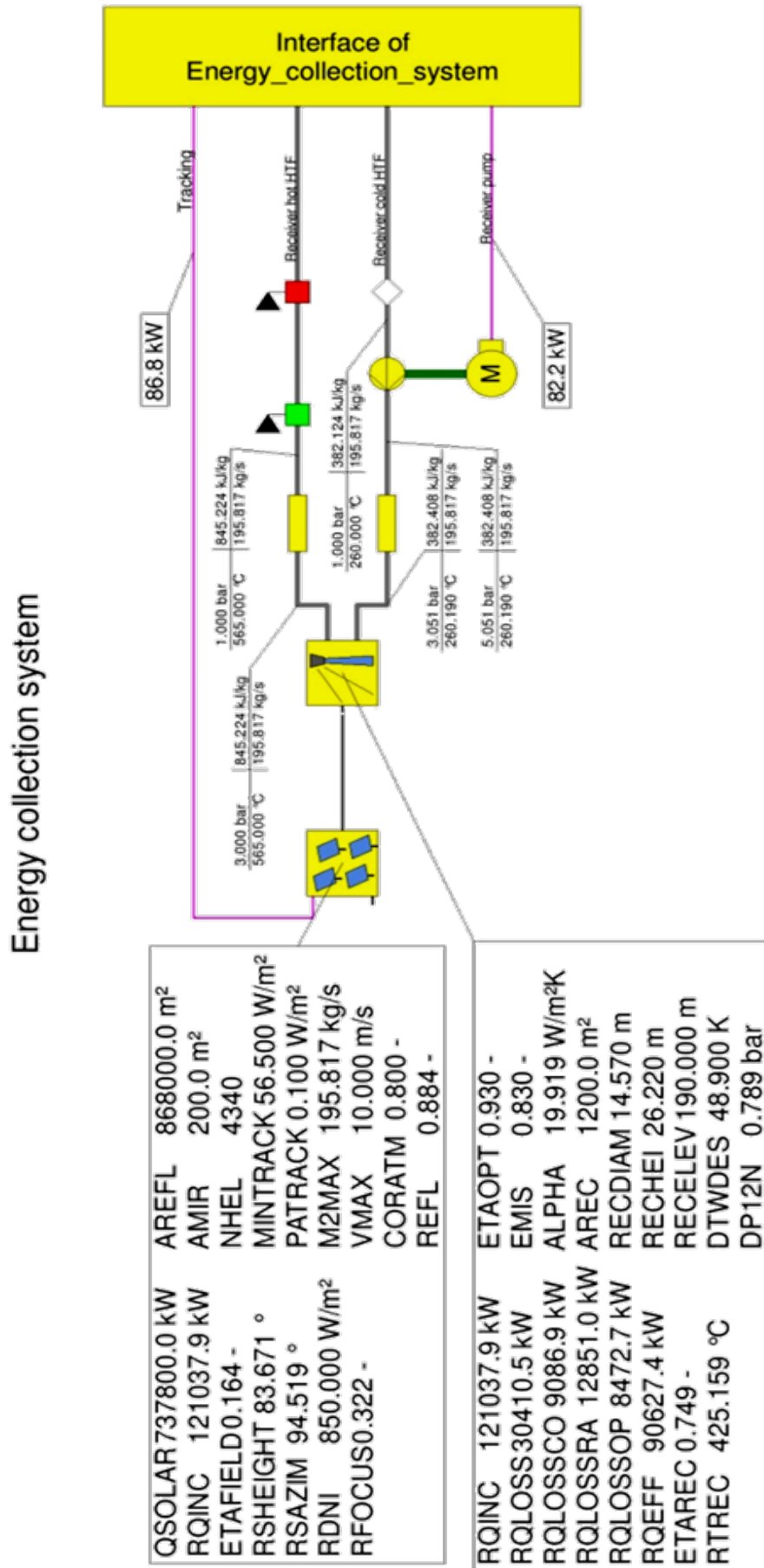


Figure 5-25: Content of the Energy Collection System macro

For the Energy Collection Switch an EbsScript was programmed, that is initiated before the calculation of the model is started. The principal function of this EbsScript is described in the following text that is written in italics and its code can be found in Appendix {1}.

If the DNI exceeds its minimum level, the Energy Collection System macro is activated (CalcState is switched from 0 to 1). In this case there are two possibilities:

- The level of the hot tank is below the maximum level → The HTF mass flow is restricted to MAXFLOWPUMP due to pump restrictions.*
- The level of the hot tank is at the maximum level → The HTF mass flow is restricted to 90% of the storage unload mass flow in order not to overflow the hot tank. If the storage unload mass flow is above MAXFLOWPUMP, the HTF mass flow is also restricted to MAXFLOWPUMP.*

If the Energy Collection System CalcState switches from 0 to 1, the Start Up macro is initialized too. If the DNI falls below its minimum level, the Energy Collection System is deactivated (CalcState is switched from 1 to 0).

The variable MAXFLOWPUMP is the maximum allowed receiver pump flow and can be defined in the specification-values tab in the properties window of the Energy Collection System macro. In this case it is defined as 110% of the maximum pump mass flow, namely 840 kg/s. The term "CalcState" describes whether the component is included into the model calculation (1) or not (0).

5.7 Heat Storage and Tank Heaters

In this chapter the Heat Storage and the Tank Heaters will be discussed in detail.

5.7.1 Heat Storage Properties

Principally all heat storage properties are determined by the calculation shown in chapter 6.2.2. These include the minimum level LEVMIN, the maximum level LEVMAX, the actual level LEVACT and the specific heat loss QLOSSR for each storage tank. Only the initial tank temperature TSTO is defined with 565°C for the hot tank and 290°C for the cold tank.

The values TSTO and LEVACT are recalculated in each time step for each tank considering inlet and outlet mass flow and temperature as well as the specific heat loss QLOSSR.

5.7.2 Heat Storage Additional Information

On top of each tank, tank vents and pressure reliefs are installed, which are required to equalize daily fluctuations in tank levels, accommodate tank overpressure events based upon an SGS tube rupture that allows steam coming into the salt flow, and other errors. Vent and relief systems must be electrically heat traced due to the salt mists that exist in each tank, which condense on each surface below 240°C. [86]

Through the vents hot air escapes the tank when it is filled and cold air flows into it when it is emptied, which causes losses that are not considered in this thesis. A common vent system that ties the two tanks together could be realized, but it is not economical since the electrical heat tracing consumption requirements of this system would far exceed any benefit of tying the two together [86].

At Solar Two, Barstow, California the cold salt tank inventory temperature was falling at a rate of 1.1 – 2.8°C/day starting from 290°C down to 260°C. The hot salt tank inventory temperature was falling at a rate of 5.5°C/day starting at 510-565°C. In both tanks the temperature gradient should not exceed 56°C/hour when loaded in order to provide sufficient time for thermal expansion of the tank structure. [86]

5.7.3 Heat Storage Cost Estimation

Pacheco et. al., 2001 [46] published costs of Solar Salt inventory, tank structure, salt-to-oil heat exchangers and filler material for a twin tank Solar Salt storage and thermocline single tank storage (Molten Salt with quartzite filler) each with a capacity of 688 MWh_{th} (Table 5-4). These values are valid for a parabolic trough power plant.

Table 5-4: Costs for a 688 MWh_{th} storage in the two-tank and the thermocline configuration [46]

Component	Two-Tank Molten Salt	Thermocline with Quartzite
Nitrate Solar Salt, \$k	11800	3800
Filler Material, \$k	0	2200
Tank(s), \$k	3800	2400
Salt-to-oil Heat Exchanger, \$k	5500	5500
Total, \$k	21100	13900
Specific Cost, \$/kWh	31	20

Based on this data the specific costs for all storage sizes could be extrapolated by making some assumptions:

- Solar Salt and Filler Material Costs grow linear with rising storage capacity.
- Salt-to-oil heat exchanger costs are integrated into the structural costs of the tank.
- The structural costs of the tank grow linear with the inner surface of the tank.
- The inner surface of the tank grows with an exponent of 2/3 with rising storage capacity. (When the volume of a body grows linear, its surface grows with an exponent of 2/3 when the proportions of the body keep the same.)

Based on these assumptions, a diagram with the specific storage costs over the storage size for the two tank storage could be created (Figure 5-26). It shows that for a storage size below 100 MWh_{th} the costs of the tank structure are getting dominant and for storage size above 1000 MWh_{th} the costs for the solar salt are more dominant. In Eq. 5-18 the cost function is illustrated, with C as the capacity in MWh_{th} and K as the total specific cost in \$/kWh_{th}.

5 Plant description

$$K = 17.2 + 119.3 \cdot C^{-\frac{1}{3}}$$

Eq. 5-18

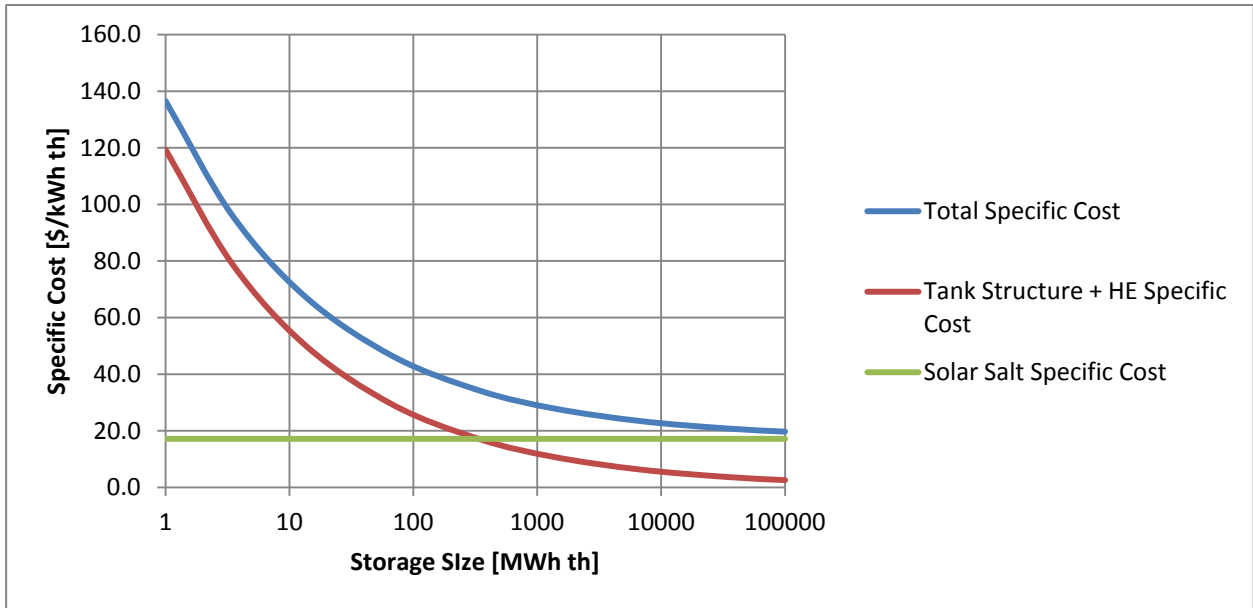


Figure 5-26: Specific storage costs for parabolic trough power plant with two tank storage

The same was done for the thermocline single tank storage (see Eq. 5-19 and Figure 5-27). It provides lower costs for structure and inventory.

$$K = 8.7 + 101.4 \cdot C^{-\frac{1}{3}}$$

Eq. 5-19

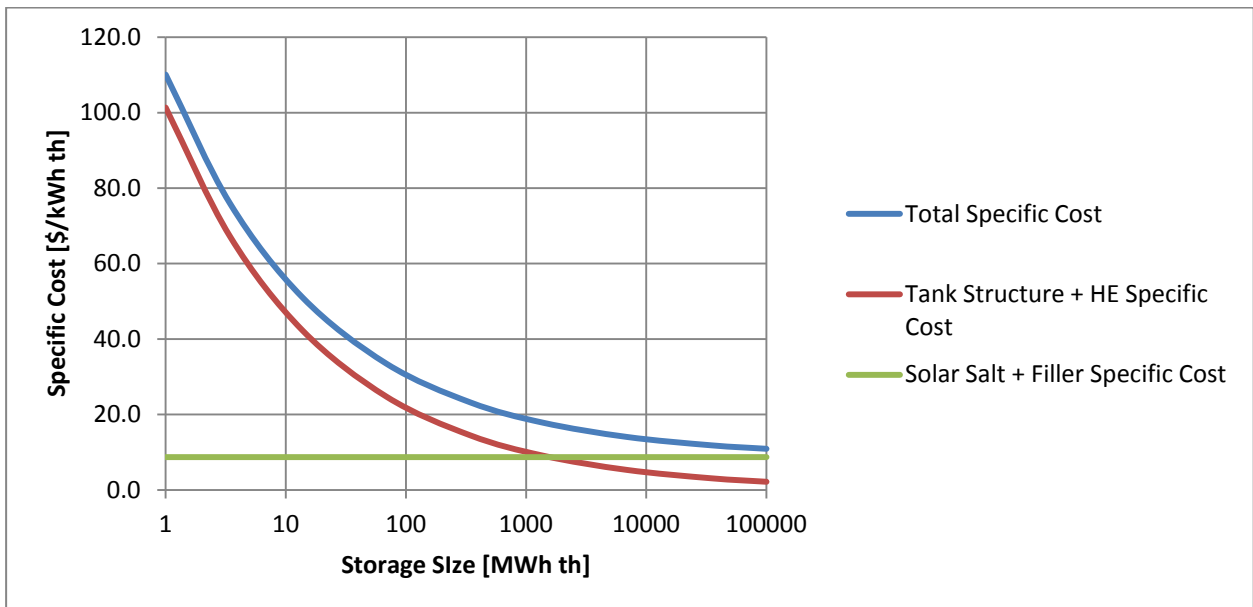


Figure 5-27: Specific storage costs for parabolic trough power plant with thermocline storage

Now it was attempted to adapt the data for solar tower power plants. For this purpose further assumptions were made:

- The salt-to-oil heat exchanger does not exist in this case, therefore its costs are not included
- To build a thermal storage for a solar tower power plant, 2.75-times smaller storage is necessary because of the 2.75-times wider temperature span used (see chapter 4.1).
- Therefore the Solar Salt cost was multiplied by 1/2.75 and the tank structure cost was multiplied by $(1/2.75)^{2/3}$

After implementing these assumptions, for two tank storage the following cost function (Eq. 5-20) and diagram (Figure 5-28) was the result. There is hardly any literature about established power plants with useful data for storage costs to validate these calculations.

In Vogel et. al. [70] for a 200MW solar tower power plant with two tank storage the costs for a 13 hour storage lies at 56 Mio. €. This leads to storage costs of 21.54 €/kWh_{el}. With an assumed efficiency of 40% this is equal to 8.6 €/kWh_{th}. The numbers in [70] are given in 2002-\$, therefore the exchange course for \$/€ is around 1. With a storage capacity of around 6500 MWh_{th} the value of 8.6 \$/kWh_{th} is used for an orientation of how good the curve fits (Figure 5-28).

$$K = 6.2 + 25.3 \cdot C^{-\frac{1}{3}} \quad \text{Eq. 5-20}$$

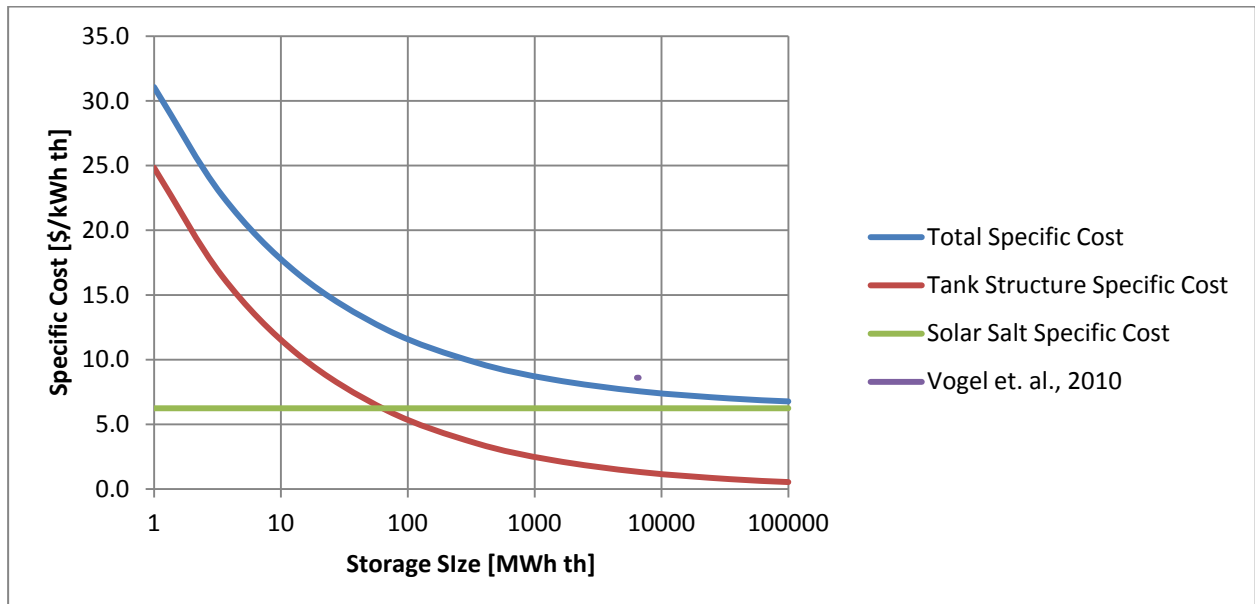


Figure 5-28: Specific storage costs for solar tower power plant with two tank storage

It shows up that the value derived from Vogel et. al. is not that far away from the total specific cost curve. The number of Vogel et. al. is about 14% higher than the graph of the total specific cost at a capacity of 6500 MWh_{th}. A final cost function (Eq. 5-21) and diagram (Figure 5-29) is now created for a solar tower power plant with thermocline storage. The costs for this kind of storage are comparatively low, they should be also validated if appropriate data is available.

$$K = 3.2 + 15.7 \cdot C^{-\frac{1}{3}}$$

Eq. 5-21

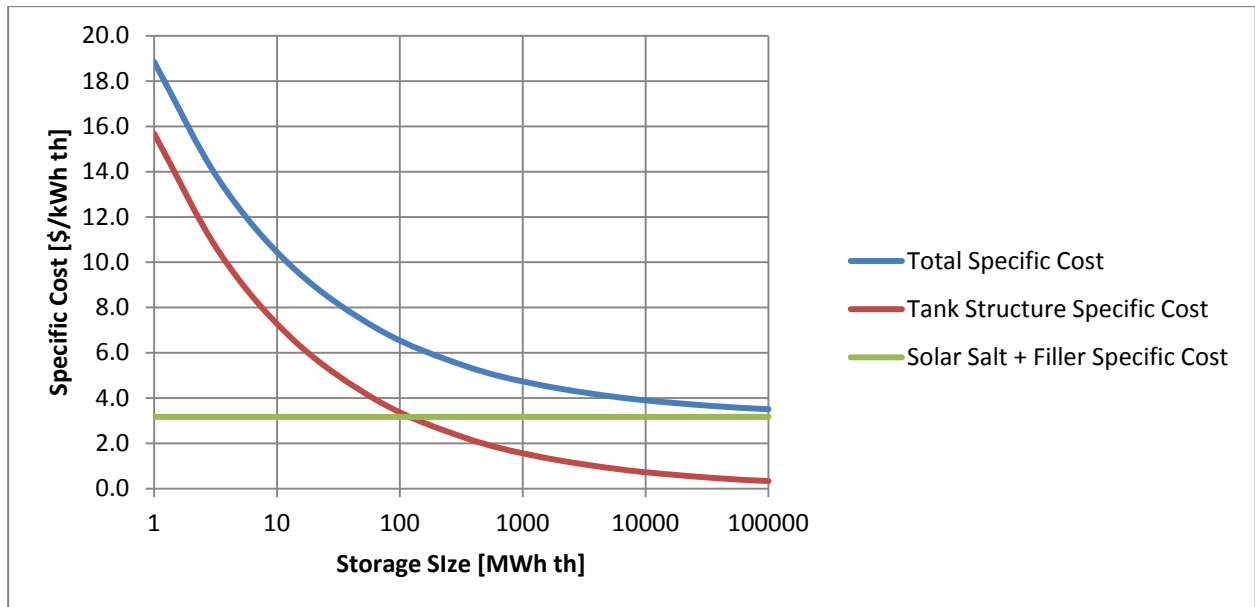


Figure 5-29: Specific storage costs for solar tower power plant with thermocline storage

As a conclusion it should be said that these diagrams should be only used as rough cost estimation. The values might be quite feasible for parabolic trough power plants with storage capacities around 688MW_{th} , but for much higher or lower values the error due to the assumptions is increasing. Despite the use of an orientation value that was quite near the total specific cost curve, the diagrams for a solar tower power plant should be handled with care. Unfortunately there are hardly any more values available to validate these diagrams.

5.7.4 Tank Heaters Properties

The tank heaters in the EBSILON model are gas powered. An exhaust gas with a temperature of 700°C is produced and cooled down to 310°C . Both tank heaters are programmed to keep a temperature of the tank inventory of 260°C .

5.7.5 Tank Heaters Additional Information

The main function of the tank immersion heaters is to prevent the salt inventory in the tanks from freezing during long term holds, where there is no salt exchange given. The temperature in the tanks drops due to heat losses through the tank wall. A tank containing frozen salt is the worst case scenario for a solar thermal power plant, because then the tank is irreparably damaged.

Immersion heater housing assemblies are capped pipes mounted in the tank walls that extend radially into each tank. To allow permanent submergence, the heaters are installed at an elevation within the heel of the tank. The cold and the hot tank immersion heaters are able to maintain the tank temperatures above 260°C . The immersion heaters in the cold tank are

capable of heating the salt inventory up to 400°C (max. 430°C on pipe surface) and the one in the hot tank are capable of heating the inventory up to 540°C (max. 593°C on pipe surface). [86]

5.7.6 Tank Heater States

The Tank Heaters Switch monitors the molten salt temperatures in both tanks and initiates the gas powered immersion heaters for the appropriate tank in order to maintain a temperature of 260°C (This value can be adjusted for each of the tanks). The content of the Tank Heaters macro is shown in Figure 5-30. On this figure one can see two kinds of lines, the pink electric lines to power the fans of the immersion heaters and violet pipes which contain natural gas in order to fuel the immersion heaters. The incoming natural gas has the same temperature like the ambient air. Both lines are split up for the Cold Tank Heater sub-macro and for the Hot Tank Heater sub-macro in order to let them operate independently.

The content of the Cold Tank Heater sub-macro is shown in Figure 5-31. The Cold Tank Heater sub-macro is currently initiated in the pictures, the Hot Tank Heater sub-macro looks principally the same. An electric motor powers a fan that blows air into a natural gas burner and two controllers adjust the mass flows in a way, that the exhaust gas enters the immersion heater (yellow block after the burner) with 700°C and exits it with 310°C. The amount of heat transferred into the tank by the immersion heater must be equal to the amount of heat that exits the tank in order to maintain the tank temperature at 260°C.

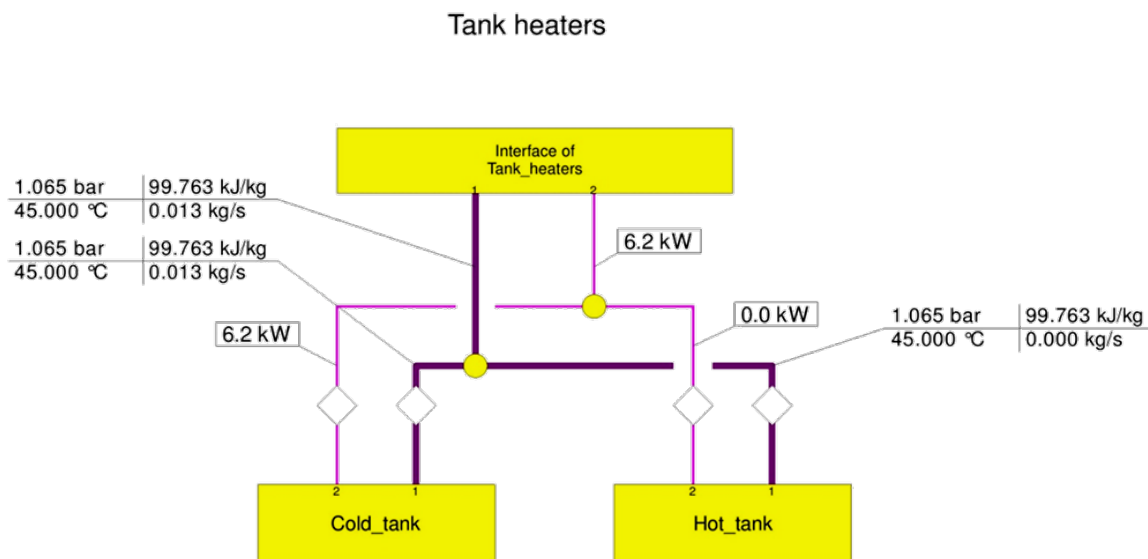


Figure 5-30: Content of the Tank Heaters macro

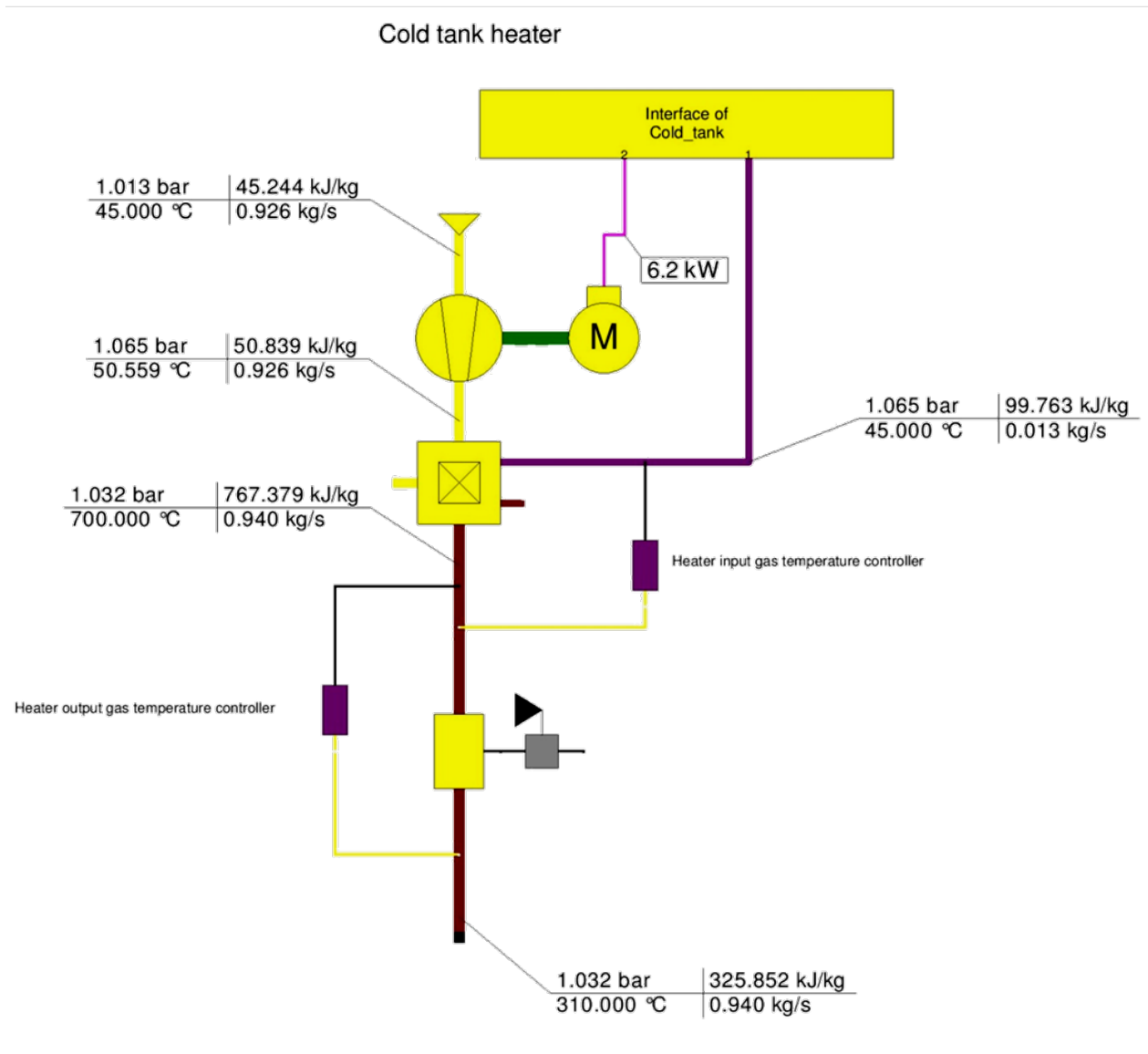


Figure 5-31: Content of the Cold Tank Heater sub-macro

For the Tank Heaters Switch an EbsScript was programmed, that is initiated after the calculation of the model is finished. The principal function of this EbsScript is described in the following text that is written in italics and its code can be found in Appendix {2}.

COLD TANK

If the temperature of the cold tank drops below 260°C, the Cold Tank Heater macro is activated (CalcState is switched from 0 to 1).

- The amount of heat transferred to the tank by the immersion heaters is equal to the amount of heat lost through the tank walls plus the heat lost by the molten salt consumption of the steam drum heaters during Hold Mode.*
- After this is done, the temperature of the cold tank is overwritten by the value 260°C.*

If the temperature of the cold tank is above 260°C, the Cold Tank Heater macro is deactivated (CalcState is switched from 1 to 0).

HOT TANK

If the temperature of the hot tank drops below 260°C, the Hot Tank Heater macro is activated (CalcState is switched from 0 to 1).

- *The amount of heat transferred to the tank by the immersion heaters is equal to the amount of heat lost through the tank walls.*
- *After this is done, the temperature of the cold tank is overwritten by the value 260°C.*

If the temperature of the hot tank is above 260°C, the Hot Tank Heater macro is deactivated (CalcState is switched from 1 to 0).

5.8 Energy Conversion System

In this chapter the Energy Conversion System will be discussed in detail. The simulation of different operation states and the transitions will also be explained.

In Figure 5-32 the content of the Energy Conversion System sub-macro is shown. It is integrated in the Energy Conversion switch that will be shown later. The description of the system is divided into four areas:

- Heat Recovery Steam Generator (HRSG) – violet dotted frame
- Steam turbine and electric generator – green dotted frame
- Steam turbine condenser – red dotted frame
- Regenerative feedwater preheating – blue dotted frame

Figure 5-33 illustrates the temperature-entropy (T-s) diagram of the Energy Conversion System for the design case. The light blue lines represent isobars and the grey lines represent isovapors. The green lines mark the course of the steam cycle process. In between the process cycle, six green lines mark the steam turbine bleedings with their appropriate feedwater preheating steps.

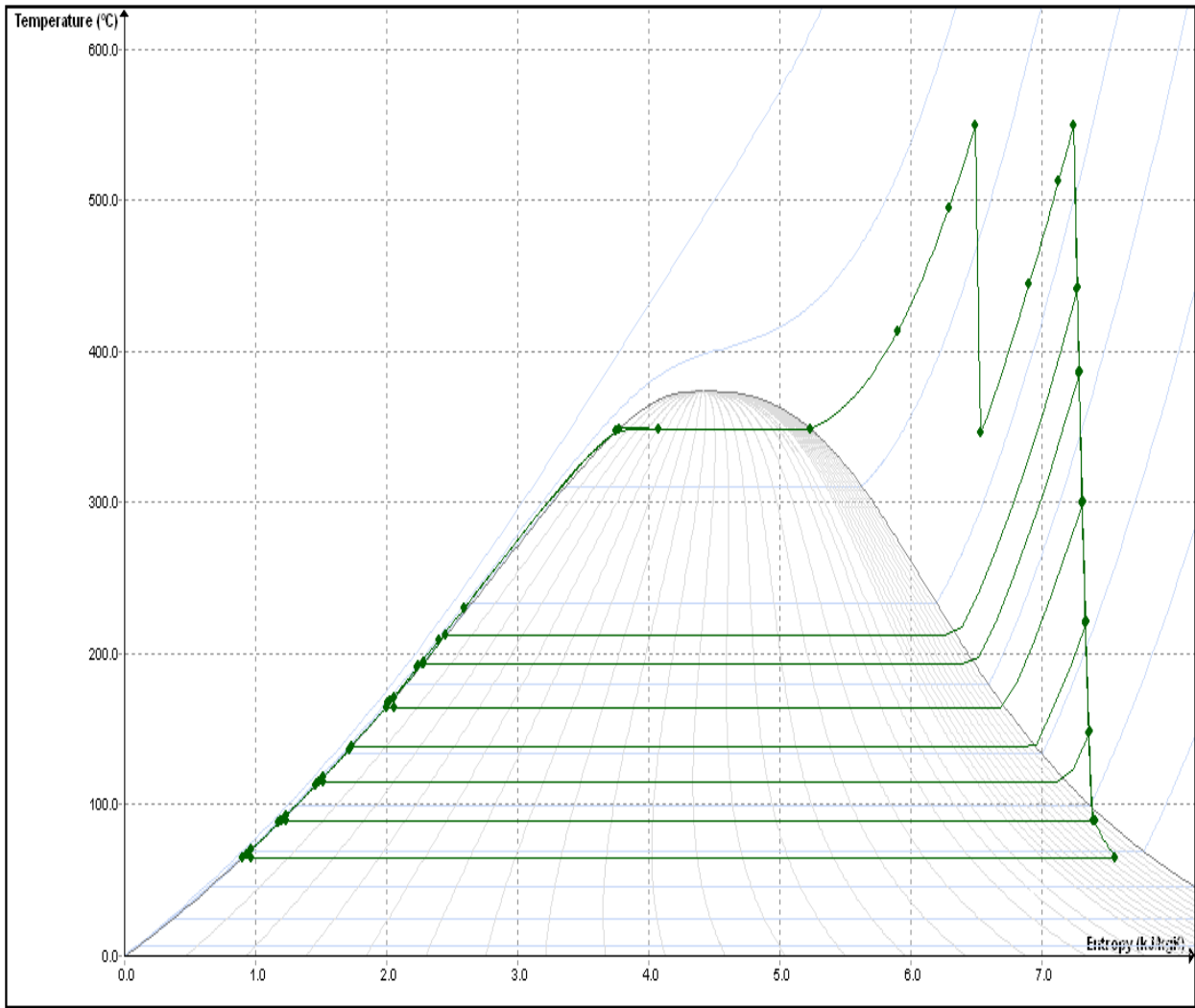


Figure 5-33: T-s – Diagram of the Energy Conversion System

5.8.1 Heat Recovery Steam Generator

The HRSG consists of a feedwater preheater, a forced circulation evaporator with a steam drum and a cascade of three super-heaters and three reheaters.

For safety reasons the feedwater temperature entering the preheater must be greater than 230°C to prevent salt freezing in the heat exchanger. Therefore, a controlled feedwater recirculation must always provide this temperature [86]. The circulation rate in the evaporator is around 5:1, which leads to a steam content at the end of the evaporator of about 20%.

For an overview of the temperatures and the heat transferred in the heat exchangers, Figure 5-34 shows a heat-temperature (\dot{Q} -T) diagram. The red line marks the molten salt flow and the blue line the feedwater/steam flow. The flows are countercurrent. The cascade circuitry of superheaters and reheaters allows the steam to reach a temperature of 550°C at the end of the superheaters and the reheaters. The rate of the transferred heat from the first superheater to the last superheater is about 3:2:1, the same applies for the reheaters. This is also illustrated in the diagram.

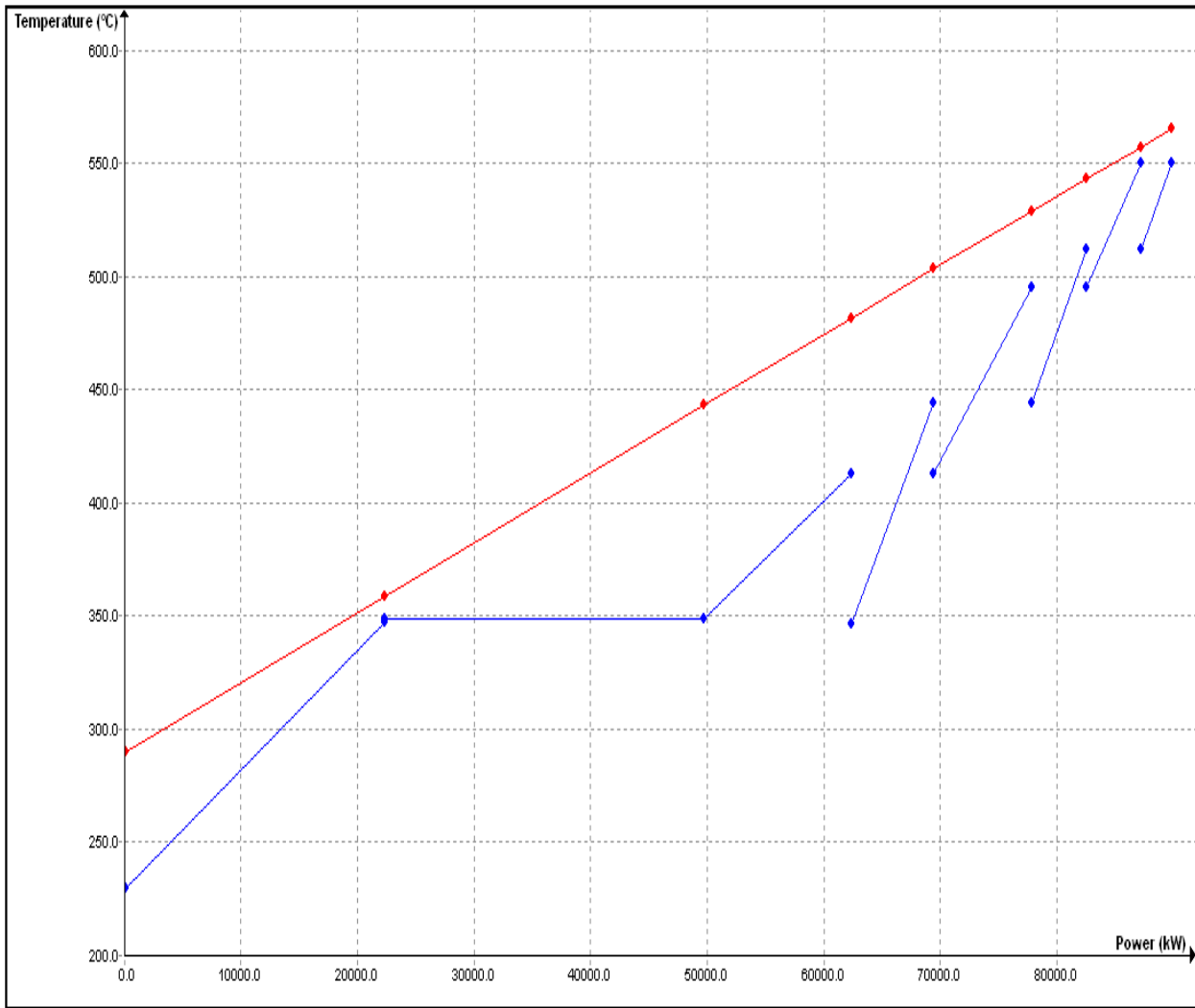


Figure 5-34: \dot{Q} -T – Diagram of the heat recovery steam generator

The water/steam side pressure drop in the preheater is 5 bar, in the evaporator it is 2 bar and in each superheater/reheater unit it is 1 bar. This leads to a total pressure drop for the superheater of 3 bar and for the reheater of 3 bar as well.

If the steam coming from the high pressure section is entering the low pressure section without reheating (e.g. no reheater is installed), the net efficiency of the conversion system drops from 39.2% to 37.3%, which is a deficiency of almost 2%. This shows that for high cycle efficiency reheating is very useful. However, an economical tradeoff must confirm that the higher costs of the reheater will be balanced by the higher efficiency and therefore higher incomes.

5.8.2 Steam Turbine and Generator

The steam turbine consists of a high pressure section and a low pressure section. The high pressure section uses live steam properties of 550°C / 160 bar coming from the superheater and the low pressure section uses steam properties of 550°C / 40 bar coming from the reheater.

The low pressure section of the turbine includes six turbine bleedings for the regenerative feedwater preheating. All bleedings are modeled with “hot extraction”, which simulates the fact that the steam temperature at the bleeding has a higher temperature compared to the average temperature of the steam flowing in the appropriate turbine section. This is because steam that passed the labyrinth-sealing is hotter than steam that passed the turbine blades and the bleedings are arranged on the outside after a labyrinth-sealing. For the last bleeding, which contains wet steam, a moisture removal could be applied that “dries” the steam before entering the last turbine section.

The generator has a nominal output power of 38 MW, which is kept constant by controlling the molten salt flow rate. The efficiency of the generator is 99%, in this value the efficiency of a gear box for the high pressure section is also included. The polytropic efficiency of high pressure and low pressure section of the turbine was assumed with 92% (the determined value might be too high for such a “small” turbine) and the mechanical efficiency with 99.8%.

Steam turbines with similar high live steam properties are used in the Ivanpah solar power complex, California, USA (see Figure 5-35).



Figure 5-35: Used turbine configuration of the Ivanpah solar tower power plant, California, USA [61]

The Ivanpah solar tower power plant uses Siemens SST-900 turbines, which are not available for outputs lower than 50MW (see Figure 5-36). Another steam turbine with similar maximum live steam properties is the SST-700 turbine, which is available for outputs from 20MW – 175MW.

5 Plant description

Type	Steam parameters	Output (MW)				
		50	100	150	200	250
SST-110	130 bar, 530° C					
SST-120	130 bar, 530° C					
SST-300	120 bar, 520° C					
SST-400	140 bar, 540° C					
SST-600	140 bar, 540° C					
SST-700	165 bar, 585° C	Dual casing / reheat or non-reheat				
SST-800	140 bar, 540° C	Single casing / reheat or non-reheat				
SST-800 & SST-500	140 bar, 540° C					
SST-900	165 bar, 585° C	Single casing / non-reheat		Dual casing / reheat		

Figure 5-36: Siemens steam turbines feasible for CSP power plants [61]

A layout of this turbine is illustrated in Figure 5-37. Between the high pressure turbine and the generator a gear box is located allowing the high pressure turbine to rotate with a higher speed. The shown condenser is for a wet cooling configuration. The modeled turbine could be based on the SST-700 design or on a similar design from another manufacturer.

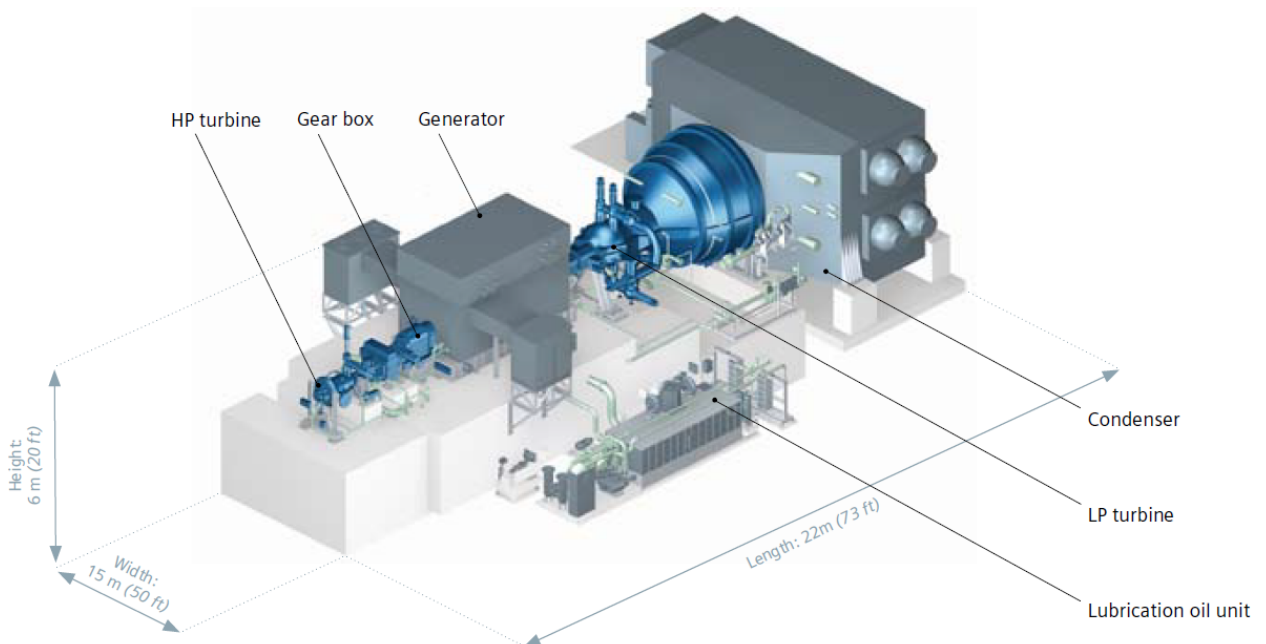


Figure 5-37: Layout of a Siemens SST-700 steam turbine [60]

5.8.3 Condenser

The modeled condenser is for a dry cooling configuration, which also includes a fan to provide the appropriate air flow. Through an optimization process it was discovered that a spread between condensation temperature and ambient temperature of 19.5 K is the optimum for this plant configuration. For lower spreads, the condensation temperature is lower, which goes along with lower condenser pressures that lead to higher efficiencies. For this advantage a higher required air mass flow from the fan that needs higher auxiliary power consumption would have to be accepted.

In arid climates often there is not enough water available for wet cooling of solar thermal power plants. The condenser fan is the highest of all auxiliary loads, which shows the high impact of dry cooling on the net efficiency of the power plant. If enough water for cooling purposes is available, wet cooling should be preferred. The steam cycle is designed for a maximum ambient temperature of 45°C because the condenser fan and all pumps must be capable to provide a generator output of 38 MW even at this temperature. This is because the lower efficiency of the steam cycle requires a higher steam flow for the same power output. The steam cycle, therefore, runs more efficient on cold days, especially during the night when the ambient temperature is lower.

5.8.4 Regenerative Feedwater Preheating

The regenerative feedwater preheating consists of five feedwater preheaters, five aftercoolers, a deaerator, a condensate pump and a feedwater pump. Steam coming from a turbine bleeding is cooled down and totally condensed in the feedwater preheater, after that, the remaining heat in the condensate is transferred to the feedwater via an aftercooler before it is throttled in order to be mixed with the feedwater in the next feedwater preheater. The \dot{Q} -T-Diagram of this process is shown in Figure 5-38. The red line indicates the steam/condensate from the bleedings and the blue line indicates the feedwater flowing countercurrent. A conspicuous discontinuity is provided in this diagram, because EBSILON cannot display the process in the deaerator because of the combined heat exchange and fluid mixing in it. The purpose of the deaerator is to extract harmful gases out of the feedwater; in this process the feedwater also gets preheated by steam from a bleeding.

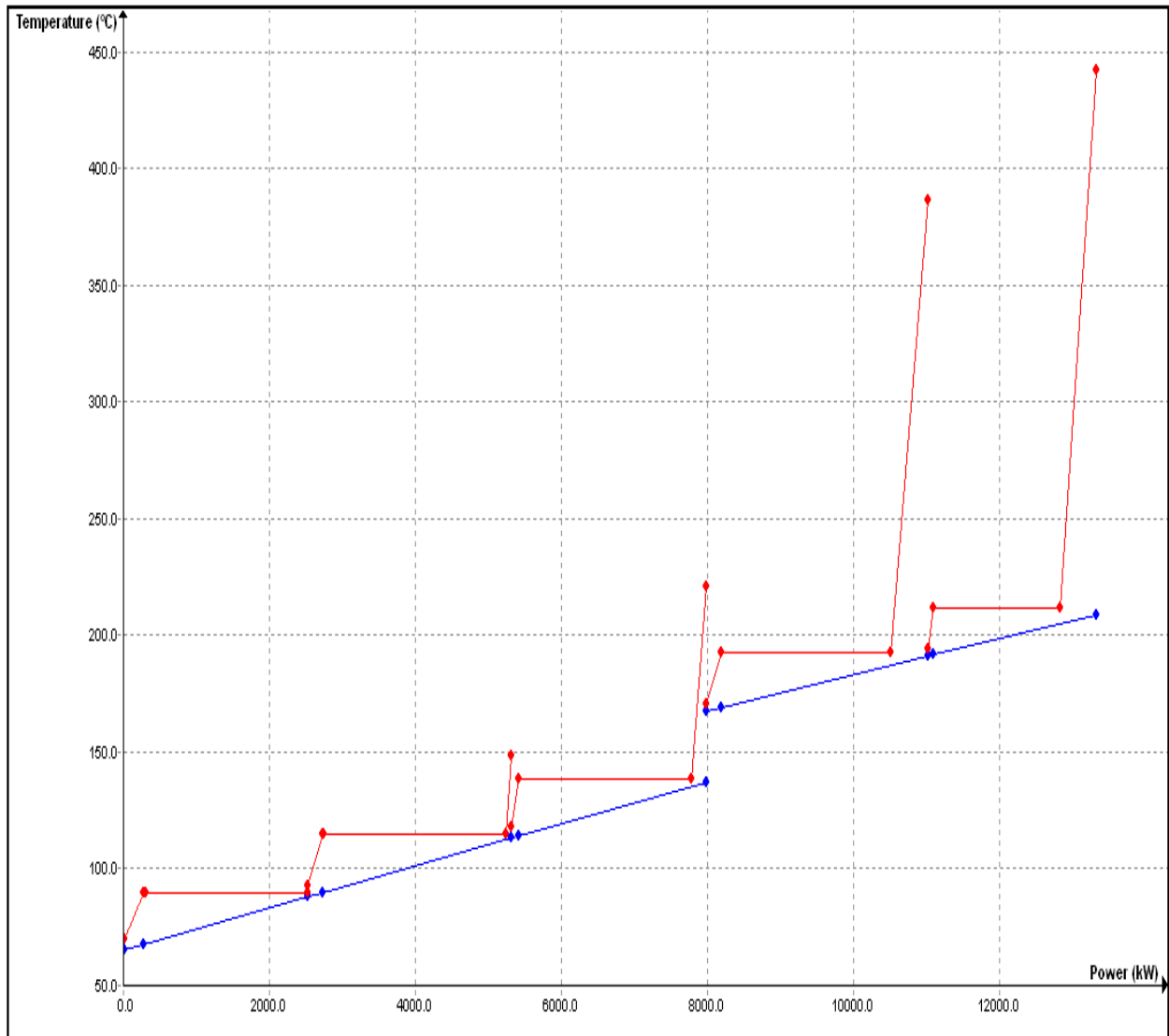


Figure 5-38: \dot{Q} -T – Diagram of the regenerative feedwater preheating

In an optimization process the pressures of the bleedings were varied in order to find the maximum efficiency of the steam cycle. The result with the highest efficiency shows a quite uniform distribution of the condensation temperatures. The feedwater preheater with the highest condensation temperature could also have a slightly higher condensation temperature that heats the feedwater even higher, but it was reduced manually to cope with lower ambient temperatures that influence this system. The amount of preheating reduced in this feedwater preheater was shifted to the feedwater recirculation.

Generally, the more turbine bleedings and feedwater preheating steps there are, the lower the exergy losses. This is because the area between the blue line and the red line is reduced by smaller steps. Again, it is an economic tradeoff, because each preheat step is costly.

To see what happens to the efficiency, attempts were made to eliminate the regenerative preheating. The result was an efficiency drop of about 4%, which mainly reflects high exergy losses in the HRSG.

5.8.5 States and Transitions

As already explained in chapter 5.5, the Energy Conversion Switch consists of the four sub-macros Energy Conversion System, Start Up, Shut Down and Hold Mode. Long Term Hold is not implemented, because this mode is often manually initiated by power plant operator decisions based on extended bad weather forecasts or maintenance. The *Hold Mode* implements the features of the Overnight Hold. Auxiliary Steam and Turbine Synchronization are combined in the *Start Up* Macro, which is always initiated when the Energy Conversion System is switched on. If the latter is switched on, the *Normal Operation* is established. To model the transition when the Energy Conversion System is switched off, the *Shut Down* macro was created.

Similar to the Start Up macro in the Energy Collection Switch, the Start Up macro here is just initiated when the Energy Conversion System is started for the first time. This initialization lasts for one time step, in this case for one hour. Even though the additional electric and molten salt consumptions need different time spans each, their determined power must be recalculated for the time span of one hour. These determined power values must be derived from detailed analysis of the Start-Up phase, which needs a lot of experience. They also could not be found in any literature.

The same is valid for the Shut Down macro, which is initiated for one time step when the Energy Conversion System is switched off. The Hold Mode macro is initiated when the Energy Conversion System macro is switched off and keeps initiated as long the latter is off.

The requirement to operate the Energy Conversion System is that the level of the hot storage tank exceeds the bottom level by the amount of molten salt required to operate the turbine for one hour plus shutdown losses. If this level is exceeded for the first time, the Energy Conversion System macro will be started one hour after that. This delay was found out to be necessary to avoid numerous switching on/off procedures during one day at unsettled weather conditions.

Figure 5-39 illustrates the content of the Energy Conversion Switch macro. One can see a network of lines that connect the interface of the Energy Conversion Switch with the appropriate sub-macros. Again electric lines are colored in pink and HTF lines are colored in grey. For a better visibility, the line for the attemperation HTF is dashed grey-green, the line for the electric steam generator is dashed pink-red and the line for the auxiliary feedwater pump is dashed pink-black.

The Energy Conversion System was already shown before; Figure 5-40, Figure 5-41 and Figure 5-42 show the content of the Start Up, the Shut Down and the Hold Mode sub macro respectively.

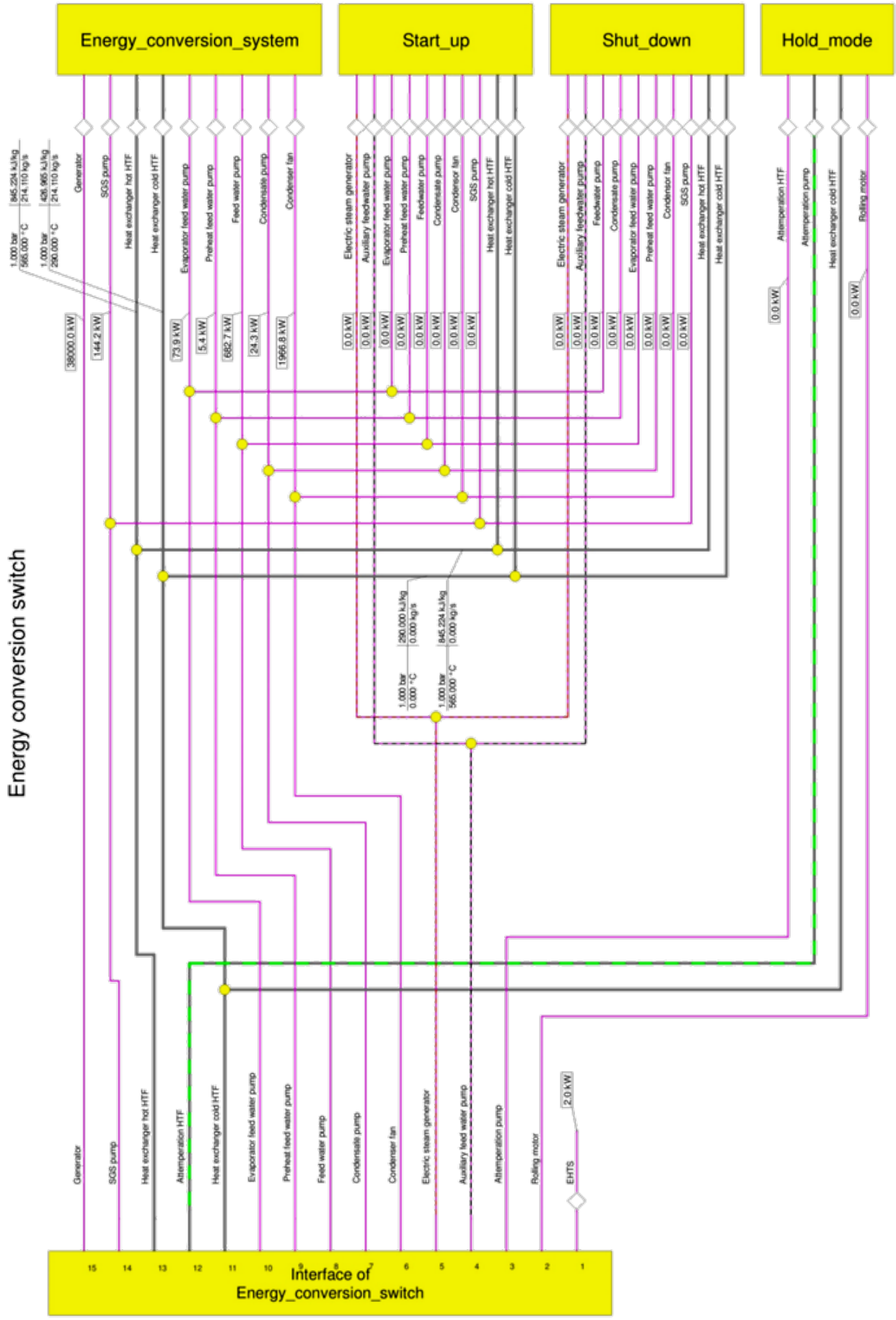


Figure 5-39: Content of the Energy Conversion Switch macro

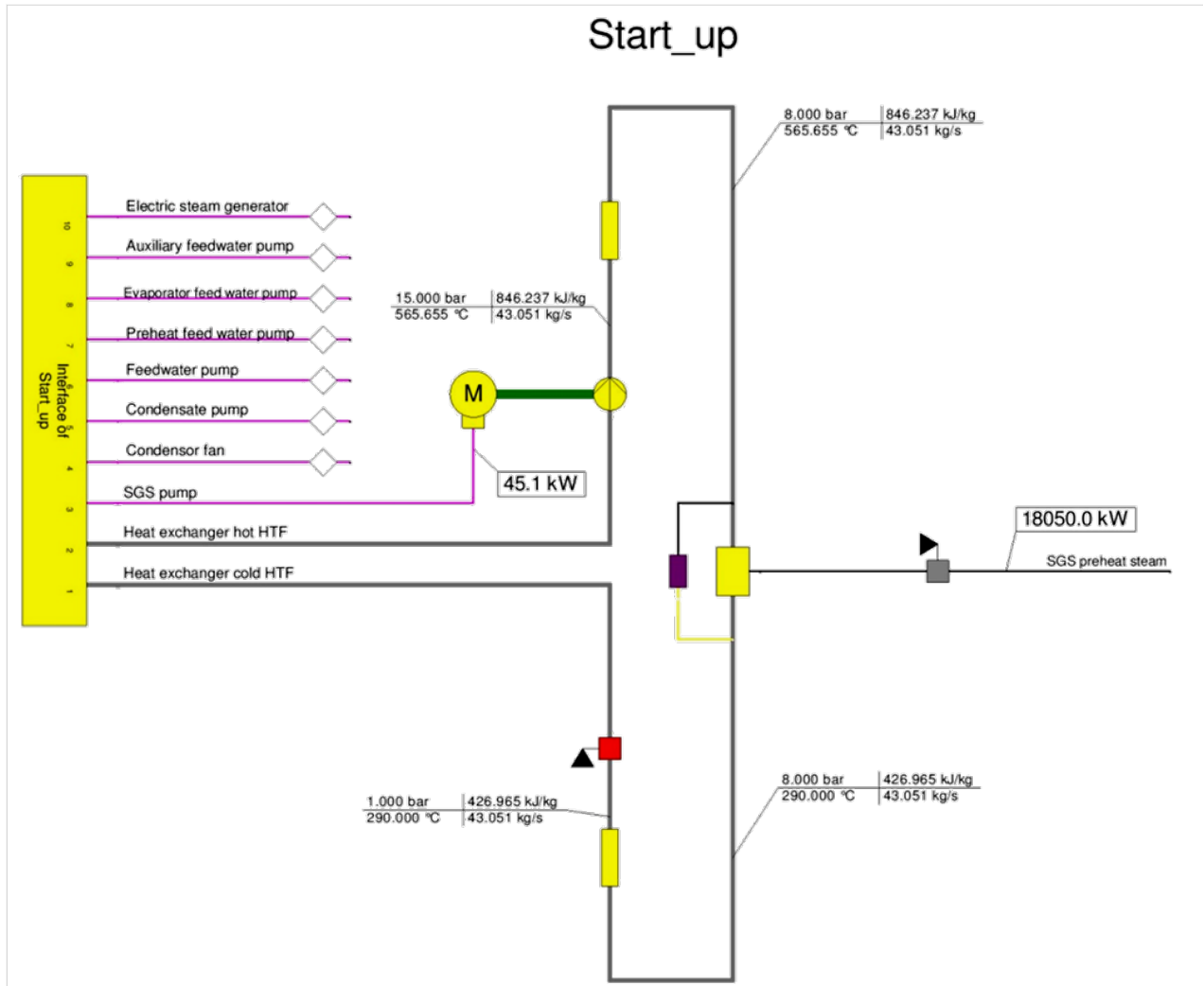


Figure 5-40: Content of the Start Up sub macro

As aforementioned, the Start Up macro is just initiated when the Energy Conversion System macro is started for the first time. The estimated power values are shown in the following:

- Electric steam generator: 20kW
- Auxiliary feedwater pump: 1kW
- Evaporator feedwater pump: 15kW (20% of nominal load)
- Preheat feedwater pump: 5kW (20% of nominal load)
- Feedwater pump: 134kW (20% of nominal load)
- Condensate pump: 3.5kW (20% of nominal load)
- Condensor fan: 400kW (20% of nominal load)
- SGS preheat system: 18050kW (20% of nominal load, used to preheat the steam circuit)

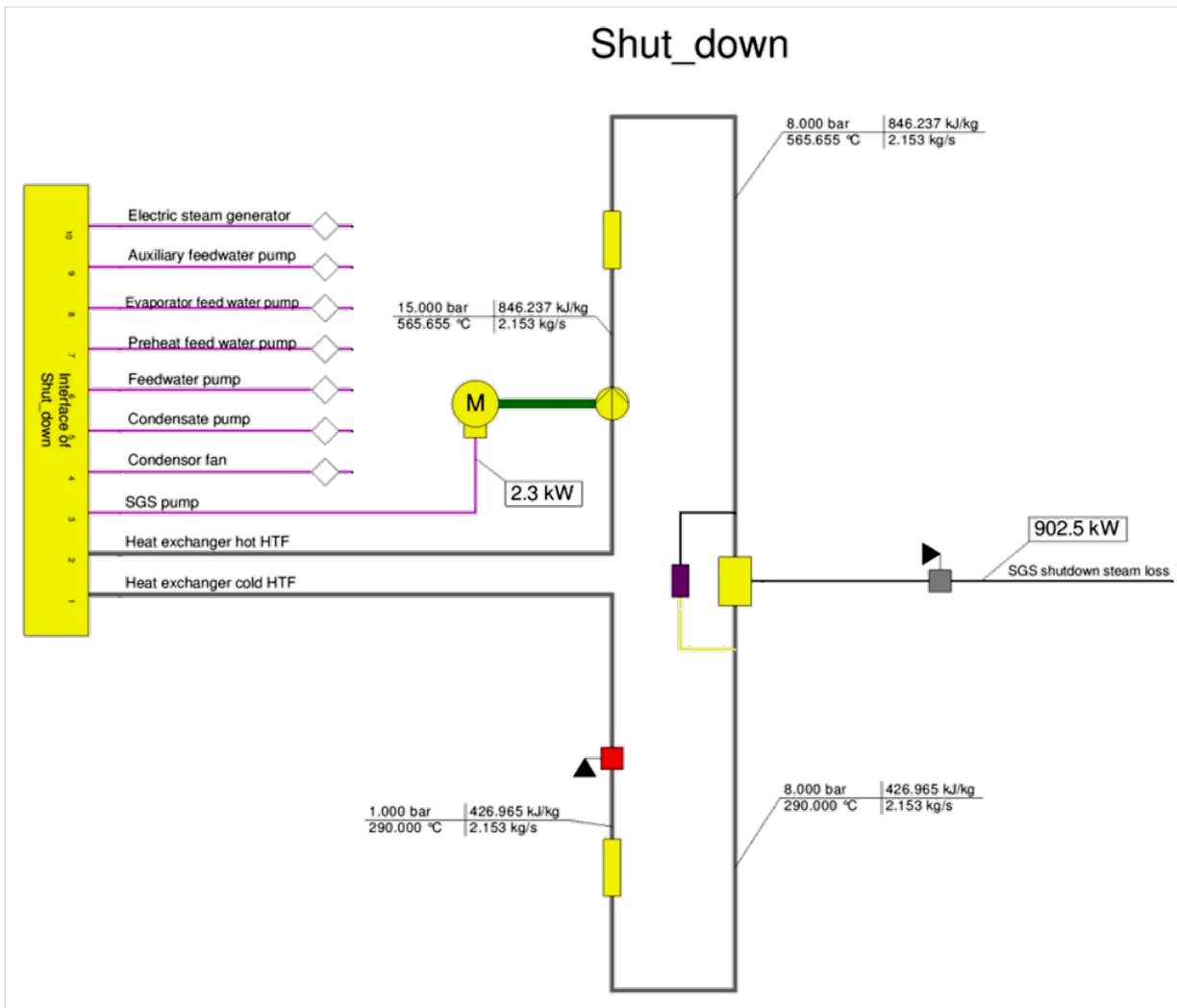


Figure 5-41: Content of the Shut Down sub macro

The Shut Down macro is just initiated for one hour if the Energy Conversion System macro is switched off. The estimated power values are:

- Electric steam generator: 20kW
- Auxiliary feedwater pump: 1kW
- Evaporator feedwater pump: 0.75kW (1% of nominal load)
- Preheat feedwater pump: 0.25kW (1% of nominal load)
- Feedwater pump: 7kW (1% of nominal load)
- Condensate pump: 0.2kW (1% of nominal load)
- Condensor fan: 200kW (10% of nominal load)
- SGS shutdown steam loss: 902.5kW (1% of nominal load, lost during SGS shut down)

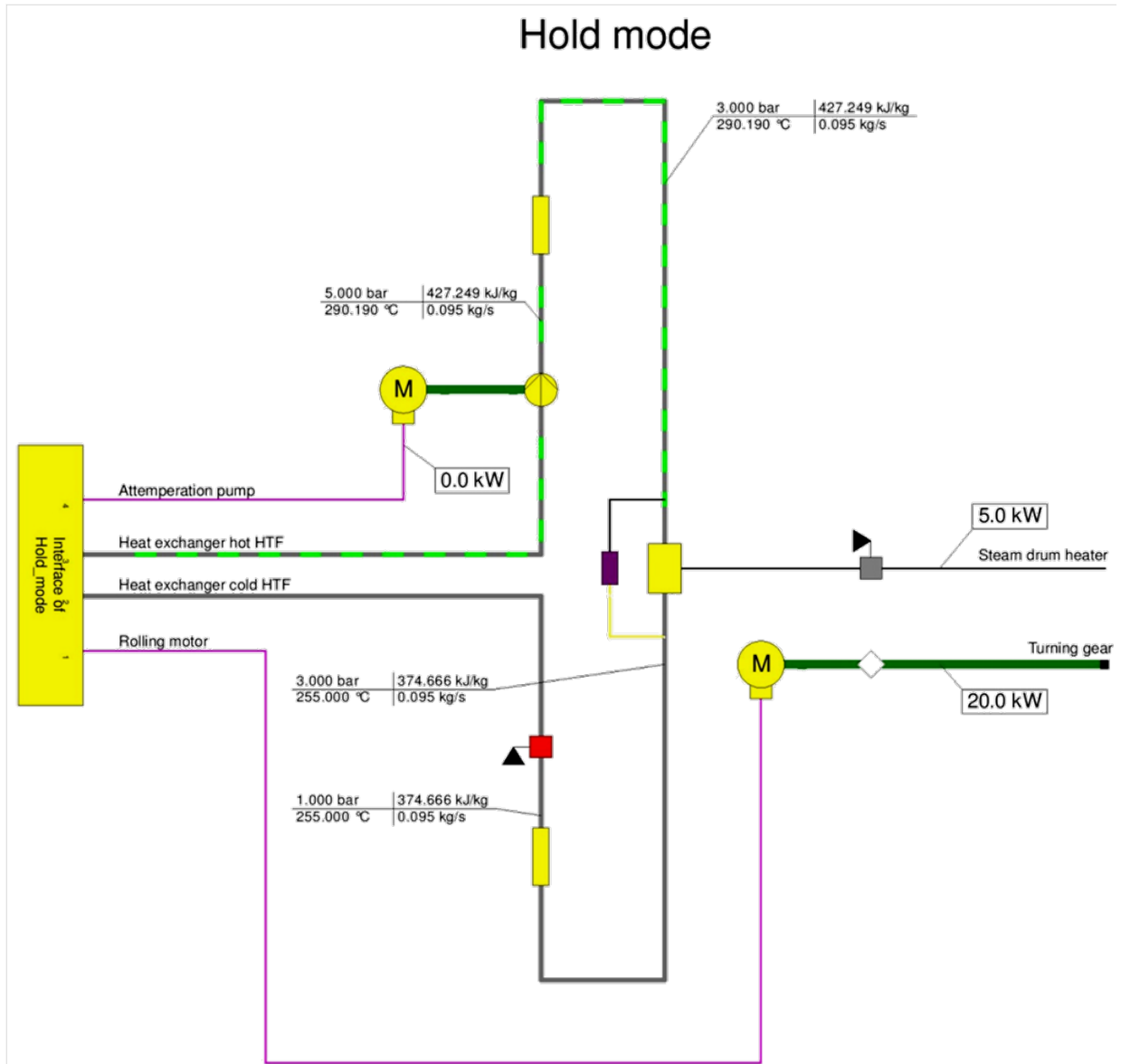


Figure 5-42: Content of the Hold Mode sub macro

The Hold Mode macro is initiated as long as the Energy Conversion System macro is switched off. The estimated power values are:

- Steam drum heater: 5kW (Attemperation HTF is used to heat the steam drum)
- Turning gear: 20kW (The turbine shaft is rotated slowly to avoid static bending)

The EHTS for the SGS was taken into account with a permanent power of 2kW. Obviously, this does not represent reality because it is operating on demand, but it should represent the annual average power for this system.

Auxiliary steam (also mentioned in chapter 5.4) is produced by two sources (according to [86]):

- Lower demand $\leq 2\%$ of the rated SGS design duty is produced by using a small electric boiler to generate sufficient steam for turbine shaft seals and establishing the condenser vacuum.
- Higher demand $>2\%$ of the rated SGS design duty using SGS is produced by using the auxiliary feedwater heater, preheater, evaporator and steam drum will be required after the condenser vacuum has been established for main steam line warm-up, feedwater heating and rolling the turbine through turbine synchronization.

For the Energy Conversion Switch an EbsScript was programmed, that is also initiated after the calculation of the model is finished. The principal function of this EbsScript is described in the following text that is written in italics and its code can be found in Appendix {3}.

ENERGY CONVERSION SYSTEM ACTIVATION

If the level of the hot tank is over its minimum level (plus the amount of molten salt needed for one hour of operation and the molten salt needed to cover the shutdown losses), the Energy Conversion System macro is activated (CalcState 1). All efficiencies will be calculated. The Hold Mode macro will be deactivated (CalcState 0).

START UP ACTIVATION

If the Energy Conversion System CalcState switches from 0 to 1, the Start Up macro is initialized for one time step (one hour).

SHUT DOWN ACTIVATION

If the Energy Conversion System CalcState switches from 1 to 0, the Shut Down macro is initialized for one time step (one hour).

HOLD MODE ACTIVATION

If the level of the hot tank is below the mentioned level, the Energy Conversion System macro is deactivated (CalcState 0). None of the efficiencies will be calculated, they are set to 0. The Hold Mode macro will be activated (CalcState 1).

6 THERMODYNAMIC SIMULATION

This section is concerned with the thermodynamic simulation of the modeled solar tower power plant. First, the capability of the EBSILON Professional software will be introduced, then in the chapter plant analysis the receiver design and the storage design will be determined and calculated, and finally several time series analysis will show some details.

6.1 EBSILON Professional

In the previous chapters, some aspects of EBSILON Professional were already anticipated. EBSILON Professional is an “All in One” solution for plant engineering. It can be used for engineering, acquisition, and planning for all kinds of power plants and other thermodynamic processes. Furthermore, the module SR::EPOS can be used for power plant monitoring and power plant optimization. EBSILON Professional enables the balancing of individual parts and components, component groups, subsystems, and complete systems regardless if these build an open or closed circulation. The solution process is a matrix solution. This requires the linearization of all dependencies. To take into account influences resulting from non-linearities, a Newton iteration conducted afterwards. In Figure 6-1 a screenshot of the EBSILON Professional window is shown. [16]

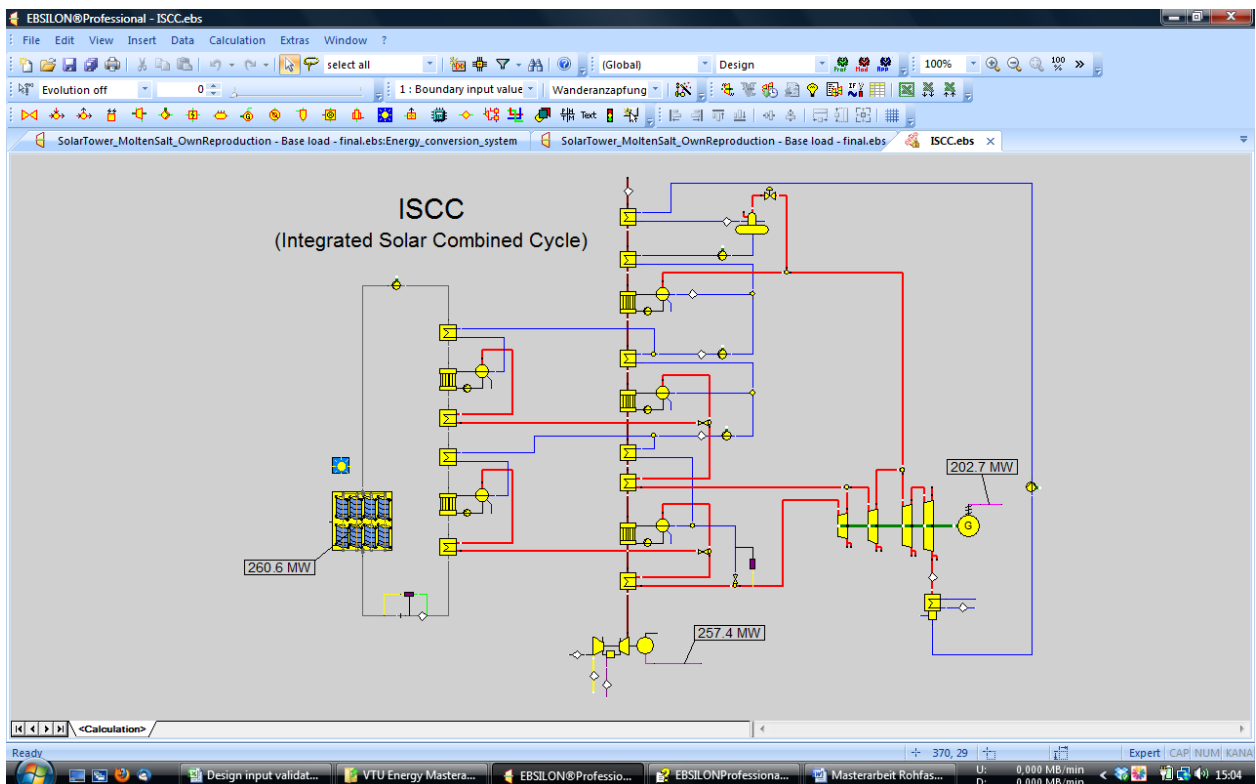


Figure 6-1: Screenshot of an ISCC power plant in EBSILON Professional

6.2 Plant Analysis

In this chapter the receiver design and the storage design are discussed in detail with all assumptions made. For the design calculation, The EBSILON-Excel interface was used, which is able to exchange values between EBSILON Professional and Microsoft Excel.

6.2.1 Receiver Design

In the receiver design calculation, preferably realistic values for DP12N, DTWDES and ALPHA have to be determined. This is done by an iterative calculation, for which this chapter should provide an overview. Several values are read out from EBSILON, used for the calculation in Excel and then the resulting values for DP12N, DTWDES and ALPHA are fed into EBSILON again. After that, a simulation in EBSILON is performed, which changes the values read out by Excel again. The number of iterations done is fixed to ten, because this number is fairly enough to gain residual values.

Values that may change during iteration are the heat absorbed by the fluid (RQEFF), the HTF massflow (M), and the mean outside wall temperature (RTREC). Figure 6-2 shows a part of the receiver design sheet in Excel, which is also included in Appendix {4}.

Description	Variable	Ebslion variable	Value	Unit	Formula \ Comment
Receiver diameter	Drec	Solar_tower.RECDIAM	14.57	m	
Receiver height	H	Solar_tower.RECHEI	26.22	m	
Receiver area	A	Solar_tower.AREC	1200	m ²	AREC = RECDIAM * π * RECHEI
Intercept receiver power		Solar_tower.RQINC	375508.7635	kW	
Heat absorbed by fluid	Q.eff	Solar_tower.RQEFF	322814	kW	RQEFF = ETAREC * RQINC
HTF massflow	m.	ThermoLiquid.M	772.383	kg/s	
HTF inlet temperature	T1	ThermoLiquid_1.T	290.00	°C	
HTF outlet temperature	T2	ThermoLiquid.T	565.00	°C	
Mean outside wall temperature	Twa,m	Solar_tower.RTREC	466.58	°C	RTREC = T1 + K * (T2 - T1) + DTWDES * Q
Mean ambient temperature	Ta,m	Solar_tower.RTAMB	45	°C	For design case or given from time serie
Wind speed at receiver height	vw	Solar_tower.RVWIND	3.9	m/s	For design case or given from time serie
Forced convection multiplier		Solar_tower.SCONV	1		Value should be set to 1 due to the con
Number of serial panels	n,pa		1		=1 for flood flow operation; >1 for serpa
Number of pipes per serial panel	n,ppp		540		
Pipe wall thickness	d		0.002	m	
Average thermal conductivity (wall)	λa,w		20.5	W/mK	e.g. AISI 316Ti (20,5 W/m ² K at 450°C ave

Figure 6-2: Screenshot of a part of the receiver design sheet in Excel

Blue values are read out from EBSILON, white are editable, yellow are calculated ones, and red values are written into EBSILON before the next simulation is performed. The calculation is only valid for cylindrical receiver types using Solar Salt as HTF and a variable receiver temperature model, but it is adaptable to any boundary conditions and input values.

The variables used in the Excel formulas differ from the EBSILON variables. Table 6-1 shows the translation from EBSILON variables into Excel variables. In the following formulas subscripts were not used to keep the same variable names used in Excel. In front of the EBSILON variables the component names like Solar_tower or Thermo_liquid mark their belonging.

Table 6-1: EBSILON variables translated into Excel variables

EBSILON Variables	Excel Variables
Solar_tower.RECDIAM	Drec
Solar_tower.RECHEI	H
Solar_tower.AREC	A
Solar_tower.RQEFF	Q.eff
ThermoLiquid.M	m.
ThermoLiquid_1.T	T1
ThermoLiquid.T	T2
Solar_tower.RTREC	Twa,m
Solar_tower.RTAMB	Ta,m
Solar_tower.RVWIND	vw
Solar_tower.DP12N	Δp
Solar_tower.DTWDES	ΔT
Solar_tower.ALPHA	$\alpha\alpha'$

a) Determination of Pressure Loss

The receiver used in the calculation operates in flood flow instead of serpentine flow (see Figure 5-22, which shows serpentine flow), which means that all receiver panels receive cold molten salt at the bottom and are connected in parallel. Therefore the number of serial panels n_{pa} was set to 1. The number of pipes per serial panels n_{ppp} (therefore also the total number of pipes n) was set to 540 and the wall thickness of the pipes d to 2 mm. The chosen material of the pipes AISI 316Ti has an average thermal conductivity $\lambda_{a,w}$ of 20.5 W/m²K at 450°C average wall volume temperature [69]. The wall roughness factor rf was set to $\pi/2$ because the cylindrical receiver has a tube wall that multiplies a smooth cylinder surface by this factor.

The average HTF temperature $T_{a,f}$ of 427.5°C is determined by the receiver inlet temperature $T1$ (290°C) and the receiver outlet temperature $T2$ (565°C).

The outer diameter of the receiver pipes Da is calculated by Eq. 6-1 and the inner diameter Di of the receiver pipes is calculated by Eq. 6-2.

$$Da = \frac{Drec \cdot \pi}{n} = 0.027m \quad \text{Eq. 6-1}$$

$$D_i = D_a - 2 \cdot d = 0.023m \quad \text{Eq. 6-2}$$

The inside cross section area of the pipe A_i (Eq. 6-3) is therefore:

$$A_i = \frac{D_i^2 \cdot \pi}{4} = 0.000415m^2 \quad \text{Eq. 6-3}$$

The properties for the average HTF density $\rho_{a,f}$ (Eq. 6-4) and dynamic viscosity $\eta_{a,f}$ (Eq. 6-5) are taken from [63]; they could be also found in [86]. Both values just depend on $T_{a,f}$. The average HTF kinematic viscosity $\nu_{a,f}$ is derived from Eq. 6-6.

$$\rho_{a,f} = 2090 - 0.636 \cdot T_{a,f} = 1818.1 \text{ kg/m}^3 \quad \text{Eq. 6-4}$$

$$\begin{aligned} \eta_{a,f} &= 22.714 - 0.12 \cdot T_{a,f} + 2.281 \cdot 10^{-4} \cdot T_{a,f}^2 - 1.474 \cdot 10^{-7} \cdot T_{a,f}^3 \\ &= 1.585 \text{ mPas} \end{aligned} \quad \text{Eq. 6-5}$$

$$\nu_{a,f} = \frac{\eta_{a,f} \cdot \rho_{a,f}}{1000} = 8.716 \cdot 10^{-7} \text{ m}^2/\text{s} \quad \text{Eq. 6-6}$$

The average HTF volumetric flow $V.a$, (Eq. 6-7) the average HTF volumetric flow per pipe $V.a,p$ (Eq. 6-8), and the average HTF flow velocity $v.a$ (Eq. 6-9) can be calculated by comparatively simple formulas.

$$V.a = \frac{\dot{m}}{\rho_{a,f}} = 0.4248 \text{ m}^3/\text{s} \quad \text{Eq. 6-7}$$

$$V.a,p = \frac{V.a}{n_{ppp}} = 0.000787 \text{ m}^3/\text{s} \quad \text{Eq. 6-8}$$

$$v.a = \frac{V.a,p}{A_i} = 1.897 \text{ m/s} \quad \text{Eq. 6-9}$$

The Reynolds number Re (Eq. 6-10) can now be calculated from the values gained by the previous formulas. The pipe friction number ξ (Eq. 6-11) depends only on the Reynolds number and its order of magnitude [4]. Here a smooth pipe is assumed.

$$Re = \frac{D_i \cdot v.a}{\nu_{a,f}} = 50\,010 \quad \text{Eq. 6-10}$$

$$\xi = \frac{0.3164}{Re^{0.25}} = 0.0212 \quad (2310 \leq Re < 10^5) \quad \text{Eq. 6-11}$$

Now the pressure loss in the receiver Δp can be determined by Eq. 6-12. This value is then fed into EBSILON as the variable DP12N.

$$\Delta p = \frac{\xi \cdot n, pa \cdot \frac{H}{D_i} \cdot \frac{v \cdot a^2}{2} \cdot \rho a, f}{10^5} = 0.78934 \text{ bar} \quad \text{Eq. 6-12}$$

b) Determination of Design Wall Temperature Difference

The design wall temperature difference is the difference between the wall temperature of the inside and the outside of the receiver pipe. To calculate this value, two more HTF properties are also needed that only depend on the average HTF temperature $T_{a,f}$, the average specific heat capacity c_p (Eq. 6-13) and the average thermal conductivity λ_t (Eq. 6-14). Both formulas are also according to [63].

$$c_p = 1443 + 0.172 \cdot T_{a,f} = 1517 \frac{J}{kg K} \quad \text{Eq. 6-13}$$

$$\lambda_t = 0.443 + 1.9 \cdot 10^{-4} \cdot T_{a,f} = 0.524 \frac{W}{m K} \quad \text{Eq. 6-14}$$

Using these values and $\eta_{a,f}$ the Prandtl number Pr of the HTF at its average temperature $T_{a,f}$ can be calculated. Pr controls the relative thickness of the momentum and thermal boundary layers.

$$Pr = \frac{c_p \cdot \frac{\eta_{a,f}}{1000}}{\lambda_t} = 4.584 \quad \text{Eq. 6-15}$$

To consider the direction of the heat transfer, the Prandtl number must be also determined for HTF that directly touches the wall (Pr,w). For this purpose, first the mean inside wall temperature $T_{wi,m}$ of the receiver pipes must be determined. Eq. 6-16 is derived from the formula Q (heat flow) = k (combined heat transfer coefficient) $\cdot A$ (area) $\cdot \Delta T$ (temperature difference), with k for cylindrical pipes taken from [69]. In this formula the heat transfer coefficients (α) are not used because it is just calculated from the outer wall surface to the inner wall surface. The outer wall surface temperature $T_{wa,m}$ is taken from EBSILON and changes at each iteration step.

$$T_{wi,m} = T_{wa,m} - \frac{Q \cdot eff}{\frac{2 \cdot \lambda_{a,w}}{D_a \cdot \ln\left(\frac{D_a}{D_i}\right)} \cdot r_f \cdot A} = 466.6 \text{ } ^\circ C \quad \text{Eq. 6-16}$$

The required temperature depending HTF properties and the Prandtl number on the inside wall of the receiver pipe were calculated, now by using the temperature $T_{wi,m}$ instead of $T_{a,f}$. The results are:

- Average dynamic viscosity at the wall $\eta_{a,f,w} = 1.409$ mPas (based on Eq. 6-5)
- Specific heat capacity at the wall $c_{p,w} = 1523$ J/kgK (based on Eq. 6-13)
- Thermal conductivity at the wall $\lambda_{t,w} = 0.532$ W/mK (based on Eq. 6-14)
- Prandtl number at the wall $Pr,w = 4.038$ (based on Eq. 6-15)

The next step is the calculation of the Nusselt number inside the pipe Nu,i . For turbulent pipe flows with $Re > 10^4$, Eq. 6-17 to Eq. 6-19 are valid according to [69]. The factor f_1 was not calculated (e.g. set to 1) since the flow is considered to be established when it reaches the receiver pipe inlet due to the piping located before the receiver pipe inlet. Factor f_2 was calculated. The Nusselt number shows the ratio between heat transfer due to convection and heat transfer due to conduction.

$$Nu,i = \frac{\left(\frac{\xi}{8}\right) \cdot Re \cdot Pr}{1 + 12.7 \cdot \left(\frac{\xi}{8}\right) \cdot \left(Pr^{\frac{2}{3}} - 1\right)} \cdot f_1 \cdot f_2 = 286.1 \quad \text{Eq. 6-17}$$

$$f_1 = 1 + \left(\frac{Di}{H}\right)^{\frac{2}{3}} \quad \text{Eq. 6-18}$$

{not calculated, but set to 1}

$$f_2 = \left(\frac{Pr}{Pr,w}\right)^{0.11} \quad \text{Eq. 6-19}$$

The convection coefficient on the inside of the pipe α_i can now be determined by Eq. 6-20. The combined heat transfer coefficient k from the outside wall of the pipe to the HTF is calculated in Eq. 6-21 [69]. Finally, the design wall temperature difference ΔT (DTWDES) is determined by Eq. 6-22.

$$\alpha_i = \frac{Nu \cdot \lambda_t}{Di} = 6526 \frac{W}{m^2 K} \quad \text{Eq. 6-20}$$

$$k = \left(\frac{Da}{2 \cdot \lambda_{a,w}} \cdot \ln \frac{Da}{Di} + \frac{Da}{Di \cdot \alpha_i}\right)^{-1} = 3502 \frac{W}{m^2 K} \quad \text{Eq. 6-21}$$

$$\Delta T = \frac{Q \cdot eff}{k \cdot A \cdot rf} = 48.9 K \quad \text{Eq. 6-22}$$

c) Determination of the Combined Convection Coefficient (Outside)

The investigation of natural heat transfer mechanisms at vertical cylinder receivers for solar tower power plants required the analysis of novel boundary conditions: [72]

- “Cylinder-walls” composed of 12-50mm tubes forming a cylinder of several meters diameter (surfaces macroscopically and microscopically rough)
- Size and operating temperature of the receiver were such that the Grashof numbers were 10 to 100 times larger than available in the literature ($Gr \approx 10^{14}$)
- Although data on forced or natural convection exists, no data is available for mixed forced and natural convection (when wind is superimposed on natural convection)

The following calculation will be done according to [72] because of the availability of a suitable calculation procedure for solar tower power plants, which includes its special peculiarities.

First, the average air temperature $T_{a,a}$ on the outside of the receiver must be determined, which is then used for the average air properties. For this purpose, the mean value of the outside receiver surface $T_{wa,m}$ and the mean ambient temperature $T_{a,m}$ is calculated by 255.8°C

For this temperature, the following air properties are calculated, which are all only valid for dry air. The average dynamic viscosity $\eta_{a,a}$ is determined in Eq. 6-23 according to [80]. The average density $\rho_{a,a}$ in Eq. 6-24 is calculated by using the equation for an ideal gas. The ambient pressure was set to $1.013 \cdot 10^5$ Pa and the gas constant is 287 J/kgK. By using these two values, the average kinematic viscosity of air $\nu_{a,a}$ can be determined (Eq. 6-25). Finally the average thermal conductivity $\lambda_{a,a}$ is calculated by Eq. 6-26 [80].

$$\eta_{a,a} = (1.723 + 0.0047 \cdot T_{a,a}) \cdot 10^{-2} = 0.0293 \text{ mPas} \quad \text{Eq. 6-23}$$

$$\rho_{a,a} = \frac{p}{R \cdot (T_{a,a} + 273.15)} = 0.6673 \text{ kg/m}^3 \quad \text{Eq. 6-24}$$

$$\nu_{a,a} = \frac{\eta_{a,a}}{\rho_{a,a}} = 4.384 \text{ m}^2/\text{s} \quad \text{Eq. 6-25}$$

$$\lambda_{a,a} = 0.02427 + 7.13 \cdot 10^{-5} \cdot T_{a,a} = 0.0425 \text{ W/mK} \quad \text{Eq. 6-26}$$

The following equations (Eq. 6-27 up to Eq. 6-34) are based on the calculation procedure in [72]. First, the outside Reynolds number Re_o (Eq. 6-27) for the whole receiver object is calculated. Using this Reynolds number, the Nusselt number $Nu_{f,o}$ (Eq. 6-28) for the forced convection outside can be calculated. This Nusselt number only depends on the Reynolds number, the Prandtl Number is included in the factors of the formula, because it is just valid for air. Finally, the outside forced convection coefficient $\alpha_{f,o}$ can be calculated (Eq. 6-29).

$$Re, o = \frac{\nu a, m \cdot Drec}{\nu a, a} = 1.296 \cdot 10^6 \quad \text{Eq. 6-27}$$

$$Nu, f, o = 0.00239 \cdot Re, o^{0.98} + 0.000945 \cdot Re, o^{0.89} = 2598.4 \quad \text{Eq. 6-28}$$

$$\alpha f, o = \frac{rf \cdot Nu, f, o \cdot \lambda a, a}{Drec} = 11.908 \frac{W}{m^2 K} \quad \text{Eq. 6-29}$$

To calculate the natural convection, the Grashof number must be calculated. The first step is a calculation of the volumetric thermal expansion coefficient β (Eq. 6-30), which is then used to calculate the Grashof number Gr (Eq. 6-31). The g in the formula is gravity with a value of 9.81 m/s². The Grashof number approximates the ratio of the buoyancy to the viscous force acting on the fluid. Now, the Nusselt number for the natural convection outside Nu, n, o can be calculated (Eq. 6-32). Again the Prandtl number is included in advance. Ultimately, the natural convection coefficient $\alpha n, o$ is calculated (Eq. 6-33).

$$\beta = \frac{1}{Ta, a} = 0.001891 \frac{1}{K} \quad \text{Eq. 6-30}$$

$$Gr = \frac{g \cdot \beta \cdot (Twa, m - Ta, m) \cdot H^3}{\nu a, a} = 7.33 \cdot 10^{13} \quad \text{Eq. 6-31}$$

$$Nu, n, o = 0.098 \cdot Gr^{0.333} \cdot \left(\frac{Ta, m}{Twa, m} \right)^{0.14} = 2925.4 \quad \text{Eq. 6-32}$$

$$\alpha n, o = \frac{rf \cdot Nu, n, o \cdot \lambda a, a}{H} = 7.450 \frac{W}{m^2 K} \quad \text{Eq. 6-33}$$

Now, the forced and natural convection coefficient can be combined to the outside combined convection coefficient αo (Eq. 6-34). This is the real value for the rough tube wall area. The predefined heliostat field data in EBSILON approximates the receiver as a smooth cylinder that area is lower by the factor $\pi/2$. To gain the same heat losses, the value αo must be multiplied with rf in order correct this issue, which leads to the corrected outside combined convection coefficient $\alpha o'$ (Eq. 6-35). This value is now equal to ALPHA in EBSILON.

$$\alpha o = (\alpha f, o^{3.2} + \alpha n, o^{3.2})^{\frac{1}{3.2}} = 12.681 \frac{W}{m^2 K} \quad \text{Eq. 6-34}$$

$$\alpha o' = \alpha o \cdot rf = 19.919 \frac{W}{m^2 K} \quad \text{Eq. 6-35}$$

Note: In order to validate this result, an attempt was made to calculate $\alpha o'$ with formulas taken from [69]. The natural convection was calculated for a vertical wall with Raleigh numbers of

10^{12} (the maximum allowed value in these formulas) and the forced convection was calculated for a cylinder, all with the same boundary values as above. The results of this calculation were of the same order of magnitude.

d) Part Load Investigation

In this section the difference between a receiver part load calculation solely by EBSILON and a part load calculation assisted by the Excel program is investigated. So, two sets of simulations were done for an earlier, but similar receiver design.

First, the receiver is designed in design mode in EBSILON by using the Excel program. Then, the load factor (essentially the DNI, which is linear connected to the receiver load) was reduced in off-design mode and several result values were taken out to draw graphs (* or blue curves in the following diagrams). In the off-design mode EBSILON handles the part load behavior of the receiver itself.

In the second attempt, the receiver design was kept the same, but this time the load factor was reduced in EBSILON design mode and for every load factor the receiver was recalculated by the Excel file. Again, graphs for several result values were drawn (** or red curves in the following diagrams).

Figure 6-3 shows the receiver pressure drop DP12 versus the load factor. The difference between these two graphs comes mainly from the consideration of the pipe friction number ξ by the Excel program. A lower load factor leads to lower pipe flow, lower pipe flow leads to a lower Reynolds number, lower Reynolds number leads to higher pipe friction number, and finally higher pipe friction number leads to higher pressure drops. If desired, this difference could be eliminated by setting a correction curve in the receiver component in EBSILON.

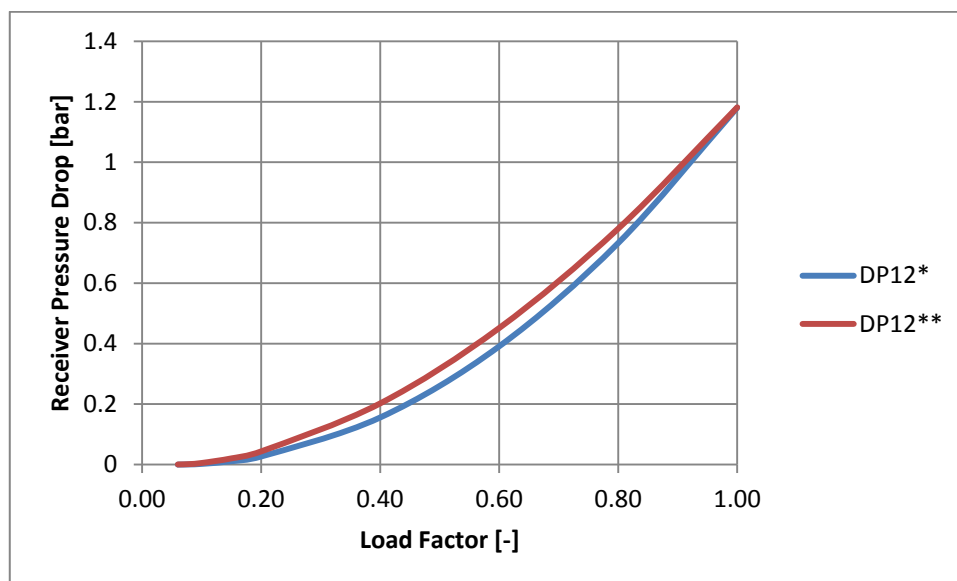


Figure 6-3: Receiver pressure drop versus the load factor

Figure 6-4 illustrates the mean receiver wall temperature RTREC versus the load factor. EBSILON models a receiver wall temperature dropping linearly with the load factor.

The bend at very low load factors in the Excel-controlled part load calculation relies on the change from turbulent to laminar flow that leads to a higher receiver wall temperature due to the lower cooling capability of laminar flows. The whole course of the Excel-controlled graph is also influenced by different formulas for the Nusselt number at laminar, turbulent, and intermediate flows.

The analytic calculation of the receiver wall temperature is a rough approximation of the reality on a solar tower power plant receiver. Therefore, the error between these two graphs (maximum around 10K) is acceptable at all.

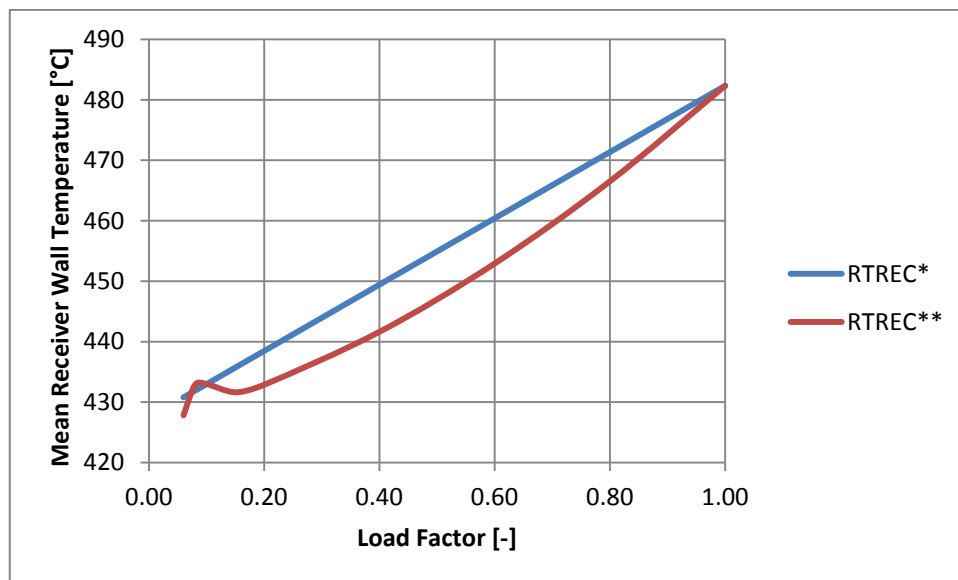


Figure 6-4: Mean receiver wall temperature versus load factor

For the Excel-controlled part load calculation, the combined convection coefficient ALPHA versus load factor (Figure 6-5) is inversely related to RTREC. This can be traced back to the fact that the air properties change with receiver temperature. For higher receiver temperatures, the surrounding air is warmer on average. Warmer air has higher viscosity, lower density and higher heat conductivity in summation, however, the effect of the higher viscosity and the lower density is stronger than the higher heat conductivity, which effectively lets ALPHA sink with rising temperature.

EBSILON keeps the value for ALPHA constant for any load factor, the maximum error from the analytic Excel solution is around 4.5% at the lowest load factor possible. This error can also be neglected and the variable ALPHA can be set as constant because the analytic solution here is also based on rough assumptions and the deviation from the constant value is quite low.

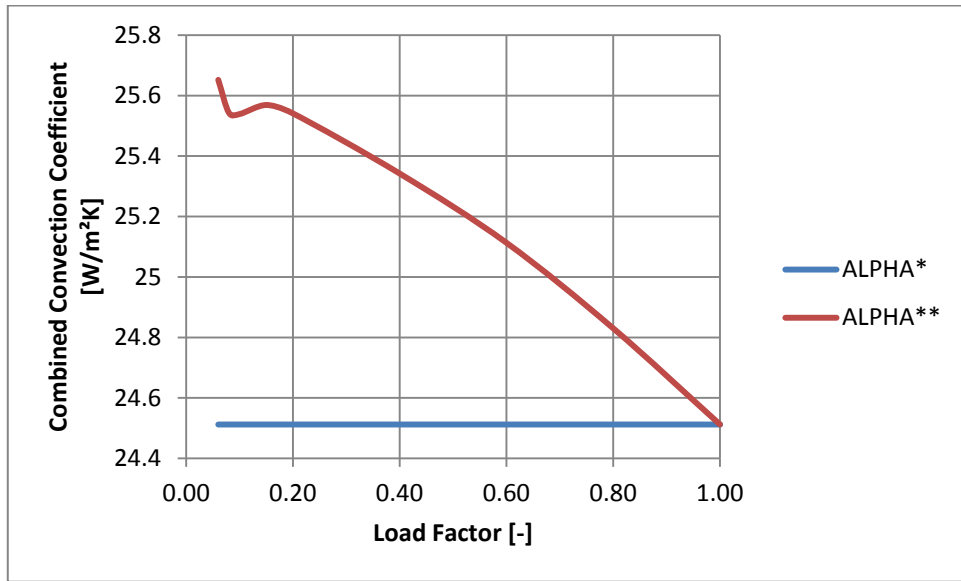


Figure 6-5: Combined convection coefficient versus load factor

Figure 6-13 shows the receiver efficiency versus the load factor. In this diagram it seems like there is no difference between these two graphs. The receiver efficiency drops dramatically for smaller load factors, especially for loads below 0.2.

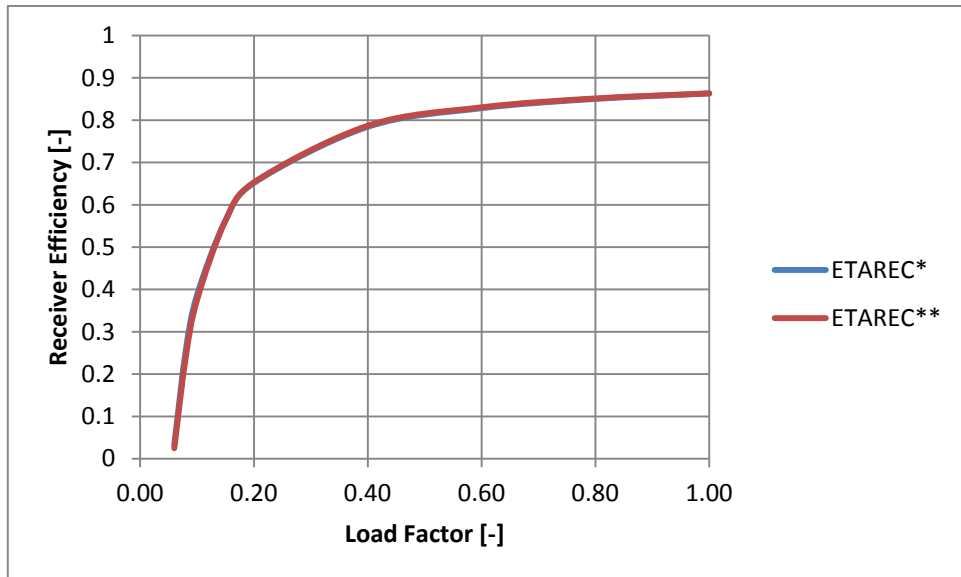


Figure 6-6: Receiver efficiency versus load factor

In Table 6-2 the difference between both graphs for every load factor is also shown. One can see that the deviation is the highest for load factors of around 0.1 and below with around 0.01.

This deviation is also tolerable and most likely evoked by the change from turbulent to laminar flow.

Table 6-2: Receiver efficiency versus load factor

Load Factor	ETAREC*	ETAREC**	ETAREC Difference
1.00	0.8633	0.8633	0.0000
0.80	0.8503	0.8514	-0.0011
0.60	0.8284	0.8304	-0.0020
0.40	0.7844	0.7869	-0.0025
0.20	0.6519	0.6531	-0.0012
0.15	0.5635	0.5626	0.0009
0.10	0.3867	0.375	0.0117
0.08	0.254	0.2379	0.0161
0.06	0.0329	0.0247	0.0082

In conclusion it should be said, that it is not overall necessary to include a detailed analytic simulation to simulate part load, but it is necessary to gain relatively realistic values in design mode. Yet, this analytic calculation could be integrated into EBSILON in order to simulate the forced convection in more detail for any hourly averaged wind speed instead of the annual average wind speed.

6.2.2 Storage Design

In the storage design calculation, preferably realistic values for QLOSSR (temperature specific heat loss), LEVMIN (minimum level of the tank), LEVMAX (maximum level of the tank) and LEVACT (actual level of the tank) for the hot tank and the cold tank have to be determined. In contrast to the receiver calculation, this is a once-through calculation without iterations. After this calculation, for the hot tank LEVACT = LEVMIN and for the cold tank LEVACT = LEVMAX. Table 6-1 shows the translation from EBSILON variables into Excel variables for the storage design.

Table 6-3: EBSILON variables translated into Excel variables

EBSILON Variables	Excel variables
Solar_tower.RTAMB	T,amb
Hot_tank.TNEW	T,hot
Cold_tank.TNEW	T,cold
..._tank.LEVMIN	m,min
..._tank.LEVMAX	m,max
Hot_tank.QLOSSR	Q,loss,ts,h
Cold_tank.QLOSSR	Q,loss,ts,h

Values read out from EBSILON are the ambient temperature RTAMB, the nominal temperature of the hot tank and the cold tank, TNEW. Figure 6-7 shows a part of the storage design sheet in Excel, which is also included in Appendix {4}.

	A	B	C	D	E	F	G
1	Molten salt (KNO3/NaNO3) storage tank design and detailed analytic solution for QLOSSR, LEVMIN, LEVMAX, LEVACT						
2	Please ensure to switch to decimal points in Excel options to avoid errors concerning the export of the QLOSSR value						
3	For Hot_tank: LEVACT = LEVMIN For Cold_tank: LEVACT = LEVMAX						
4							
5	value read out from EBSILON						
6	editable value						
7	calculated value						
8	calculated value written into EBSILON						
9							
10	<i>Description</i>	<i>Variable</i>	<i>Ebsilon variable</i>	<i>Value</i>	<i>Unit</i>	<i>Formula \ Comment</i>	
11	Ambient temperature (HTF)	T,amb	Solar_tower.RTAMB	45	°C		
12	Hot tank nominal temperature (HTF)	T,hot	Hot_tank.TNEW	565	°C		
13	Cold tank nominal temperature (HTF)	T,cold	Cold_tank.TNEW	290	°C		
14	Total energy capacity	Q,tot		1,354	MWh _{th}		
15	Area specific heat loss	kΔT,hot		75	W/m ²	outside and inside α neglect	
16	Area specific heat loss	kΔT,cold		200	W/m ²	outside and inside α neglect	
17	Free board (Ullage gas)	H,f		1.30	m	Should be around 1,3m accor	
18	Heel level (HTF)	H,min		1.00	m	Should be around 1m accordi	
19	Pump barrel length	H,p		14.00	m	Should be ≤ 14m according to	
20	Usable height	H,u		11.70	m	H,u = H,p - H,f - H,min	
21	Storage height (inside)	H		14.00	m	H = H,p	
22	Average temperature (HTF)	T,m		427.5	°C	T,m = (T,hot+T,cold)/2	
23	Average specific heat capacity (HTF)	cp,m		1517	J/kgK	f(T,m) from SQM solar salt br	
24	Usable capacity	m,u		11,688	t	m,u = (Q,tot*1000000*3600)/(i	
25	Minimum level	m,min	..._tank.LEVMIN	999.0	t	m,min = m,u * (m,u / H,u) * t	
26	Maximum level	m,max	..._tank.LEVMAX	12686.9	t	m,max = m,u + m,min	
27	Hot tank Density (HTF)	ph,f		1730.7	kg/m ³	f(T,hot) from SQM solar salt t	

Figure 6-7: Screenshot of a part of the storage design sheet in Excel

First, the required total energy capacity Q_{tot} must be determined, which is 1354 MWh_{th} for this power plant (see chapter 6.3.2).

Then, the area specific heat loss for the cold tank ($k\Delta T_{cold}$) is determined with 200 W/m² and the area specific heat loss for the hot tank ($k\Delta T_{hot}$) is determined with 75 W/m². These two values were found out by time series analysis, in which a temperature loss rate for the empty hot tank of 5.5°C/day and for the full cold tank of 2°C/day was reached. This is according to a storage design guideline by [86]. Outside α and inside α are neglected, because they are high compared to k.

Also according to [86], a freeboard height for ullage gas (H,f) of 1.3m, a tank heel level of 1m (H,min) and pump barrel length (H,p) of 14m is defined. The storage height on the inside (H) is equal to H,f with 14m. The usable height H,u is the difference between HTF maximum level and minimum level and is calculated by Eq. 6-36.

$$H,u = H,p - H,f - H,min = 11.7m \quad \text{Eq. 6-36}$$

The average temperature of the HTF in the storage T,m is determined by Eq. 6-37. For this average HTF temperature the average specific heat capacity cp,m is calculated by Eq. 6-38 [63].

$$T,m = \frac{T,hot + T,cold}{2} = 427.5^{\circ}C \quad \text{Eq. 6-37}$$

$$cp,m = 1443 + 0.172 \cdot T,m = 1517 \frac{J}{kg K} \quad \text{Eq. 6-38}$$

The useable capacity m,u in tons is then derived by Eq. 6-39. Based on this mass, the mass in the tank at its minimum level m,min (Eq. 6-40) and the mass at its maximum level m,max (Eq. 6-41) can be calculated.

$$m,u = \frac{Q,tot \cdot 10^6 \cdot 3600}{cp,m \cdot 10^3 \cdot (T,hot - T,cold)} = 11\,688\,t \quad \text{Eq. 6-39}$$

$$m,min = m,u \cdot \frac{H,min}{H,u} = 999.0\,t \quad \text{Eq. 6-40}$$

$$m,max = m,u + m,min = 12\,686.9\,t \quad \text{Eq. 6-41}$$

Now, the heat losses should be calculated. To calculate the surface of the storage tank, first the HTF density for the hot tank $\rho h,f$ must be calculated because the hot molten salt needs the most space per kg or ton (Eq. 6-42) [63]. The maximum needed volume V,max is then calculated in Eq. 6-43.

$$\rho h,f = 2090 - 0.636 \cdot T,hot = 1730.7\,kg/m^3 \quad \text{Eq. 6-42}$$

$$V,max = \frac{m,max}{\frac{\rho h,f}{10^3}} \cdot \left(1 + \frac{H,f}{H,u + H,min}\right) = 8081.1\,m^3 \quad \text{Eq. 6-43}$$

The storage diameter D can be calculated for a given V,max and H with Eq. 6-44. With this diameter, the total inner storage surface (cylinder surface) A can be calculated with Eq. 6-45.

$$D = \sqrt{\frac{4 \cdot V,max}{\pi \cdot H}} = 27.11\,m \quad \text{Eq. 6-44}$$

$$A = 2 \cdot \frac{D^2 \cdot \pi}{4} + D \cdot \pi \cdot H = 2346.8\,m^2 \quad \text{Eq. 6-45}$$

For information purposes or for designing the insulation, the k-value is also calculated for the hot tank insulation k, req, h and for the cold tank insulation k, req, c (Eq. 6-46 and Eq. 6-47).

$$k, req, h = \frac{k\Delta T, hot}{T, hot - T, amb} = 0.144 \frac{W}{m^2 K} \quad \text{Eq. 6-46}$$

$$k, req, c = \frac{k\Delta T, cold}{T, cold - T, amb} = 0.816 \frac{W}{m^2 K} \quad \text{Eq. 6-47}$$

Next, the heat loss for the hot tank $Q, loss, h$ (Eq. 6-48) and for the cold tank $Q, loss, c$ (Eq. 6-49) can be calculated and finally, the temperature specific heat losses for the hot tank $Q, loss, ts, h$ (Eq. 6-50) and for the cold tank $Q, loss, ts, c$ (Eq. 6-51) are determined.

$$Q, loss, h = k\Delta T, hot \cdot A \cdot 10^{-3} = 176 \text{ kW} \quad \text{Eq. 6-48}$$

$$Q, loss, c = k\Delta T, cold \cdot A \cdot 10^{-3} = 469.4 \text{ kW} \quad \text{Eq. 6-49}$$

$$Q, loss, ts, h = \frac{Q, loss, h}{T, hot - T, amb} = 0.3385 \frac{\text{kW}}{K} \quad \text{Eq. 6-50}$$

$$Q, loss, ts, c = \frac{Q, loss, c}{T, cold - T, amb} = 1.9157 \frac{\text{kW}}{K} \quad \text{Eq. 6-51}$$

6.3 Time Series Analysis

The components of EBSILON Professional are based on physical equations that are only valid in the steady state. Non-steady-state calculations are not possible as a rule. For processes taking place on a time scale for which dynamic effects can be neglected (“quasi-steady states”), such processes can well be covered by a series of EBSILON Professional calculations. This is particularly of interest when the purpose is to evaluate the behavior of plants over a certain period of time, like over one day or over one year. This kind of evaluation is supported by the module “Time-series calculation”, which is connected to the “Sun” component in the model. [16]

The changing conditions like day, time, DNI, ambient temperature and wind speed are written into the “Sun” component and a simulation is started for each time step. The “Sun” component also calculates the position of the sun on the sky. Components like the “Heliostat field”, the “Solar tower receiver” and others depend on data given by the sun in order to calculate their result values. Also, the storage collaborates with the “Time-series calculation” module in order to compute tank levels and tank temperatures at every time step. In Table 6-4, a time-series simulation is illustrated.

Table 6-4: Overview of a time series simulation table in EBSILON Professional

Time-Series-Calculation										
TimeSeries Calculate View Edit Extras										
1354MWh_t_38MWB_final_design [13] >										
Break Recalc time <input checked="" type="checkbox"/> auto-scroll Profile Copy_of_TimeSeries_master_D										
	A	B	C	D	E	F	G	H	I	J
1			DNI (W/m ²)	Temp. (°C)	Wind (m/s)	Hot tank level ...	Hot tank (°C)	Cold tank (°C)	Load (kg/s)	Unload (kg/s)
2	Date / Time	auto...	spec	spec	spec	result	result	result	result	result
3			Sun.DNI	Sun.TAMB	Sun.VWIND	(Hot_tank.LEV...	Hot_tank.TSTO	Cold_tank.TSTO	Hot_tank.MLD	Hot_tank.MU...
4										
5										
6	2005-01-01 03:00:00		0	17.6	2.0	0	565	290	0	0
7	2005-01-01 04:00:00		0	17.4	1.3	0	564.568	289.9	0	0
8	2005-01-01 05:00:00		0	17.2	1.6	0	564.136	289.8	0	0
9	2005-01-01 06:00:00		0	17.8	2.0	0	563.704	289.7	0	0
10	2005-01-01 07:00:00		218	19.8	1.3	0	563.273	289.601	0	0
11	2005-01-01 08:00:00		336	21.8	1.6	0	562.844	289.502	134.405	0
12	2005-01-01 09:00:00		446	23.9	1.3	0.0413982	563.203	289.402	302.874	0
13	2005-01-01 10:00:00		352	25.4	2.1	0.134687	563.755	289.296	258.38	253.442
14	2005-01-01 11:00:00		492	26.7	2.0	0.136208	563.967	289.162	401.077	209.467
15	2005-01-01 12:00:00		686	27.9	4.6	0.195225	564.225	289.014	588.84	208.834
16	2005-01-01 13:00:00		541	28.3	4.4	0.312271	564.442	288.852	452.689	208.563
17	2005-01-01 14:00:00		672	28.2	4.6	0.387465	564.512	288.679	566.206	208.523
18	2005-01-01 15:00:00		357	27.3	5.3	0.497635	564.581	288.498	261.529	208.77
19	2005-01-01 16:00:00		0	25.9	5.9	0.513885	564.573	288.32	0	209.317
20	2005-01-01 17:00:00		0	25.9	5.9	0.449413	564.509	288.179	0	209.387
21	2005-01-01 18:00:00		0	25.1	5.3	0.38492	564.437	288.066	0	209.79
22	2005-01-01 19:00:00		0	24.3	6.9	0.320302	564.354	287.979	0	210.208
23	2005-01-01 20:00:00		0	23.5	5.3	0.255556	564.256	287.913	0	210.609
24	2005-01-01 21:00:00		0	22.7	5.3	0.190686	564.138	287.862	0	211.023
25	2005-01-01 22:00:00		0	21.9	4.0	0.125688	563.988	287.824	0	211.443
26	2005-01-01 23:00:00		0	21.1	3.4	0.0605617	563.783	287.795	0	211.858
27	2005-01-02 00:00:00		0	20.3	2.9	6.06603e-009	563.489	287.777	0	0
28	2005-01-02 01:00:00		0	19.5	1.7	6.06603e-009	563.06	287.679	0	0
29	2005-01-02 02:00:00		0	18.7	1.3	6.06603e-009	562.631	287.58	0	0
30	2005-01-02 03:00:00		0	17.9	1.2	6.06603e-009	562.202	287.482	0	0

Starting on the left side, the first column shows the date and the time, the time step between every calculation is one hour. The second column is reserved for markings of automatically generated time steps. These steps are generated when storage got empty or full at a certain time in between the regular time steps and is marked with an “x”. It is possible to delete these additional time steps automatically after the simulation in order to have e.g. exactly 8760 rows for every year.

In the next three columns (C, D, E) the ambient conditions DNI, ambient temperature, and wind speed are given as an input data. These values are taken from weather data calculated for Al Mirfa in the United Arab Emirates by the database METEONORM 6.1.0.20, kindly provided by Zuniga F. [88].

In the next three columns (F, G, H) the hot tank level ratio is given as well as the temperatures of the molten salt in the hot tank and in the cold tank. In the columns I and J the load and the unload rate of the hot tank is shown. In further columns (not illustrated here) the current net electric power of the whole power plant, the cumulated plant output in MWh, the three efficiency factors (gross, net, total) as well as the gas consumption of the tank heaters are indicated.

6.3.1 Theoretic Considerations for Storage and Turbine Size Optimization

Designing a solar thermal power plant, the logical first step would be the determination of the nominal generator output in MW. Often, this is one of the important criteria in order to gain a certain feed-in tariff or public subsidies. After that, the capacity factor and the solar multiple are chosen. The dimensionless capacity factor (CF) expresses, based on the nominal yearly output W_a in MWh, the part of the year in which the generator is running at its nominal output P_{out} in MW (Eq. 6-52) [72].

$$CF = \frac{W_a}{P_{out} \cdot 8760} \quad \text{Eq. 6-52}$$

The solar multiple (SM) is the relation between the thermal output power of the receiver P_{Re} at a certain design day (normally noon of June 21st) of the year and the nominal thermal input power of the steam cycle P_{Cy} (Eq. 6-53) [72].

$$SM = \frac{P_{Re}}{P_{Cy}} \quad \text{Eq. 6-53}$$

These numbers depend on economic considerations and must be refined by detailed time-series analysis. Before this is done, some more theoretic background is given. Figure 6-8 shows the ideal operating sequence of a solar plant with storage on a cloudless day, assuming negligible time delays between input and output. Between sunrise at t_1 and the receiver startup t_2 , incoming radiation is too low for an operation of the receiver. During τ_R , receiver thermal output is still insufficient to run the energy conversion cycle at its minimum rating (although this output could be stored as well). During τ_C , receiver output exceeds the required nominal input power for the energy conversion cycle and surplus energy E_c charges the storage system with a charging utilization factor γ_C . During τ_D , the energy difference required to keep the energy conversion cycle running at rated power is retrieved from storage with a discharge utilization factor γ_d . From sunset at t_5 through τ_D , the process runs at its rated power from storage only. Thus, with storage, only the receiver needs to be designed for peak load P_{Re} . Since charge and discharge utilization factors are <1 due to storage and heat exchanger losses, less energy is transferred to the energy conversion cycle via the storage system than when transferred from the receiver directly. [72]

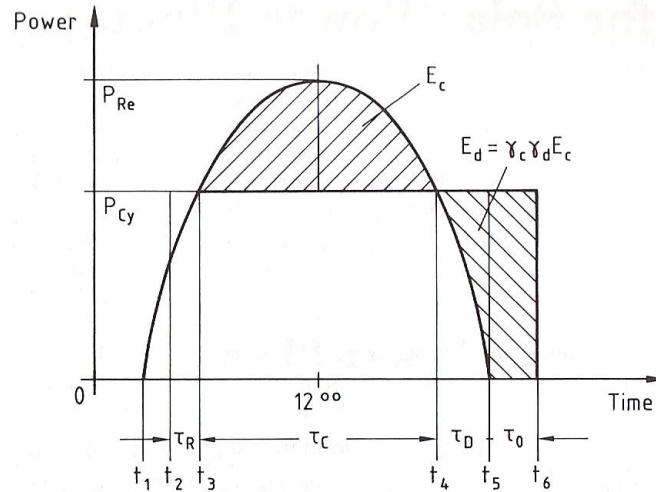


Figure 6-8: Qualitative daily operating sequence of a thermal solar power plant with storage [72]

If δ_{St} is the fraction of annual absorbed receiver energy sent to storage, and γ_c / γ_d the average annual charge / discharge utilization factor, the annual plant system efficiency is reduced by the annual storage loss factor γ_{St} . This relationship is shown in Eq. 6-54 [72].

The factor δ_{St} represents also the fraction of heat transfer fluid that is not directly used for steam generation but buffered in storage. The factors γ_c / γ_d can be interpreted as charging / discharging efficiencies, comparable with an electric accumulator. The reduced plant efficiency aroused by the storage is then shown by the factor γ_{St} .

$$\gamma_{St} = 1 - \delta_{St} \cdot (1 - \gamma_c \cdot \gamma_d) \quad \text{Eq. 6-54}$$

If 50% of the receiver output was charged into a storage system with a 90% annual charge/discharge utilization factor, then thermal plant output would be reduced to 95%. To compensate for this loss, the leveling effect of storage on cycle operation should improve annual cycle efficiency by 5%. The use of storage is attractive if increased revenues can pay for the additional storage costs, e. g. when the production is shifted from low- to high-tariff periods. Figure 6-9 shows achievable rated power operating hours on a cloudless December 21st and June 21st for SM ranging from 1.0 to 2.8 in Almería, Spain. While a SM of 2.8 is sufficient for fully day operation in summer, only 12 hours are possible in winter. A minimum of SM of 5 would be required to achieve 24-hour-operation in winter. [72]

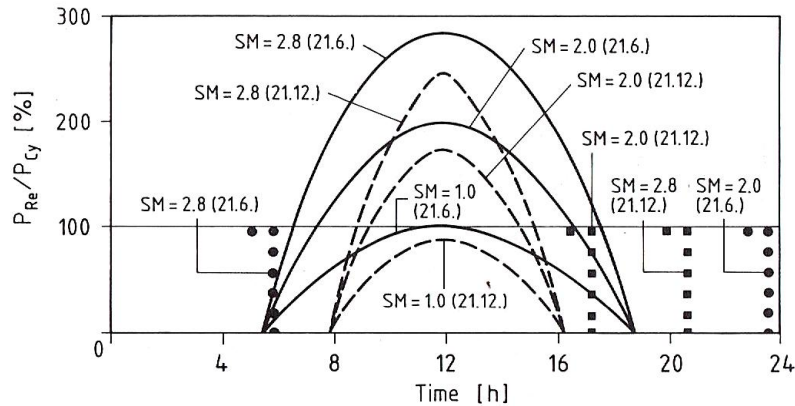


Figure 6-9: Achievable operating hours for different solar multiples in summer and winter [72]

EBSILON Professional is not able to design solar fields. Instead of this, values of heliostat fields designed by other programs can be stored in a data exchange file and be read by EBSILON Professional. In EBSILON Professional 10, four predefined heliostat fields are available, calculated with the program HFLCAL [57] by DLR. Due to the non-availability of a license for a heliostat field design software, one of the predefined heliostat fields is used. Therefore, in the case of this thesis, another design philosophy has to be chosen: the optimization of the turbine-storage combination for a given heliostat field. For the regular design philosophy without using a predefined heliostat field, the reader should refer to a very detailed sizing procedure from Zavoico (2001) [86].

A heliostat field with a 400-MW-design receiver output power was chosen at geographic latitude of 25° north. The Gemasolar power plant near Sevilla, Spain is currently the only 24-hour-operation capable power plant available to gain data from. The initial design of the solar tower power plant created in EBSILON Professional was based on data from Gemasolar, which was scaled up. Gemasolar uses a nominal 120-MW-receiver output power and a 19.9-MW-turbine [9]. The chosen 400-MW-receiver is under the suggested Al Mirfa conditions implemented in EBSILON Professional at about 323 MW output power. Most of this reduction is caused by atmospheric attenuation. This output is still higher than the one from the Gemasolar receiver by a factor of 2.7. The turbine could be scaled up to 54 MW to keep the relation but it was set to 50 MW as a first step, keeping in mind the lower average DNI in the United Arab Emirates compared to Spain. This would lead to a smaller turbine anyway.

Another difference to the commercially operated Gemasolar power plant is its capability to integrate future weather data into its operation in a way to optimize its profitability. This circumstance could not be integrated into the current model. For example, the turbine is often operated at a defined part load power output rating when the tank was not completely filled the day before in order to avoid emptying the tank before the tank is filled by the receiver again (see Figure 6-10). At the beginning the gross power is at around 4 MW and then it is reduced to about 3 MW. The stored energy is slowly decreasing until the solar field power is high enough to fill the storage again. During the time of a high power solar field, the gross power is raised to around 18 MW, after that again the gross power is reduced. This time to roughly 13 MW, for this

value also a steeper decrease of the stored energy can be seen. The different chosen gross power outputs reflect different boundary conditions. For example, the day before could have had a lower average DNI level leading to an only partly filled storage, therefore the gross power was reduced to 4MW during the night. The current day seems to allow operating the turbine with 13 MW during the following night. In addition, the gross power could be raised for times with high electricity demand and be decreased after that in order to avoid the storage becoming empty.

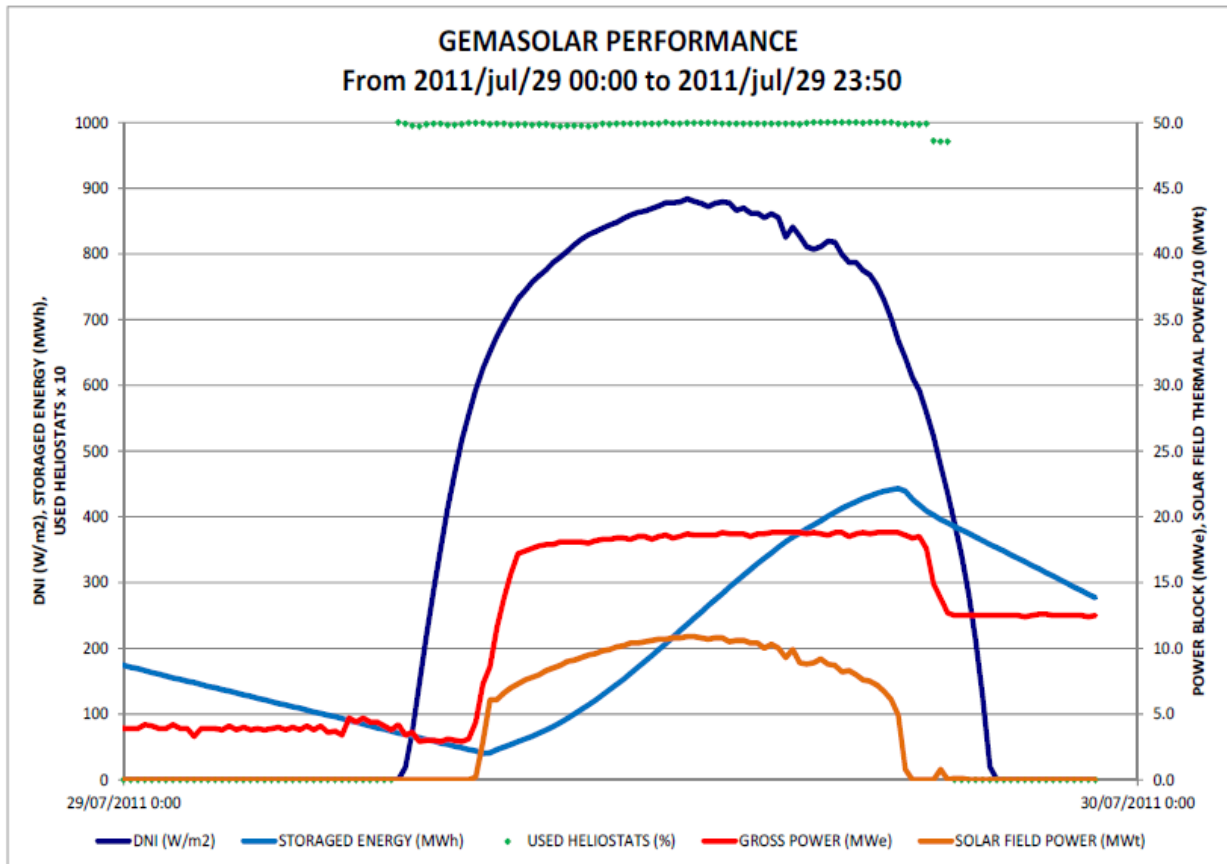


Figure 6-10: Gemasolar power plant performance on 29th July 2011 [22]

Also, part load mode is activated due to bad weather conditions or cloudy days (see Figure 6-11). For an optimal operation, data from a weather forecast is used by a plant model in order to find out the best operation strategy. One can see that this data fits quite well to the operation then realized in reality. Because of very good weather conditions at the day before, a gross power of 19.9 MW can be maintained for almost the whole day. In noon and afternoon, the weather conditions get bad and the solar field power starts to fluctuate. Once the solar field power is even at zero; here the gross power is also throttled in order not to reduce the hot tank level too fast. After this day with fluctuating tank levels, the remaining stored energy is comparatively low, therefore the gross power must be reduced to around 12 MW.

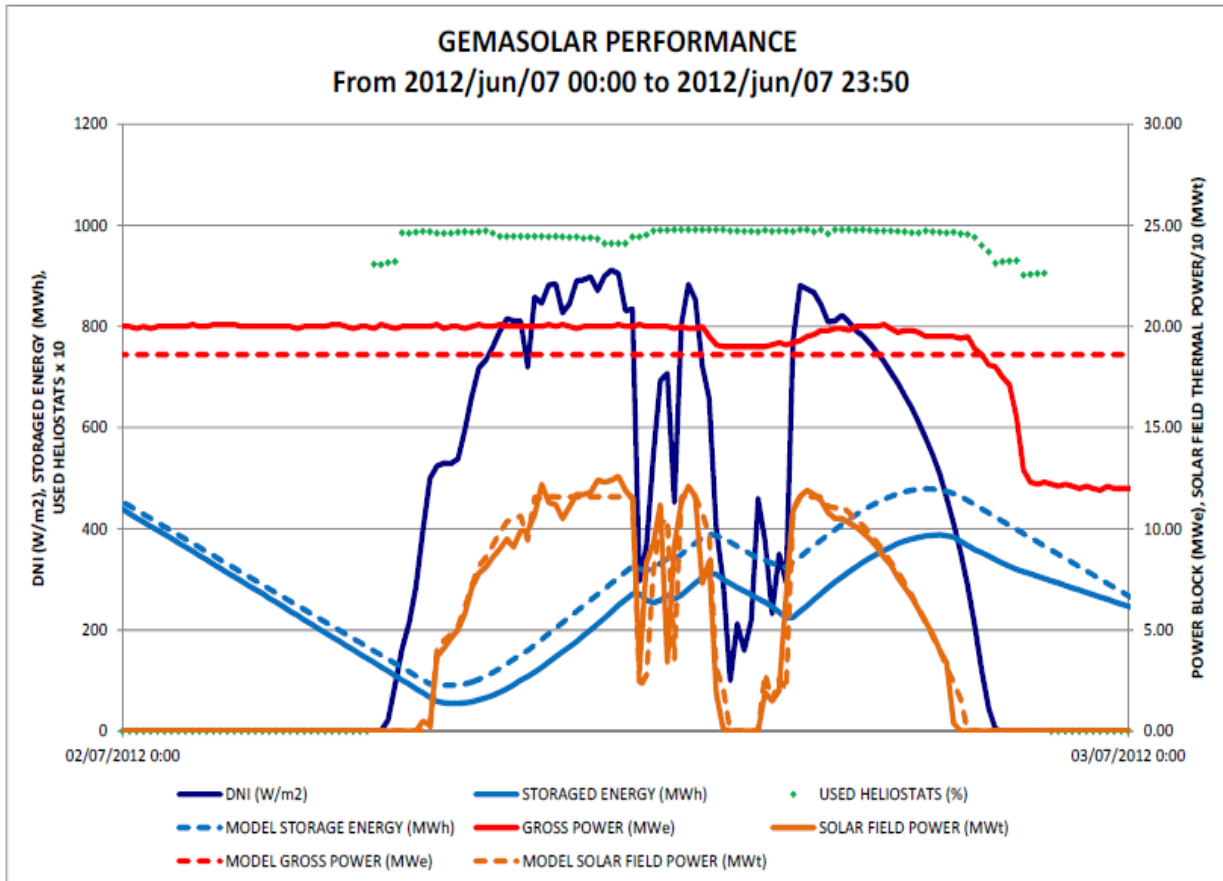


Figure 6-11: Gemasolar power plant performance on 7th June 2011 [22]

The storage of Gemasolar is capable of running the turbine for 15 hours at full load. A storage hour is defined as the storage capacity necessary to run a process connected to it at rated output power P_{out} for one hour [72]. This means that Gemasolar is capable to feed 298.5 MWh into the Grid only powered by its initially full 15-h-storage. With an assumed efficiency of 0.45, the storage of Gemasolar should provide around 663 MWh_{th} of capacity. When scaling this up by the factor of 2.7, this leads to 1800 MWh_{th} when rounded up. In total, everything leads to a roughly 2.7-times up-sized Gemasolar power plant.

6.3.2 Storage and Turbine Size Optimization

As mentioned before, due to the different weather conditions, it is supposed that the turbine will be over-dimensioned for the location at Al Mirfa. To analyze this fact, seven time-series simulations were executed, keeping all parameters the same (including the storage with 1800 MWh_{th}) but changing the turbine/generator size from 50 MW down to 20 MW in 5 MW steps (see Figure 6-12).

6 Thermodynamic simulation

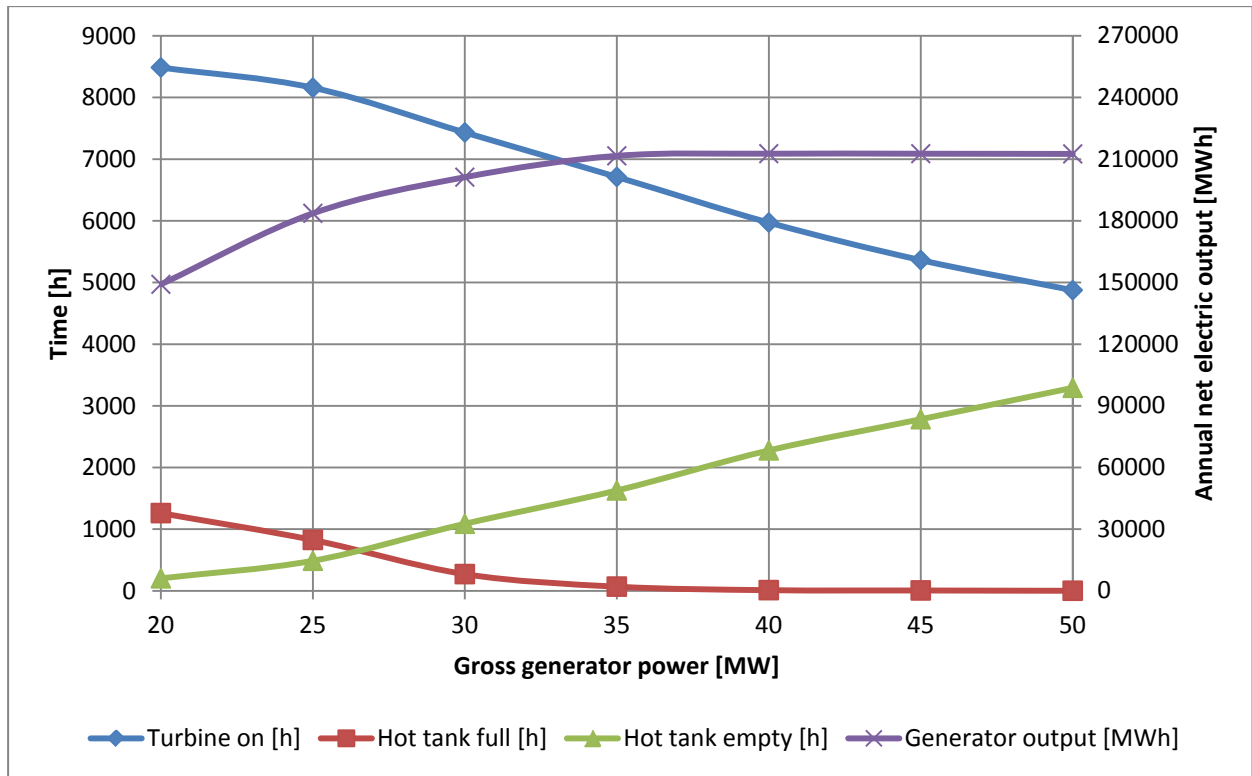


Figure 6-12: Time-series simulation of different turbine sizes with constant 1800MWh storage
(ca.15h for 50MW)

In this diagram, one can see that lower generator power leads to a higher runtime of the turbine, which is positive because of fewer losses due to more seldom startup and shut-down procedures and a higher utilization level of the turbine. But also the number of hours when the hot storage tank is full increases. This happens especially on days of high average DNI on which heliostats must be defocused in order to reduce the receiver HTF output, which avoids an overflowing of the hot tank. Defocusing of heliostats obviously leads to harvest losses, which in the end results in lower annual net electric outputs. The number of hours in which the hot tank is empty is not that important as the number of hours in which it is full, but for the sake of completeness, this value is also plotted.

Considering this diagram, an optimum would be between 35 MW and 40 MW. The data from Figure 6-12, is shown again in Table 6-5 with some additional information.

Table 6-5: Time-series simulation of different turbine sizes with constant 1800MWh storage
(ca.15h for 50MW)

Power [MW]	Turbine on [h]	Hot tank full [h]	Hot tank empty [h]	Generator output [MWh]	Capacity factor [-]	Solar multiple [-]	Storage hours [h]
20	8486	1260	202	149,095	0.851	6.82	37.9
25	8159	825	487	183,618	0.838	5.45	30.3
30	7433	271	1087	201,218	0.766	4.54	25.3
35	6712	68	1627	211,607	0.690	3.90	21.7
40	5972	11	2277	212,646	0.607	3.41	18.9
45	5363	6	2783	212,635	0.539	3.03	16.8
50	4875	1	3292	212,540	0.485	2.73	15.2

In this table, one can see that the generator output falls rapidly for gross generator power below 35 MW. Above, the generator output slightly increases up to 40 MW and then slightly falls again, which is the result of a higher number of switch-on/shut-off procedures and standby hours that cause losses.

The storage hours increase with smaller turbine sizes due to the constant storage capacity of 1800 MWh_{th}. If the storage was very large and the turbine small enough, an 8760-hour per year operation is feasible. This is reached when the hot tank is empty exactly once a year. For such an operation, a very good tank insulation would be necessary to keep the losses low, otherwise a lot of the energy transferred into the storage would be lost when taken out again several weeks or months later.

Nevertheless, storage capacity is expensive. At least at the moment it does not seem to be economic to store energy for a very long time. Also avoiding storage is not an option since the low capacity factor means a low usage of the equipment. The tradeoff to be made here for an optimum storage size is a comparison at given turbine power: Higher income due to more feed-in Euro compared to higher storage depreciation of one year in Euro. Out of a lack of economic data, it is again decided to lean on the Gemasolar design. It includes a 15-h-storage capacity.

Gemasolar has an official annual output of 110 000 MWh per year [9], which results in a capacity factor of 0.631, which is expected to be between 35 MW and 40 MW in our model case. The solar multiple for Gemasolar will be around 2.7 (assumed steam cycle efficiency 0.45), which would be above 50 MW. This was expected since it had been calculated before to have a 54 MW turbine for directly scaling up Gemasolar. As mentioned before, a simple scaling up is not possible due to different weather conditions. So, the solar multiple of Gemasolar does not help because this value just represents a design case for Spanish conditions. The capacity factor of Gemasolar is useful, though, because it represents an economic turbine size when the number of storage hours is given. In the following year cycles, a turbine size should be determined for which capacity factor is near 0.631 with a storage size of 15 h (see Table 6-6).

Table 6-6: Time-series simulation of different turbine sizes with constant 15h storage

Power [MW]	Turbine on [h]	Hot tank full [h]	Hot tank empty [h]	Generator output [MWh]	Capacity factor [-]	Solar multiple [-]	Storage hours [h]
40	5943	59	2271	211,138	0.603	3.41	15.0
37.5	6271	134	1973	208,757	0.635	3.64	15.0
38	6214	112	2036	209,580	0.630	3.59	15.0
38	6169	109	2043	208,453	0.626	3.59	15.0

In comparison to Table 6-6, the capacity factor is now reduced from 0.607 to 0.603 due to the storage reduction from 18.9 hours to 15 hours. This value is still too low; therefore, the generator power was reduced to 37.5 MW, which led to a higher capacity factor of 0.635. Because this value was too high now, the generator power was changed to 38 MW. After this iterative process, the capacity factor was now quite near to the Gemasolar value with 0.630. This configuration was added by assumed values for transient losses, which led in the end to a

capacity factor of 0.626. The 38-MW-turbine in combination with a 15-hour-storage (1354 MWh_{th}) was now fixed in this configuration as the design for the Al Mirfa base load solar tower power plant. The different duration curves of the tank levels are shown for these final simulations in Figure 6-13.

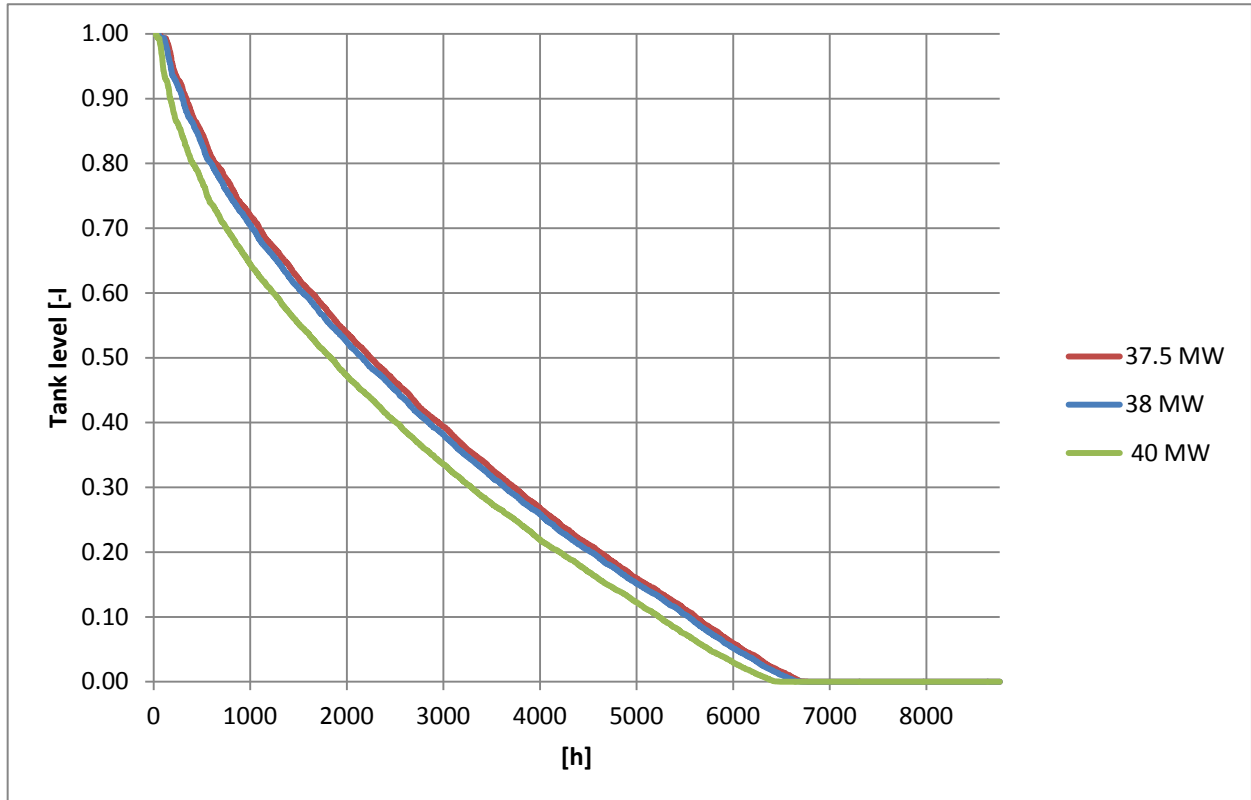


Figure 6-13: Duration curves of the tank level for different turbine sizes, each with 15h storage

The 40-MW-turbine has the lowest average tank level as well as the lowest number of full hot tank hours per year according to Table 6-6. When the turbine size is reduced, the average tank level and the number of full tank hours per year increase. One can also see that the hours of empty cold tanks are reduced. The slope of the duration curve at the higher tank levels is higher than the slope at the lower tank levels, which means that higher tank levels do not occur that often as lower tank levels.

In Figure 6-13, the variation of the turbine power with constant storage hours in order to find the optimum turbine size was illustrated. In order to show what happens if an oversized storage is reduced, time-series simulations were done for a 40-MW-plant with varying storage hours. The results are shown in Table 6-7 and Figure 6-14. The numbers of hours with an empty hot tank slightly decrease, while the number of full hot tank hours increase overproportionally. The operating hours of the turbine, the annually generator output and the capacity factor also decrease. An interesting fact in Figure 6-14 is that the slope of the 18.9-h-curve is very steep at high tank levels, which means that these peak loads for the storage are reached quite seldom. This suggests an overdimensioning of the tank and also explains why the number of full hot tank hours increases overproportional as said before. Shortening the storage means a “shaving”

of this peak, which has a fine tip and downwards an overproportionally increasing wide base at lower tank levels.

Table 6-7: Time-series simulations of constant turbine size (40 MW) with varying storage sizes

Power [MW]	Turbine on [h]	Hot tank full [h]	Hot tank empty [h]	Generator output [MWh]	Capacity factor [-]	Solar multiple [-]	Storage hours [h]
40	5943	59	2271	211,138	0.603	3.41	15.0
40	5966	20	2274	212,414	0.606	3.41	17.1
40	5972	11	2277	212,646	0.607	3.41	18.9

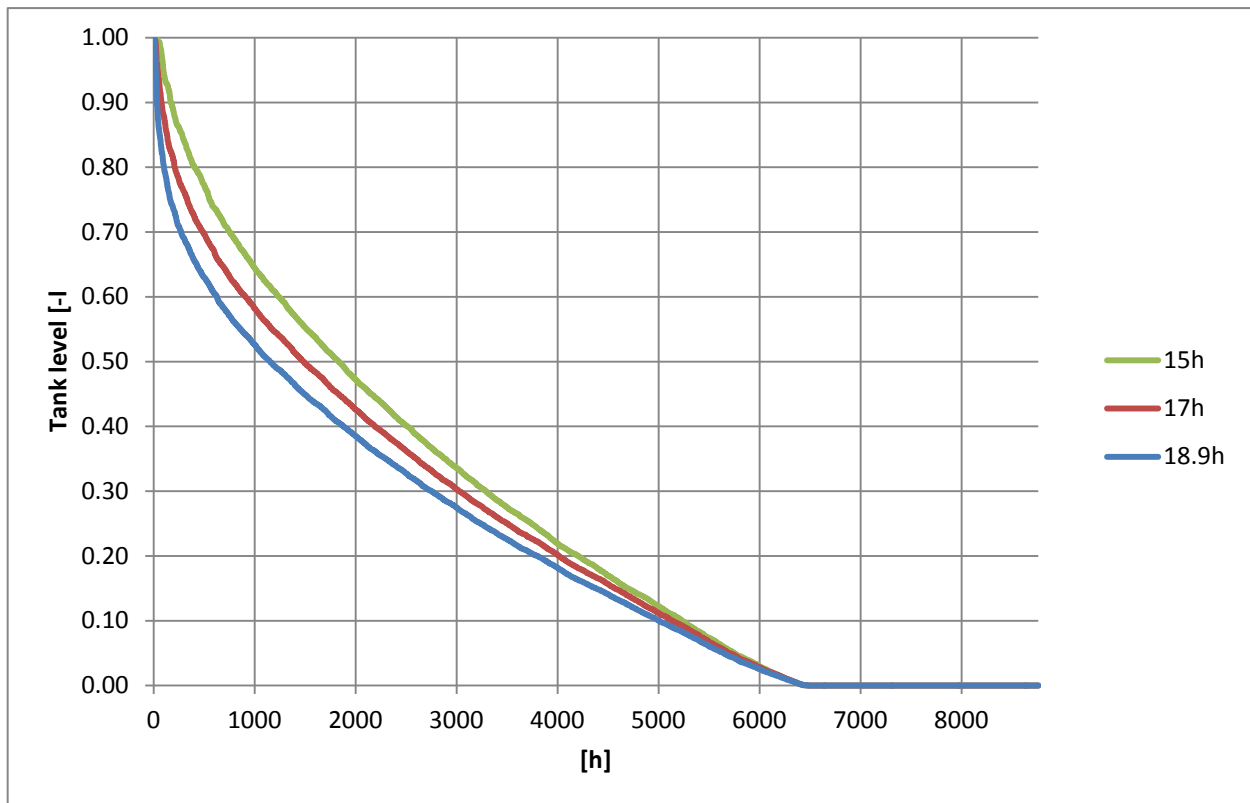


Figure 6-14: Duration curves of the tank level for constant turbine size (40 MW) with varying storage sizes

6.3.3 Annual Output Sensitivity Analysis

In order to analyze the behavior of the final 38-MW-turbine / 15-h-storage design on changing environmental conditions and also some design changes, sensitivity analysis were made. At first, a standard condition was simulated in a time-series analysis for a whole year and after that, one of the input values was varied while all the other kept the same. The most important result value of the time-series analysis was the annual plant output in MWh. The impact on this number is shown in the following. The final design in Table 6-6 shows a value of 208 453 MWh for the annual plant output, which will represent the 100% value in the following.

a) Daily varying Ambient Conditions

First, the daily varying environmental conditions such as DNI, wind speed and ambient temperature are investigated. While DNI and wind speed can be varied with a fixed percentage, this is not reasonable for the ambient temperature since negative temperatures could occur as well. Hence, the temperature is varied with fixed numbers. DNI and wind speed values for each hour are multiplied by 0.8 or 1.2 in the appropriate time-series input data, while the ambient temperature for each hour is changed by adding 5 K or subtracting 5 K. Furthermore, the receiver design in Excel was updated since a change of the average annual wind speed is connected with a change of the magnitude of forced convection, which resulted in changed Solar_tower.ALPHA and Solar_tower.DWTDES values that were kept constant over the year. The change of the average ambient temperature in the magnitude of some degrees did affect the named variables in a lower order of magnitude and was neglected in this case. The results of these time-series simulations are illustrated in Figure 6-15.

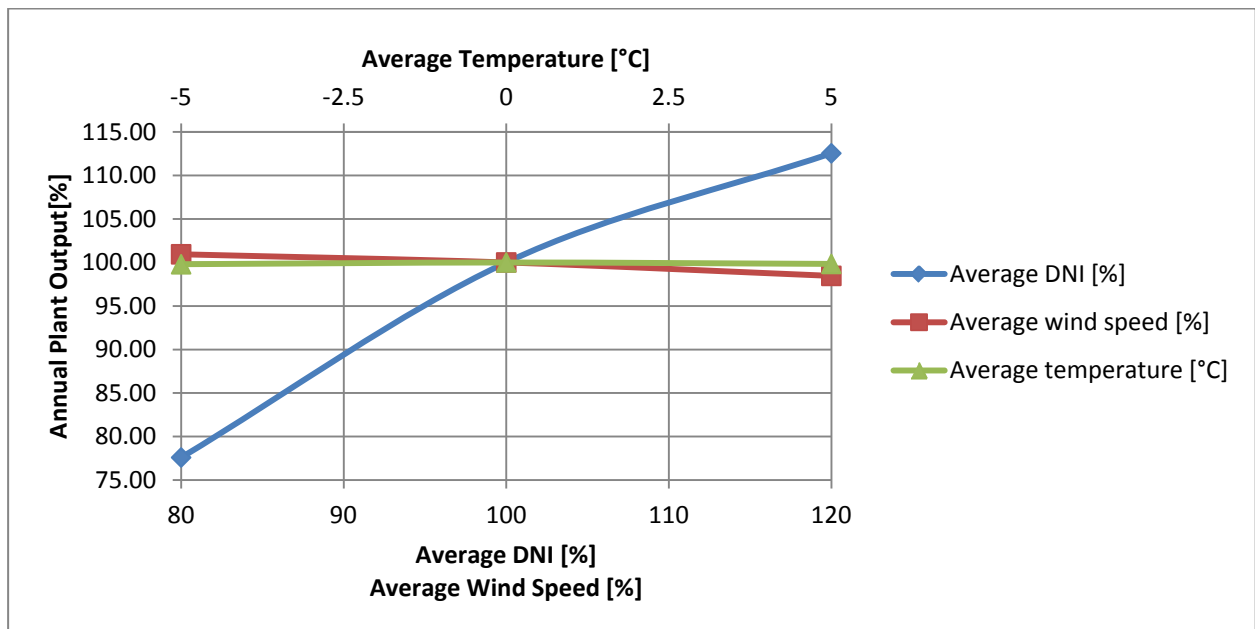


Figure 6-15: Sensitivity analysis of daily varying ambient conditions

The highest impact on the annual plant output has the average annual DNI. It can be noted that a 20% higher DNI results in an output increased by 13%, but a 20% lower DNI results in a 22% lower output. This nonlinearity is mainly based on two effects. First, the high DNI leads to losses because of a hot tank that is often full, and second, the receiver pump works more often 10% above its design flow rating, which is its limit. In both cases, heliostats must be defocused in order not to overflow the tank or to overheat the receiver. A smaller part of the losses is due to the higher receiver surface temperature at higher receiver loads. On the other end of the curve, the lower DNI leads to a higher amount of losses due to a lower turbine usage and a higher amount of on-/off-switching losses of the energy conversion system.

A lower wind speed leads to higher annual plant output because of a lower heat loss rate due to forced convection at the receiver and because of a less frequent heliostat switching to stow position. The deviation here is about 2-3%.

An interesting fact is that the outside temperature has the lowest impact of all named factors on the annual plant output. The trend of the appropriate curve in Figure 6-15 is difficult to see, hence, the values are displayed in Table 6-8 again. It is astonishing that reduction and increasing of the ambient temperature both show a decreasing annual output. A possible interpretation of this phenomenon could be that with falling ambient temperature, the impact of the heat losses of the receiver and the storage is higher than the improvement of the cycle efficiency due to lower condenser pressures. With around 0.9%, the deviation from the standard case is low. At increased ambient temperature, the annual output also falls for about 0.9%. This can be explained due to the now dominant steam cycle efficiency drop-down, which overcompensates other heat loss reductions.

Table 6-8: Sensitivity analysis of daily varying ambient conditions / Average temperature

Average temperature [°C]	Annual output [%]
-5	99.10
0	100.00
5	99.13

b) Atmospheric Attenuation

The atmospheric attenuation is an ambient condition, which may vary during the course of the day. Time series analysis do not consider this variation as there is no data available in literature. To quantify the effect of attenuation in this sensibility analysis, annual average has been varied to quantify this sensitivity.

According to [26], there is a lot of research considering this data done at the moment but as a rough estimation, a value of 0.8 could be assumed, a value of 1 would be valid for Spanish conditions (1 means no additional atmospheric attenuation). As the determination of this value is quite insecure, a sensitivity analysis could show how strong errors on assuming this value could impact on the yearly generator output. In Figure 6-16, the value for the design case 0.8 is added by 0.6 and 1.0.

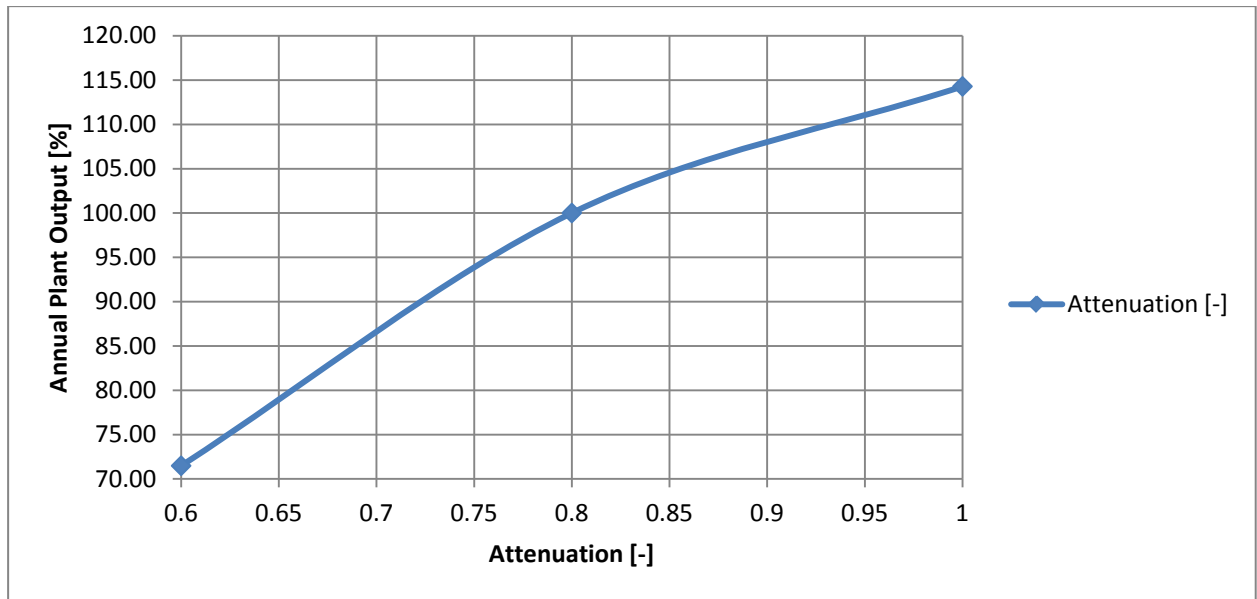


Figure 6-16: Sensitivity analysis of the atmospheric attenuation

The characteristic of this curve looks similar to the one of the average DNI, both values influence the annual plant output in qualitatively the same way. The radiation arriving at the receiver changes linear with DNI and attenuation factor, hence, a similar interpretation for this sensitivity analysis is valid.

c) Heliostat Reflectivity

Three time-series simulations were run to find the annual plant output values for other reflectivity factors beside the design factor of 0.8841 (the use of factors was preferred instead of percentages in this case because the reflectivity value used in EBSILON Professional is also given as a factor). This factor is a combination of a design reflectivity factor and a cleanliness factor. In the simulations, only the total reflectivity is investigated. The theoretic value of 1 for a perfect reflectivity is the upper limit and the values of 0.75 and 0.5 represent dirty mirrors (see Figure 6-17). The relation of the heliostat reflectivity to the annual plant output is almost linear, just between the design factors 0.8841 and 1, the slope of the curve becomes flatter. As mentioned in the sensitivity analysis for DNI and attenuation factor, this is due to losses because of partial receiver overload and a lack of storage capacity.

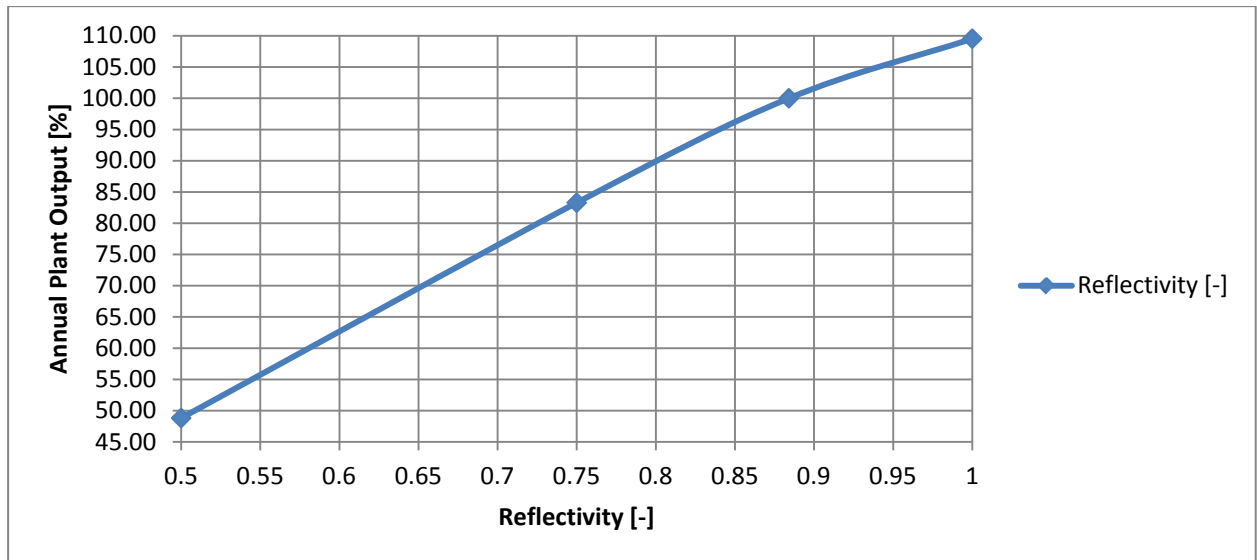


Figure 6-17: Sensitivity analysis of the heliostat reflectivity

d) Absorptivity and Emissivity

The next simulation considers absorptivity and emissivity of the receiver (see Figure 6-18). For all changed values, the receiver was redesigned in Excel. The absorptivity is varied in the range of 0.8 and 1, whereas 0.93 is the standard value. The almost linear curve shows a high impact of the absorptivity on the annual plant output. This illustrates the importance of receiver coating that provides high absorptivity. The design value of the emissivity is quite high (0.83), so it is especially of interest how high the impact of better receiver coatings with less emissivity would be. Therefore, the values for an emissivity of 0, 0.5 and 1 were calculated. For example, a reduction of the emissivity to 0.3 would lead to a higher annual plant output of about 5%.

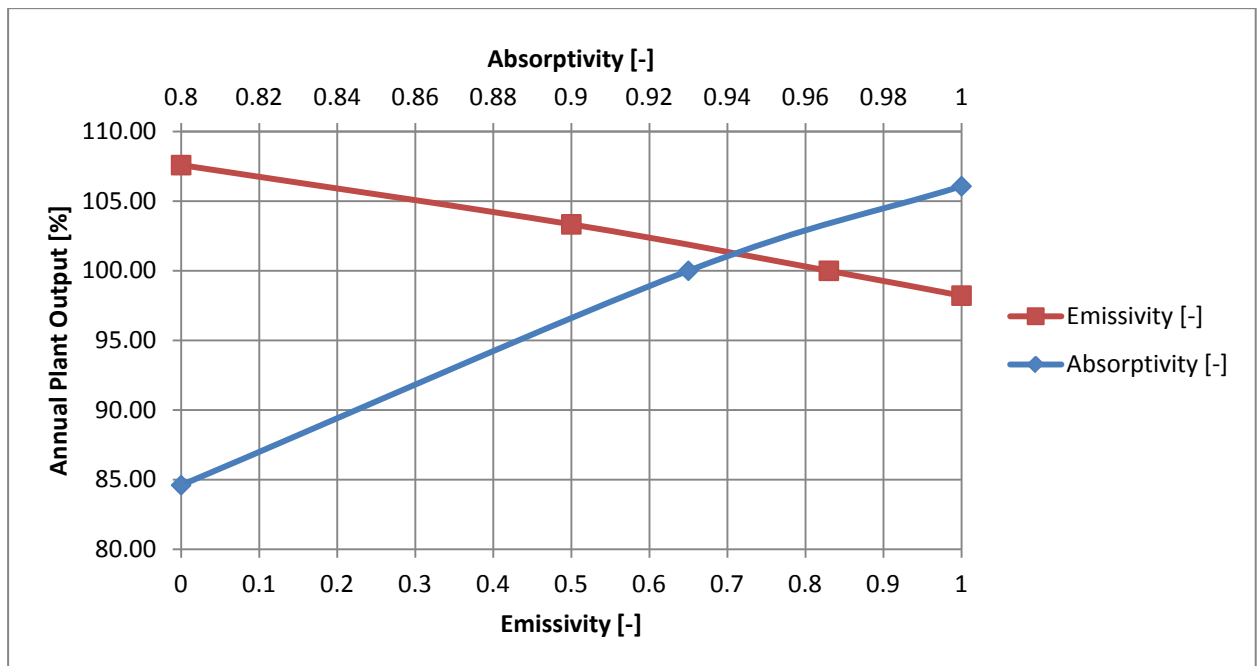


Figure 6-18: Sensitivity analysis of receiver absorptivity and emissivity

e) Heliostat Field Tracking Consumption

The specific heliostat field tracking consumption was considered to be 0.1 W/m^2 . This value is quite insecure and could be also set to zero because of its relatively low relevance [26], but to visualize the impact, it is varied from 0% to 1000% of the standard value. Figure 6-19 shows a quite linear relationship which is obvious since the number of hours per year on which the heliostat field is in operation do not change and only the tracking consumption changes. The difference between the design case and the case in which the tracking consumption is ignored is around 0.2%.

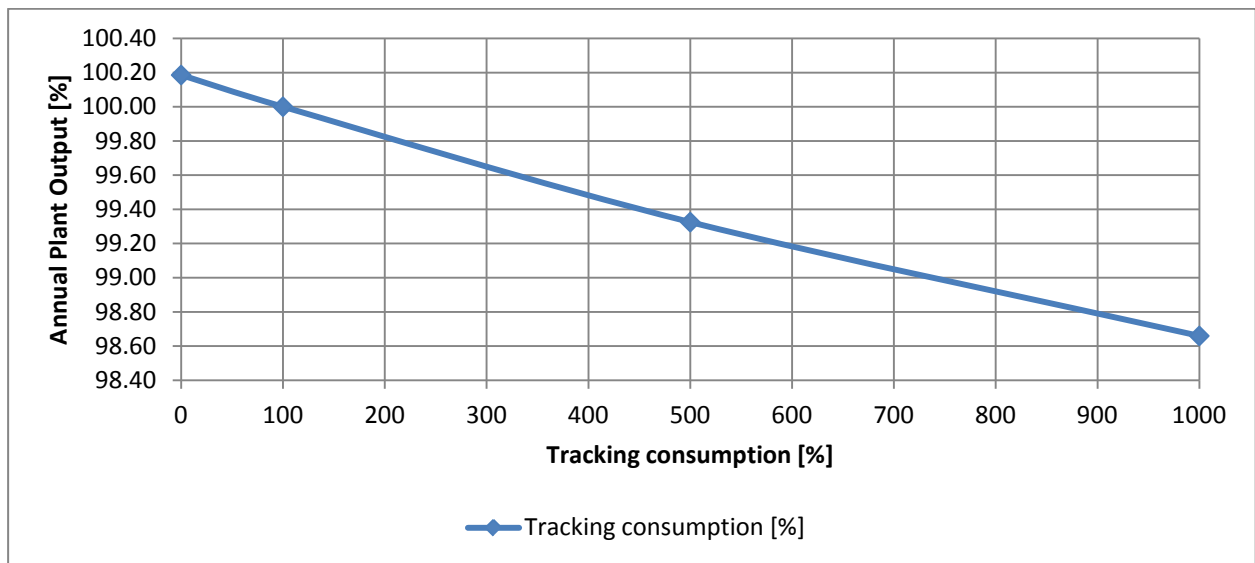


Figure 6-19: Sensitivity analysis of the heliostat field tracking consumption

f) Heliostat Field maximum tolerated Wind Speed

According to Figure 5-5, the maximum wind speed at 10 m above the ground seldom exceeds 10 m/s (this represents the average value for an hour); in fact it does not reach 12 m/s. The heliostat field maximum tolerated hourly averaged wind speed is 10 m/s in the standard case, which represents the state of the art for heliostats [86]. Above this value, the heliostats move to their stow position, which means that the total field will be defocused. This number is now varied from 8 m/s to 12 m/s, and the results are illustrated in Figure 6-20. One can see that a tolerated wind speed of 8 m/s leads to a lower output of around 0.9%. A higher wind resistance goes along with fewer improvements, which are around 0.1%.

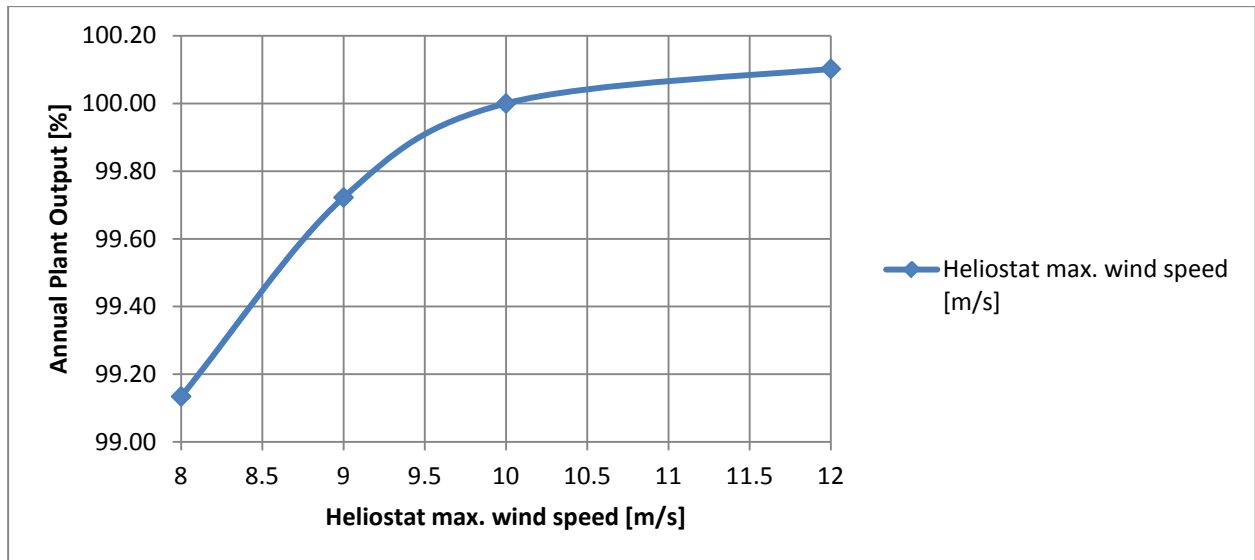


Figure 6-20: Sensitivity analysis of the heliostat field maximum tolerated wind speed

g) Heliostat Field minimum DNI for tracking activation

The absolute minimum DNI for tracking activation is at 55 W/m^2 . Below this value, the heat losses of the receiver are too high for heating the molten salt up to 565°C . At 56.5 W/m^2 , the amount of heat transferred by the molten salt coming from the receiver is theoretically sufficient to compensate the electrical consumption of the heliostat field. In the following sensitivity analysis, the initial value of 56.5 W/m^2 was raised in 10% steps up to 150% (84.8 W/m^2) and finally 100 W/m^2 and 150 W/m^2 (see Figure 6-21). It turned out that the impact, especially at low values for the minimum DNI, was small. Also, the result was very sensitive at low values, which made it difficult to interpret the behavior of this correlation. A possible reason for this phenomenon could be the fact that the time-series analysis is quite rough with time steps of 1 hour, including inputs of average DNIs for each hour. The variability might be reduced by smaller time steps – preconditioned the availability of appropriate weather data is given (which is not the case for this thesis).

Summing up, it can be said that the trend is going downwards with a higher minimum DNI, so the theoretically defined initial value for it seems to be feasible in this consideration. To underline this argumentation, the mentioned time-series analysis containing smaller time steps could be made.

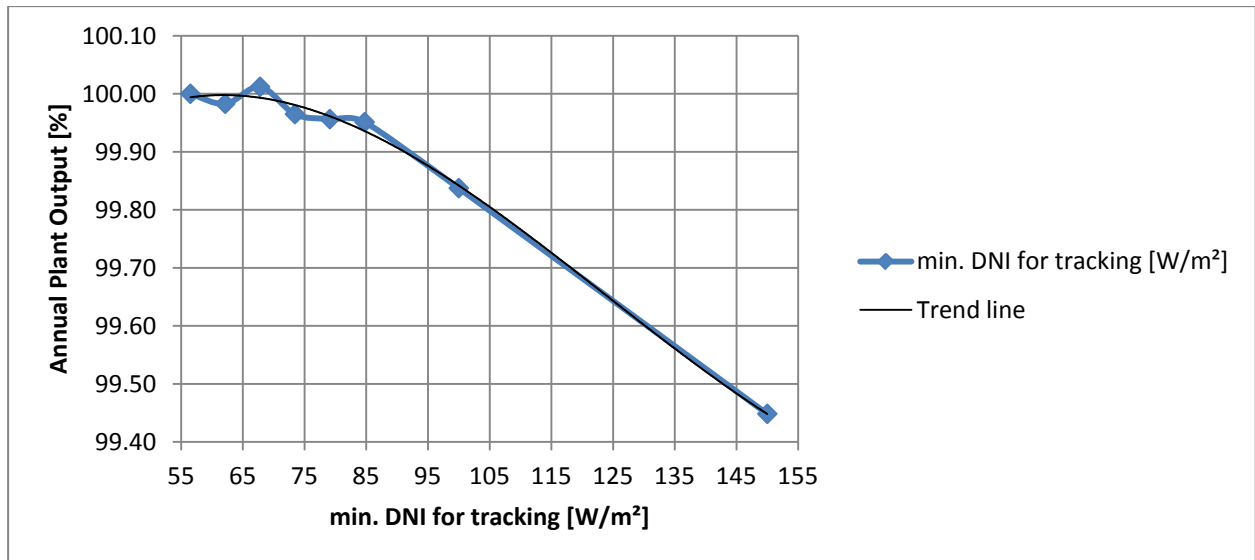


Figure 6-21: Sensitivity analysis of the heliostat field minimum DNI for tracking activation

6.3.4 Day Analysis

In this section hourly changing variables of the power plant will be investigated in diagrams, which show the process over several days.

First, the relation between DNI, storage level and net power plant efficiency is analyzed. The illustration of the net power plant efficiency was chosen because it also displays if the steam cycle is switched on or off.

In Figure 6-22 this relation is shown for four sunny days in May, as an example of the desired weather conditions. The storage level rises during the day and sinks during the night and the power plant is capable of producing electricity 24 hours a day. At the beginning of this period, the steam cycle is switched off, even though the storage is not completely empty. This is due to the fact that the EBSILON model assumes an empty storage during the following hour and therefore, shuts the steam cycle down. This could be avoided by the integration of a predicting program that switches the steam cycle into part load to bridge the time until the storage is refilled.

In the following days, the storage is optimally used in order to operate the turbine 24 hours a day. It is then fully filled in the afternoon, on the fourth day, where some heliostats must be defocused for a short time in order not to overfill the hot tank.

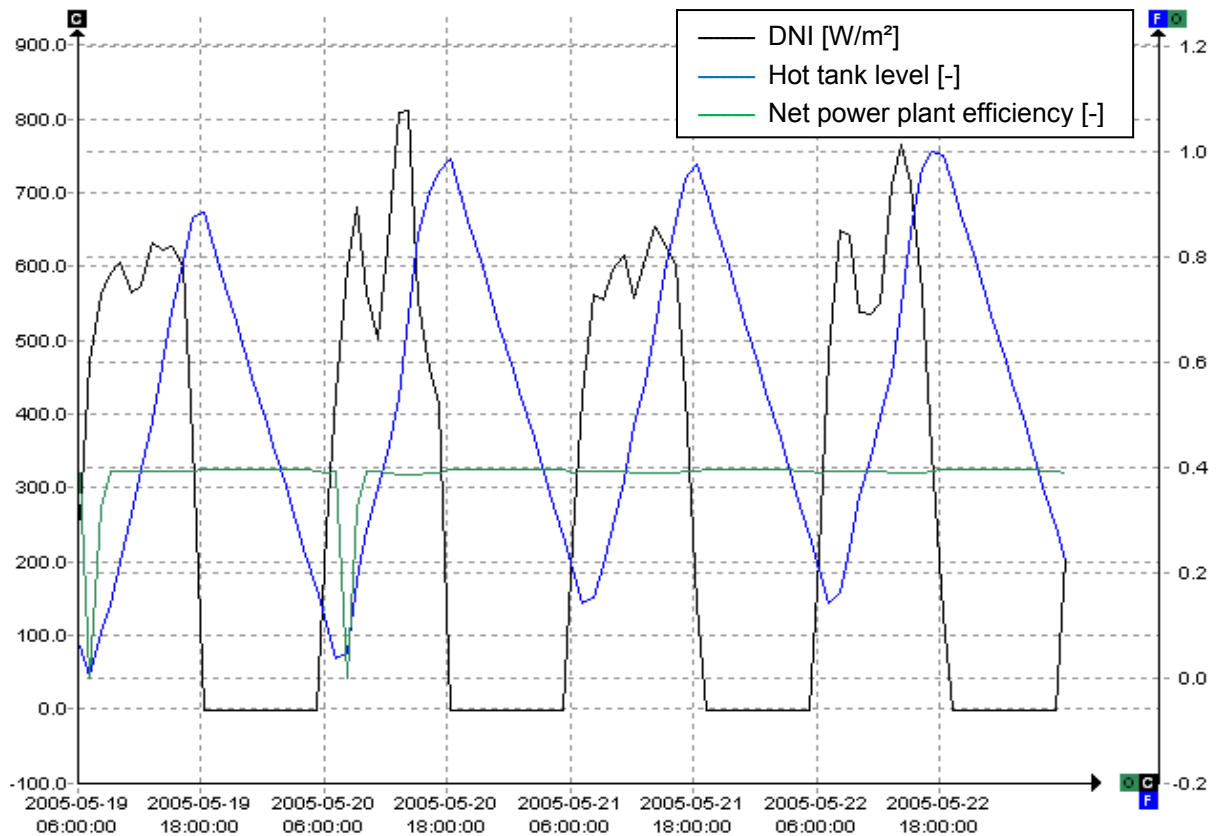


Figure 6-22: DNI (black) in W/m^2 , Hot tank level (blue) and net power plant efficiency (green) for four sunny days in May

In Figure 6-23 the same kind of diagram is now shown for three very sunny days in May. In these three days the power plant produces electricity continuously and the lowest level of the storage is around 0.15. One can also clearly see the “peak shaving” due to heliostat defocusing when the storage tank is full, which causes DNI harvest losses.

In Figure 6-24 the diagram is shown for five days in December near winter solstice. One can see that for sunny periods in winter, similar magnitudes of DNI can be reached as in May, but for fewer hours in the day. On one of these three sunny days the storage is even completely full, but the full storage tank cannot provide continuous electricity production through the night because the night is too long in winter. Also here, the integration of a predicting program that switches the steam cycle into part load to bridge the time until the storage is refilled, would be helpful.

On the second day in Figure 6-24, the DNI is at a level where it allows the receiver to fill the storage with approximately half of the steam cycle molten salt consumption. The result is that the steam cycle is started when the tank level is sufficient and later on is once again switched off due to a lack of storage charge. This happens in this case four times a day. As with the other issues mentioned before, this can also be eliminated by implementing prediction features.

6 Thermodynamic simulation

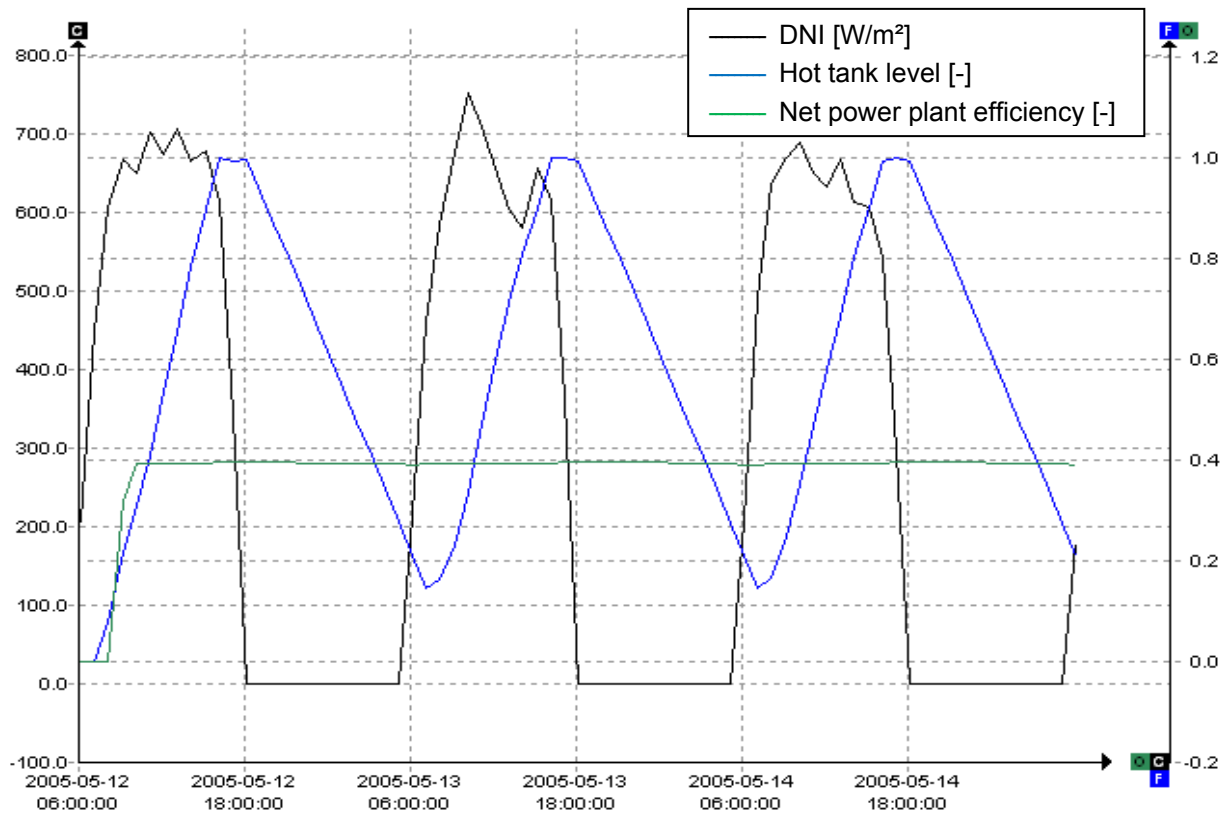


Figure 6-23: DNI (black) in W/m^2 , Hot tank level (blue) and net power plant efficiency (green) for three very sunny days in May with full storage in the afternoon

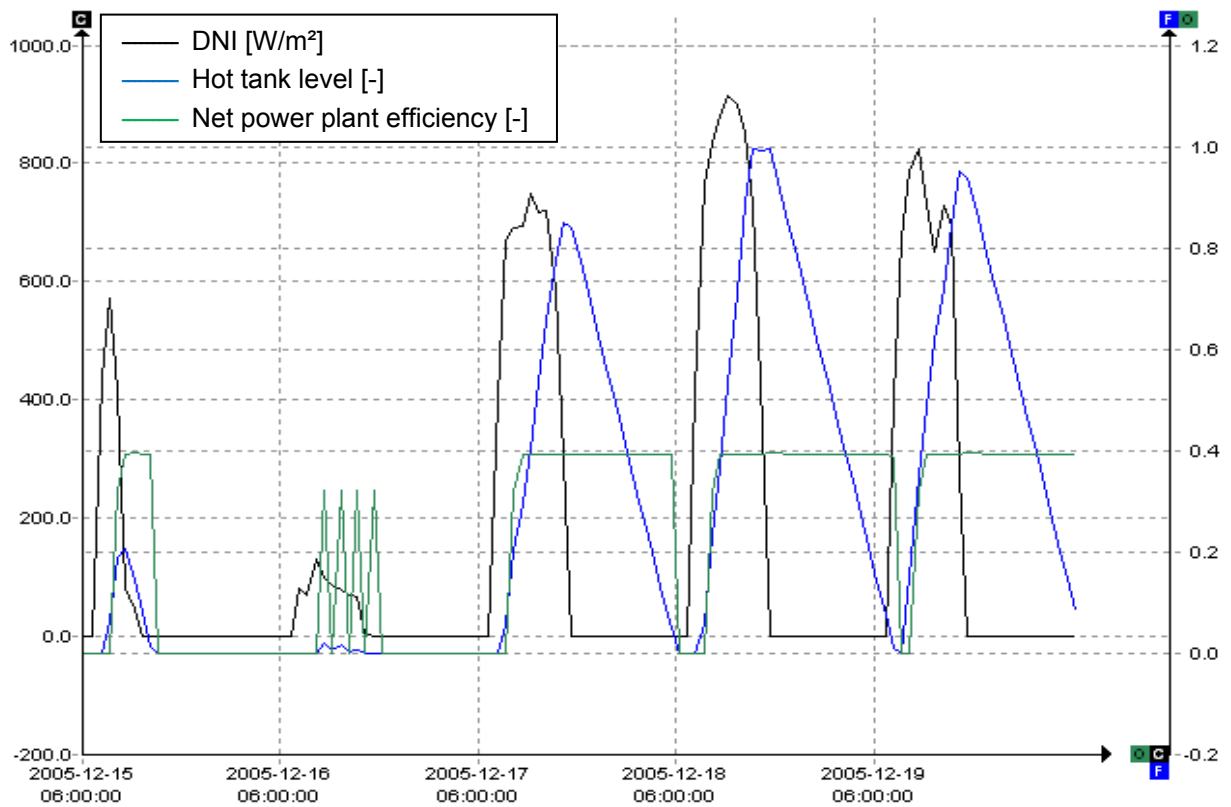


Figure 6-24: DNI (black) in W/m^2 , Hot tank level (blue) and net power plant efficiency (green) for five days in December near winter solstice

Figure 6-25 shows four days during period of bad weather in early March. On the first and the third day the DNI is again insufficient or rather the weather is unstable. The oscillations of the steam cycle now happen at higher average daily DNI's. In order to prevent this, the steam cycle always starts at the earliest two hours after the beginning of storage filling. In this case, this is not sufficient. A general later starting of the steam cycle could minimize this effect, but then the heat storage is filled faster and full more often in the year, which again leads to losses. An intelligent control could also help here.

On the second day the receiver is not even activated, because the DNI is too low to heat the molten salt. The fourth day is also unsettled, but here the time of lower DNI can be bridged by storage loading achieved in the preceding hours.

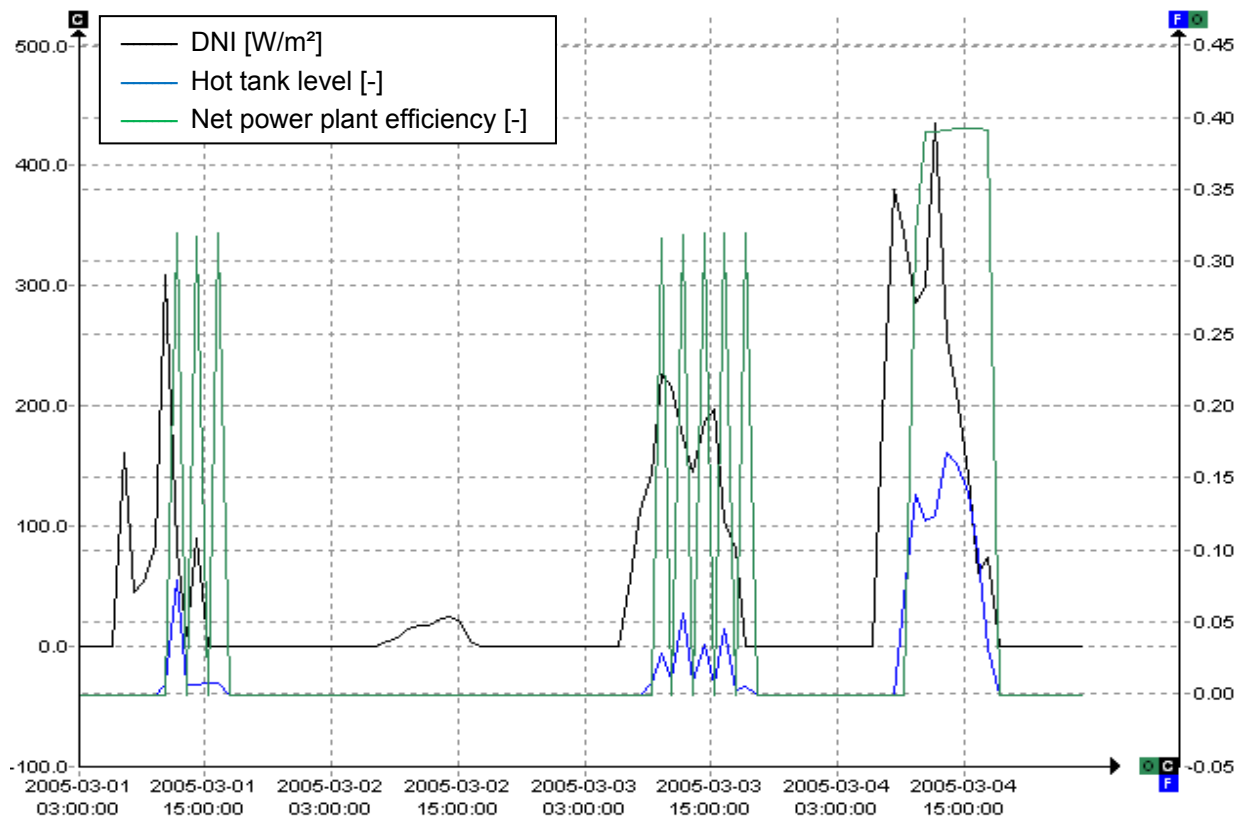


Figure 6-25: DNI (black) in W/m^2 , Hot tank level (blue) and net power plant efficiency (green) for four days in a bad weather period in early March

In Figure 6-26 a different diagram is now shown. Here, the correlation between the hot tank level and the hot tank temperature can be seen for the same sunny days in May like in Figure 6-22. The temperature of the hot tank always rises when hot molten salt (565°C) comes from the receiver and mixes with the storage inventory. The temperature then falls again when there is no loading by hot molten salt and the heat escapes through the tank insulation.

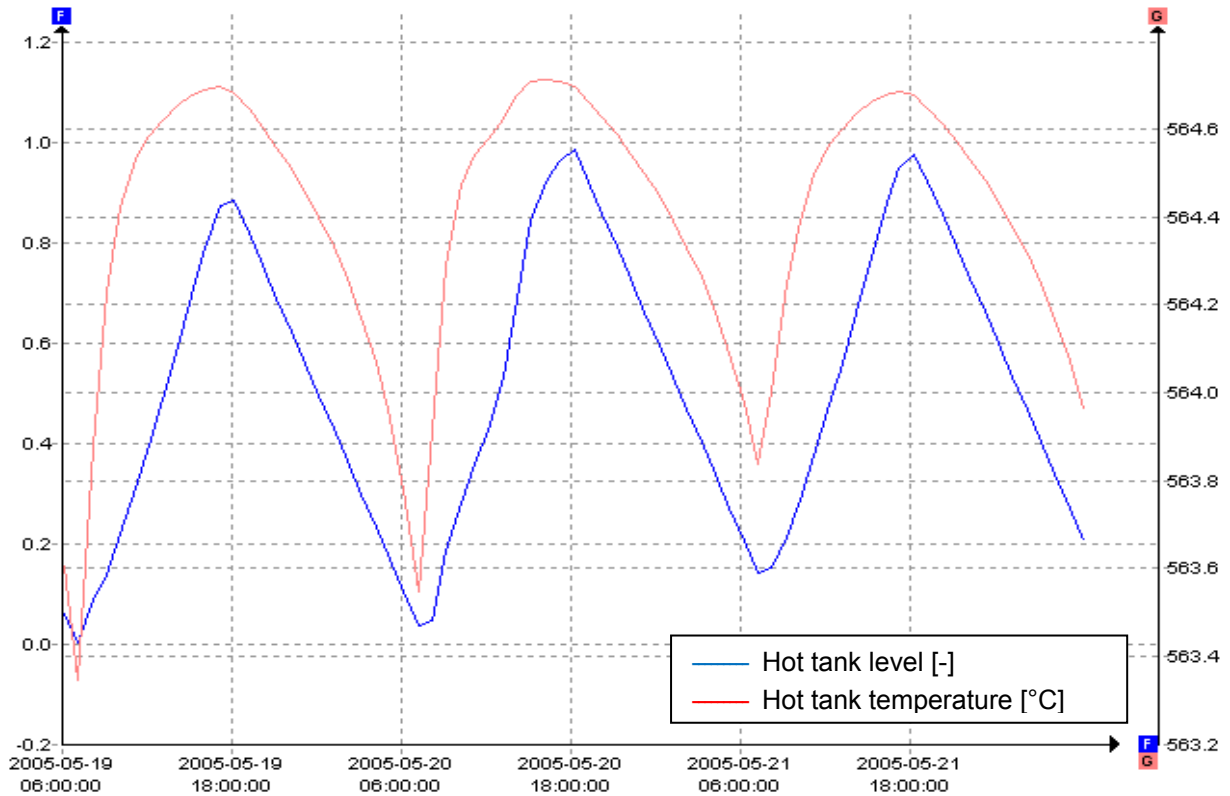


Figure 6-26: Hot tank level (blue) and hot tank temperature in °C (red) for four sunny days in May

The same is investigated now for the cold tank in Figure 6-27. Here, the process of the temperature graph is more complicated. The cold tank is heated by cold molten salt coming from the HRSG (290°C) and it also loses heat through the tank insulation. The heat losses per ton of molten salt in the cold tank (which is also valid for the hot tank) are higher for the low tank levels than for the high tank levels.

The temperature reaches its minimum on normal days around midnight and then rises because the heat losses per ton of molten salt are decreased due to the rising cold tank level, (which is obviously inversed to the hot tank level). From this point on, the tank temperature is effectively rising due to the cold molten salt coming from the HRSG.

When the receiver is activated and consumes cold molten salt from the cold tank, the tank level in the cold tank sinks quickly. This again leads to a small temperature drop.

During the day, when the hot tank is loaded and the cold tank is unloaded, the temperature of the cold tank rises because its inventory decreases and continuously mixes with molten salt coming from the HRSG.

Just before 6 p.m., the temperature falls again until around midnight because of the high heat losses when the tank is at a lower level. As seen in the temperature data of the first day, this process does not always look quite the same because it is very sensitive to the actual tank level

and the amount of molten salt coming from the HRSG and exiting into the receiver (All these values are individual for each hour and each day).

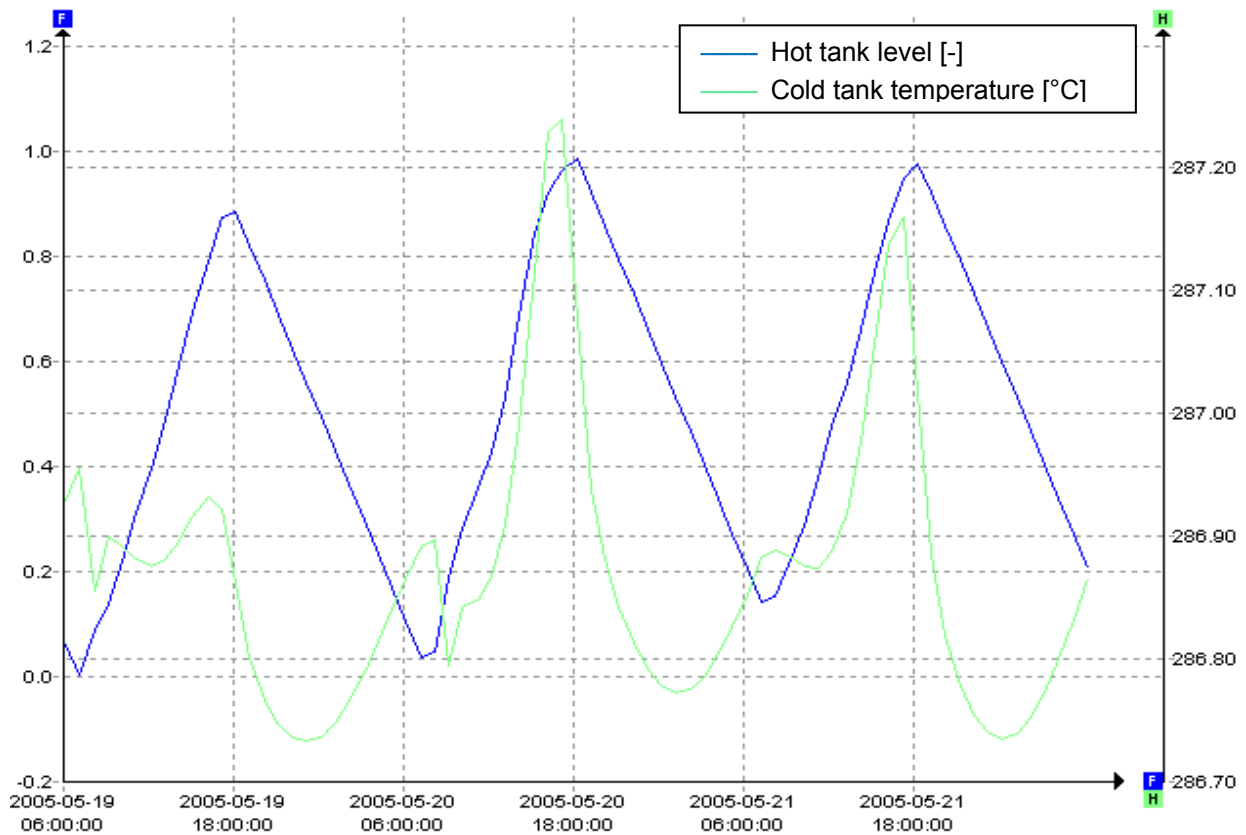


Figure 6-27: Hot tank level (blue) and cold tank temperature in °C (green) for three sunny days in May

The process of the hot and the cold tank temperature is now investigated for the same period of bad weather in early March as already shown in Figure 6-25.

In Figure 6-28 one can see that the tank temperature falls almost linearly when there is no loading of the empty hot tank. The rate is at about 10°C/day, which deviates from the design value of 5.5°C/day. Therefore, the insulation should be slightly improved. With a rate of 10°C per day, the tank would need around 30 days to cool down to 260°C, where the tank immersion heaters will be activated. When the tank is loaded with hot molten salt coming from the receiver, the temperature rises quickly towards 565°C, even if the storage level is raised just up to some per cent of its capacity. This is because of mixing of the incoming hot molten salt with the comparatively low amount of molten salt stored in the heel level of the tank.

In Figure 6-29, the temperature decrease in the cold tank is at a rate of slightly above 2°C/day, which is according to the design value. With this rate the tank needs around 14 days to cool down to 260°C. The temperature increase rate is not that high as it is for the hot tank because the cold tank is almost full when molten salt is coming from the HRSG that is heating the cold tank inventory.

6 Thermodynamic simulation

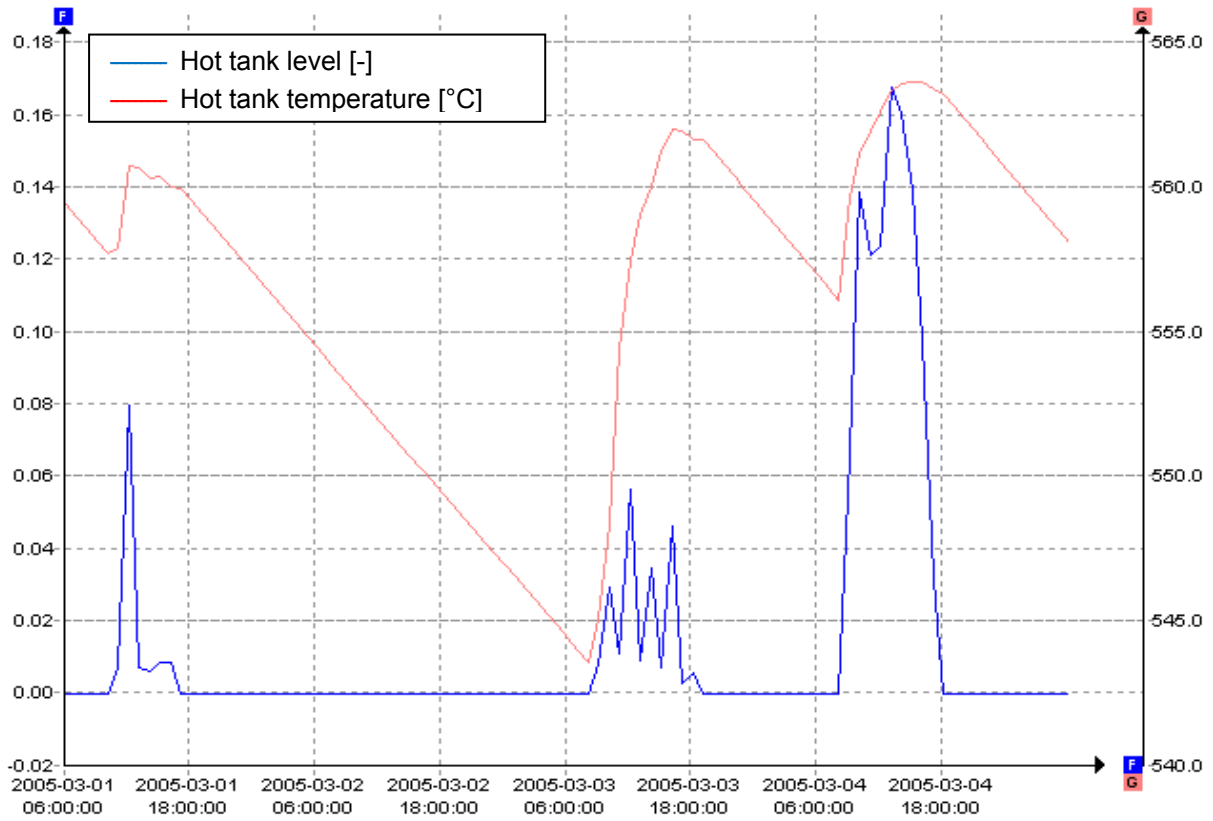


Figure 6-28: Hot tank level (blue) and hot tank temperature in °C (red) for four days in a bad weather period in early March

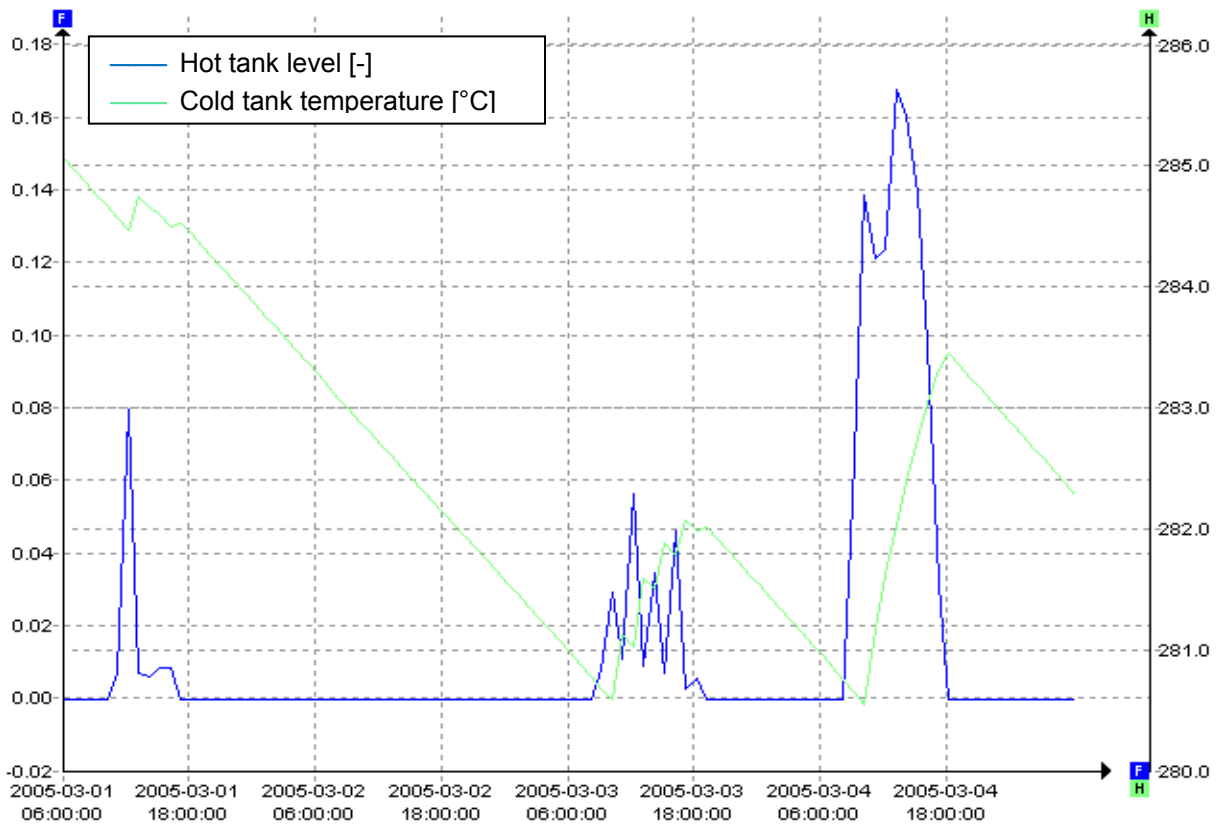


Figure 6-29: Hot tank level (blue) and cold tank temperature in °C (green) for four days in a bad weather period in early March

In Figure 6-30 one can see the maximum daily DNI for the whole year and the cumulated net power plant output. For a better estimation of the progress of the cumulated net power plant output graph, a straight line was also added connecting the start and the end point of this graph, which also represents its average slope.

Despite the fact that it is obvious that the slope of the cumulated output graph is lower during winter time than during summer time, some correlations to the daily DNI can be also seen.

From January up to around the middle of April, the DNI curve includes longer periods of low DNI, which can be seen by the white zones, which drop deeply at this time of the year. The cumulated output graph deviates downwards from the average slope line.

From the middle of April up to the end of July, there are in principle no white zones in the DNI graph drop deeply. The maximum DNI is comparatively moderate, but constant, which impacts the slope of the cumulated output, and even breaks through the average slope line.

From the end of July, until the end of the year, many days pass with a maximum DNI above 800 W/m², but there also some periods where there is low DNI. In sum, this causes the production of a cumulated output graph that is almost parallel to the average slope line for most of the time. During December the graph approaches the average slope line again.

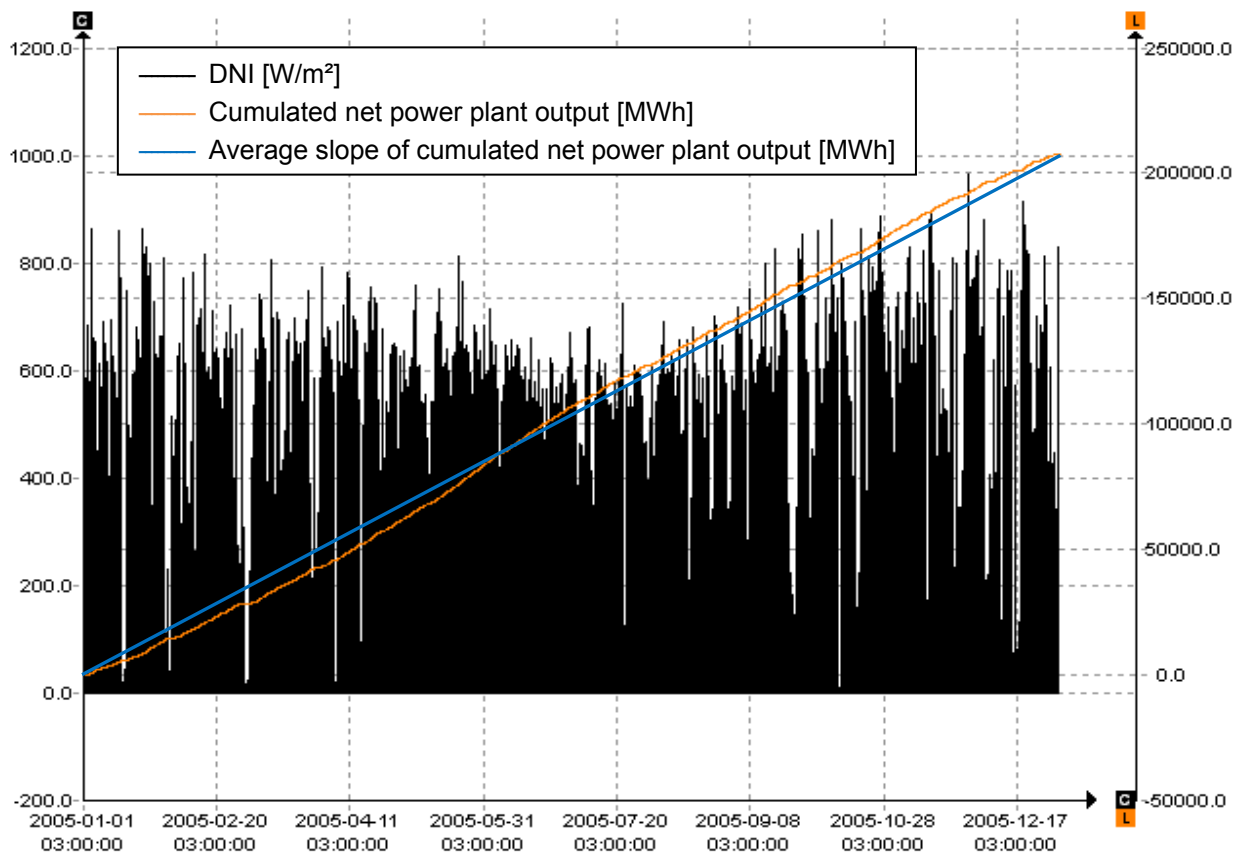


Figure 6-30: DNI (black) in W/m², cumulated net power plant output in MWh (orange) and a straight line connecting the start and end point of the output (blue) for the year 2005

6.3.5 Theoretic Attempt for an Integration of a Longtime Storage

As already discussed, there is an optimum storage size based on economic boundary conditions. If storage capacity was available for sufficiently low prices, long-time energy storage could be realized. In this chapter, a theoretic attempt is made to analyze the behavior of a solar thermal power plant with integrated long-time storage.

In an annual average, the storage is loaded with a molten salt flow rate of about 148 kg/s. If storing energy was free of losses (which is of theoretic nature, see Eq. 6-54), an average unloading of about the same rate would be necessary in order to have a turbine capable of running the whole year. This unload rate would be between 25 and 30 MW turbine power. In the first attempt, the turbine power was set to 25 MW because the losses due to energy storage are considered to be high as the insulation values of the storage tanks are not improved as a start. The storage has a capacity of 5 days ($8250 \text{ MWh}_{\text{th}}$). The hot tank level in the course of the year is shown for this case in Figure 6-31.

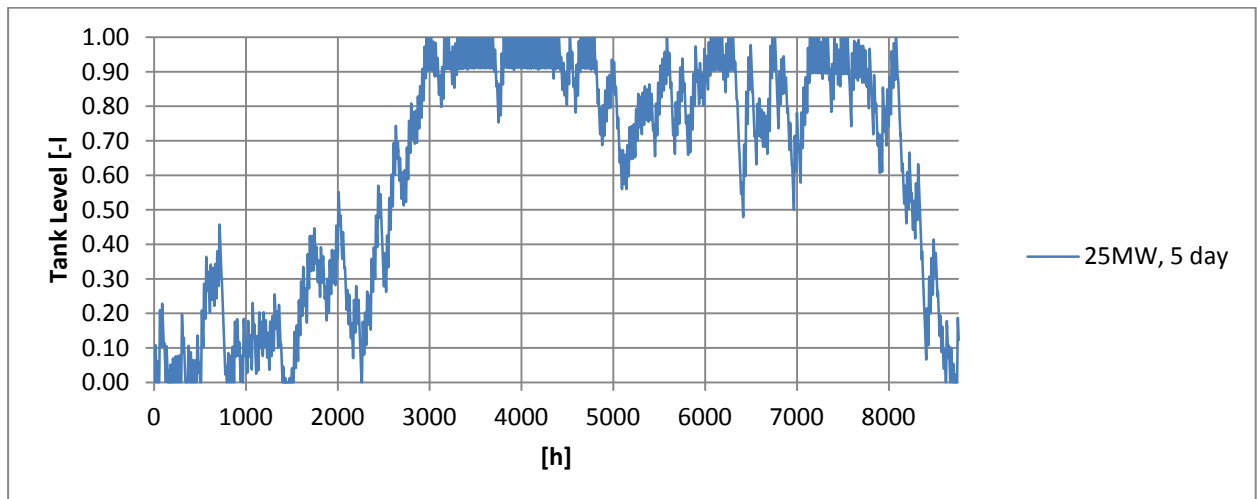


Figure 6-31: Storage level in the course of a year for a 25 MW turbine / 5 day storage configuration

The simulation starts on January 1st, so the tank is empty quite often at the beginning. But it can be seen that the 5-day-storage is able to overcome the whole summer and some periods in the winter without getting empty. Unfortunately, the tank is full quite often in the summer, which causes high losses. So, for the next attempt, the storage size has to be larger and the start of the simulation should be set at a time when there is a high-average daily irradiation.

In the following time series simulation (Figure 6-32), the start of the simulation was set to April 17th, 2005 at 7am, and the simulation ended on April 17th, 2006 at 6am. The generator output stayed at 25 MW but the storage was now increased up to 15 days ($24\,750 \text{ MWh}_{\text{th}}$). Now, the storage size for this configuration was more than sufficient and the start time was chosen in a way that the storage did not go empty. But it could be seen clearly that there was not enough energy transferred from summer time to winter time in order to allow a full year operation of the turbine. The tank level went towards its bottom mark again in about 1000 hours between simulation hour 5500 and 6500. There were two ways to extend the operation hours of the

turbine: improving the insulation of the tanks or decreasing the turbine power combined with an increasing of the storage capacity.

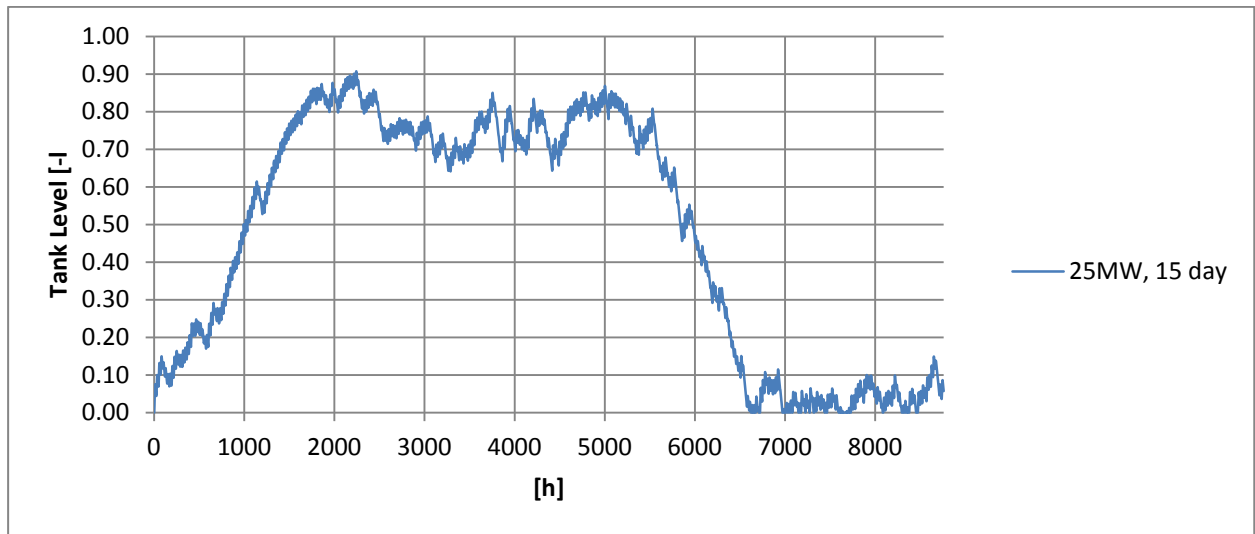


Figure 6-32: Storage level in the course of a year for a 25 MW turbine / 15 day storage configuration (Start at April 17th instead of January 1st)

Both ways were tried now. To reduce the high heat losses of the tanks, the specific heat loss coefficients were reduced to 50 W/m². Also the turbine was downsized to 20 MW and the storage was upsized to 25 days (41 250 MWh_{th}). The simulation year was again started on April 17th. The simulation result showed that all methods combined were too much (see Figure 6-33).

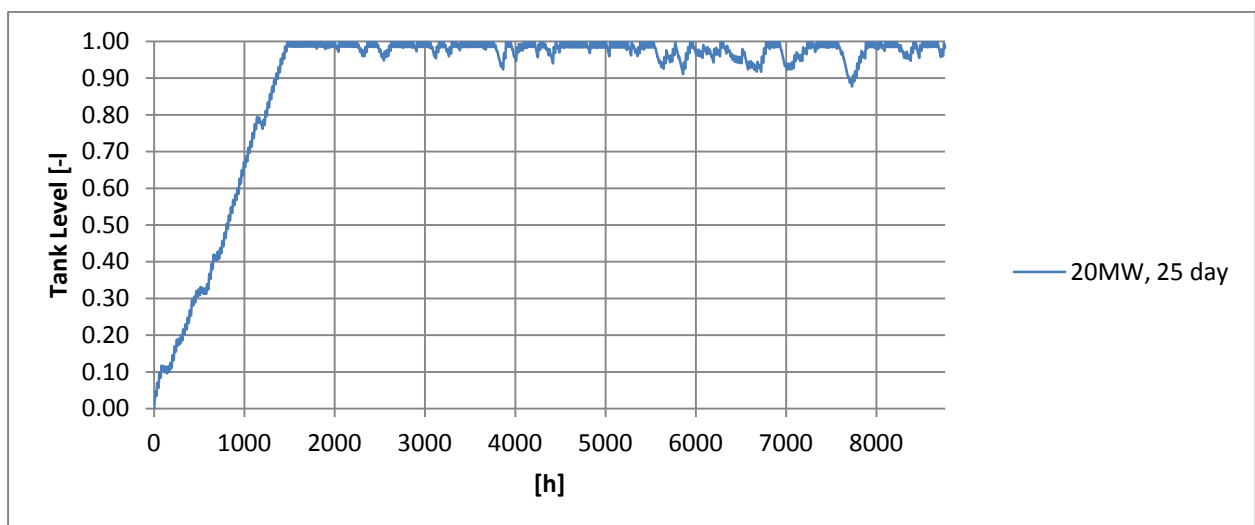


Figure 6-33: Storage level in the course of a year for a 20 MW turbine / 25 day storage configuration (Start at April 17th instead of January 1st)

The hot tank was now full after about 1500 simulation hours. The turbine was way too small now. The next attempt reset the turbine size to 25 MW again. In this case, the result was quite usable, as illustrated in Figure 6-34. The storage size could be reduced now but it is now shown, that, with this configuration, an almost full-year operation of the turbine is possible. The tank is empty for only 3 days between 8000 and 8500 hours after the start of the simulation. By a further refinement, these 3 days could be avoided as well but this simulation should be analyzed in the following in order to show the behavior of such long-time energy storage.

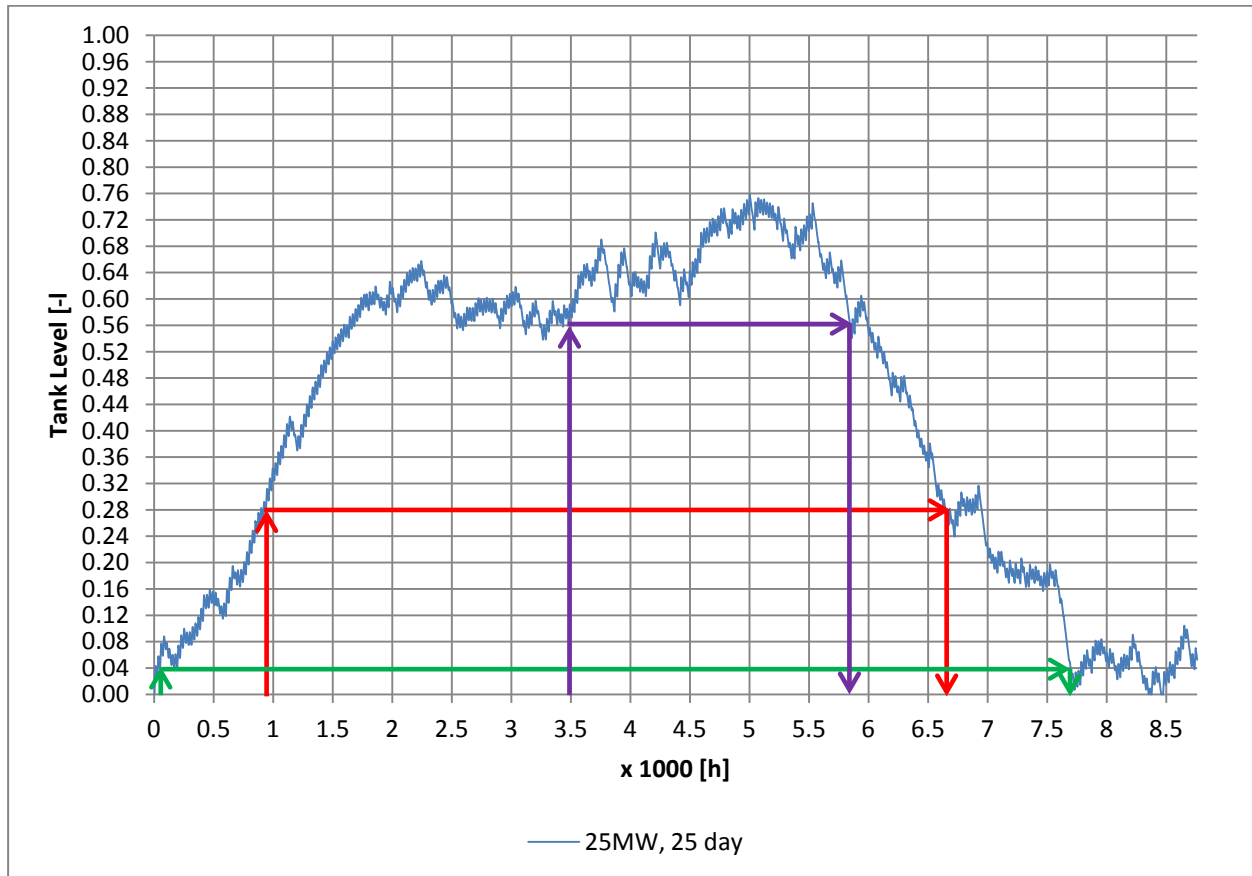


Figure 6-34: Storage level in the course of a year for a 25 MW turbine / 25 day storage configuration (Start at April 17th instead of January 1st)

Table 6-6 showed an annual plant output of 209 580 MWh for the chosen 38-MW-turbine / 15-h-storage design. In the last 25-MW-turbine / 25-day-storage design, an annual plant output of 201 277 MWh could be reached, which represents a minus of about 4%. This is because of the losses due to the longtime storage although the insulation of the tanks was improved. In Figure 6-34, arrows are also shown which indicate when the 1-day-level (green, 4% of the 25 day storage), 7-day-level (red, 28%) and 14-day-level (violet, 56%) is exceeded (arrow up) and goes below (arrow down) without being interrupted. One can see that the 1-day-level is not used for a large part of the year. The 7-day-level is also exceeded without interruption for around 2/3 of the year and the 14-day-level is exceeded for about 1/4 of the year.

In Figure 6-35, the duration curve of the tank level is illustrated which clarifies the total storage usage over the year a little better. The green arrow shows that the storage level of 1 day is exceeded for around 8250 hours per year, which means that this level is not used for about 94% of the year. The red arrow marks the exceeding of the 7-day-level at around 5800 hours (ca. 66%) and the violet arrow marks the exceeding of the 14-day-level at around 4200 hours (ca. 48%) of the year. As mentioned before, the storage capacity could be shortened to about 19 days of storage (76% of 25 days). As shown in these last two figures, the different storage levels are used with a different intensity in storage for full-year operation. In later summer, the higher storage levels and in later winter, the lower storage levels are used more intensively. The intermediate storage levels are mainly used for loading the storage in early summer and unloading it in early winter. The necessary storage tanks for the reduced 19-day-storage would have a diameter of around 130 m at a height of 14 m and would require in total about 317 000 tons of Solar Salt. As a comparison, the 15-h-storage for the 38-MW-turbine needs less than 14 000 tons of Solar Salt.

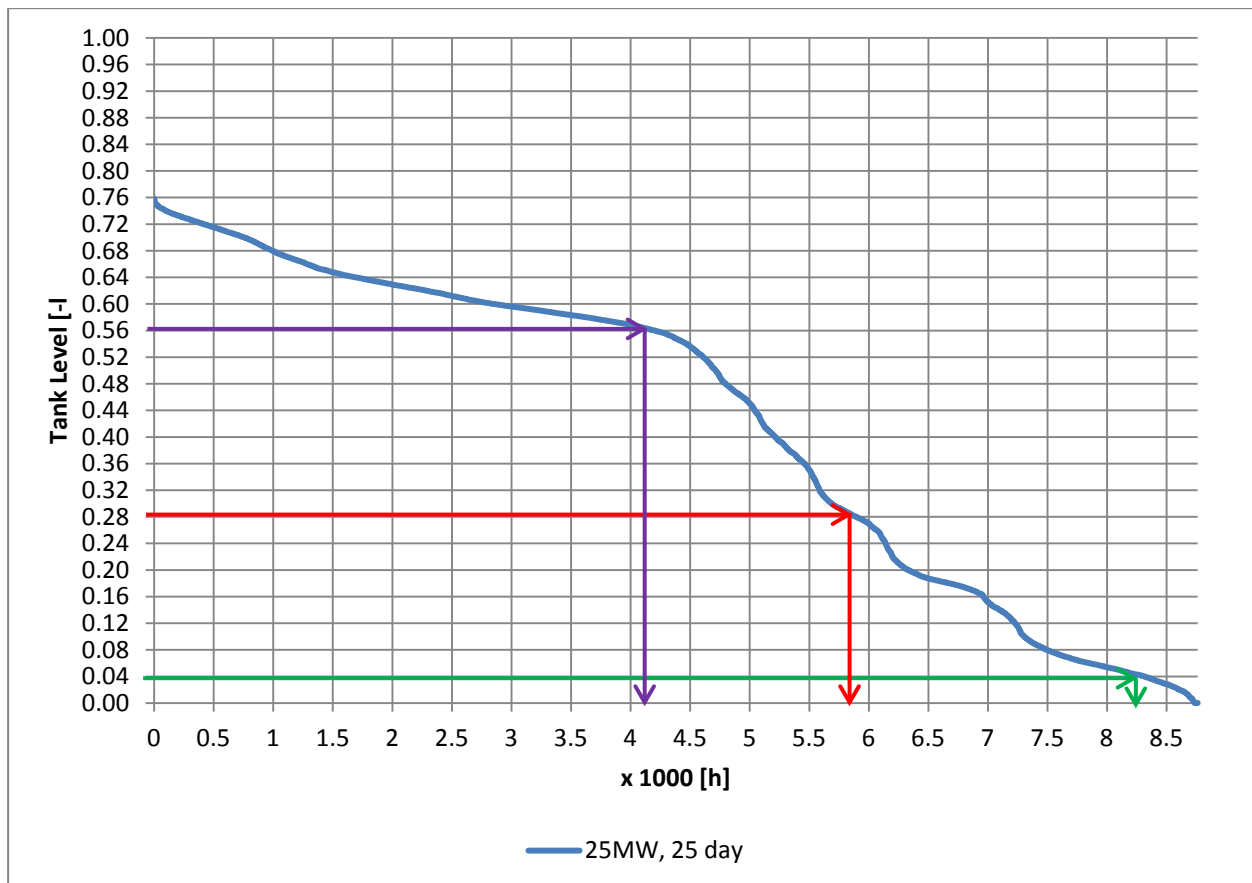


Figure 6-35: Duration curve of the tank level for a 25 MW turbine / 25 day storage configuration

7 SIMULATION RESULTS

For the design of the receiver, preferably realistic values for the pressure loss in the receiver tubes DP12N, the design wall temperature difference DTWDES, and the combined convection coefficient ALPHA for the outer surface of the receiver were determined by using an analytic calculation method. Especially for DTWDES and ALPHA, the determined values go along with an uncertainty. This is because the analytic calculation for this kind of heat transfer problems is not very precise and can be only used as an estimate.

Furthermore, some simplifications were made in order to model the solar tower receiver, particularly the assumption that the average receiver temperature is uniformly distributed all over the receiver surface. In reality, this is not the case and is a very complex issue, which depends on the receiver heat flux distribution control. More precise values could be determined by sophisticated CFD analysis, but further practical experience in receiver operation from existing solar tower power plants would close the gap to a realistic simulation.

Nevertheless, the determined values could be used for a first estimate. For an investigation of the part load behavior of the receiver in EBSILON, the DNI was reduced, keeping the other ambient conditions constant, and the part load was calculated once by EBSILON itself and once by using the Excel program. The more realistic calculation of the receiver pressure drop DP12 by the Excel program could be implemented in EBSILON by an equation or an adaption function. The deviation of the other values, wall temperature difference DTW, and heat transfer coefficient ALPHA, is comparatively low. Since the analytic part load calculation in Excel is also only estimation, the part load calculation in EBSILON can also be seen as a valid estimation method. The receiver efficiency ETAREC also shows low deviation for the bigger part of the load range.

The design of the storage tanks could be calculated quite precisely. For a given storage capacity in MWh_{th} and some geometry constraints, the amount of molten salt for the minimum (LEVMIN) and maximum storage level (LEVMAX) in each tank could be determined. Furthermore, the value specific heat loss (QLOSSR) for each tank could be determined by using appropriate insulation values in order to find daily tank temperature drops according to [86]. The hot tank daily temperature drop deviates from that desired value, therefore the insulation values could be adapted.

In the section time series analysis, after some theoretic considerations, the size of the storage and of the turbine was optimized for a given heliostat field / receiver. In this optimization process the specific values of the Gemasolar solar tower power plant in Spain provided some orientation for an economic relation of the component sizes. Gemasolar is the first commercial solar tower power plant that is capable to produce electricity 24/7. It uses a storage capacity of 15 hours combined with a capacity factor of 0.631. After this optimization process a 15 hour storage capacity was also determined, as well as a capacity factor of 0.626, which is reached by a 38MW turbine.

It was also discovered that undersized storage is completely full for many hours in the year, which leads to solar irradiation harvest losses, because in this case a part of the heliostats must be defocused in order not to overflow the storage.

In some sensitivity analysis, several conditions were varied in order to investigate, how this makes an impact on the annual power plant output in MWh. From the daily varying ambient conditions, the average annual DNI has the most impact on the output, whereas the average ambient temperature and the average wind speed show relatively little impact. Similar to the average annual DNI, the average annual atmospheric attenuation highly impacts the output rate of the power plant.

This means that an optimal location for the power plant should provide high average annual DNI and low atmospheric attenuation rates. Average wind speed and temperatures are not that important.

A low average reflectivity of the whole heliostat field also highly reduces annual output. Therefore, heliostat washing is very important, but there is also an economic limit of the maximum washing rate. For the plant location, a place with a low natural soiling rate should be preferred in order to keep the average reflectivity as high as possible.

A higher absorptivity and a lower emissivity would also reduce optical losses on the receiver. While the absorptivity of the most feasible coating Pyromark is still quite high with 0.93, a high temperature resistant selective receiver coating (still needing to be developed) with lower emissivity than 0.83, could reduce the heat emission, and therefore substantially improve the annual output.

The heliostat field properties (tracking consumption, maximum tolerated wind speed, and minimum DNI for tracking activation) were also investigated in a sensitivity analysis. Even though the impact of these properties on the average annual output is comparatively low in the investigated range, the impact of deviating values was interesting enough to illustrate a “what-if” scenario. If one of these properties changes moderately, the annual output is not significantly influenced.

During some day analysis, the behavior of the power plant in the time series simulation was investigated. It was discovered that the power plant functions quite well at medium to high rates of DNI and at very low DNI rates. In certain weather conditions or with certain DNI rates, the power plant tends to switch on for one hour and to switch off after that. This may happen several times a day. The reason for this is that there is no weather prediction function implemented that would switch the steam cycle to part load to bridge phases of low DNI in order to avoid start-up and shut-down transients. The same function would help avoiding a turbine switch off in early morning, just before the tank refills again.

In the last section an attempt was made to discover which conditions would be necessary to realize a full year and full load operation of the turbine for the chosen heliostat field. The result

was a 25MW turbine combined with a 19-day storage and improved tank insulation. For a 4% smaller annual output, around 23 times more molten salt would be required.

8 CONCLUSIONS

The aim of this master thesis was the preparation of a realistic model of a solar tower power plant. After a literature research the state of the art of solar thermal power plants in common and of the solar power tower technology (including the heliostat field) and several heat storage options was documented.

Much information was also used to build up an EBSILON Professional model. Therefore, the basics of the operation of a solar tower power plant were documented as well as a detailed functional description of the modeled power plant.

The basics of the operation include a description of the power plant systems, process flow diagrams, as well as operating states and transitions. The description of the modeled power plant documents the realized plant structure in EBSILON, and provides a detailed explanation of all relevant components. Furthermore, the states and transitions adapted to the EBSILON model are also explained.

For an accurate simulation of the receiver and the storage, an Excel program was created that calculates their properties analytically. To design a power plant with an optimum turbine and storage size, several time series simulations were run by using weather data for a place in the United Arab Emirates. For this purpose, data from the Gemasolar power plant in Spain was also used, in order to reference a commercially operated solar tower power plant that provides full day operation.

Several conditions were varied in sensitivity analysis in order to investigate the impact on the annual power plant output. Furthermore, day analysis provided an overview of the models behavior during different weather conditions.

To conclude, a preferably realistic model of a solar tower power plant was designed including different operating states and transitions. This model was then analyzed under real weather conditions for one year in time series analyses. Much additional technical and economic information was documented in order to provide an overview of the function and the challenges of solar thermal power plants, especially, solar tower power plants.

The information in this document could be used for further attempts for a preferably realistic simulation of solar tower power plants. In addition, the EBSILON model is easily adaptable and can be used for other plant configurations.

The analysis of the model showed that it would be very helpful to integrate a function that simulates weather prediction and switches the steam cycle to a defined part load rate in order to bridge longer times of no or few DNI (for unstable weather and during the night). It would be also possible to start the steam cycle later in the case of unstable weather. However, the unintelligent orientation of the Energy Conversion Switch on the hot tank level, which starts the steam cycle, if the tank level is sufficiently high, is rather suboptimal because it has no

predictive capability. Power plants like Gemasolar are controlled by human beings, who adjust the turbine power in a manner where startup and shut down losses are minimized by using predictive weather data.

Additionally, the content of the Excel program could be implemented into an EbsScript in EBSILON that calculates the heat transfer properties of the receiver for every time increment. This could improve the accuracy of the calculation even though the analytic calculation represents an approximation.

Moreover, the values of the additional losses in the model operating states could be refined by doing dynamic simulations to gain data or adapting data from plants that are in operation. Other more sophisticated ways, like a detailed programming of the losses, could also be feasible.

A possibility to reduce costs would be an integration of a thermocline molten salt storage with an integrated packed bed. This could be realized using the “Indirect Storage” component in EBSILON. The use as a peak load power plant could be also investigated, which could for example, cooperate with photovoltaic power plants.

LITERATURE

- [1] **Argonne National Laboratory** [Online]; *Sodium as a fast reactor coolant; Topical Seminar Series on Sodium Fast Reactors (Presentation)*;
http://www.ne.doe.gov/pdfFiles/SodiumCoolant_NRCpresentation.pdf (22.01.2013)
- [2] **Bai F., Xu C.**, 2011: *Performance analysis of a two-stage thermal energy storage system using concrete and steam accumulator*, Applied Thermal Engineering, vol. 31, p. 2764 – 2771
- [3] **Bauer T., Braun M., Eck M., Pflieger N. Laing D.**, 2012: *Development of salt formulations with low melting temperatures*; German Aerospace Center (DLR), Köln, Germany (SolarPACES 2012 proceedings)
- [4] **Beater P.**, 1999: *Entwurf Hydraulischer Maschinen*; Springer Verlag, Berlin, Germany; ISBN: 3-540-65444-5
- [5] **Bellard D., Ferriere A., Pra F., Couturier R.**, 2012: *Experimental characterization of a high pressurized air solar absorber for the PEGASE project; CEA-LETH, Grenoble, France (SolarPACES 2012 proceedings)*
- [6] **Boerema N., Morrison G., Taylor R., Rosengarten G.**, 2012: *Liquid sodium versus Hitec as a heat transfer fluid in solar thermal central receiver systems*; Solar Energy, Vol. 86, p. 2293–2305
- [7] **Böss F., Fluri T. P., Branke R., Platzer W. J.** 2012: *Simulation of parabolic trough power plants with molten salt as heat transfer fluid*, Fraunhofer ISE, Freiburg, Germany (SolarPACES 2012 proceedings)
- [8] **Buck R.**, 2012: *Heliostat Field Layout Using Non-Restricted Optimization*; Deutsches Zentrum für Luft- und Raumfahrt e.V. (DLR), Stuttgart, Germany (SolarPACES 2012 proceedings)
- [9] **Burgaleta J. I., Ternero A., Vindel D., Salbidegoitia I., Azcarraga G.**, 2012: *Gemasolar, Key points of the operation of the plant*; Torresol Energy, Getxo, Spain (SolarPACES 2012 proceedings)
- [10] **Burgess G., Lovegrove K., Mackie S., Zapata J. Pye J.**, 2011: *Direct steam generation using the SG4 500m2 paraboloidal dish concentrator*, Australian National University (ANU), Canberra, Australia (SolarPACES 2011 proceedings)
- [11] **Coastal Chemical Co. L.L.C.**, 2004: *HITEC Heat Transfer Salt (Datasheet)*, Houston, Texas, USA
- [12] **Coastal Chemical Co. L.L.C.**; E-mail correspondence with Liike T. N., HiTec Global Manager (8.10.2012)

-
- [13] **del Pozo N., Dunn R., Pye J.**, 2011: *Molten salt as heat transfer fluid for a 500 m² dish concentrator*; Australian National University (ANU), Canberra, Australia (SolarPACES 2011 proceedings)
- [14] **Denk T., Valverde A., Diaz R., Soler J. F., Vidal A.**, 2012: *CRS-SSPS Solar tower: A 2.7 MW remodeled test-bed for solar thermal hydrogen production*; PSA-CIEMAT, Tabernas, Spain (SolarPACES 2012 proceedings)
- [15] **DLR** [Online]; *Fresnel reflector at the Plataforma Solar de Almeria*; http://www.dlr.de/en/desktopdefault.aspx/tabid-4530/3681_read-9671/gallery-1/51_read-1/ (17.01.2013)
- [16] **EBSILON® Professional**, 2012: EBSILONProfessional Online Help (integrated in EBSILON® Professional 10.00)
- [17] **Eissa Y., Marpu P. R., Ghedira H., Ouarda T. B. M. J., Chiesa M.**, 2012: *Analyzing temporal and spatial variations of direct normal, diffuse horizontal and global horizontal irradiances estimated from an artificial neural network based model*; Research Center for Renewable Energy Mapping and Assessment, Masdar Institute, Abu Dhabi, UAE
- [18] **Feldhoff J. F., Schmitz K., Eck M., Laing D., Ortiz-Vives F., Schnatbaum-Lauman L., Schulte-Fischedick J.**, 2011: *Comparative System Analysis of Parabolic Trough Power Plants with DSG and Oil using Integrated Thermal Energy Storage*; German Aerospace Center (DLR), Solar Research, Stuttgart, Germany (SolarPACES 2011 proceedings)
- [19] **Florida Power & Light Company** [Online] *Clean Energy for the Next Generation: Martin Next Generation Solar Energy Center*; <http://www.fpl.com/environment/solar/martin.shtml> (23.01.2013)
- [20] **Flueckiger S., Yang Z., Garimella S. V.**, 2011: *An integrated thermal and mechanical investigation of molten-salt thermocline energy storage*; Applied Energy, vol. 88, p. 2098–2105
- [21] **Fragol GmbH & Co. KG**, 2012: *Produktinformation Therminol VP-1*, Mühlheim, Germany
- [22] **García E., Calvo R.**, 2012: *One year operation experience of Gemasolar plant*; SENER ingeniería y sistemas S.A., Getxo, Vizcaya, Spain (SolarPACES 2012 proceedings)
- [23] **Gobereit B., Amsbeck L., Buck R., Pitz-Paal R., Müller-Steinhagen H.**, 2012: *Assessment of a falling solid particle receiver with numerical simulation*; German Aerospace Center (DLR), Institute of Solar Research, Point Focusing Systems, Stuttgart, Germany (SolarPACES 2012 proceedings)
- [24] **Hall A., Ambrosini A., Ho C.**, 2012: *Solar selective coating for concentrating solar power central receivers*; Sandia National Laboratories, Albuquerque, New Mexico; Advanced Materials & Processes, January 2012

-
- [25] **Häberle A., Zahler C., Lerchenmüller H., Mertins M., Wittwer C., Trieb F., Dersch J.**, 2002: *The Solarmundo line focussing Fresnel collector. Optical and thermal performance and cost calculations.*; PSE GmbH, Freiburg, Germany (SolarPACES 2002 Proceedings)
- [26] **Hirsch T. and Giuliani S.** (Institute for Solar Research, DLR, Germany); Phone conference on December 3rd 2012
- [27] **Kattke K., Vant-Hull L. L.**, 2012: *Optimum target reflectivity for heliostat washing*; Abengoa Solar Inc., Lakewood, Colorado, USA (SolarPACES 2012 proceedings)
- [28] **Kitzmilller K., Miller F., Frederickson L.**, 2012: *Design, construction, and preliminary testing of a lab-scale small particle solar receive*; San Diego State University, USA (SolarPACES2012 proceedings)
- [29] **Kraus H.**, 2008: *Grundlagen der Grenzschicht-Meteorologie*, Springer Verlag Berlin/Heidelberg, Germany; ISBN: 978-3-540-78980-5
- [30] **Krüger D., Krüger J., Pandian Y., O'Connell B., Feldhoff J. F., Karthikeyan R., Hempel S., Muniasamy K., Hirsch T., Eickhoff M., Hennecke K.**, 2012: *Experiences with Direct Steam Generation at the Kanchanaburi Solar Thermal Power Plant*; German Aerospace Center (DLR), Solar Research, Köln, Germany (SolarPACES 2012 proceedings)
- [31] **López S., Míguez A., del Hoyo I., Mesonero I.** 2012: *Dynamic modelling of a parabolic test loop focused on molten salt technology*; IK4-TEKNIKER, Mechanical Engineering Unit. Polo Tecnológico de Eibar, Eibar (Gipuzkoa), Spain (SolarPACES 2012 proceedings)
- [32] **Lovegrove K., Luzzi A., Soldiani I., Kreetz H.**, 2004: *Developing ammonia based thermochemical energy storage for dish power plants*; Solar Energy Vol.76, p. 331–337
- [33] **Mancini T. R.**, 2000: *Catalogue of Solar Heliostats*; Sandia National Laboratories, Solar Thermal Technology, Albuquerque, New Mexico, USA
- [34] **Mertins M., Link E., Tscheche E., Henning L.** 2012: *Extended abstract – Experiences of operation of 30MW solarthermal power station based on fresnel collector technology*, Novatec Solar GmbH, Karlsruhe, Germany (SolarPACES 2012 proceedings)
- [35] **Montes M.J., Abbas R., Rovira A., Martinez-Val J.M., Munoz-Anton J.** 2012: *Analysis of linear Fresnel collectors design to minimize optical and geometrical losses*; Universidad Nacional de Educación a Distancia (UNED), Madrid, Spain (SolarPACES 2012 proceedings)
- [36] **Morin G., Kirchberger J., Lemmertz N., Mertins M.** 2012: *Operational results and simulation of a superheating fresnel collector*, Novatec Solar GmbH, Karlsruhe, Germany (SolarPACES 2012 proceedings)

- [37] **Narula M., Gleckman P.** 2012: *Central Receivers vs. Linear Fresnel: A Comparison of Direct Molten Salt CSP Plants*; Areva Solar Inc., Mountain View, California, USA (SolarPACES 2012 proceedings)
- [38] **Nithyanandam K., Pitchumani R.**, 2011: *Analysis and optimization of a latent thermal energy storage system with embedded heat pipes*; Advanced Materials and Technologies Laboratory, Department of Mechanical Engineering, Virginia Tech, Blacksburg, Virginia, USA; International Journal of Heat and Mass Transfer, vol. 54, p. 4596–4610
- [39] **Noone C. J., Torrilhon M., Mitsos A.**, 2012: *Heliostat field optimization: A new computationally efficient model and biomimetic layout*; Solar Energy Vol. 86 p. 792–803
- [40] **Novatec Solar GmbH** [Online]; *Solar Boiler*;
<http://www.novatecsolar.com/20-1-Nova-1.html> (17.01.2013)
- [41] **NREL.gov** [Online]; *Engineering Evaluation of a Molten Salt HTF in a Parabolic Trough Solar Field*; http://www.nrel.gov/csp/troughnet/pdfs/ulf_herrmann_salt.pdf; (23.01.2013)
- [42] **NREL.gov** [Online]; *Ivanpah Solar Electric Generation Station*;
http://www.nrel.gov/csp/solarpaces/project_detail.cfm/projectID=62; (24.01.2013)
- [43] **Oh S., Sung Kwon H., Kodama T., Seo T.**, 2012: *Two-step thermochemical cycles for solar hydrogen production with dish type solar thermal system*; Department of Mechanical Engineering, Inha University, In-cheon, Korea (SolarPACES 2012 proceedings)
- [44] **Ordóñez F., Caliot C., Bataille F., Lauriat G.**, 2012: *Optimization of a spectrally absorbing and anisotropically scattering 1D particle solar receiver*; PROMES Lab., UPR CNRS 8521, Font Romeu, France (SolarPACES 2012 proceedings)
- [45] **Ott T., Konietzko F.**, 2004: *Solarturmkraftwerke*; Solar-Seminar SS 2004: Solare Kraftwerke und Solarzellenkosten, Fachhochschule Kiel, Germany
- [46] **Pacheco J. E., Showalter S. K., Kolb W. J.**, 2001: *Development of a molten-salt thermocline thermal storage system for parabolic trough plants*; Sandia National Laboratories, Solar Thermal Technology Department, Albuquerque, New Mexico, USA (Proceedings of Solar Forum 2001, Solar Energy: The Power to Choose, Washington DC, USA)
- [47] **Pappakokkinos G., Falcoz Q., Py X.**, 2012: *Recycled Ceramics from Vitrified Fly-Ashes as Potential Filler for Thermocline Thermal Energy Storage System - Numerical and Experimental Investigations*, University of Perpignan, France
- [48] **Prieto C., Jove A., Ruiz F., Rodriguez A., Gonzalez E.**, 2012: *Commercial thermal storage: Molten salts vs. Steam accumulators*; Abengoa (SolarPACES 2012 proceedings)

- [49] **Rau C., Alexopoulos S., Breitbach G., Hoffschmidt B., Latzke M., Koll G., Doerbeck T., Sahraoui T., Khedim A., Schrüfer J.**, 2012: *Transient Simulation for Hybrid Solar Tower Power Plant with Open-Volumetric Receiver in Algeria*; FH Aachen, University of Applied Sciences Aachen, Solar-Institut Jülich, Germany (SolarPACES 2012 proceedings)
- [50] **Riffelmann K.-J. Lüpfer E., Richert T., Nava P.** 2012: *Performance of the ultimate trough® collector with molten salt as heat transfer fluid*, Flabeg GmbH, Köln, Germany (SolarPACES 2012 proceedings)
- [51] **Robak C. W., Bergman T. L., Faghri A.**, 2011: *Economic evaluation of latent heat thermal energy storage using embedded thermosyphons for concentrating solar power applications*; Department of Mechanical Engineering, University of Connecticut, 191 Auditorium Road, Storrs, Connecticut, USA; Solar Energy, vol. 85, p. 2461–2473
- [52] **Rogers D., Slack M., Cassity B.**, 2012: *Addressing the Challenges Associated with eSolar's Unique Approach to Central Receiver Power Plants*; eSolar, California, USA (SolarPACES 2012 proceedings)
- [53] **SANDIA National Laboratories** [Online]; *Dish Stirling*
<http://energy.sandia.gov/wp/wp-content/gallery/uploads/Dish-Stirling.jpg>; (22.01.2013)
- [54] **Säck J.-P., Roeb M., Sattler C., Pitz-Paal R., Heinzl A.**, 2012: *Development of a system model for a hydrogen production process on a solar tower*, Solar Energy, Vol. 86 p. 99–111
- [55] **Schlaich J.**, 1995: *The Solar Chimney*; Edition Axel Menges, Stuttgart, Germany; ISBN 3-930698-69-2
- [56] **Schwaiger K., Haider M., Walter H., Puigpinos M., Proetsch A.**, 2012: *Thermal storage of superheated steam in a combined sensible/latent TES*, Institute for Energy Systems and Thermodynamics, Technical University of Vienna, Austria (SolarPACES 2012 proceedings)
- [57] **Schwarzbözl P., Schmitz M., Pitz-Paal R.**, 2009: *Visual HFLCAL, a software tool for layout and optimization of heliostat fields*; German Aerospace Centre, Solar Research, Köln, Germany (SolarPACES 2009 proceedings)
- [58] **Siemens AG** [Online]; *Andasol-1*;
<https://www.cee.siemens.com/web/at/en/corporate/topics4you/articles2009/PublishingImages/AndaSol.jpg>; (21.01.2013)
- [59] **Siemens AG**, 2012: *Neuer Siemens-Receiver UVAC 6G steigert die Effizienz von solarthermischen Kraftwerken (Press release)*; Marrakech, Morocco
- [60] **Siemens AG**, 2011: *SST-700 industrial steam turbines (Brochure)*; Erlangen, Germany
- [61] **Siemens AG**, 2010: *Steam turbines for CSP plants (Brochure)*; Erlangen, Germany

- [62] **Spelling J., Favrat D., Martin A., Augsburg G.**, 2012: *Thermoeconomic optimization of a combined-cycle solar tower power plant*; Energy Vol. 41, p. 113-120
- [63] **SQM Europe N.V.**, 2012: *SQM's Thermo-Solar Salts (Brochure)*, Antwerpen, Belgium (handed out at SolarPACES 2012, Marrakech, Morocco)
- [64] **Stine W. B., Harrigan R. W.**, 1985: *Solar Energy Fundamentals and Design*; John Wiley & Sons, Canada; ISBN 0-471-88718-8
- [65] **Sukhatme S. P., Nayak J. K.**, 2008: *Solar Energy; Principles of Thermal Collection and Storage*; Tata McGraw-Hill, New Delhi, India; ISBN 978-0-07-026064-1; ISBN 0-07-026064-1
- [66] **Suravut S.**, 2011: *The Design for Possible Commercial Medium Insolation Solar Thermal Generation System Using Water as Working Fluid in Hot and Humid Climate*; Asian Renewable Energy Development and Promotion Foundation, Bangkok, Thailand (SolarPACES 2011 proceedings)
- [67] **Tahboub Z. M., Dahleh B., Goebel O.**, 2012: *Solar Mirrors Soiling Campaign – Abu Dhabi*; Masdar Power, Abu Dhabi, United Arab Emirates (SolarPACES 2012 proceedings)
- [68] **Trieb F., Schillings C., O'Sullivan M., Pregger T., Hoyer-Klick C.**, 2009: *Global Potential of Concentrating Solar Power*, German Aerospace Center, Institute of Technical Thermodynamics, Stuttgart, Germany (SolarPACES 2009 proceedings)
- [69] **Verein Deutscher Ingenieure**, 2006: *VDI-Wärmeatlas*; Springer Verlag, Berlin, Germany; ISBN-10: 3-540-25504-4; ISBN-13: 978-3-540-2504-8
- [70] **Vogel W., Kalb H.**, 2010: *Large-Scale Solar Thermal Power (Technologies, Costs and Development)*; WILEY-VCH Verlag GmbH & Co. KGaA, Weinheim, Germany; ISBN 978-3-527-40515-2
- [71] **Wei X., Lu Z., Wang Z., Yu W., Zhang H, Yao Z**, 2010: *A new method for the design of the heliostat field layout for solar tower power plant*; Renewable Energy Vol. 35 p.1970–1975
- [72] **Winter C.-J., Sizmann R. L., Vant-Hull L. L.**, 1991: *Solar Power Plants; Fundamentals, Technology, Systems Economics*; Springer Verlag, Berlin, Germany; ISBN 3-540-18897-5; ISBN 0-387-18897-5
- [73] **www.brightsourceenergy.com** [Online];
http://www.brightsourceenergy.com/stuff/contentmgr/files/0/cfa763e1633b24cd334f4eae9ae2044b/files/3161_ivanpah_mingasson_1.jpg (28.02.2013)

- [74] **www.camelclimatechange.org** [Online]; *Stirling dish system at Plataforma Solar de Almeria, Spain. Source: Sandia National Laboratory*;
<http://www.camelclimatechange.org/articles/view/156097/?topic=65884> (22.01.2013)
- [75] **www.csirosolarblog.com** [Online]; *Gemasolar Heliostat*;
<http://csirosolarblog.com/tag/gemasolar/> (24.01.2013)
- [76] **www.geotimes.org** [Online]; *Desert Power: A Solar Renaissance*
http://www.geotimes.org/apr08/article.html?id=feature_solar.html (22.01.2013)
- [77] **www.hydrogenembassadors.com** [Online]; *Impressions Parabolic trough solar power plant Andasol 1, near Granada, Andalusia, Spain*;
<http://www.hydrogenembassadors.com/meet-aae/andasol/index.php> (15.01.2013)
- [78] **www.renewableenergyfocus.com** [Online];
<http://www.renewableenergyfocus.com/view/17095/csp-developments-in-heat-transfer-and-storage-materials/>; (08.10.2012)
- [79] **www.sdstate.edu** [Online]; *Research interests*;
<http://www.sdstate.edu/chem/faculty/brian-logue/interests.cfm> (26.02.2013)
- [80] **www.thermoconsult.de** [Online]; http://www.thermoconsult.de/01_TechInfo/Stoffwerte.pdf
(15.11.2012)
- [81] **www.torresolenergy.com** [Online];
http://www.torresolenergy.com/EPORTAL_IMGS/GENERAL/SENERV2/IMG2-cw4e412471dd97d/gemasolar-plant-june2011-1b.jpg (28.02.2013)
- [82] **www.verdantliving.blogspot.co.at** [Online]; *Heliostats lifted on pylons*;
<http://verdantliving.blogspot.co.at/2012/11/ivanpahclean-renewable-energy-on.html>
(24.01.2013)
- [83] **ZAMG Steiermark**, Kundenservicestelle Graz, Austria ; Phone talk (05.11.2012)
- [84] **Zanganeh G., Pedretti A., Zavattoni S., Barbato M., Steinfeld A.**, 2012: Packed-bed thermal storage for concentrated solar power – Pilot-scale demonstration and industrial-scale design; *Solar Energy*, vol. 86, p. 3084–3098
- [85] **Zarza E., Valenzuela L.**, 2004: *Direct steam generation in parabolic troughs: Final results and conclusions of the DISS project*. *Energy*, Vol. 29, 5-6, p. 635-644
- [86] **Zavoico A. B.**, 2001: *Solar Power Tower Design Basis Document (Revision 0)*; Nexant, San Francisco, California, USA

- [87] **Zhao** C. Y., **Wu** Z. G., 2011: *Thermal property characterization of a low melting-temperature ternary nitrate salt mixture for thermal energy storage systems*, Solar Energy Materials & Solar Cells 95, p. 3341–3346
- [88] **Zuniga** F., Suntrace GmbH, Hamburg, Germany; e-mail received on April 14th, 2011

APPENDIX

{1} Code of the EbsScript in the Energy Collection Switch Macro

```

// ENERGY COLLECTION SWITCH

var
CalcState_old_Collection:integer;
MAXFLOWPUMP:real;

begin

// ENERGY COLLECTION STARTUP:
// If the solar irradiation EXCEEDS the level for net power production, the
// Energy_collection_system is activated. In this case there are 2 possibilities:
// 1. The level of the hot tank is below the maximum level -> The HTF massflow is restricted
// to MAXFLOWPUMP due to pump restrictions.
// 2. The level of the hot tank is at the maximum level -> The HTF massflow is restricted
// to e.g. 90% of the storage unload massflow not to overflow the hot tank / empty the cold
// tank. If the storage unload massflow is above MAXFLOWPUMP, the HTF massflow is again
// restricted to MAXFLOWPUMP kg/s.
//
// If the Energy_collection_system calc state switches from 0 to 1, the Start_up macro is
// initialized
//
// ENERGY COLLECTION SHUTDOWN:
// If the solar irradiation FALLS BELOW the level for net power production, the
// Energy_collection_system is deactivated.

CalcState_old_Collection := getCalcState("Energy_collection_system");

MAXFLOWPUMP:=Macrointerface.MaxFlowPump;

if ::Sun.DNI >= ::Energy_collection_switch::Energy_collection_system::Heliostat_field.MINTRACK
then
// If the solar irradiation EXCEEDS the level for net power production, the
Energy_collection_system is activated.

    begin
        setCalcState("Value_1",0); // Deactivation of shutdown-values
        setCalcState("Value_2",0); // Deactivation of shutdown-values
        setCalcState("Value_3",0); // Deactivation of shutdown-values
        setCalcState("Value_4",0); // Deactivation of shutdown-values
        setCalcState("Energy_collection_system",1);
        // Activation of the Energy_collection_system macro

        if ::Hot_tank.LEVACT < ::Hot_tank.LEVMAX then
            // Possibility 1: The level of the hot tank is below the maximum level -> The HTF
            massflow is restricted to MAXFLOWPUMP due to pump restrictions.

            begin
                ::Energy_collection_switch::Energy_collection_system::Heliostat_field.M2MAX :=
                MAXFLOWPUMP;
            end

        else
            // Possibility 2: The level of the hot tank is at the maximum level -> The HTF
            massflow is restricted to e.g. 90% of the storage unload massflow not to overflow
            the hot tank / empty the cold tank. If the storage unload massflow is above
            MAXFLOWPUMP, the HTF massflow is again restricted to MAXFLOWPUMP.

            begin

                if ::Hot_tank.MUNLD > MAXFLOWPUMP then

                    begin
                        ::Energy_collection_switch::Energy_collection_system::Heliostat_field.M2MAX
                        := MAXFLOWPUMP;
                    end

                else

                    begin

```

Appendix

```
        ::Energy_collection_switch::Energy_collection_system::Heliostat_field.M2MAX
        := ::Hot_tank.MUNLD * 0.9;
    end;
end;

end

else
// If the solar irradiation FALLS BELOW the level for net power production, the
Energy_collection_system is deactivated.

begin
    setCalcState("Value_1",1); // Activation of shutdown-values
    setCalcState("Value_2",1); // Activation of shutdown-values
    setCalcState("Value_3",1); // Activation of shutdown-values
    setCalcState("Value_4",1); // Activation of shutdown-values
    setCalcState("Energy_collection_system",0);
    // Deactivation of the energy_collection_system macro
end;

// START_UP MACRO INITIALISATION:

if CalcState_old_Collection < getCalcState("Energy_collection_system") then
// If the Energy_collection_system calc state switches from 0 to 1, the Start_up macro is
initialized

begin
    setCalcState("Start_up",1); // Activation of the Start_up macro
    setCalcState("Value_5",0); // Deactivation of shutdown-values
    setCalcState("Value_6",0); // Deactivation of shutdown-values
    setCalcState("Value_7",0); // Deactivation of shutdown-values
end

else

begin
    setCalcState("Start_up",0); // Deactivation of the Start_up macro
    setCalcState("Value_5",1); // Activation of shutdown-values
    setCalcState("Value_6",1); // Activation of shutdown-values
    setCalcState("Value_7",1); // Activation of shutdown-values
end;

end;
```

{2} Code of the EbsScript in the Tank Heaters Macro

```
// TANK HEATERS

begin

if ::Cold_tank.TSTO < 260 then
begin
  ::Cold_tank.TSTO := 260;
  // If tank temperature reaches 260°C, the tank heaters keep it at this temperature
  ::Tank_heaters::Cold_tank::Value.MEASM := ::Cold_tank.QSLOSS +
  ::Energy_conversion_switch::Hold_mode::Measuring_point_1.MEASM;
  // The amount of heat produced by the tank heaters is equal to the tank heat losses plus
  // the steam drum heat consumption
  setCalcState("Cold_tank_1",0);
  setCalcState("Cold_tank_2",0);
  setCalcState("Cold_tank",1);
end
else
begin
  setCalcState("Cold_tank_1",1);
  setCalcState("Cold_tank_2",1);
  setCalcState("Cold_tank",0);
end;

if ::Hot_tank.TSTO < 260 then
begin
  ::Hot_tank.TSTO := 260;
  // If tank temperature reaches 260°C, the tank heaters keep it at this temperature
  ::Tank_heaters::Hot_tank::Value.MEASM := ::Hot_tank.QSLOSS;
  // The amount of heat produced by the tank heaters is equal to the tank heat losses
  setCalcState("Hot_tank_1",0);
  setCalcState("Hot_tank_2",0);
  setCalcState("Hot_tank",1);
end
else
begin
  setCalcState("Hot_tank_1",1);
  setCalcState("Hot_tank_2",1);
  setCalcState("Hot_tank",0);
end;

end;
```

{3} Code of the EbsScript in the Energy Conversion Switch Macro

```

// ENERGY CONVERSION SWITCH

var
CalcState_old_Conversion:integer;

begin

// ENERGY CONVERSION START UP:
// If the level of the hot tank is OVER its minimum level, the Energy_conversion_system macro,
// all efficiencies WILL be calculated and the
// Hold_mode macro WILL NOT be calculated.

// ENERGY CONVERSION SHUT DOWN:
// If the level of the hot tank is AT its minimum level, the Energy_conversion_system macro,
// all efficiencies WILL NOT be calculated and the
// Hold_mode macro WILL be calculated.

CalcState_old_Conversion := getCalcState("Energy_conversion_system");
// Before any calc state is switched, the old one is stored

if ::Hot_tank.LEVACT > ::Hot_tank.LEVMIN +
(::Energy_conversion_switch::Shut_down::Heat_extraction.M1N + ::Hot_tank.MUNLD) * 3600 * 1.02
then // The factor 1.02 avoids tank errors, the factor 3600 is to convert kg/s to kg/h

begin // true block
setCalcState("Energy_conversion_system_1",0);
// Deactivation of the Energy_conversion_system shut down values
setCalcState("Energy_conversion_system_2",0);
// Deactivation of the Energy_conversion_system shut down values
setCalcState("Energy_conversion_system_3",0);
// Deactivation of the Energy_conversion_system shut down values
setCalcState("Energy_conversion_system_4",0);
// Deactivation of the Energy_conversion_system shut down values
setCalcState("Energy_conversion_system_5",0);
// Deactivation of the Energy_conversion_system shut down values
setCalcState("Energy_conversion_system_6",0);
// Deactivation of the Energy_conversion_system shut down values
setCalcState("Energy_conversion_system_7",0);
// Deactivation of the Energy_conversion_system shut down values
setCalcState("Energy_conversion_system_8",0);
// Deactivation of the Energy_conversion_system shut down values
setCalcState("Energy_conversion_system_9",0);
// Deactivation of the Energy_conversion_system shut down values
setCalcState("Hold_mode_1",1); // Activation of the Hold_mode shut down values
setCalcState("Hold_mode_2",1); // Activation of the Hold_mode shut down values
setCalcState("Hold_mode_3",1); // Activation of the Hold_mode shut down values
setCalcState("Hold_mode_4",1); // Activation of the Hold_mode shut down values
setCalcState("Energy_conversion_system",1); // Activation of the Energy_conversion_system macro
setCalcState("Hold_mode",0); // Deactivation of the Hold_mode macro
setCalcState("::Efficiency_gross",1); // Activation of the Efficiency_gross measurement
setCalcState("::Efficiency_net",1); // Activation of the Efficiency_net measurement
setCalcState("::Efficiency_net_total",1); // Activation of the Efficiency_net_total measurement
end

else

begin // false block
setCalcState("Energy_conversion_system_1",1);
// Activation of the Energy_conversion_system shut down values
setCalcState("Energy_conversion_system_2",1);

```

Appendix

```
// Activation of the Energy_conversion_system shut down values
setCalcState("Energy_conversion_system_3",1);
// Activation of the Energy_conversion_system shut down values
setCalcState("Energy_conversion_system_4",1);
// Activation of the Energy_conversion_system shut down values
setCalcState("Energy_conversion_system_5",1);
// Activation of the Energy_conversion_system shut down values
setCalcState("Energy_conversion_system_6",1);
// Activation of the Energy_conversion_system shut down values
setCalcState("Energy_conversion_system_7",1);
// Activation of the Energy_conversion_system shut down values
setCalcState("Energy_conversion_system_8",1);
// Activation of the Energy_conversion_system shut down values
setCalcState("Energy_conversion_system_9",1);
// Activation of the Energy_conversion_system shut down values
setCalcState("Hold_mode_1",0); // Deactivation of the Hold_mode shut down values
setCalcState("Hold_mode_2",0); // Deactivation of the Hold_mode shut down values
setCalcState("Hold_mode_3",0); // Deactivation of the Hold_mode shut down values
setCalcState("Hold_mode_4",0); // Deactivation of the Hold_mode shut down values
setCalcState("Energy_conversion_system",0); // Deactivation of the Energy_conversion_system macro
setCalcState("Hold_mode",1); // Activation of the Hold_mode macro
setCalcState("::Efficiency_gross",0); // Deactivation of the Efficiency_gross measurement
setCalcState("::Efficiency_net",0); // Deactivation of the Efficiency_net measurement
setCalcState("::Efficiency_net_total",0); // Deactivation of the Efficiency_net_total measurement
end;

// START_UP MACRO INITIALISATION:

if CalcState_old_Conversion < getCalcState("Energy_conversion_system") then
// If the Energy_conversion_system calc state switches from 0 to 1, the Start_up macro is
initialized

begin
    setCalcState("Start_up",1); // Activation of the Start_up macro
    setCalcState("Start_up_1",0); // Deactivation of shutdown-values
    setCalcState("Start_up_2",0); // Deactivation of shutdown-values
    setCalcState("Start_up_3",0); // Deactivation of shutdown-values
    setCalcState("Start_up_4",0); // Deactivation of shutdown-values
    setCalcState("Start_up_5",0); // Deactivation of shutdown-values
    setCalcState("Start_up_6",0); // Deactivation of shutdown-values
    setCalcState("Start_up_7",0); // Deactivation of shutdown-values
    setCalcState("Start_up_8",0); // Deactivation of shutdown-values
    setCalcState("Start_up_9",0); // Deactivation of shutdown-values
    setCalcState("Start_up_10",0); // Deactivation of shutdown-values
end

else

begin
    setCalcState("Start_up",0); // Deactivation of the Start_up macro
    setCalcState("Start_up_1",1); // Activation of shutdown-values
    setCalcState("Start_up_2",1); // Activation of shutdown-values
    setCalcState("Start_up_3",1); // Activation of shutdown-values
    setCalcState("Start_up_4",1); // Activation of shutdown-values
    setCalcState("Start_up_5",1); // Activation of shutdown-values
    setCalcState("Start_up_6",1); // Activation of shutdown-values
    setCalcState("Start_up_7",1); // Activation of shutdown-values
    setCalcState("Start_up_8",1); // Activation of shutdown-values
    setCalcState("Start_up_9",1); // Activation of shutdown-values
    setCalcState("Start_up_10",1); // Activation of shutdown-values
end;

// SHUT_DOWN MACRO INITIALISATION:
```

Appendix

```
if CalcState_old_Conversion > getCalcState("Energy_conversion_system") then
// If the Energy_conversion_system calc state switches from 1 to 0, the Shut_down macro is
initialized

begin
    setCalcState("Shut_down",1); // Activation of the Start_up macro
    setCalcState("Shut_down_1",0); // Deactivation of shutdown-values
    setCalcState("Shut_down_2",0); // Deactivation of shutdown-values
    setCalcState("Shut_down_3",0); // Deactivation of shutdown-values
    setCalcState("Shut_down_4",0); // Deactivation of shutdown-values
    setCalcState("Shut_down_5",0); // Deactivation of shutdown-values
    setCalcState("Shut_down_6",0); // Deactivation of shutdown-values
    setCalcState("Shut_down_7",0); // Deactivation of shutdown-values
    setCalcState("Shut_down_8",0); // Deactivation of shutdown-values
    setCalcState("Shut_down_9",0); // Deactivation of shutdown-values
    setCalcState("Shut_down_10",0); // Deactivation of shutdown-values
end

else

begin
    setCalcState("Shut_down",0); // Deactivation of the Start_up macro
    setCalcState("Shut_down_1",1); // Activation of shutdown-values
    setCalcState("Shut_down_2",1); // Activation of shutdown-values
    setCalcState("Shut_down_3",1); // Activation of shutdown-values
    setCalcState("Shut_down_4",1); // Activation of shutdown-values
    setCalcState("Shut_down_5",1); // Activation of shutdown-values
    setCalcState("Shut_down_6",1); // Activation of shutdown-values
    setCalcState("Shut_down_7",1); // Activation of shutdown-values
    setCalcState("Shut_down_8",1); // Activation of shutdown-values
    setCalcState("Shut_down_9",1); // Activation of shutdown-values
    setCalcState("Shut_down_10",1); // Activation of shutdown-values
end;

if CalcState_old_Conversion = 0 then

begin
    ::Efficiency_gross.ETA:=0;
    // Additional set to 0 of the Efficiency_gross measurement to avoid useless values
    ::Efficiency_net.ETA:=0;
    // Additional set to 0 of the Efficiency_net measurement to avoid useless values
    ::Efficiency_net_total.ETA:=0;
    // Additional set to 0 of the Efficiency_net measurement to avoid useless values
end;

// updateModel;
// Optional function to update the model view for every time step to visualize the changes

end;
```

{4} Excel Program for Receiver and Storage Design

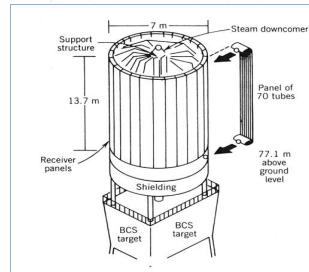
Molten salt (KNO3/NaNO3) central receiver design and detailed analytic solution for ALPHA, DTWDES, DP12N

Only valid for cylindrical receiver types

Calculation procedure for FHLOSS=2 (variable receiver temperature)

*Complemented by a calculation method of combined convection coefficient by C.-J. Winter et. al. 1991: Solar Power Plants, P. 194

Solar One Design (Source: <http://www.governmentresearch.com/Book/chapter20/chapter20.html>)



value read out from EBSILON

editable value

calculated value

calculated value written into EBSILON

Description	Variable	Ebsilon variable	Value	Unit	Formula \ Comment
Receiver diameter	Drec	Solar_tower.RECDIAM	14.57	m	
Receiver height	H	Solar_tower.RECHEI	26.22	m	
Receiver area	A	Solar_tower.AREC	1200	m ²	AREC = RECDIAM * π * RECHEI
Intercept receiver power		Solar_tower.RQINC	375508.7635	kW	
Heat absorbed by fluid	Q.eff	Solar_tower.RQEFF	322814	kW	RQEFF = ETAREC * RQINC
HTF massflow	m.	ThermoLiquid.M	772.383	kg/s	
HTF inlet temperature	T1	ThermoLiquid_1.T	290.00	°C	
HTF outlet temperature	T2	ThermoLiquid.T	565.00	°C	
Mean outside wall temperature	Twa,m	Solar_tower.RTREC	466.58	°C	RTREC = T1 + K * (T2 - T1) + DTWDES * QINC / QINCDES
Mean ambient temperature	Ta,m	Solar_tower.RTAMB	45	°C	For design case or given from time series
Wind speed at receiver height	vw	Solar_tower.RVWIND	3.9	m/s	For design case or given from time series
Forced convection multiplier		Solar_tower.SCONV	1		Value should be set to 1 due to the combined convection calculation method
Number of serial panels	n.pa		1		=1 for flood flow operation; >1 for serpentine flow operation according to Zavoico 2001, P. 61
Number of pipes per serial panel	n.ppp		540		
Pipe wall thickness	d		0.002	m	
Average thermal conductivity (wall)	λa,w		20.5	W/mK	e.g. AISI 316Ti (20.5 W/m ² K at 450°C average wall volume temperature) - VDI Wärmeatlas 2006, Dea 11
Wall roughness factor	rf		1.5708		*rf = π / 2 for rough tube walls
Number of pipes	n		540		n = n.pa * n.ppp
Average HTF temperature	Ta,f		427.50	°C	Ta,f = (T1 + T2) / 2
Outer diameter	Da		0.0270	m	Da = Drec * π / n
Inner diameter	Di		0.0230	m	Di = Da - 2 * d
Inside cross section area	Ai		0.000415	m ²	Ai = Di ² * π / 4
Average HTF Density	ρa,f		1818.1	kg/m ³	f(Ta,f) from SQM solar salt brochure, SolarPaces 2012
Average HTF dynamic viscosity	ηa,f		1.585	mPas	f(Ta,f) from SQM solar salt brochure, SolarPaces 2012
Average HTF kinematic viscosity	υa,f		8.71559E-07	m ² /s	υa = (ηa/1000) * ρa,f
Average HTF volumetric flow	V.a		0.4248	m ³ /s	V.a = m. * ρa,f
Average HTF volumetric flow per pipe	V.a,p		0.000787	m ³ /s	V.a,p = V.a / n.ppp
Average HTF flow velocity	v.a		1.897	m/s	v.a = V.a,p / Ai
Reynolds number	Re		50,010		Re = (Di * v.a) / υa,f
Pipe friction number	ζ		0.0212		Re<2310: ζ = 64/Re Re<10 ⁴ : ζ = 0,3164/Re ^{0,25} Re<10 ⁸ : ζ = [1,8 * log(Re) - 1,5] ^ -2 smooth pipe assumed Beater P.: Entwurf Hydraulischer Maschinen, P. 53
Pressure loss	Δp	Solar_tower.DP12N	0.78934	bar	Δp = ζ * n.pa * H / Di * v.a ² / 2 * ρa,f
Specific heat capacity (HTF)	cp		1517	J/kgK	f(Ta,f) from SQM solar salt brochure, SolarPaces 2012
Thermal conductivity (HTF)	λt		0.524	W/mK	f(Ta,f) from SQM solar salt brochure, SolarPaces 2012
Prandtl Number	Pr		4.584		Pr = (cp * (ηa,f/1000)) / λt
Mean inside wall temperature	Twi,m		466.56	°C	Twi,m = Twa,m - Q.eff / ((2 * λa,w / (Da * LN(Da/Di))) * rf * A)
Average dynamic viscosity (HTF) wall	ηa,f,w		1.409	mPas	f(Twi,m) from SQM solar salt brochure, SolarPaces 2012
Specific heat capacity (HTF) wall	cp,w		1523	J/kgK	f(Twi,m) from SQM solar salt brochure, SolarPaces 2012
Thermal conductivity (HTF) wall	λt,w		0.532	W/mK	f(Twi,m) from SQM solar salt brochure, SolarPaces 2012
Prandtl Number wall	Pr,w		4.038		Pr = (cp,w * (ηa,f,w/1000)) / λt,w
Nusselt number laminar inside	Nu _{i,l}		7.6		Nu _{i,l} = (3,66 ³ +0,664 ³ *Pr*(Re*Di/(H*n.pa)) ^(3/2)) ^(1/3) \ Formelsammlung Wärmetechnik 2, P.2, TU Graz 2012
Nusselt number Re=2300	Nu _{i,2300,i}		3.8		Nu _{i,2300,i} = (3,66 ³ +0,664 ³ *Pr*(2300*Di/(H*n.pa)) ^(3/2)) ^(1/3) \ Formelsammlung Wärmetechnik 2, P.2, TU Graz 2012
Nusselt number Re=10 ⁴	Nu _{i,10⁴,i}		57.2		Nu _{i,10⁴,i} = ((ζ/8) * 10 ⁴ * Pr) / (1+12,7*(ζ/8) ^(1/2) *(Pr ^{(2/3)-1})) * (Pr/Pr,w) ^{0,11} \ Formelsammlung Wärmetechnik 2, P.2, TU Graz 2012 \ VDI Wärmeatlas 2006, Ga 5 (26), Ga 8 (40)
Nusselt number turbulent inside	Nu _{i,t}		286.1		Nu _{i,t} = ((ζ/8) * Re * Pr) / (1+12,7*(ζ/8) ^(1/2) *(Pr ^{(2/3)-1})) * (Pr/Pr,w) ^{0,11} \ Formelsammlung Wärmetechnik 2, P.2, TU Graz 2012 \ VDI Wärmeatlas 2006, Ga 5 (26), Ga 8 (40)
Nusselt number inside	Nu _i		286.1		Re<2300: Nu _i = Nu _{i,l} Re<10 ⁴ : Nu _i = (1-(Re-2300)/7700) * Nu _{i,2300,i} + ((Re-2300)/7700) * Nu _{i,10⁴,i} Re>10 ⁴ : Nu _i = Nu _{i,t} \ Formelsammlung Wärmetechnik 2, P.2, TU Graz 2012 \ VDI Wärmeatlas 2006, Ga 5 (29)
Convection coefficient inside	αi		6525.5	W/m²K	αi = (Nu * λt) / Di
Heat transfer coefficient	k		3502.4	W/m ² K	k = ((Da / (2*λa,w)) * LN(Da/Di) + Da/(Di*αi)) ⁻¹ \ Formelsammlung Wärmetechnik 2, P.1, TU Graz 2012
Design wall temperature difference	ΔT	Solar_tower.DTWDES	48.3	K	ΔT = Q.eff / (k * A * rf)
Average air temperature	Ta,a		260.00	°C	Ta,a = (Tw,m + Ta,m) / 2
Average dynamic viscosity (air)	ηa,a		0.0295	mPas	f(Ta,a) from http://www.thermoconsult.de/01_TechInfo/Stoffwerte.pdf
Average density (air)	ρa,a		0.6620	kg/m ³	ρa,a = 1,013 * 10 ⁵ Pa / (287 J/kgK * (Ta,a + 273,15)) \ ideal gas / 1013mbar
Average kinematic viscosity (air)	υa,a		4.44843E-05	m ² /s	υa,a = (ηa,a/1000) / ρa,a
Average thermal conductivity (air)	λa,a		0.0428	W/mK	f(Ta,a) from http://www.thermoconsult.de/01_TechInfo/Stoffwerte.pdf
Reynolds number outside	Re,o		1.277E+06		*Re,o = (va,m * Drec) / υa,a
Nusselt number forced outside	Nu _{f,o}		2561.6		*Nu _{f,o} = 0,00239 * Re,o ^{0,98} + 0,000945 * Re,o ^{0,89}
Forced convection coefficient out.	αf,o		11.822	W/m²K	*αf,o = (rf * Nu _{f,o} * λa,a) / Drec
Volumetric thermal expansion coeff.	β		0.001876	1/K	*β = 1 / Ta,a
Grashof number	Gr		7.07E+13		*Gr = (g * β * (Twa,m - Ta,m) * H ³) / υa,a ²
Nusselt number natural outside	Nu _{n,o}		2889.4		*Nu _{n,o} = 0,098 * Gr ^{0,333} * (Ta,m/Twa,m) ^{0,14}
Natural convection coefficient out.	αn,o		7.410	W/m²K	*αn,o = (rf * Nu _{n,o} * λa,a) / H
Combined convection coefficient out.	αo		12.594	W/m²K	*αo = (αf,o ³ + αn,o ³) ^(1/3)
Corr. combined convection coefficient out.	αo'	Solar_tower.ALPHA	19.783	W/m²K	αo' = αo * rf Note: AREC is calculated for a smooth receiver, since AREC is locked in Ebsilon, αo must be corrected by a roughness factor

ModelFile C:\Users\Ernst\Desktop\VTU Energy Masterarbeit\Epsilon Simulation\Dokumentiert\SolarTower_MoltenSalt_OwnReproduction - Base load - final.eb

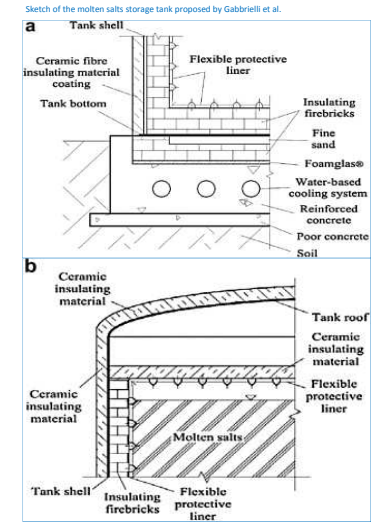
BeginData	Type	Name	Description	Unit	FirstProfile	LastProfile
		@ProfileName			Design	
		@Errors			0	
		@Warnings			0	
		@Status			Success	
		@ExecutionTime			19:12:14	
result		Energy_collection_switch::Energy_Receiver diameter / width / base diameter		m	14.57	
result		Energy_collection_switch::Energy_Receiver height / diameter / length of edge / length of surface line		m	26.22	
result		Energy_collection_switch::Energy_Receiver aperture area (defined by heliostat field matrix)		m ²	1200	
result		Energy_collection_switch::Energy_Calculated incident power on receiver aperture APEC		kW	375508.763	
result		Energy_collection_switch::Energy_Heat absorbed by fluid		kW	322813.661	
result		ThermoLiquid.M	Mass flow	kg/s	772.382712	
result		ThermoLiquid_1.T	Temperature	°C	290	
result		ThermoLiquid.T	Temperature	°C	565	
result		Energy_collection_switch::Energy_Effective receiver temperature		°C	466.582655	
result		Energy_collection_switch::Energy_Ambient temperature used in calculation		°C	45	
result		Energy_collection_switch::Energy_Wind speed used in calculation		m/s	3.9	
result		Energy_collection_switch::Energy_Correction factor for wind impact used in calculator		-	1	
result		Energy_collection_switch::Energy_Receiver efficiency =RQEFF/RQINC		-	0.85967011	
spec		Energy_collection_switch::Energy_Pressure drop (nominal)		bar	0.78934	
spec		Energy_collection_switch::Energy_Design wall temperature difference		K	48.9	
spec		Energy_collection_switch::Energy_Convective heat loss coefficient		W/m ² K	19.78	
EndData						

Molten salt (KNO3/NaNO3) storage tank design and detailed analytic solution for QLOSSR, LEVMIN, LEVMAX, LEVACT

Please ensure to switch to decimal points in Excel options to avoid errors concerning the export of the QLOSSR value
 For Hot_tank: LEVACT = LEVMIN | For Cold_tank: LEVACT = LEVMAX

value read out from EBSILON	
editable value	
calculated value	
calculated value written into EBSILON	

Description	Variable	Epsilon variable	Value	Unit	Formula \ Comment
Ambient temperature	T,amb	Solar_tower.RTAMB	45	°C	
Hot tank nominal temperature (HTF)	T,hot	Hot_tank.TNEW	565	°C	
Cold tank nominal temperature (HTF)	T,cold	Cold_tank.TNEW	290	°C	
Total energy capacity	Q,tot		1,354	MWh th	
Area specific heat loss, hot tank	kΔT,hot		75	W/m ²	outside and inside α neglected, Solar two: 75 W/m ²
Area specific heat loss, cold tank	kΔT,cold		200	W/m ²	outside and inside α neglected, Solar two: 200 W/m ²
Free board (Ullage gas)	H,f		1.30	m	Should be around 1,3m according to Zavoico 2001, P.75
Heel level (HTF)	H,min		1.00	m	Should be around 1m according to Zavoico 2001, P.75
Pump barrel length	H,p		14.00	m	Should be ≤ 14m according to Zavoico 2001, P. 75
Usable height	H,u		11.70	m	H,u = H,p - H,f - H,min
Storage height (inside)	H		14.00	m	H = H,p
Average temperature (HTF)	T,m		427.5	°C	T,m = (T,hot+T,cold)/2
Average specific heat capacity (HTF)	cp,m		1517	J/kgK	f(T,m) from SQM solar salt brochure, SolarPaces 2012
Usable capacity	m,u		11,688	t	m,u = (Q,tot*1000000*3600/(cp,m*(T,hot-T,cold)))/1000
Minimum level	m,min	..._tank.LEVMIN	999.0	t	m,min = (m,u / H,u) * H,min
Maximum level	m,max	..._tank.LEVMAX	12686.9	t	m,max = m,u + m,min
Hot tank Density (HTF)	ph,f		1730.7	kg/m ³	f(T,hot) from SQM solar salt brochure, SolarPaces 2012
Maximum needed volume	V,max		8081.1	m ³	V,max = (m,max/(ph,f/1000))*(1+(H,f/(H,u+H,min)))
Storage diameter (inside)	D		27.110	m	D = ((4 * V,max) / (Pi() * H))^(1/2)
Storage surface (inside)	A		2346.8	m ²	A = 2 * (D^2*PI())/4 + D*π*H
Required k-Value (hot tank insulation)	k,req,h		0.144	W/m ² K	k,req,h = kΔT,hot / (T,hot - T,amb)
Required k-Value (cold tank insulation)	k,req,c		0.816	W/m ² K	k,req,c = kΔT,cold / (T,cold - T,amb)
Heat loss hot tank	Q,loss,h		176.0	kW	Q,loss,h = kΔT,hot * A / 1000
Heat loss cold tank	Q,loss,c		469.4	kW	Q,loss,c = kΔT,cold * A / 1000
Temperature specific heat loss (hot tank)	Q,loss,ts,h	Hot_tank.QLOSSR	0.338479	kW/K	Q,loss,ts,h = Q,loss,h / (T,hot -T,amb)
Temperature specific heat loss (cold tank)	Q,loss,ts,c	Cold_tank.QLOSSR	1.915742	kW/K	Q,loss,ts,c = Q,loss,c / (T,cold -T,amb)



ModelFile C:\Users\Ernst\Desktop\VTU Energy Masterarbeit\Epsilon Simulation\Dokumentiert\SolarTower_MoltenSalt_OwnReproduction - Base load - final.eb

BeginData	Type	Name	Description	Unit	FirstProfile	LastProfile
		@ProfileName			Design	
		@Errors			0	
		@Warnings			0	
		@Status			Success	
		@ExecutionTime			13:49:18	
	result	Energy_collection_switch::Energy_Ambient temperature used in calculation		°C	45	
	result	Hot_tank.TNEW	New temperature (at the end of time interval)	°C	565	
	result	Cold_tank.TNEW	New temperature (at the end of time interval)	°C	290	
	spec	Hot_tank.LEVMIN	Minimum level	t	999	
	spec	Hot_tank.LEVMAX	Maximum level	t	12,687	
	spec	Hot_tank.LEVACT	Actual level (at the start of the time interval)	t	999	
	spec	Hot_tank.QLOSSR	Specific heat loss	kW/kgK	0.338479	
	spec	Cold_tank.LEVMIN	Minimum level	t	999	
	spec	Cold_tank.LEVMAX	Maximum level	t	12,687	
	spec	Cold_tank.LEVACT	Actual level (at the start of the time interval)	t	12,687	
	spec	Cold_tank.QLOSSR	Specific heat loss	kW/kgK	1.915742	
EndData						